

The Effect of Velocity and Orientation on the Simulation and
Experimental Characterization of an AUV Tunnel Thruster

by

Aaron Saunders

B. Eng., University of Alberta, 2000

A Thesis Submitted in Partial Fulfillment of the
Requirements for the Degree of

MASTER OF APPLIED SCIENCE

in the Department of Mechanical Engineering.

We accept this thesis as conforming
to the required standard


Dr. M. Nahon, Supervisor (Department of Mechanical Engineering)


Dr. Z. Dong, Departmental Member (Department of Mechanical Engineering)


Dr. J. Collins, Outside Member (Department of Electrical Engineering)


Dr. R. Lueck, External Examiner (Department of Earth and Ocean Sciences)

© AARON SAUNDERS, 2002

University of Victoria

All rights reserved. This thesis may not be reproduced in whole or in part, by
photocopy or other means, without permission of the author.

Supervisor: Dr. M. Nahon

Abstract

Streamlined Autonomous Underwater Vehicles (AUV's) have traditionally been used in high-speed missions that require the vehicle to traverse long distances. Missions such as profiling of salinity and temperature of large-scale water phenomena like the Gulf Stream required measurements to be taken over many hundreds of kilometers. Some new applications require an AUV capable of completing missions including both high-speed straight-line runs and slow maneuvers or station keeping tasks. These missions could include oceanographic sampling, environmental monitoring, iceberg profiling, and pipeline inspection. At low, or zero, forward speeds the AUV's control surfaces become ineffective, and this presents difficulties in accommodating these types of missions. To enable or improve an AUV's low speed maneuverability, while maintaining a low drag profile, through-body tunnel thrusters have become a popular addition to modern AUV systems.

Small underwater vehicles react quickly to changes in the magnitude and direction of thrust. This causes the overall system dynamics during low speed maneuvering to be strongly affected by the dynamics of the thrusters themselves. Improvements in the mathematical models used to describe the dynamics of underwater thrusters have led to improved control systems, capable of precise low speed maneuvering. Presently there are several dynamic models that have been developed to represent the performance of tunnel thrusters. However, these models do not include the effects of forward vehicle motion or yawed orientation on 'through-body' thrust performance.

In order to adapt the current tunnel thruster models to include the effects of vehicle motion, an experimental system was designed to characterize the effects of forward vehicle speed and yaw angle on tunnel thruster performance. This full scale system includes a transverse tunnel thruster mounted in a streamlined AUV. A 6-axis load cell balance mounted internally was used to measure the thrust directly. The AUV was attached to a yaw plate assembly in Memorial University of Newfoundland's tow tank, and several tests were run to characterize the effect of vehicle motion on the transient and steady state thruster performance. This thesis will present and discuss the experimental setup as well as the results obtained from the tow tank tests. The trends shown by the experimental results are highlighted and the relevant parameters which affect thruster performance are identified. Finally, a conventional thruster model is modified to include the effect of these parameters.

Examiners:



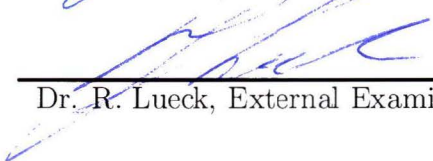
Dr. M. Nahon, Supervisor (Department of Mechanical Engineering)



Dr. Z. Dong, Departmental Member (Department of Mechanical Engineering)



Dr. J. Collins, Outside Member (Department of Electrical Engineering)



Dr. R. Lueck, External Examiner (Department of Earth and Ocean Sciences)

Table of Contents

Abstract	ii
Table of Contents	iv
List of Figures	vii
List of Tables	xiii
Nomenclature	xiv
Acknowledgements	xv
1 Introduction	1
1.1 AUV Technology	1
1.2 C-SCOUT Development	3
1.3 URV Propulsion	6
1.3.1 Main Propulsor	6
1.3.2 Maneuvering Propulsor	7
1.4 Literature Review	8
1.4.1 Ship Maneuvering	8
1.4.2 Propeller Modeling	8
1.4.3 Tunnel Thruster Modeling	10
1.4.4 Experimental Validation	11
1.5 Scope of Thesis	12
2 Experimental Thruster System	14
2.1 Experimental Interface	16
2.2 Data Acquisition and Control	17
2.3 Motor Controller/Amplifier	18
2.4 Tunnel Thruster Unit	20
2.4.1 General Description	20
2.4.2 Propeller	21

2.4.3	Servo Motor	22
2.4.4	Tunnel Thruster Assembly	23
2.4.4.a	Gearing	23
2.4.4.b	Thruster Leg	24
2.4.4.c	Thruster Assembly	26
2.4.5	C-SCOUT Module Configuration	26
2.5	Force/Torque Sensor	28
2.5.1	Sensor Specifications	28
2.5.2	Waterproof Housing	30
2.5.3	Sensor Mounting	31
3	Small Tank Testing	33
3.1	Experimental Setup	34
3.1.1	Tank Design	34
3.1.2	Test Considerations	36
3.2	Small Tank Results	39
3.2.1	Steady State Tests	39
3.2.2	Transient Tests	40
3.3	Small Tank Test Conclusions	41
4	Tow Tank Testing	47
4.1	Experimental Setup	48
4.1.1	Tow Tank	49
4.1.2	C-SCOUT Model	50
4.1.3	Test Considerations	52
4.2	Test Procedure	53
4.3	Tow Tank Results	54
4.3.1	Steady State Tests	55
4.3.1.a	Maneuvering Range	58
4.3.1.b	Forward Travel	59
4.3.1.c	High Speed Turning	63
4.3.2	Transient Tests	65
4.4	Testing Conclusions	66
5	Modeling	71
5.1	Steady State Modeling	72
5.2	Transient Modeling	72
5.2.1	Propeller Model	73
5.2.1.a	Conventional Open-Water Propeller Data Method	73
5.2.1.b	Blade Element Method	76
5.2.2	Static Thruster Hydrodynamic Model	79

5.2.3	Basic Simulation	82
5.3	Modeling the Effects of Forward Vehicle Speed and Orientation . . .	85
5.3.1	Augmented Simulation	87
5.4	Simulation Results	90
5.4.1	Basic Model	90
5.4.1.a	Steady State Simulation Results	91
5.4.1.b	Transient Simulation Results	91
5.4.2	Augmented Model	96
5.4.2.a	Steady State Simulation Results	97
5.4.2.b	Transient Simulation Results	102
6	Conclusions and Recommendations	106
6.1	Experimental System Design and Testing	106
6.2	Modeling and Simulation	109
6.3	Recommendations	110
6.4	Future Work	110
A	Experimental Results	112
B	LabVIEW	159
B.1	LabVIEW Program	159
B.2	Data File Structure	168
C	Simulink Diagrams	169
C.1	Basic Simulation Simulink Program	169
C.2	Augmented Simulation Simulink Program	171
	References	175

List of Figures

1.1	C-SCOUT Configurations: BC- Base Configuration and FAC- Fully Actuated Configuration	4
1.2	C-SCOUT FAC Tunnel Thruster Locations	5
1.3	Four-Quadrant Propeller Operation	10
2.1	Thruster System Schematic	15
2.2	LabVIEW Experimental Graphical User Interface	17
2.3	Experimental Interface	18
2.4	Maxon Motor Controller	19
2.5	Thruster Schematic	20
2.6	Propeller Fabrication at IMD	21
2.7	Gear Box	23
2.8	Thruster Leg Diagram	25
2.9	Thruster Unit	27
2.10	Tunnel Thruster Module Mounted in C-SCOUT Test Model	28
2.11	Tunnel Thruster Module	29
2.12	ATI F/T 6-axis Loadcell	30
2.13	Loadcell Mounted in C-SCOUT thruster Module	31
3.1	Small Tank Setup	34
3.2	Small Testing Tank	35
3.3	Thruster Unit Mounted in Testing Tank	36
3.4	Power Spectrum of Fx After Disturbances	37
3.5	Current Control vs Speed Control	38
3.6	Steady State Axial Thrust	43
3.7	Long Period Triangular Wave Response	44
3.8	Short Period Triangular Wave Response	44
3.9	Square Wave Response	45
3.10	Square Wave Response with no Tunnel	45
3.11	Experimental Results from Healey <i>et al.</i> [12]	46
3.12	Experimental Results from Healey <i>et al.</i> [12]	46

4.1	Side View and Cutaway of the Experimental Tunnel Configuration . .	48
4.2	Tow Tank Facility	49
4.3	C-SCOUT Model Mounted On Tow Tank Carriage	50
4.4	C-SCOUT Experimental Setup	51
4.5	Body Axes Definitions	52
4.6	Tow Tank Test Matrix	54
4.7	Experimental Thruster Outlet Cases	55
4.8	Yaw -50 [deg], Carriage Speed 0.4 [m/s]	57
4.9	Yaw 50 [deg], Carriage Speed 0.4 [m/s]	57
4.10	Maneuvering Range Axial Thrust Intercept Values	60
4.11	Maneuvering Range Axial Thrust Slope Values	60
4.12	Forward Travel Axial Thrust Intercept Values	62
4.13	Forward Travel Axial Thrust Slope Values	62
4.14	Side-Slip Range Axial Thrust Intercept Values	64
4.15	Side-Slip Range Axial Thrust Slope Values	64
4.16	Square Wave Response, Yaw Angle 50 [deg]	67
4.17	Square Wave Response, Yaw Angle 30 [deg], Raw Data	67
4.18	Square Wave Response, Yaw Angle -30 [deg], Aligned at First Step .	68
4.19	Square Wave Response, Yaw Angle 30 [deg], Aligned at First Step . .	68
4.20	Square Wave Response, Yaw Angle 20 [deg], Aligned at First Step . .	69
4.21	Square Wave Response, Carriage Speed 0.4 [m/s], Aligned at First Step	69
5.1	Typical Propeller Performance Curves [9]	74
5.2	Four-Quadrant Propeller Operation, Figure 1.3 reproduced here for convenience.	75
5.3	Tunnel Configuration	76
5.4	System Block Diagram from [12] (Note: Block diagram symbols are different than those used in this thesis)	83
5.5	System Block Diagram for the Basic Simulation	84
5.6	System Block Diagram for the Augmented Tunnel Thruster Model . .	89
5.7	Basic Model Thrust Compared with Experimental Data, Forward Ramp Control	92
5.8	Basic Model Thrust Compared with Experimental Data, Reverse Ramp Control	92
5.9	Basic Model Thrust Compared with Experimental Data, Square Wave Control	94
5.10	Basic Model Thrust Compared with Experimental Data, Sine Wave Control	94
5.11	Basic Model Thrust Compared with Experimental Data, Ramp, V_{carriage} $= 0.1$ [m/s] and $\text{Yaw} = 0$ [deg]	95

5.12	Basic Model Thrust Compared with Experimental Data, Square, $V_{\text{carriage}} = 0.1$ [m/s] and Yaw = 0 [deg]	95
5.13	Basic Model Thrust Compared with Experimental Data, Ramp, $V_{\text{carriage}} = 0.5$ [m/s] and Yaw = 90 [deg]	95
5.14	Basic Model Thrust Compared with Experimental Data, Square, $V_{\text{carriage}} = 0.5$ [m/s] and Yaw = 90 [deg]	95
5.15	Model Thrust Compared with Experimental Data, Ramp Control, $V_{\text{carriage}} = 0.1$ [m/s] and Yaw = 0 [deg]	99
5.16	Model Thrust Compared with Experimental Data, Ramp Control, $V_{\text{carriage}} = 0.2$ [m/s] and Yaw = -70 [deg]	99
5.17	Model Thrust Compared with Experimental Data, Ramp Control, $V_{\text{carriage}} = 2.5$ [m/s] and Yaw = 0 [deg]	99
5.18	Model Thrust Compared with Experimental Data, Ramp Control, $V_{\text{carriage}} = 0.2$ [m/s] and Yaw = 70 [deg]	99
5.19	Model Thrust Compared with Experimental Data, Ramp Control, $V_{\text{carriage}} = 0.3$ [m/s] and Yaw = -20 [deg]	100
5.20	Model Thrust Compared with Experimental Data, Ramp Control, $V_{\text{carriage}} = 0.4$ [m/s] and Yaw = -50 [deg]	100
5.21	Model Thrust Compared with Experimental Data, Ramp Control, $V_{\text{carriage}} = 0.3$ [m/s] and Yaw = 20 [deg]	100
5.22	Model Thrust Compared with Experimental Data, Ramp Control, $V_{\text{carriage}} = 0.4$ [m/s] and Yaw = 50 [deg]	100
5.23	Model Thrust Compared with Experimental Data, Ramp Control, $V_{\text{carriage}} = 0.5$ [m/s] and Yaw = -90 [deg]	101
5.24	Model Thrust Compared with Experimental Data, Ramp Control, $V_{\text{carriage}} = 1.5$ [m/s] and Yaw = -10 [deg]	101
5.25	Model Thrust Compared with Experimental Data, Ramp Control, $V_{\text{carriage}} = 0.5$ [m/s] and Yaw = 90 [deg]	101
5.26	Model Thrust Compared with Experimental Data, Ramp Control, $V_{\text{carriage}} = 1.5$ [m/s] and Yaw = 10 [deg]	101
5.27	Model Thrust Compared with Experimental Data, Square Wave Control, $V_{\text{carriage}} = 0.1$ [m/s] and Yaw = 0 [deg]	103
5.28	Model Thrust Compared with Experimental Data, Square Wave Control, $V_{\text{carriage}} = 0.2$ [m/s] and Yaw = -70 [deg]	103
5.29	Model Thrust Compared with Experimental Data, Square Wave Control, $V_{\text{carriage}} = 2.5$ [m/s] and Yaw = 0 [deg]	103
5.30	Model Thrust Compared with Experimental Data, Square Wave Control, $V_{\text{carriage}} = 0.2$ [m/s] and Yaw = 70 [deg]	103
5.31	Model Thrust Compared with Experimental Data, Square Wave Control, $V_{\text{carriage}} = 0.3$ [m/s] and Yaw = -20 [deg]	104

5.32	Model Thrust Compared with Experimental Data, Square Wave Control, $V_{\text{carriage}} = 0.4$ [m/s] and Yaw = -50 [deg]	104
5.33	Model Thrust Compared with Experimental Data, Square Wave Control, $V_{\text{carriage}} = 0.3$ [m/s] and Yaw = 20 [deg]	104
5.34	Model Thrust Compared with Experimental Data, Square Wave Control, $V_{\text{carriage}} = 0.4$ [m/s] and Yaw = 50 [deg]	104
5.35	Model Thrust Compared with Experimental Data, Square Wave Control, $V_{\text{carriage}} = 0.5$ [m/s] and Yaw = -90 [deg]	105
5.36	Model Thrust Compared with Experimental Data, Square Wave Control, $V_{\text{carriage}} = 1.5$ [m/s] and Yaw = -10 [deg]	105
5.37	Model Thrust Compared with Experimental Data, Square Wave Control, $V_{\text{carriage}} = 0.5$ [m/s] and Yaw = 90 [deg]	105
5.38	Model Thrust Compared with Experimental Data, Square Wave Control, $V_{\text{carriage}} = 1.5$ [m/s] and Yaw = 10 [deg]	105
A.1	Values for Intercept, Data Fit for Steady State Tests	113
A.2	Values for Intercept, Data Fit for Steady State Tests	114
A.3	Detailed Test Matrix and File Name Convention	115
A.4	Tow Tank Data, Test Matrix Elements A01 to A04	116
A.5	Tow Tank Data, Test Matrix Elements A05 to A08	117
A.6	Tow tank Data, Test Matrix Elements A09 to A12	118
A.7	Tow tank Data, Test Matrix Elements A13 to B03	119
A.8	Tow tank Data, Test Matrix Elements B04 to B07	120
A.9	Tow tank Data, Test Matrix Elements B08 to B11	121
A.10	Tow tank Data, Test Matrix Elements B12 to C02	122
A.11	Tow tank Data, Test Matrix Elements C03 to C06	123
A.12	Tow tank Data, Test Matrix Elements C07 to C10	124
A.13	Tow tank Data, Test Matrix Elements C11 to D01	125
A.14	Tow tank Data, Test Matrix Elements D02 to D05	126
A.15	Tow tank Data, Test Matrix Elements D06 to D09	127
A.16	Tow tank Data, Test Matrix Elements D10 to D13	128
A.17	Tow tank Data, Test Matrix Elements E01 to E04	129
A.18	Tow tank Data, Test Matrix Elements E05 to E08	130
A.19	Tow tank Data, Test Matrix Elements E09 to E12	131
A.20	Tow tank Data, Test Matrix Elements E13 to F07	132
A.21	Tow tank Data, Test Matrix Elements F08 to G06	133
A.22	Tow tank Data, Test Matrix Elements G07 to G09	134
A.23	Tow tank Data, Test Matrix Elements H05 to H08	135
A.24	Tow tank Data, Test Matrix Elements H09 to I08	136
A.25	Tow tank Data, Test Matrix Elements J07 to K07	137
A.26	Tow tank Data, Test Matrix Elements M01 to M04	138

A.27	Tow Tank Data, Test Matrix Elements M05 to M08	139
A.28	Tow tank Data, Test Matrix Elements M09 to M12	140
A.29	Tow tank Data, Test Matrix Elements M13 to N03	141
A.30	Tow tank Data, Test Matrix Elements N04 to N07	142
A.31	Tow tank Data, Test Matrix Elements N08 to N11	143
A.32	Tow tank Data, Test Matrix Elements N12 to O02	144
A.33	Tow tank Data, Test Matrix Elements O03 to O06	145
A.34	Tow tank Data, Test Matrix Elements O07 to O10	146
A.35	Tow tank Data, Test Matrix Elements O11 to P01	147
A.36	Tow tank Data, Test Matrix Elements P02 to P05	148
A.37	Tow tank Data, Test Matrix Elements P06 to P09	149
A.38	Tow tank Data, Test Matrix Elements P10 to P13	150
A.39	Tow tank Data, Test Matrix Elements Q01 to Q04	151
A.40	Tow tank Data, Test Matrix Elements Q05 to Q08	152
A.41	Tow tank Data, Test Matrix Elements Q09 to Q12	153
A.42	Tow tank Data, Test Matrix Elements Q13 to R07	154
A.43	Tow tank Data, Test Matrix Elements R08 to S06	155
A.44	Tow tank Data, Test Matrix Elements S07 to S09	156
A.45	Tow tank Data, Test Matrix Elements T05 to T08	157
A.46	Tow tank Data, Test Matrix Elements T09 to U08	158
B.1	LabVIEW Program: Main Diagram Part 1 of 2	161
B.2	LabVIEW Program: Main Diagram Part 2 of 2	162
B.3	LabVIEW Program: Sequence 1, Frame 1	163
B.4	LabVIEW Program: Sequence 1, Frame 2	163
B.5	LabVIEW Program: Sequence 1, Frame 3	164
B.6	LabVIEW Control Wave Program: Main Frame, with Sub Frame 4	164
B.7	LabVIEW Control Wave Program: Sub Frame 0, Sine Wave	165
B.8	LabVIEW Control Wave Program: Sub Frame 1, Square Wave	165
B.9	LabVIEW Control Wave Program: Sub Frame 2, Triangular Wave	165
B.10	LabVIEW Control Wave Program: Sub Frame 3, Step Wave	166
B.11	LabVIEW Control Wave Program: Sub Frame 5, Contant Forward Speed	166
B.12	LabVIEW Control Wave Program: Sub Frame 6, Contant Reverse Speed	166
B.13	LabVIEW Program: Case 1, State TRUE	166
B.14	LabVIEW Program: Case 2, State FALSE	167
B.15	LabVIEW Program: Case 3, State TRUE	167
B.16	Data File Structure	168
C.1	Basic Simulation Simulink Diagram	169
C.2	Sub System: 1	171
C.3	Sub System: S1	172

C.4	Augmented Simulation Simulink Diagram	172
C.5	Sub System: 2	173
C.6	Sub System: S2-1	174
C.7	Sub System: S2-2	174
C.8	Sub System: 3	174
C.9	Sub System: 4	174

List of Tables

5.1	Model Parameters for the Basic Simulation.	91
5.2	Model Parameters for the Augmented Simulation.	97

Nomenclature

Symbol	Description	Units
A	cross sectional tunnel area	m^2
C_L	propeller blade lift coefficient	
C_D	propeller blade drag coefficient	
D	propeller blade drag	N
F_a	propeller hydrodynamic axial force	N
F_p	propeller hydrodynamic tangential force	N
J	advance ratio	$\frac{1}{\text{rev}}$
K_T	propeller thrust coefficient	$\frac{1}{\text{rev}^2}$
K_Q	propeller torque coefficient	$\frac{1}{\text{rev}^2}$
l	tunnel duct length	m
L	propeller blade lift	N
P	propeller geometric pitch	m/rad
Q	volumetric flow rate in tunnel	m^3/s
T_p	propeller hydrodynamic torque load	Nm
U_a	axial fluid velocity in tunnel	m/s
U_p	tangential water velocity	m/s
U_∞	fluid velocity far upstream of propeller	m/s
U_w	axial fluid velocity in wake	m/s
V_a	velocity of advance	m/s
α	angle of incidence (fluid / blade angle of attack)	radian
γ	added mass coefficient	
$\Delta\beta$	flux moment coefficient	
η	propeller efficiency ($0 \leq \eta \leq 1$)	
θ	hydrodynamic pitch angle	rad
μ	dynamic viscosity	N-s/ m^2
ρ	fluid density	kg/m^3
ϕ	propeller pitch angle	radian
ω_p	propeller rotational speed	rad/s

Acknowledgements

I would like to express my deepest gratitude to all those who have supported me throughout my education.

First and foremost, I would like to thank my supervisor, Professor Meyer Nahon. Every challenge along the way was met with excellent guidance and support. His patience and genuine interest in his students and their work made him an excellent supervisor.

I would like to thank Professors Roger Toogood and Mark Ackerman for encouraging me to continue on to do this M.A.Sc degree.

I would like to thank my fellow graduate students, especially Juan Antonio Carretero and Brad Buckham, for lending their ears and minds.

I would also like to thank the members of the research group located at the Memorial University of Newfoundland and the Institute for Marine Dynamics in St. Johns. Their support and cooperation was vital in successfully traveling across Canada to complete experimental testing. Financial support for this project came from the Natural Sciences and Engineering Research Council of Canada (NSERC) through a Strategic Research Grant entitled "Ocean Environmental Risk Engineering Using Autonomous Underwater Vehicles".

And finally, and most importantly, I would like to thank Laura who selflessly and lovingly followed me to a different province so that I could continue my education.

To Laura, your unconditional love and support has made it all possible.

To my Mother and Father for all the years of guidance to get me here.

To my Grandparents for the constant encouragement, specially to my GranAnne
who has always told me the bar was never too high.

And to the rest of my family and friends, thank you for your support.

Chapter 1

Introduction

Underwater vehicles have become standard tools for completing various research and industrial tasks in the undersea world. Presently, Autonomous Underwater Vehicle (AUV) technology has advanced to a point where it has begun to show commercial viability. The motivation behind this thesis is to improve the understanding of a particular form of AUV propulsion, tunnel thrusters, in order to contribute to the development of offshore environmental engineering using AUV technology.

1.1 AUV Technology

An AUV is a self-propelled underwater vehicle capable of performing a predetermined mission without the need for direct human interaction. AUVs can be hundreds of miles from any support vessel or shoreline, and completely out of contact for long periods of time. These missions could include things like oceanographic sampling, environmental monitoring, iceberg profiling, pipeline surveys, searching for lost wrecks, under-ice surveys, pipeline tracking and inspection, and military applications such

as mine detection and counter measures. AUVs are particularly suited to hazardous applications because they reduce the risk to human life and equipment through direct connection with a surface support team. Eliminating direct contact with a support vessel makes AUV systems well suited for the types of missions mentioned above. This autonomy is the defining feature of an AUV; but it is also what makes these vehicle systems extremely complicated. Data storage/transmission, vehicle power systems, and the ability to make simple 'decisions' now have to be carried directly on the vehicle rather than being transferred through a tether.

Streamlined AUVs have traditionally been used in high-speed missions that require the vehicle to cover large distances or long missions that require high endurance. Missions, such as salinity and temperature profiling of large-scale water phenomena like the Gulf Stream, require measurements to be taken over many hundreds of kilometers. Tasks that involve precision positioning, have in most cases, been beyond the capabilities of streamlined AUVs. Missions that involve positioning generally make use of bluff bodied Remotely Operated Vehicles (ROV). ROVs are usually cage style vehicles designed with high maneuverability in mind. This is often achieved by mounting several thrusters as far apart as possible on the perimeter of the vehicle. Unfortunately this configuration dramatically increases the overall drag of the vehicle. Bluff bodied ROVs also have important limitations: firstly they are generally unable to cover a large grid fast enough to accurately measure large scale dynamic phenomena and secondly they have severe range constraints imposed by the direct connection of the vehicle through a tether. By contrast, streamlined AUV's are designed to have low hydrodynamic drag, enabling them to move efficiently through the water, a major consideration for a vehicle that must carry its own power supply

over long distances.

Streamlined AUVs generally use hydrodynamic control surfaces that are rotated to steer the vehicle. These control surfaces require the hydrodynamic force of moving water to create a turning force which poses major limitations for low speed operations. One way to enable this type of vehicle to complete low speed station-keeping tasks is to add additional control thrusters. Adding external thrusters would have a major effect on the AUV's low drag profile. In order to provide the increased maneuverability at low speeds without changing the low drag profile of the AUV, 'through-body' thrusters, commonly referred to as tunnel thrusters, can be added. Several AUVs such as the NPS ARIES [14], NPS PHOENIX, Proteus [26], C-SCOUT [10], OTTER [24], CETUSTM, and REDERMOR [13] make use of tunnel thrusters for low speed maneuverability. Adding tunnel thrusters enables the vehicle to travel long distances at high speeds to a desired destination and then perform tasks that require station keeping such as environmental inspection. This effectively merges the maneuverability strengths of ROVs with the hydrodynamic efficiency of AUVs.

1.2 C-SCOUT Development

The C-SCOUT (Canadian Self-Contained Off-the-shelf Underwater Testbed) AUV [10] is part of an NSERC Strategic Project entitled "Offshore Environmental Engineering Using Autonomous Underwater Vehicles". The C-SCOUT testbed was designed to enable graduate level research in various vehicle systems, including tunnel thrusters. The research project is concerned with the development of AUVs for environmental missions in assessing the impact of discharges from offshore oil and gas

operations. The project is based at Memorial University of Newfoundland (MUN) and the work is being done in conjunction with the National Research Council's Institute for Marine Dynamics (NRC-IMD), the University of Victoria, Petro-Canada, ISE Ltd., and Geo-Resources.

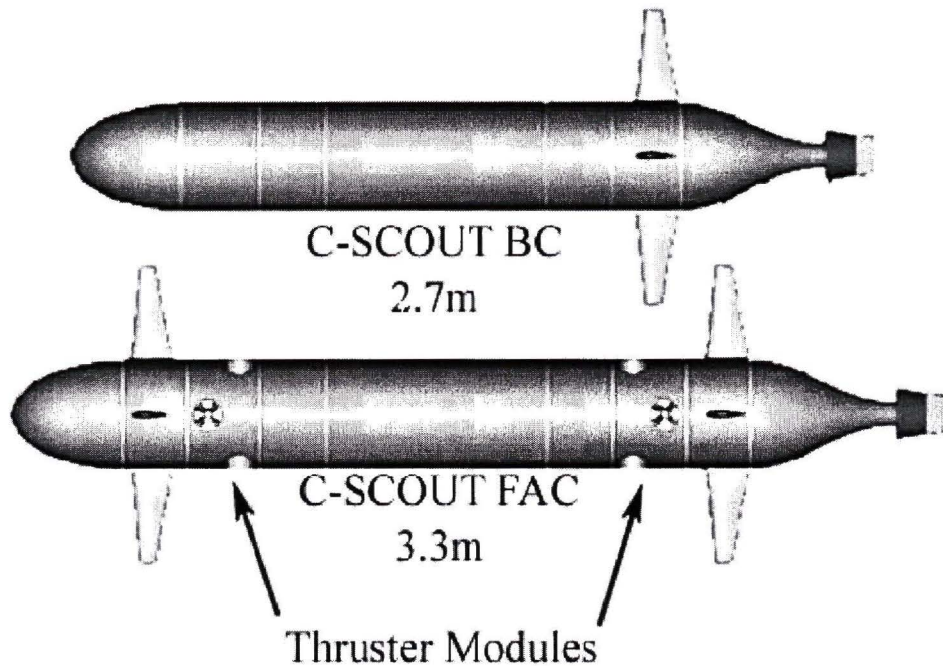


Figure 1.1. C-SCOUT Configurations: BC- Base Configuration and FAC- Fully Actuated Configuration

The C-SCOUT was designed to be able to cruise ahead or astern with a high degree of maneuverability, and to hover, even in a cross-current. It was therefore designed to be streamlined in shape, with an ellipsoid nose, parallel cylindrical midbody, and a cubic spline tail, and to have multiple motion control actuators including control planes for control while underway, and through-body tunnel thrusters for hover and low speed control, as shown in Figure 1.1.

The design of the vehicle is to be accomplished in stages. The baseline configu-

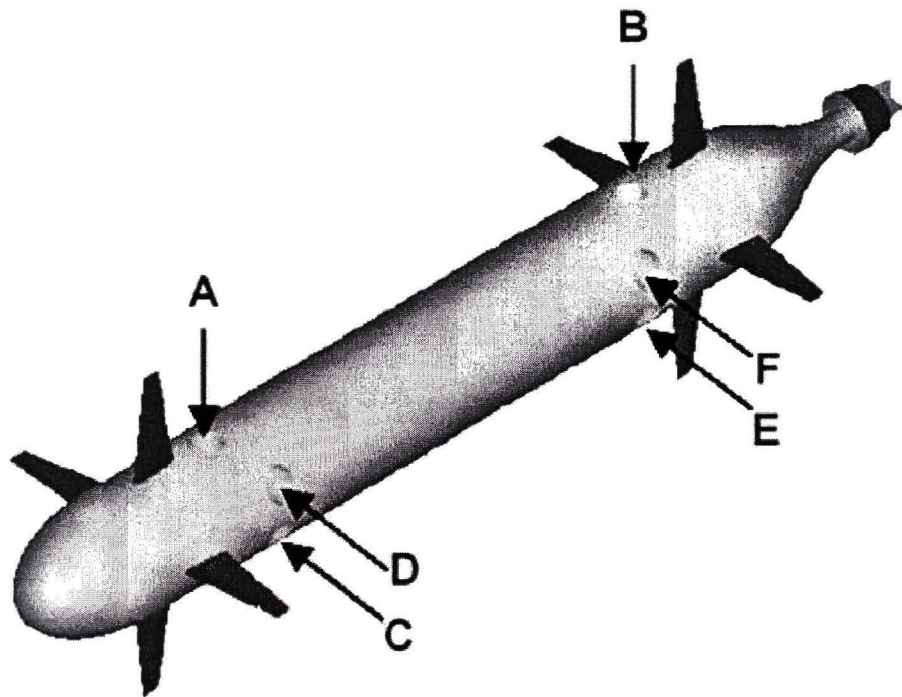


Figure 1.2. C-SCOUT FAC Tunnel Thruster Locations

ration (BC) of the vehicle has four control surfaces aft, and a single thruster aft for propulsion. The fully-actuated configuration (FAC) has the four aft control surfaces, but also four control surfaces forward of the center of gravity. In addition, the fully actuated version is equipped with six through-body thrusters. Figure 1.2 shows the tunnel thruster locations, two thrusters are to be placed vertically; one forward (A) and one aft (B), and the remaining four are to be placed horizontally two forward (C,D) and two aft (E,F). The tunnel thruster placements give low-speed control in pitch, heave, yaw, roll, and sway, with surge control accomplished by the main propulsor. Presently the baseline configuration has been built and is undergoing testing at IMD.

To make the vehicle easily adaptable, the originally designers concentrated on

keeping the components as simple and modular as possible. By building C-SCOUT in sections the lengthening and shortening of the vehicle to accommodate various payloads and control actuator configurations is a fairly simple procedure. This design enables the remote development of specialized modules.

1.3 URV Propulsion

1.3.1 Main Propulsor

Consideration of AUV propulsion usually relates to the main propulsor mounted at the rear of the vehicle. For the most part, control of the main propulsor only requires knowledge of steady-state and quasi-steady state thruster performance since streamlined AUVs are generally not designed to operate at low or zero forward speeds where control fins provide little or no steering forces. Main propulsors can often be optimized to provide optimal performance for a particular operating condition. This is in contrast to low-speed maneuvering thrusters that typically operate bi-directionally and at various thrust levels. The most significant difference between main propulsors and maneuvering propulsors in predicting performance is in the way they are modeled. For steady-state conditions, the thruster's axial thrust can be represented by a simple quadratic function of propeller rotational velocity squared. For transient conditions, a more complicated four quadrant non-linear dynamical model must be used (these topics will be covered in detail in Chapter 5).

1.3.2 Maneuvering Propulsor

Small underwater vehicles react quickly to changes in the amount and direction of thrust from maneuvering thrusters. This causes the overall system dynamics during low speed maneuvering to depend strongly on the dynamics of the thrusters themselves [26]. Because the dynamics of the thrusters can dominate the control of the vehicle, their behavior must be properly modelled to ensure good controller results. Improvements in the mathematical models used to describe the dynamics of underwater thrusters have led to improved control systems capable of more precise low speed manoeuvring.

A good discussion of how thruster dynamics affect URV (Underwater Robotic Vehicle) control is presented by Yoerger, Cooke and Slotine [27]. They concluded that the dynamics of underwater vehicles can be dominated by the dynamics of thrusters, especially during low speed or hover operations. This supports similar statements made by Whitney and Smith [26]. Yoerger, Cooke and Slotine suggest that if compensation for these dynamics are not included in the control system, the closed-loop system will be bandwidth limited and may lead to limit cycling behavior.

Limit-cycling is a term that refers to the oscillatory behavior of the vehicle about a desired position. Vehicle motion can become oscillatory if the reference control forces continually lag or lead the thruster force, in essence pushing the vehicle past the desired set-point. This limit-cycling behavior reduces the ability of the vehicle to perform precise station keeping tasks and is a major design consideration for URV systems.

1.4 Literature Review

1.4.1 Ship Maneuvering

A historical summary on early ship propulsion can be found in the 1980 paper by Norrby and Ridley [19]. A large part of this work is focused on early developments in 'bow-thrusters' (or lateral thrusters) which date back to the 1950's. The basic concept of through-body tunnel thrusters in AUV systems and 'bow-thrusters' in large ships is the same. The lateral thrusters provide the yawing moment to manoeuvre the ship. Work by Beveridge [5] discusses the hydrodynamic forces and moments produced by bow thrusters. In the case of AUV systems, this is extended to additional planes of motion. The work contained in [2], [5], [19] and similar, deal with the steady-state bow thruster performance. They report on thruster effectiveness for forward and astern travel or bollard pull conditions, of the lateral thrusters, and not the dynamic response. To obtain more insight into the dynamic response, a closer look at the propeller dynamics is necessary.

1.4.2 Propeller Modeling

Most naval architecture and marine engineering texts, see e.g. [8] [9], apply momentum theory to show that the axial thrust will depend on the square of the flow velocity through a propeller actuator disc. These texts emphasize that this theory does not include the details necessary to capture the effects of blade shape. To capture this detail, blade element theory uses lift and drag forces generated from each element of the blade cross section, summed over the total length of the blade. To use this method, a representation of the lift and drag curves as a function of the incident

flow angle is required. This information is readily available from aerodynamical design texts for a large variety of airfoil cross-sections for small angles of attack [1]. During thrust reversal, the local angle of attack spans a full 360 degrees. Rickards [20] discusses how these nominal lift drag curves can be created for the lift and drag coefficients by ignoring the discontinuities that arise during blade stall. In order to create these nominal lift and drag coefficient curves, data for large angles of attack is required. Because this data is not readily available, major assumptions must be made. This then allows full flow reversal to be modeled using simplified single term sinusoidal functions [4] [12].

These difficulties often lead to the use of propeller specific dimensionless thrust and torque coefficients. The coefficients are related to the advance velocity and rotational speed of the propeller, often referred to as 'open water propeller data'. This data can be presented for four-quadrants of propeller operation, as shown in Figure 1.3, based on the relative directions of advance velocity and propeller rotation. First quadrant data for most types of modern day propellers is readily available, but again full four-quadrant data is hard to find. Fossen [11] describes a method for using a linear approximation of thrust and torque coefficients to represent four-quadrant thrust. Fossen also reports that under heavy transients this method can be up to 40% erroneous. To use these types of non-dimensional coefficients accurately, extensive experimental data would be required. One of the first attempts to look at this data in depth was by Lammeren, Manen and Oosterveld [23]. Data for the Wagenin-gen B-Series propellers was fitted by a 20 term Fourier series to enable numerical representation of the full four-quadrant thrust and torque coefficients. While this is valuable for B-Series open propellers, it is not directly transferable to other propellers

such as the shrouded Kaplan typically found on URVs. Because of the complexity of the experimental tests and the propeller dependent results, the results in [23] are not transferable.

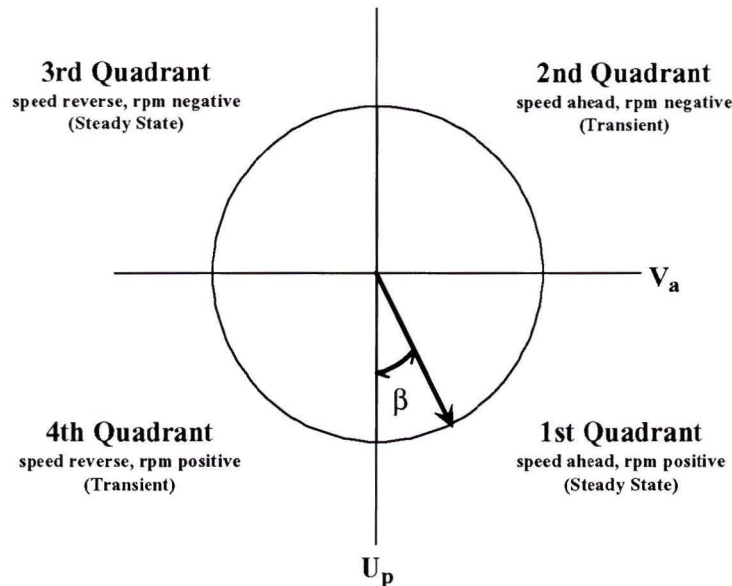


Figure 1.3. Four-Quadrant Propeller Operation

1.4.3 Tunnel Thruster Modeling

Several dynamic models have been developed to represent the performance of tunnel thrusters using momentum theory with a blade element model for the propeller. However, no work exists on the effect of forward speed and yawed orientation on tunnel thruster performance. A historical summary of recent work in lumped-parameter thruster dynamics modeling is given by Whitcomb and Yoerger [25]. The first work directly related to small AUV tunnel thrusters was done by McLean [16] in 1991 at the Naval Postgraduate School on the AUV II tunnel thruster. In 1993, Brown [7] [12] adapted McLean's momentum based model to use the blade element, lift/drag,

theory to model the propeller in a tunnel thruster. Models presented by Bachmayer, Whitcomb and Grosenbaugh [3] [4] later expanded the basic four-quadrant models to include additional fluid effects such as rotations and presented a method for experimentally determining nonsinusoidal lift/drag curves.

1.4.4 Experimental Validation

An important step to modeling the performance of any physical system is validating the numerical model. The experiments completed by [4], [7], [16], and [26] made use of small tanks or water channels to measure the performance of a stationary thruster. McLean briefly discusses the limitation of testing in a small tank, specifically in regards to the 'slosh mode', which affects the measured thrust data. The initial work by McLean [16] and Brown [7] [12] was only concerned with measuring the axial thrust. In Brown's model, four parameters tied to the specific design of the tunnel and propeller were determined empirically by matching the computer simulation with the experimental axial force data. The experimental setup in [4] and [26] used a more sophisticated 6-axis load balance setup for measuring axial thrust and hydrodynamic torque. From the additional force data, intermediate (or internal) simulation values can be verified. The work in [4] and [26] also use a 3-D Doppler flow meter to measure 3 axis flow velocity at the thruster intake and outlet. The 3-D flow information enables investigation into the rotational component of the thruster flow as well as the creation of empirically derived lift/drag coefficient curves.

1.5 Scope of Thesis

Presently, the models mentioned above do not include the effects of forward vehicle motion or vehicle orientation on 'through-body' thrust performance. In order to adapt the current tunnel thruster models to include the effects of vehicle motion, an experimental system was designed to characterize the effects of forward vehicle speed and yaw angle on tunnel thruster performance. This full scale system includes a transverse tunnel thruster mounted in the C-SCOUT model and a 6-axis load cell balance mounted internally to measure thrust. The model was attached to a yaw plate assembly in Memorial University of Newfoundland's tow tank, and several tests were run to characterize the effect of vehicle motion on the transient and steady state thruster performance. This thesis will discuss the experimental setup, as well as the results obtained from small tank and tow tank testing of a single tunnel thruster. The trends shown by the experimental results are highlighted and the relevant parameters which affect thruster performance are identified. Conventional thruster models are then modified to include the effect of these parameters and these effects are then implemented in a computer simulation.

In Chapter 1, the author has presented a brief overview of underwater vehicle technology as it applies to this work. Chapter 2 will discuss the development of the tunnel thruster module for C-SCOUT as well as the corresponding experimental testbed for measuring the static thruster performance including control, data acquisition and force measurement. Chapter 3 will present the results of the small tank testing, similar to the results presented by other research groups. Chapter 4 contains the main original contribution of this work; the experimental results of yaw angle and forward speed effects on tunnel thruster performance, obtained using the tow

tank facilities at MUN. Chapter 5 discusses the various existing numerical models to predict thruster performance, and presents a method for including the effects of forward speed and vehicle orientation. Chapter 6 presents a corresponding simulation assembled in Matlab's Simulink environment and compares results from the computer simulation to the experimental data. In Chapter 7, conclusions are drawn, recommendations are made for improvements, and suggestions for future work are discussed. The appendices provide additional detail on the test setup, the data collected, and the simulation.

Chapter 2

Experimental Thruster System

Until now, testing at IMD on the C-SCOUT vehicle has involved only the base configuration of the vehicle (see Figure 1.1) with no through-body thrusters. Therefore, in order to test a through-body thruster, the design and construction of one unit was necessary. The tunnel thruster unit needed to fit in a C-SCOUT thruster module and ideally, provide enough thrust to hold the vehicle in a 0.5 m/s cross current. In addition to the tunnel thruster components, a sensor for measuring the dynamic thruster loads also had to be mounted within the module. This chapter discusses the design, selection of components and assembly of the experimental thruster system.

The basis behind the design of the experimental setup was the use of plug and play components that could be integrated with ease and be highly portable. The scope of this research included the design, construction, testing and simulation of one tunnel thruster unit. It was therefore very important to make use of as many off-the-shelf components as possible in order to reduce development time. Portability was also very important because the construction and initial testing took place at the

University of Victoria, while the second stage of testing required the specialized tow tank facilities across Canada at MUN. Figure 2.1 shows the high level layout of the thruster system. The major components include:

- Personal Computer (PC) running LabVIEW software for the control and data acquisition user interface.
- Keithley PCI Data Acquisition Card (DAC), interface to the Maxon controller
- Maxon servo amplifier/controller
- Thruster Unit: Maxon motor, gearbox, propeller
- ATI Force/Torque load cell and ISA controller card to power the load cell and convert the raw sensor data into 6-axis force information.

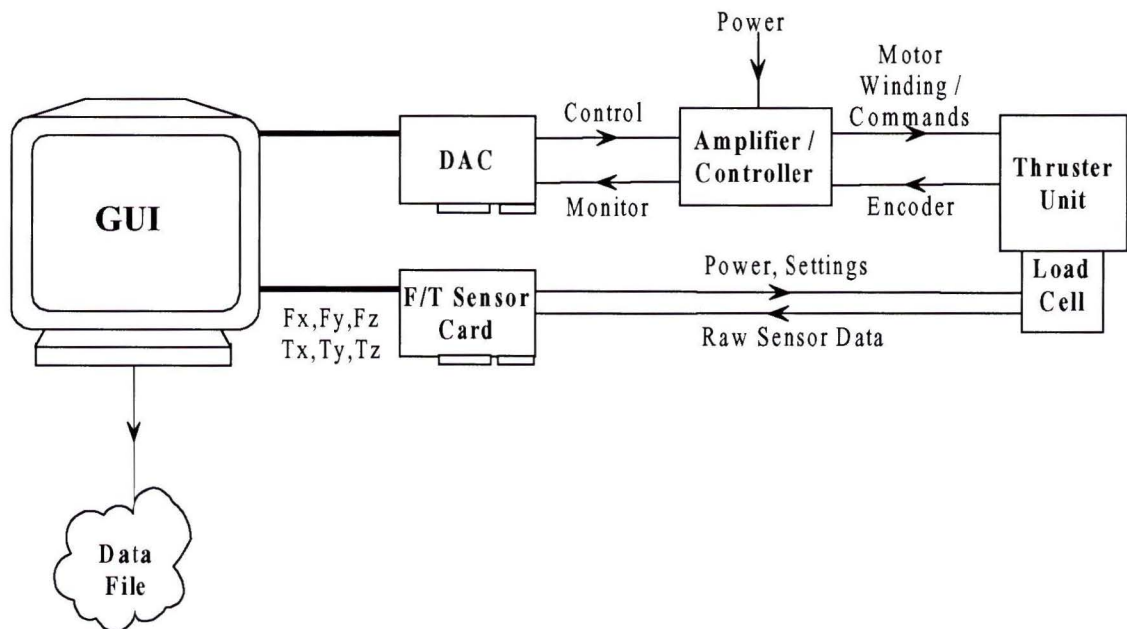


Figure 2.1. Thruster System Schematic

2.1 Experimental Interface

The software interface to the motor control and data acquisition systems was written in National Instruments LabVIEW software [18]. The LabVIEW user interface software enabled interactive control of the thruster system by making use of extensive virtual instrument (VIs) libraries supplied with the various system components. The Maxon servo controller, ATI F/T load cell, and Keithley DAC come with factory VIs that allow the user to specify system functionality by assembling block diagrams. As the various VIs are connected together, a Graphical User Interface (GUI) is created to provide access to various hardware functions. Figure 2.2 shows the LabVIEW GUI developed for the experimental system. The GUI displays real time test information, enabling the user to monitor the experimental results and detect equipment errors as the test proceeds, ensuring the data being written to file has no major errors.

Through the various entry fields in the GUI, the required information for each experiment is entered and the test parameters are set. Entry fields allow the user to set the length of the test and the sampling rate as well as enter other general information that will be written into the data file header. More information on the format of the data files can be found in Appendix B. In addition to structuring the data file, the GUI also enables the user to select the type of motor voltage control scheme required for a given test. Once current or speed control has been selected the control wave is set up to be outputted continuously from one of the DAC analog output pins for the duration of the test. The following output are available: Forward, Reverse, Ramp, Step, Square, Sine, and Triangular. For each of these waveforms, the amplitude and duration of the motor control voltage can be specified as well as the period of the periodic control. The programming block diagrams for the GUI can

be found in Appendix B.

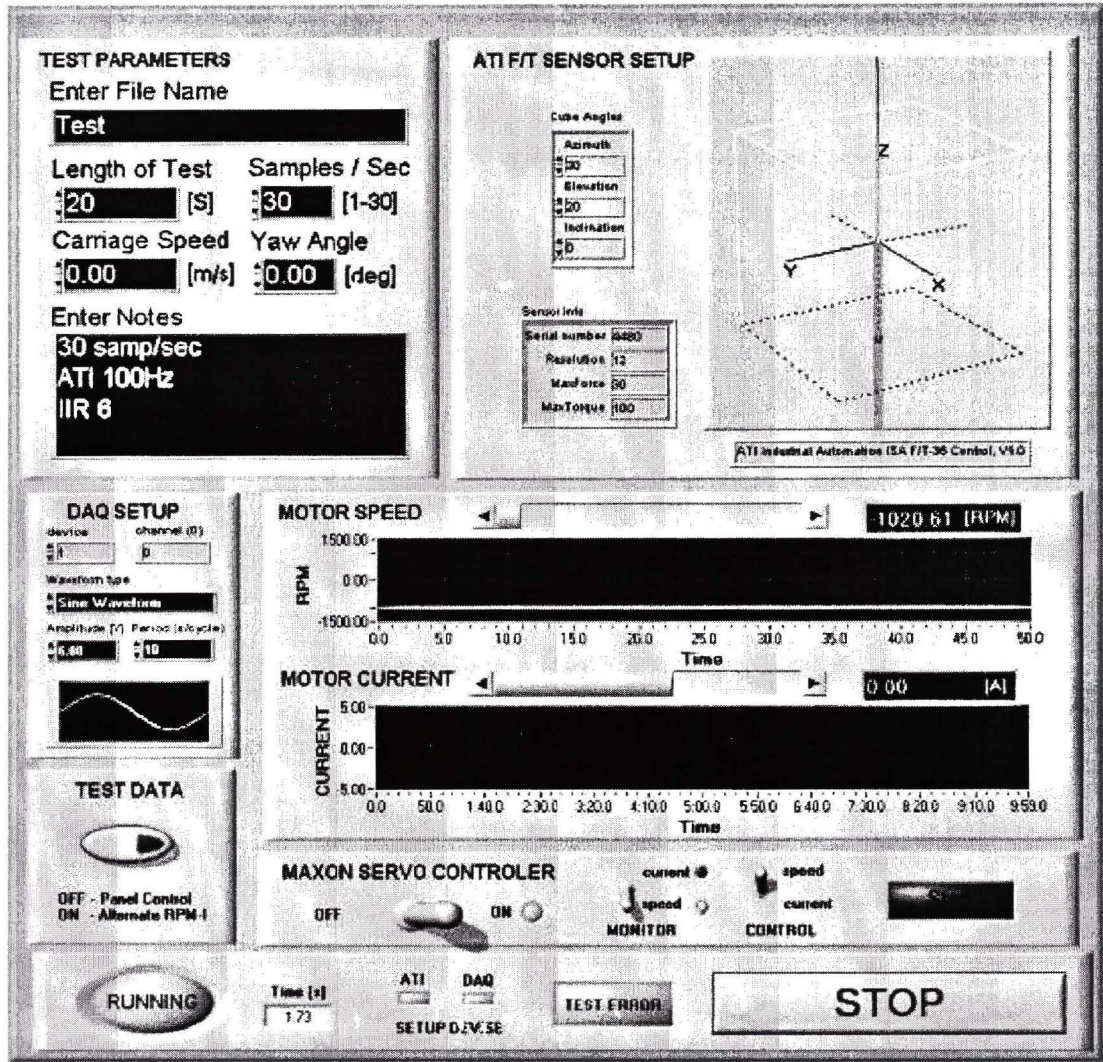


Figure 2.2. LabVIEW Experimental Graphical User Interface

2.2 Data Acquisition and Control

The backbone of the experimental system is a Keithley PC-based data acquisition card, model KPCI-3108. The KPCI-3108 features 16 single-ended or 8 differential analog inputs, two $\pm 10V$ analog outputs and 23 digital I/O lines. Figure 2.3

shows how the DAC expansion I/O boards are connected to the Maxon servo controller/amplifier. More details about the Maxon controller can be found in the following section.

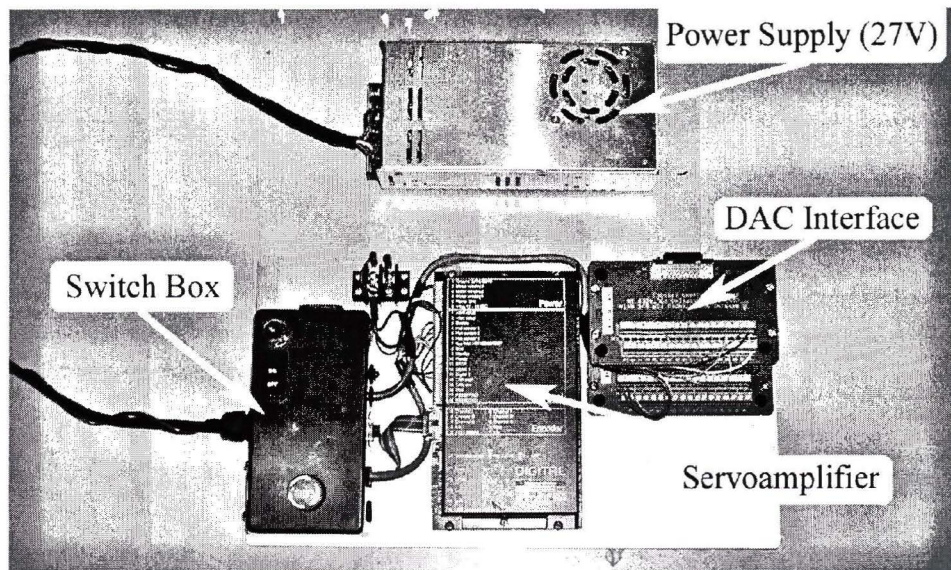


Figure 2.3. Experimental Interface

The data acquisition card is used for both data acquisition and thruster control. The Maxon servo controller is controlled using two of the digital outputs to select control options and one analog output to control the speed or current of the motor. The pattern of the control signal is selected by the user in the GUI and determined by the functions programmed into the LabVIEW experimental interface.

2.3 Motor Controller/Amplifier

The Maxon EC 45 motor is controlled by the Maxon 4-Q-EC Servoamplifier model DES 50/5, Figure 2.4 (order number 205679). This servo controller has the capability to drive 50V and 5Amp continuously. The DES (Digital EC Servoamplifier) is a

digital servoamplifier with sinusoidal current commutation for precision control of Maxon EC motors. The sinusoidal commutation results in minimal torque ripple and low motor noise.

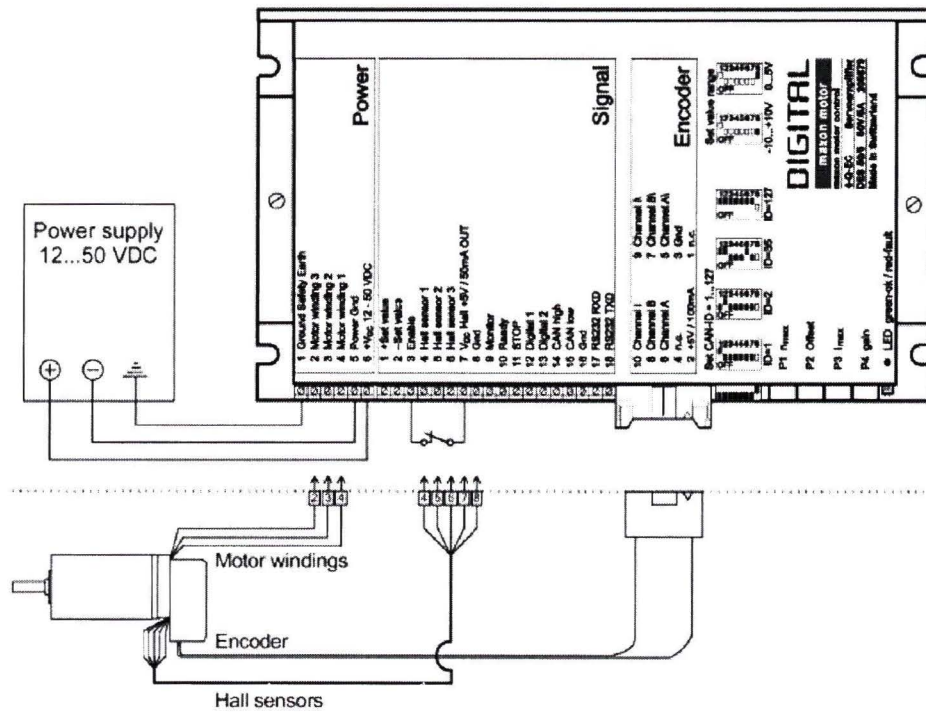


Figure 2.4. Maxon Motor Controller

The DES features both gain tunable shaft speed control and current control. This option is set using one digital input and controlled using the $\pm 10V$ 'set value' input. Other digital inputs include: Enable, Stop. In either control mode two output options are available for monitoring the motor: speed or current. All of these functions are controlled by the experimental interface GUI as described in section 2.2 above.

2.4 Tunnel Thruster Unit

2.4.1 General Description

The thrust requirements were selected based on the need to hold the C-SCOUT in an 0.5m/s current. The worst case scenario would be with the C-SCOUT broad side to the incoming current flow. Since there are 4 lateral through body thrusters the force required per horizontal tunnel is approximated as 1/4 the drag load of a cylinder in a cross-flow [9]. Assuming a cylinder diameter of 0.4 m and a drag coefficient of 0.764, a required thruster force of 22 N is found.

Figure 2.5 shows a general layout of the thruster components. The tunnel thruster units consists of the following major components: Maxon Servo Motor, Reduction Gearbox (5 : 1), Thruster Leg, Propeller, and a 4" ID PVC Tunnel. The following sections will discuss the design and selection of the various thruster components.

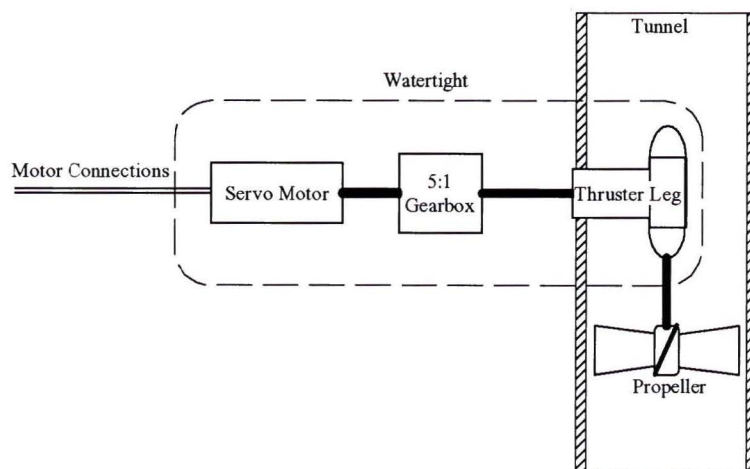


Figure 2.5. Thruster Schematic

2.4.2 Propeller

Initially a propeller from a small ROV¹ was used. Unfortunately this propeller had a very large hub diameter and the blade did not have a proper profile. It was necessary to have a custom propeller fabricated due to the difficulties in locating an off-the-shelf solution for the 4in tunnel diameter. A new propeller for our thruster unit was designed and fabricated by Tony Randell at the IMD, shown in Figure 2.6. The propeller designed and fabricated for our application is a standard four blade Kaplan style propeller with the following characteristics:

- Pitch to diameter ratio $P/D = 1$
- Blade area ratio of 0.55
- 100.33 mm (3.95 in) OD
- 23.8125 mm (0.9375 in) hub diameter

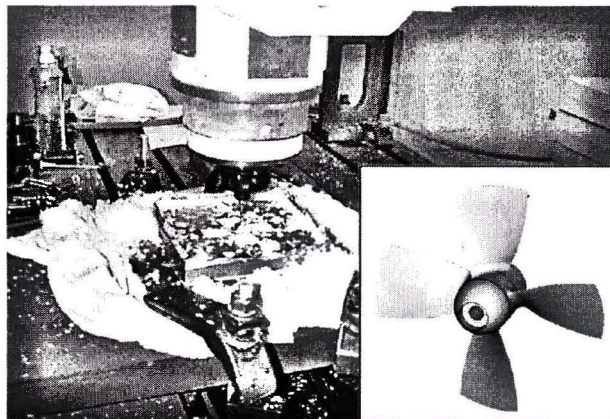


Figure 2.6. Propeller Fabrication at IMD

¹Figure 2.9 shows the original ROV propeller from Hydrovision Limited

2.4.3 Servo Motor

In order to produce 22 N axial thrust at 1000RPM with the four blade Kaplan propeller, based on the hydrodynamical torque requirements for our specific propeller, 1060mNm of continuous torque is required. A Maxon EC motor was selected with the following characteristics:

- Model - EC45, brushless (order number 136207)
- Size - 45 mm diameter by 144 mm long, refer to (Appendix A)
- Power - 250 Watt
- Voltage - 24 V
- Speed - 5000 RPM
- Torque - 283 mNm continuous at 5000 RPM (1415 mNm through a 5:1 gearbox)
- Weight - 1150 g
- Sensors - Digital Encoder, 500 CTP, 3 channels (order number 137959)

This motor is a brushless external rotor DC servo motor. There is no mechanical commutation and therefore operational lifetime is limited by bearing life only (up to 10,000hrs compared to 3,000hrs for a standard DC motor [15]). This setup also allows for higher speeds at lower voltages and shorter time constants. In addition, the brushless external rotor setup also has a very low noise signature. This motor is not environmentally sealed and therefore required a housing. A simple PVC housing was constructed, as shown in Figure 2.9.

2.4.4 Tunnel Thruster Assembly

2.4.4.a Gearing

The gearbox is the central component that connects all the pieces together. The servo motor, thruster leg and tunnel mount directly to the back plate of the gearbox. The gearing is done using a single stage spur gear, Figure 2.7 shows the open gearbox. The gear material is Delrin, a light weight material that requires very little lubrication. The gear ratio used for the work done in this thesis was 5 : 1. If different gear ratios are required, the spur gears can be replaced to achieve the desired ratio (within a given size limit). When bolted together the two halves of the gearbox are sealed by an o-ring face seal.

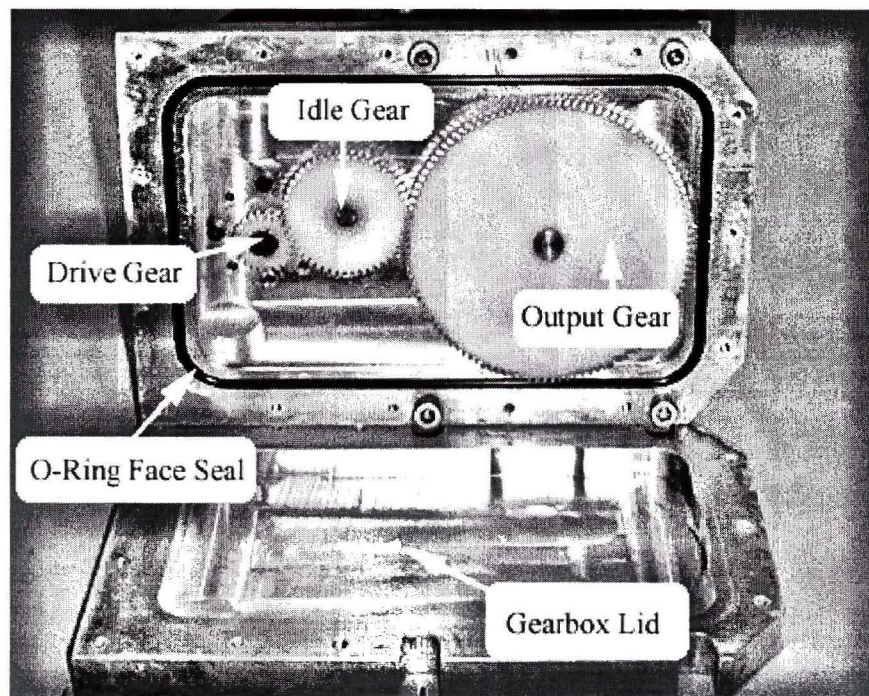


Figure 2.7. Gear Box

2.4.4.b Thruster Leg

There are two basic drive configurations for a tunnel thruster system; one where the actuator is mounted inside the tunnel and one where the actuator is mounted externally and power is transmitted into the tunnel. In general, it is hard to find electric actuators with a small enough size to power ratio to fit inside small tunnels without blocking too much of the flow. For example, the Maxon servo sized for this application, if mounted inside the tunnel, would block over 85% of the tunnel's cross-sectional area. Since water is an incompressible fluid there is no benefit in a large blockage of flow, therefore the Maxon servo motor had to be mounted outside the tunnel. The torque is delivered to the propeller by means of the thruster leg, where the gearbox output is taken into the tunnel and re-directed 90°. It is the only component that has a dynamic seal, the propeller shaft seal, between the watertight gearbox/servo motor housings and the surrounding water. Figure 2.8 illustrates the internal workings of the thruster leg. The main strut is attached directly to the gearbox where it is connected internally to the output drive gear. A shaft runs down the center strut where it is connected to the propeller shaft through a 1 : 1 bevel gear set. The standard hub assembly carries the bevel gear, output shaft, bearings, and seal. Removal or exchange of this hub is accomplished by simply un-threading the unit. When this is done all the internal components are also removed. A static radial o-ring seal makes this threaded assembly watertight.

A unique feature of this thruster leg is the ability to re-configure the output shaft. The design allows the flexibility to test both a single propeller and a double, contra-rotating, propeller setup. By simply replacing the blank hub with another standard hub assembly, the contra-rotating setup can be achieved (see inset Figure 2.8). For

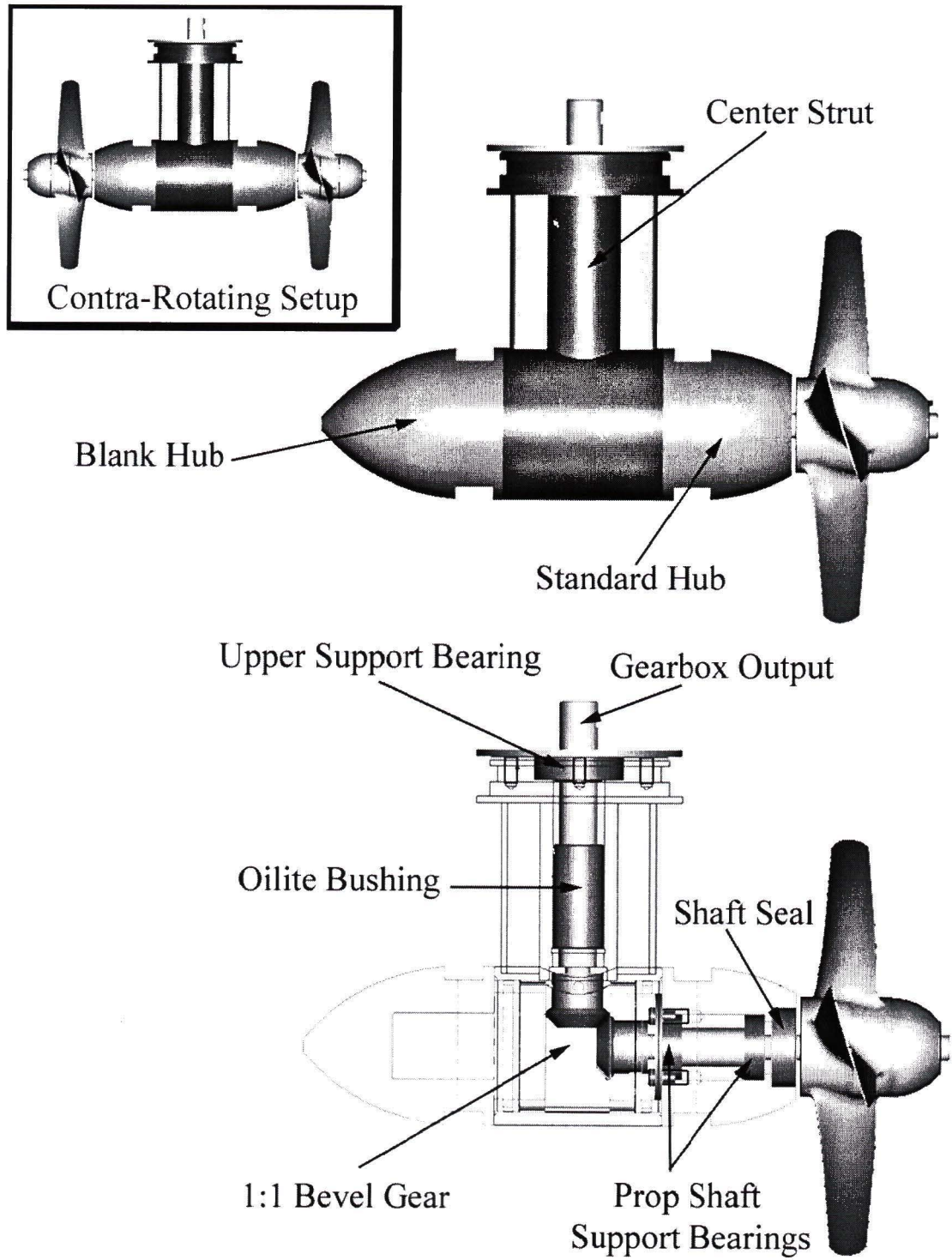


Figure 2.8. Thruster Leg Diagram

the work in this thesis, only the single propeller configuration was used.

2.4.4.c Thruster Assembly

Figure 2.9 shows the thruster unit in various stages of assembly. This unit, attached to the load cell housing, can then be mounted directly to the frame of a small test tank or in the C-SCOUT thruster module (as described below in section 2.4.5). In Figure 2.9, frame A shows the basic thruster components: the motor in its white and grey housing in the upper left; the drive shaft going down to the gearbox at the bottom; the thruster leg coming out of the gearbox on the right and into the propeller hub. Frames B and C show the tunnel mounts being assembled. These mounts enable the exchange of the tunnel end segments. This added flexibility will make it possible to test different module configurations in the future. Frame D shows the fully assembled thruster unit. The tunnel segments and intakes shown are designed to fit inside the C-SCOUT module.

2.4.5 C-SCOUT Module Configuration

In order to test the tunnel thruster in the full scale C-SCOUT model all of the thruster components including the load cell, needed to be mounted inside a 0.3048 m (12 in) long tunnel thruster module. The resulting module is illustrated in Figures 2.10 and 2.11. In the experimental system a crucial issue in mounting the thruster unit into the module is insuring the mechanical isolation of the thruster unit from the module (or hull). Because the load cell is measuring the forces generated by the entire thruster unit, any contact between the hull and tunnel entrances would result in incorrect load information. The tunnel entrances were designed to match the

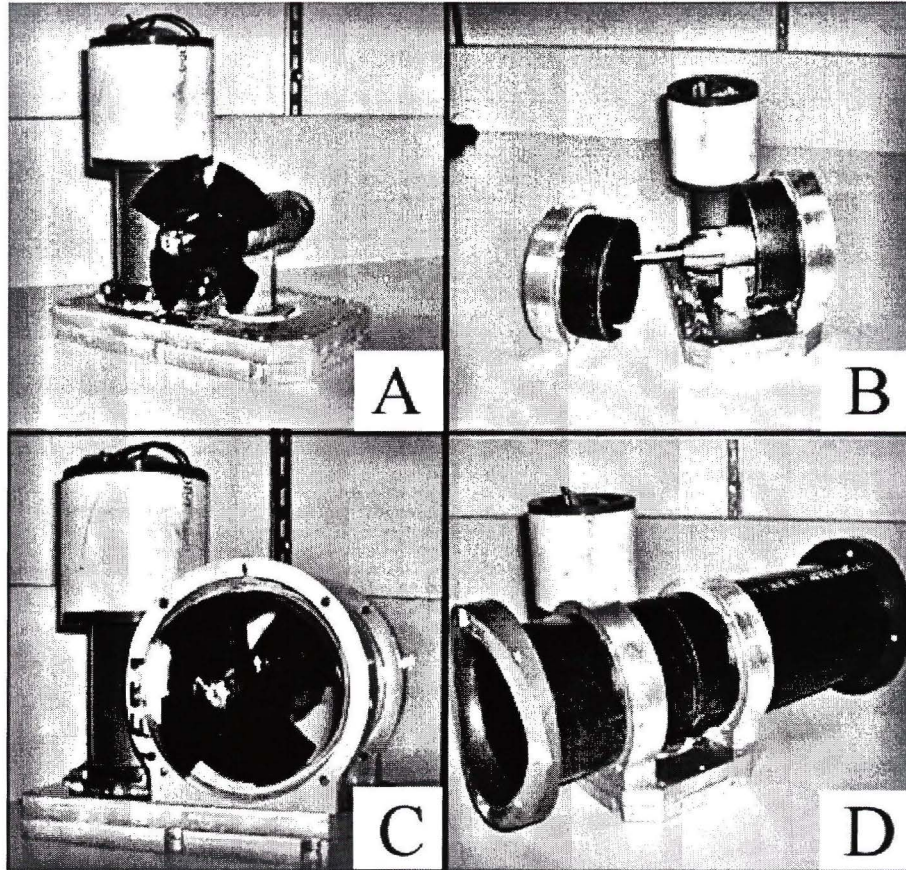


Figure 2.9. Thruster Unit

hull shape and be offset by ~ 1.6 mm ($1/16$ in). The design of the intakes was not optimized for this thesis, they simply match the hull curvature and have ~ 22 mm ($7/8$ in). rounded edges.

The module was bolted directly into the C-SCOUT model at MUN, Figure 2.10, and the entire model was mounted to the yaw assembly and connected to the tow tank carriage. Details of the experimental setup for the tow tank testing will be discussed in Chapter 4.

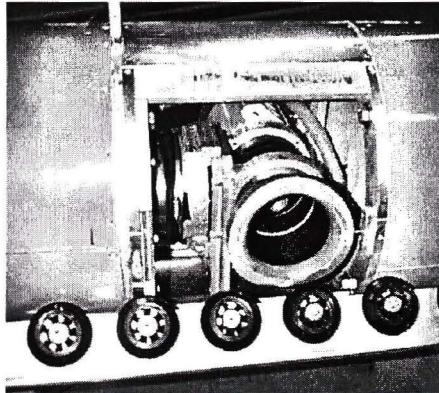


Figure 2.10. Tunnel Thruster Module Mounted in C-SCOUT Test Model

2.5 Force/Torque Sensor

2.5.1 Sensor Specifications

An ATI multi-axis force/torque (F/T) sensor was selected to measure the required thruster loads. The Gamma F/T transducer shown in Figure 2.12 was selected with its F_x and F_y measurement range of $\pm 133.4 \text{ N}$ ($\pm 30 \text{ lbf}$), F_z of $\pm 444.8 \text{ N}$ ($\pm 100 \text{ lbf}$) and all three torque axis $\pm 11.3 \text{ N}\cdot\text{m}$ ($\pm 100 \text{ lb}\cdot\text{in}$). The Gamma sensor offers extremely high-strength with maximum allowable loads are 6.9 to 31 times the rated capacities. This, in combination to being very stiff, makes it an ideal transducer for this application.

This ATI transducer also has a very high signal-to-noise ratio which makes it ideal for applications where high electrical noise will be generated, like around the tow carriage drive motors. The sensor uses silicon strain gauges that provides a signal 75 times stronger than conventional foil gauges and provides a significantly increased overload range. In addition to this, the signal is amplified at the transducer, resulting in very low noise distortion. Using factory communications cable the transducer is accurate to 1% of full scale measurement.

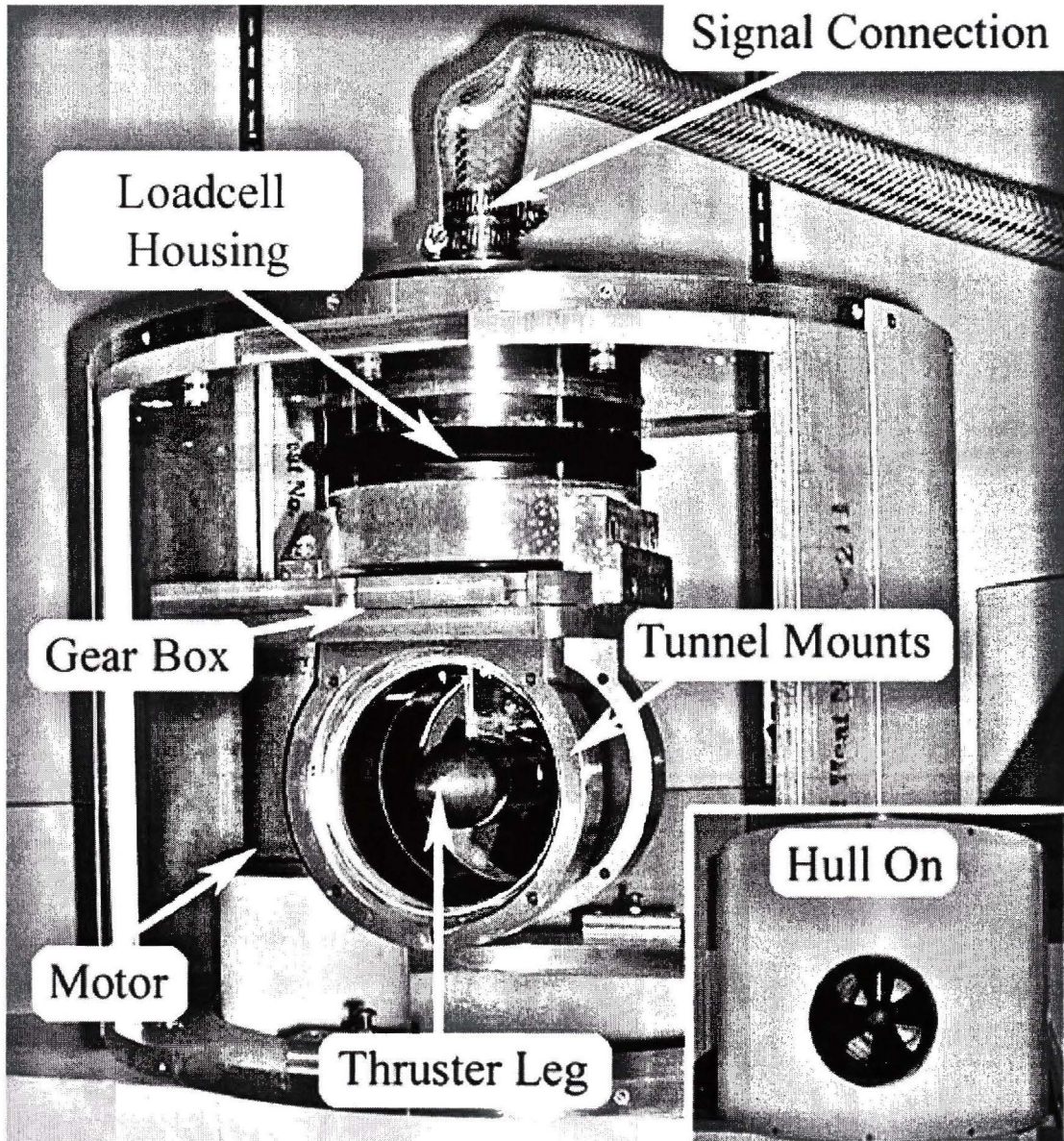


Figure 2.11. Tunnel Thruster Module

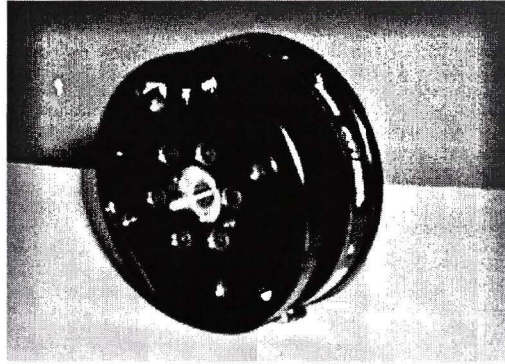


Figure 2.12. ATI F/T 6-axis Loadcell

The PC based F/T controller's analog-to-digital converter digitizes the amplitude analog strain gauge signals. The digitized strain values are then converted to forces and torques using a factory calibrated transformation matrix. The controller provides a variety of built in functions, of which the following are used in this application: adjustable signal conditioning, tool transformations, translate and/or rotate the F/T reference frame, peak analysis to store minimum and maximum values, and biasing to remove dead weight.

The only aspect of the ATI transducers that is not favorable for this application is that they are not environmentally sealed and therefore require additional components to waterproof the sensor.

2.5.2 Waterproof Housing

The ATI load cell is not environmentally sealed and so, a waterproof housing was required to protect the load cell while submerged. Because the load cell measures forces transmitted through it, the housing had to be water tight but not rigid. One side of the housing had to be mounted to a fixed body and the other to the thruster unit,

therefore the housing was built in two parts with a rubber boot providing the flexible seal, see Figure 2.13. This type of housing is meant for shallow water applications only, since the air inside is not pressure compensated and would not withstand the high pressures of deep water. For the work done in this thesis, the water depth never exceeded 2 m, and therefore no pressure compensation was required.

2.5.3 Sensor Mounting

Figure 2.11 showed the complete assembly of the tunnel thruster module. Below, Figure 2.13, shows a more detailed view of the load cell mounting. First the load cell is attached to the frame of the module. Secondly the bottom half of the load cell housing is attached to the load face of the F/T sensor. And finally the flexible rubber boot is secured to both halves of the housing, sealing the gap without carrying any of the thruster loads.

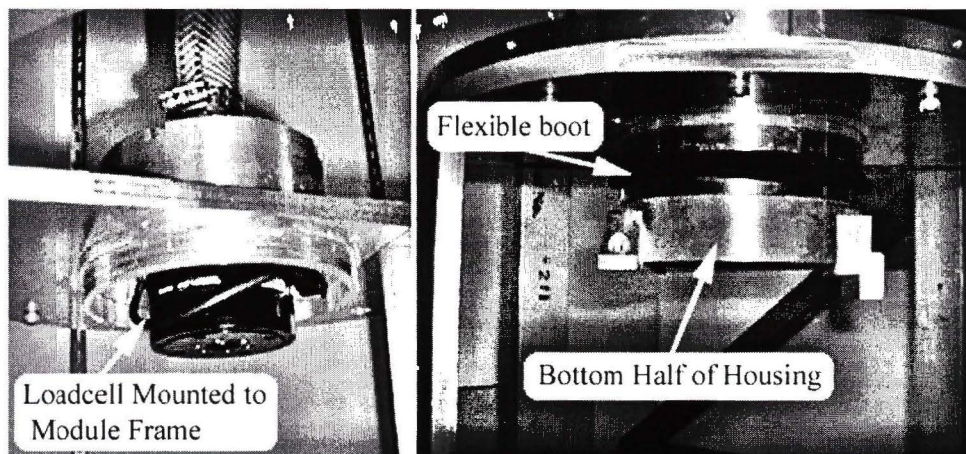


Figure 2.13. Loadcell Mounted in C-SCOUT thruster Module

The cable running from the load cell to the PC carrying sensor power and strain gauge signals can also be seen at the top (left) side of the image. Again, the cable

was run inside a flexible plastic hose therefore no custom underwater connectors were required.

Chapter 3

Small Tank Testing

Prior to the experimental work done for this thesis, the University of Victoria did not have adequate facilities for testing small URV thrusters. In order to verify the setup of the experimental system and investigate basic thruster dynamics, a small test facility was needed. A small stand-alone tank was constructed to allow this initial phase of testing. The goals of the small tank testing were to debug the control of the thruster and gathering of data from the F/T sensor. Additionally, results from these initial tests could be compared with those published by other research groups using similar thrusters such as [7] [12] [26]. Finally, the initial set of tests allow us to establish the basic transient and steady state axial thrust performance as well as the response to step, triangular, and sinusoidal control inputs for a single stationary tunnel thruster. The following chapter will discuss the test tank setup, introduce the reader to basic tunnel thruster performance, and discuss some of the limitations of the small test facility. Later, in Chapter 5, this information will be used to tune several model parameters and validate the basic simulation.

3.1 Experimental Setup

The previous chapter of this thesis discussed the components and instrumentation that make up the experimental thruster system. This section will discuss how the components are arranged to form the small tank testbed. Figure 3.1 illustrates the setup of the testbed system. The PC and experimental interface are placed beside the test tank, two connections are required to the equipment in the tank (one to the F/T sensor and one to the thruster motor). This arrangement is simple and compact, occupying a very small area of the laboratory.

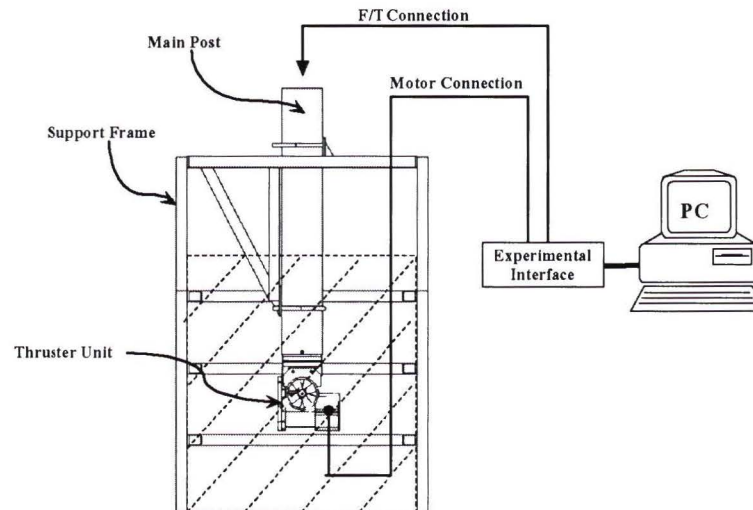


Figure 3.1. Small Tank Setup

3.1.1 Tank Design

The design of small tank facility is similar to the one used in [4] with a slightly smaller tank size. The tank was constructed with 9.5 mm (0.375 in) polyethylene sheet with welded plastic joints as seen in Figure 3.2. The tank dimensions are 1.83 m (72 in)

long, 0.86m (34in) wide and 1.22m (48in) tall. Due to the large pressure loading from the water inside the tank a heavy steel frame was built to support the thin tank walls. The steel frame also serves to support for the main post to which the F/T sensor housing is mounted.

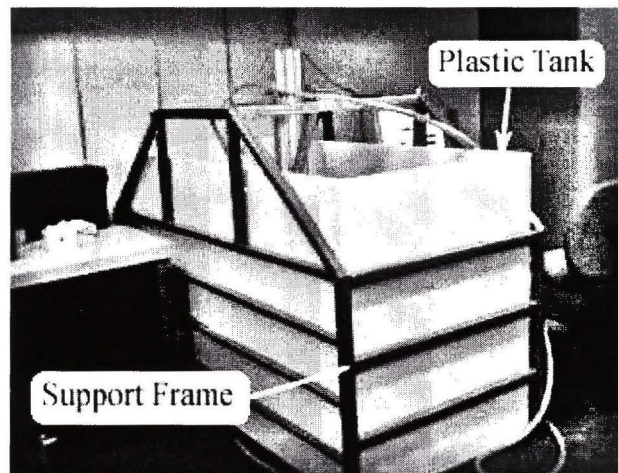


Figure 3.2. Small Testing Tank

The F/T sensor housing is mounted into the bottom of a size 5 schedule 40 aluminium pipe, labeled as the main post in Figure 3.1. The top half of the load cell housing is different than the one shown in Figure 2.13, and is designed to fit directly into the end of the pipe. The pipe is mounted to the support frame using two large U-bolts, the lower of which can be seen in Figure 3.3. By loosening the U-bolts, both the thruster depth in the tank and orientation (through 360 degrees of rotation) can be easily adjusted. The connection cable to the load sensor runs down through the pipe thus avoiding the need for another underwater cable and connection. The thruster unit is then mounted directly to the F/T sensor housing, Figure 3.3, in the same way it is mounted in the thruster module.

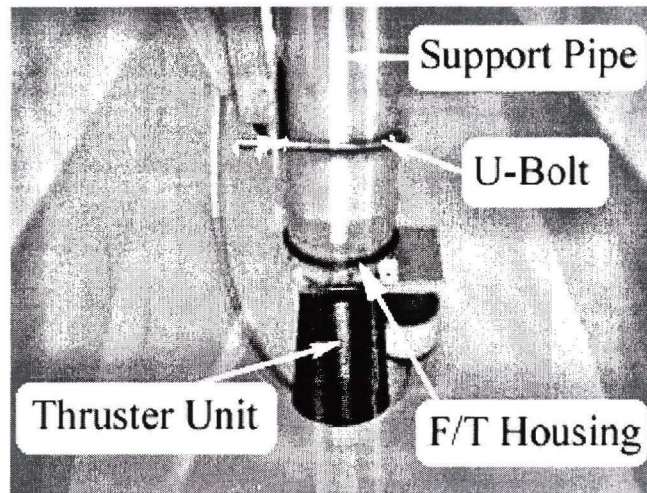


Figure 3.3. Thruster Unit Mounted in Testing Tank

3.1.2 Test Considerations

There are several limitations that must be recognized when testing in a small tank, the following section will discuss a few of these considerations. Effects such as re-circulation, turbulence and slosh can have major effects on thruster performance and the measured loads. Both re-circulation and turbulence are hard to quantify but the effect of slosh is quite evident in the test data. The slosh frequency can be defined as the frequency of the standing waves that form in the testing tank after an external disturbance. This frequency is directly dependent on the dimensions of the tank, McLean [16] reported a slosh mode frequency of 0.5Hz for the small test tank used in his experiments. Our tank is similar in size so we would expect to see a similar slosh frequency. In order to isolate the frequency of tank slosh in our tank the load cell data was monitored after a variety of disturbances in the tank: low frequency thrust reversal, high frequency thrust reversal, random disturbance from a paddle, and a constant forward thrust. Figure 3.4 shows the frequency content of the load cell data after the disturbances. A very distinct slosh mode frequency can be seen at 0.6Hz

for all types of disturbances, and therefore reported as the natural slosh frequency of the tank. In larger testing tanks there is room to install screens or baffles around the exterior of the tank to damp out any standing waves and turbulence created from testing disturbances. Because of the limited space inside a small tank, these additions are not as simple, and therefore extra time must be taken between tests to ensure the water has settled.

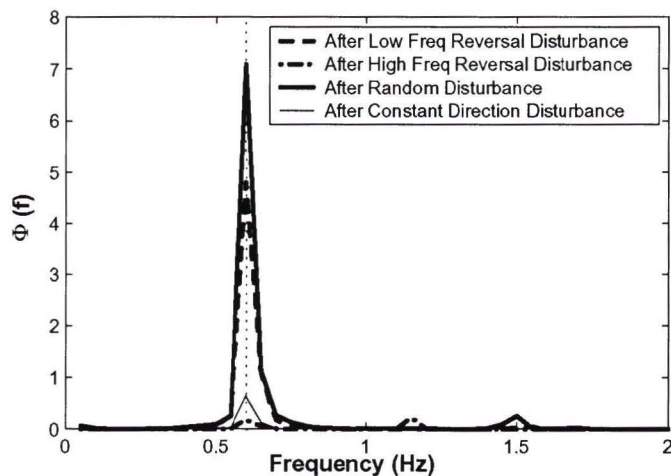


Figure 3.4. Power Spectrum of F_x After Disturbances

The following sections will introduce basic tunnel thruster performance using a series of steady state and transient tests. However, before continuing the issue of control type must be addressed. A distinction between speed and current control must be made in order to compare results with other publications. For example the work by Bachmeyer *et al.* [4] used an amplifier configured as a current controller. During heavy transients, the hydrodynamical load on the propeller spikes, resulting in a much higher current demand on the motor. When the current to the motor is limited, the propeller RPM has a much longer rise time which results in a very different thrust response. The end result is a significant difference in peak axial thrust during

propeller reversal. This is illustrated in Figure 3.5, in which the thruster has been commanded with a step change of speed, and a step change of current. For the work contained in this thesis, speed control will be used. More details on features of the transient plots will be discussed in section 3.2.2. However, we note here that the slosh frequency is apparent in the oscillations of thrust in Figure 3.5.

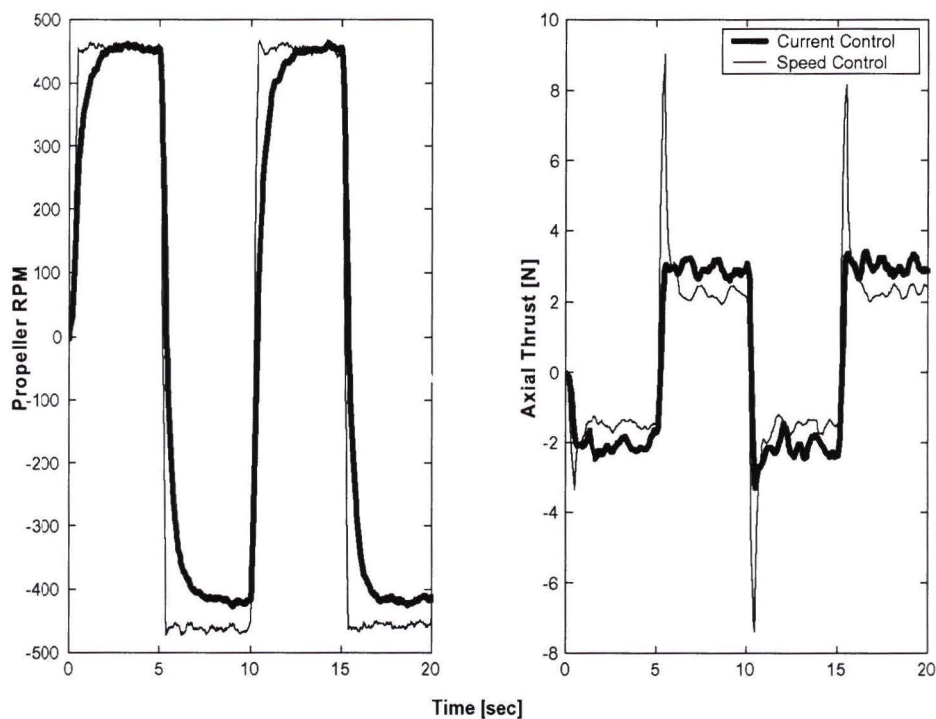


Figure 3.5. Current Control vs Speed Control

The last significant limitation to the testing in the small tank (as well as all other testing) revolves around the maximum sampling period of the experimental system. The software was designed to acquire load cell readings at frequencies up to 30 samples/sec. Due to communication issues between the F/T card and the LabVIEW software, the actual maximum sampling rate turned out to be 10

samples/sec. As a result, the sharp thrust spikes may be slightly under-sampled during heavy transients.

3.2 Small Tank Results

3.2.1 Steady State Tests

The steady state tests consisted of running the thruster at constant forward and reverse speeds while measuring axial thrust. Figure 3.6 frames a) and d) show the axial thrust and propeller rotational speed, respectively, as a function of time. Figure 3.6 frame b) shows a quadratic relationship when axial thrust is plotted against propeller RPM. As expected, this results in a linear relationship when axial thrust is plotted against propeller speed squared, Figure 3.6 frame c). The maximum steady state thrust is $-10.2N$ with a slope of $-1.154 \times 10^{-5} \frac{N}{RPM^2}$ and $12.8N$ with a slope of $-1.462 \times 10^{-5} \frac{N}{RPM^2}$ in the forward and reverse directions respectively. The fundamental linear relationship will be described in more detail in Chapter 5. For now, a few important observations can be made, the most important being the difference in thrust between the forward and reverse propeller directions. In frame d), when the slope of the forward prop speed is projected into the opposite quadrant, a large difference in thrust is apparent. This difference is due to the asymmetrical performance of the thruster. This is not unusual as very few thrusters are capable of producing fully symmetrical performance. The propeller fabricated for our application was designed to be as close to symmetrical as possible using the Kaplan style blade profile. The majority of the asymmetry is due to the obstruction caused by the thruster leg, water flow in one direction must pass around the thruster leg before entering the propeller.

Asymmetry in thrust must be accounted for when designing and modeling a thruster for positioning systems. In order to achieve symmetrical steady state thrust it is often necessary to compensate for the asymmetrical effects in the control scheme.

3.2.2 Transient Tests

The most common bi-directional control patterns used with positioning thrusters are triangular and square wave control. In applications where the immediate response of the thruster is important, the square wave control is often used because it provides rapid propeller response to directional changes. In applications that require a more delicate transition between directions, triangular wave control is preferable. Using the triangular wave control, the propeller is ramped up to speed rather than instantly changing direction. This prevents the large current spike, both reducing stress on the amplifier and the mechanical system. Figure 3.7 and 3.8 show the tunnel thruster's response to both short and long period triangular wave control. Overall, the pattern of the thruster results closely match those published in [7] and [12]. The long period triangular wave can be considered quasi steady-state and is equivalent to the steady-state map of propeller thrust versus speed, similar to that shown in Figure 3.6. As the period of the triangular control wave is shortened, the influence of the inertial response of the water column inside the tunnel becomes more evident.

Square wave control best illustrates the effects of water column inertia during sharp transients. During the sudden reversal of the propeller direction, several interesting features become apparent. The most noticeable feature is the large axial thrust spike (overshoot) that directly follows prop reversal. Figure 3.9 shows that this spike is quite significant, about twice the steady state value. This spike can

be attributed to the inertial loads that occur when the water in the system has to be reversed, which results in a momentary increase in the hydrodynamical loading of the propeller. To illustrate this, the same tests were run with the tunnel segments removed and the results are plotted in Figure 3.10. The force spike has almost disappeared without the added inertial effect of the water in the tunnel. A similar effect can also be seen in short period triangular wave control, as shown in Figure 3.8.

3.3 Small Tank Test Conclusions

The experimental data obtained from the small tank testing highlighted a few significant features, the most important of which are summarized here:

- Experimental data verified the linear relationship between steady state thrust and the square of propeller angular velocity.
- In comparing the forward and reverse axial thrust, it is apparent that there is a significant asymmetry in performance. The thruster produced 27% less thrust for a given propeller RPM in the forward direction than in the reverse. This is attributed to the asymmetry in the thruster configuration and design of the propeller.
- The transient tests exhibit a large spike after thrust reversal, which is due to the inertia of the water column.

The testing completed in the small tank also allowed for the development and debugging of the software, instrumentation and test procedure. Our results were

found to be similar to those of others. For example, our results in Figures 3.7 and 3.9 closely match the overall trends seen in Figures 3.11 and 3.12, taken from [12]. This comparison allows the next phase of testing in the towing tank to proceed with confidence in the setup of the thruster system and data acquisition.

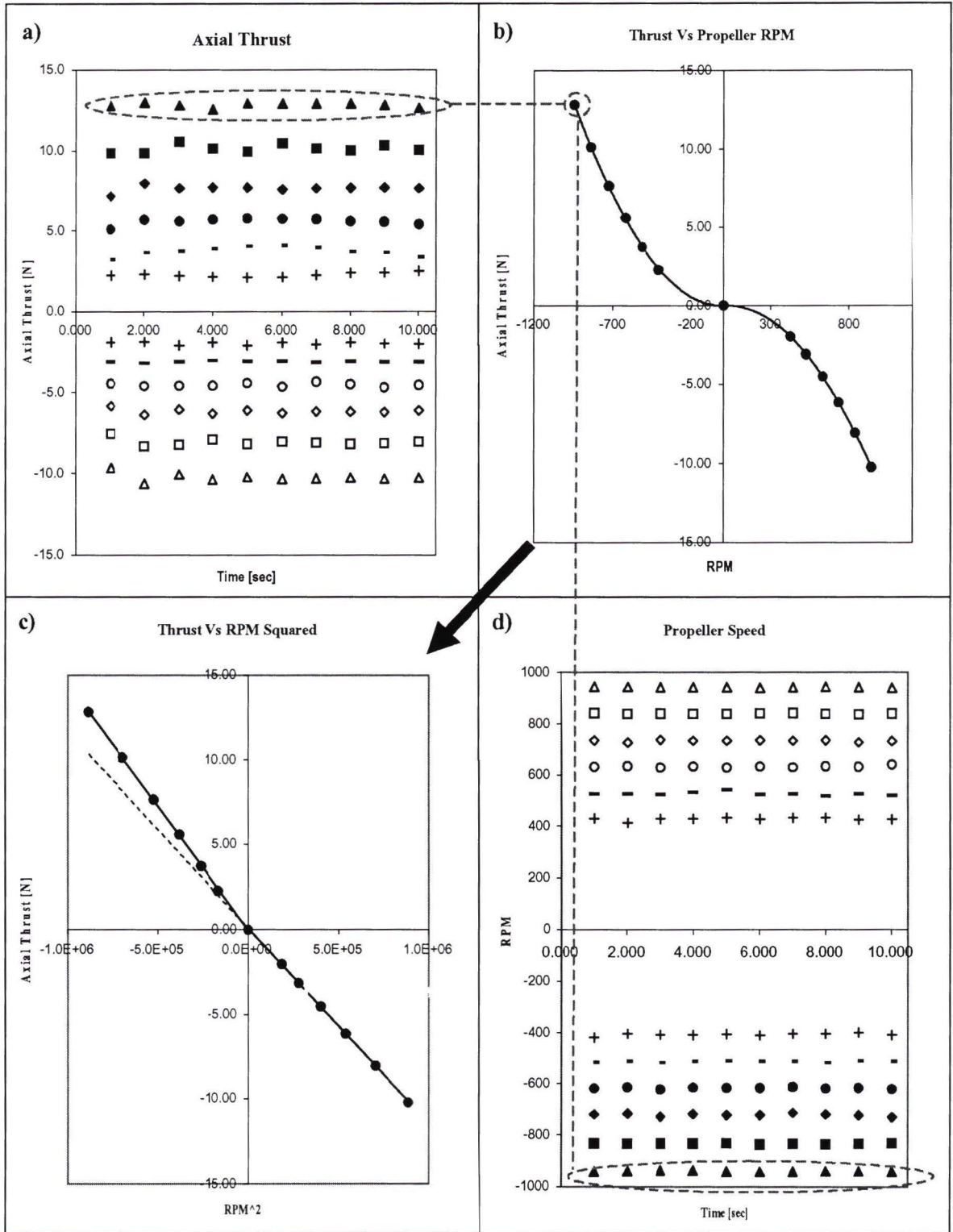


Figure 3.6. Steady State Axial Thrust

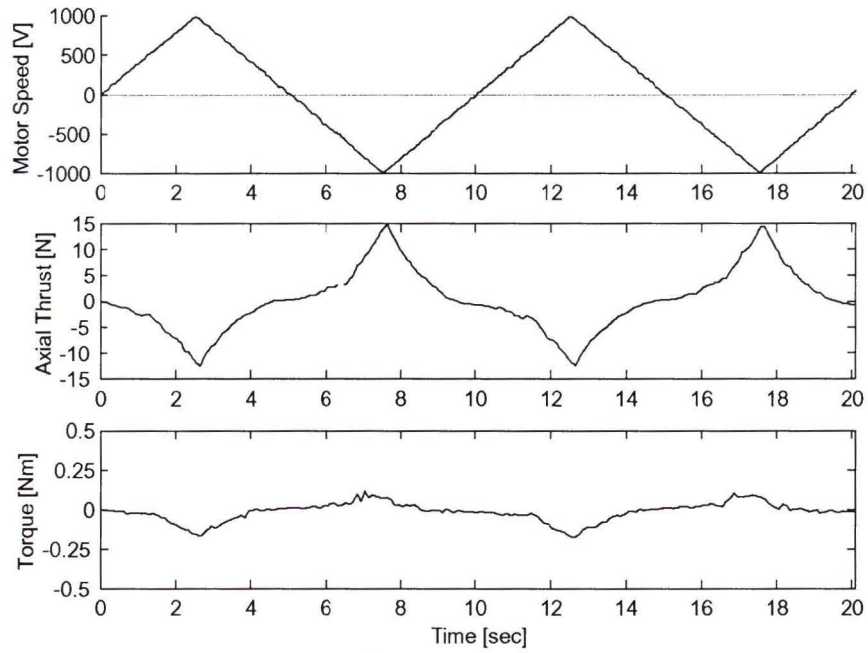


Figure 3.7. Long Period Triangular Wave Response

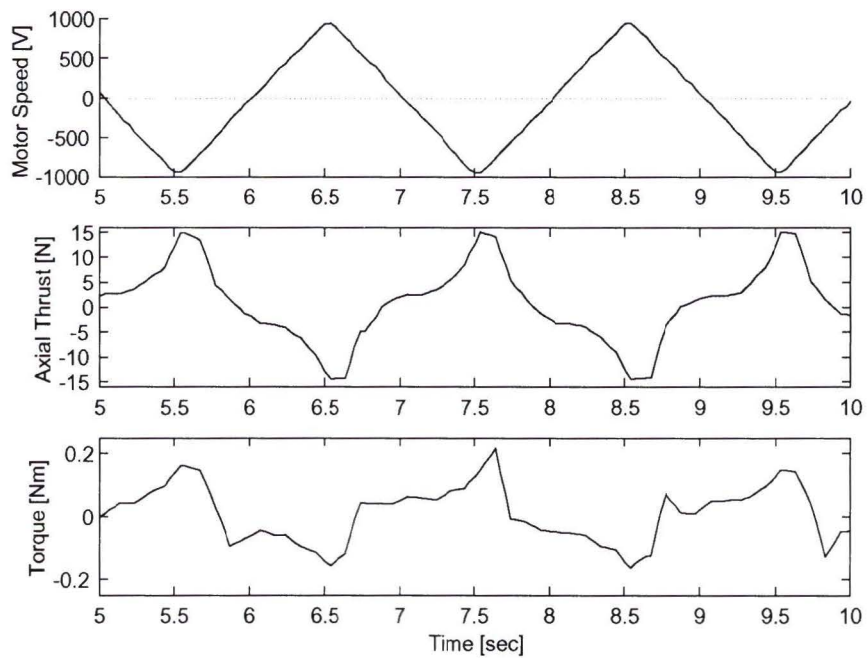


Figure 3.8. Short Period Triangular Wave Response

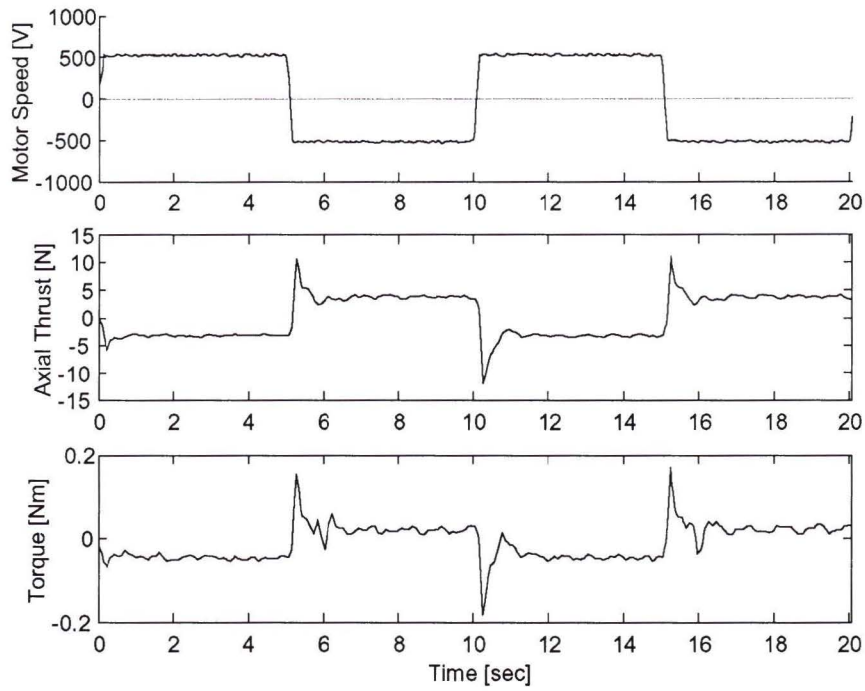


Figure 3.9. Square Wave Response

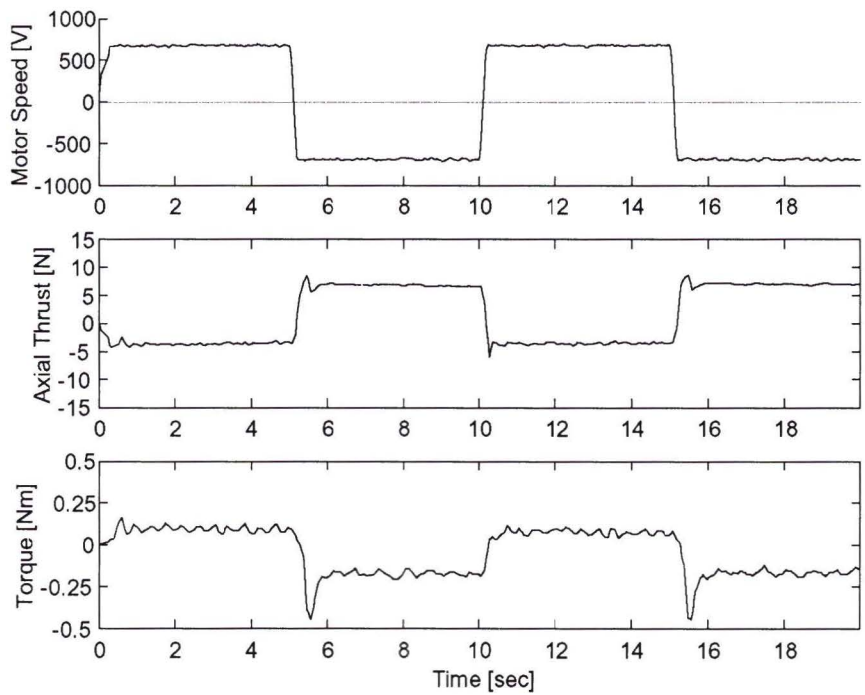


Figure 3.10. Square Wave Response with no Tunnel

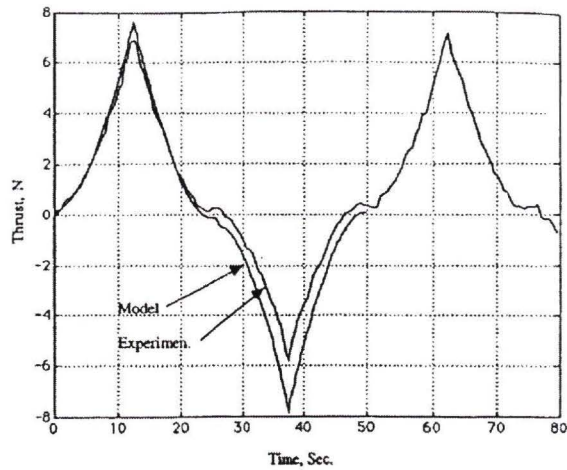


Fig. 12. Model thrust (N) compared with experimental data for 50-s period triangular wave inputs of voltage.

Figure 3.11. Experimental Results from Healey *et al.* [12]

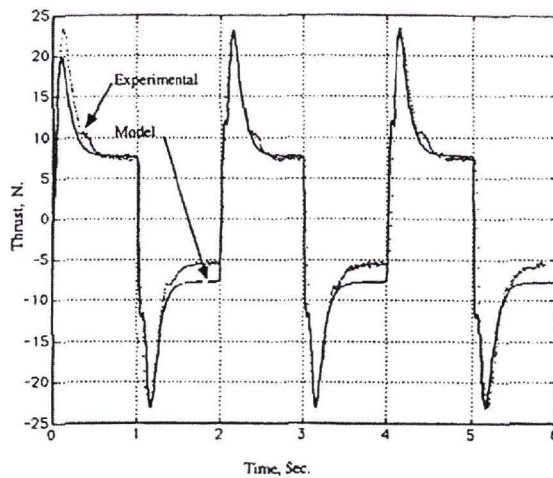


Fig. 13. Model compared with experimental thrust (N) data for square wave inputs of voltage.

Figure 3.12. Experimental Results from Healey *et al.* [12]

Chapter 4

Tow Tank Testing

Once basic performance characteristics have been determined using stagnant tank tests, the next step is to look at how these characteristics are affected by forward velocity and orientation. In order to quantify the effects of vehicle speed and orientation on thruster performance, a tow tank at the Memorial University of Newfoundland (MUN) was used to move a full scale model of the C-SCOUT AUV through the water at various constant yaw angles and speeds. At the time this thesis was written, there were no previous publications regarding experimental work investigating yaw angle and forward speed on AUV tunnel thrusters. Therefore, the model and tow tank, as well as the testing procedures, had to be designed.

During a forward speed maneuver, an AUV will often be at an angle to incoming flow, experience side-slip during a turn and be subject to the effects of external water currents. A through-body tunnel thruster will be affected in several ways by a combination of forward speed and yaw angle. In order to ensure controllability of the AUV under these conditions, their effect on thruster performance must be

quantified. The following sections will discuss the experiments performed to give insight into the behavior of tunnel thrusters during these operational conditions. The experimental testing focussed on a single thruster in the forward tunnel module, mounted transversely as illustrated in Figure 4.1. Later, in Chapter 5, the results of these tests will be used to adapt the existing tunnel thruster models to include the effects of forward speed and orientation.

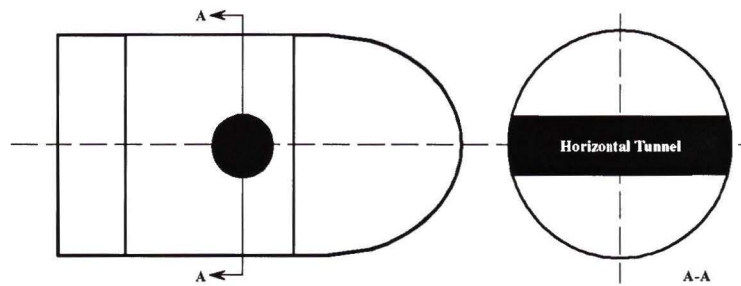


Figure 4.1. Side View and Cutaway of the Experimental Tunnel Configuration

4.1 Experimental Setup

The tow tank facilities used were located at Memorial University Newfoundland in St. John's, Newfoundland, Canada. The overall setup of the testing equipment for the tow tank is the same as that used in the small tank testing of Chapter 3. By keeping the setup the same, many of the complications involved with testing in a remote location are avoided. This section will discuss the general setup of the testing equipment, as depicted in Figure 4.2. The tow tank setup consists of a tow tank and its associated carriage on which is mounted a model of the C-SCOUT. The thruster module, described in Chapter 2, is mounted in the C-SCOUT model. The

PC and experimental interface, developed at the University of Victoria and discussed in Chapters 2 and 3, was placed on the tow carriage. Communication and power cables were then connected directly to the C-SCOUT tunnel thruster module.

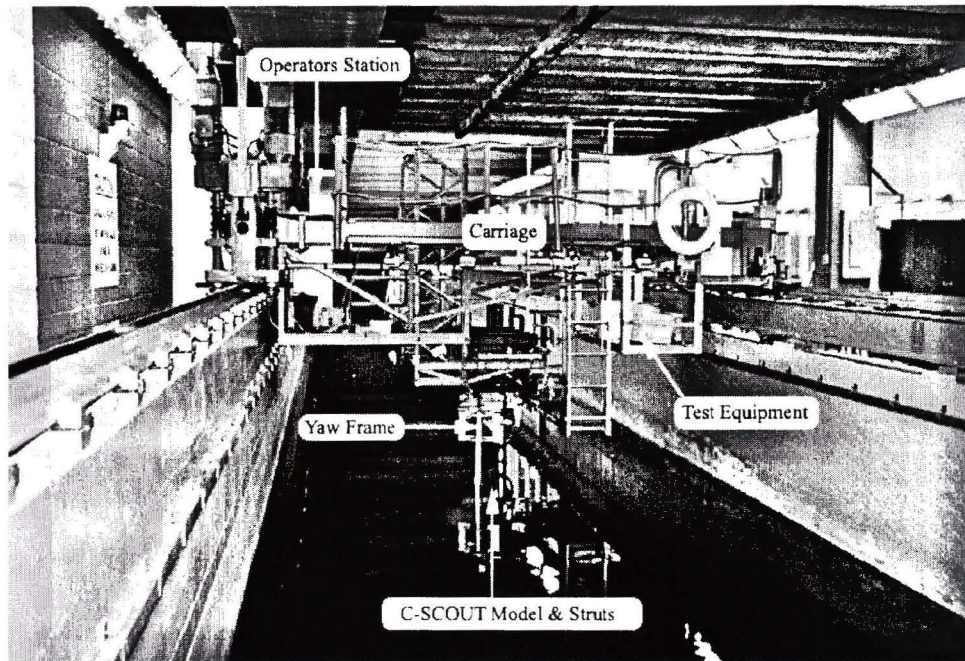


Figure 4.2. Tow Tank Facility

4.1.1 Tow Tank

The tow tank is 54.7 m long (about 32.2 m usable), 4.57 m wide with an adjustable water depth up to 2.5 m and a top carriage speed of 5.0 m/s. The carriage requires one operator to drive the carriage in addition to the person(s) running the experiment. The operator can run the carriage in a manual or automatic mode. While in automatic mode, the carriage executes a pre-set acceleration and settles on the desired speed.

The C-SCOUT model had to be held below the water and set at various yaw angles. To do this, a Yaw Frame was designed to mount to the tow carriage load

points and hold the two struts on the C-SCOUT model, shown in Figure 4.3. The lower half of the yaw frame can be rotated and fixed through $\pm 90^\circ$ of rotation in 5° increments. The design of the Yaw assembly was completed by several graduate and undergraduate students working at IMD and fabricated by MUN Technical Services.

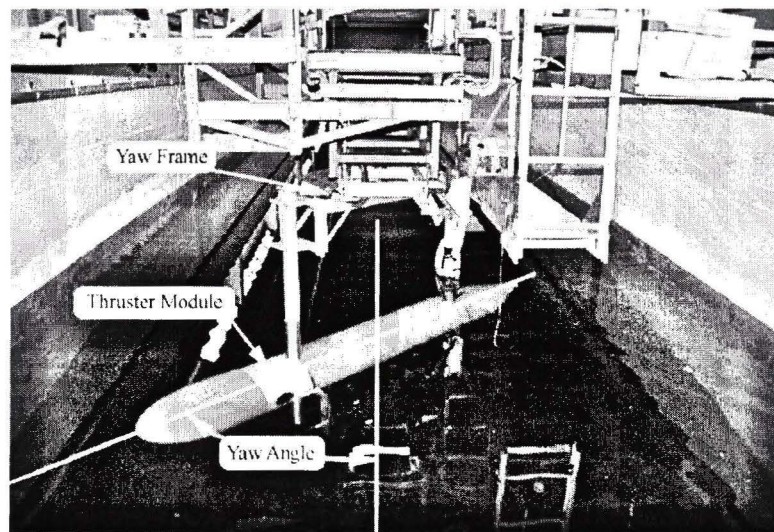


Figure 4.3. C-SCOUT Model Mounted On Tow Tank Carriage

4.1.2 C-SCOUT Model

The AUV model used for these experiments was a full scale replica of the C-SCOUT vehicle. This model was built at IMD to enable research on the hydrodynamic properties of the C-SCOUT AUV and various types of propulsion systems currently being developed. Figure 4.4 shows the configuration of the C-SCOUT model as mounted on the tow carriage. As mentioned in Section 2.4.5, the tunnel thruster module was bolted into the C-SCOUT model, and the entire model was mounted to the Yaw Frame. As shown in Figure 4.4, the module was placed between the main body section and the forward fin module. For the testing completed in this thesis

the fins were not attached to the fin module.

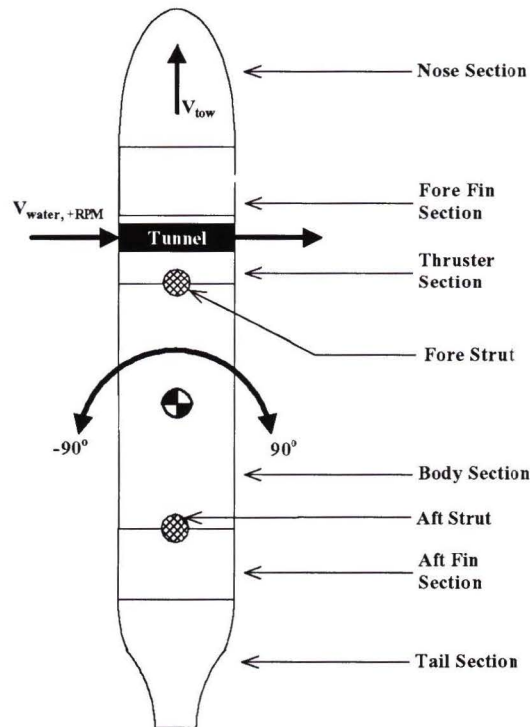


Figure 4.4. C-SCOUT Experimental Setup

In the previous chapter, the results were presented without discussing how they are applied to the vehicle. We are now interested in discussing the effects of vehicle orientation, and so the direction of thrust is important. It is therefore important to understand the directions of the body-fixed and load cell reference frames. The reference frames used for the remainder of this thesis are shown in Figure 4.5. For a positive propeller speed, water is pushed from left to right, the resulting body force (axial thrust) will be along the negative y-direction.

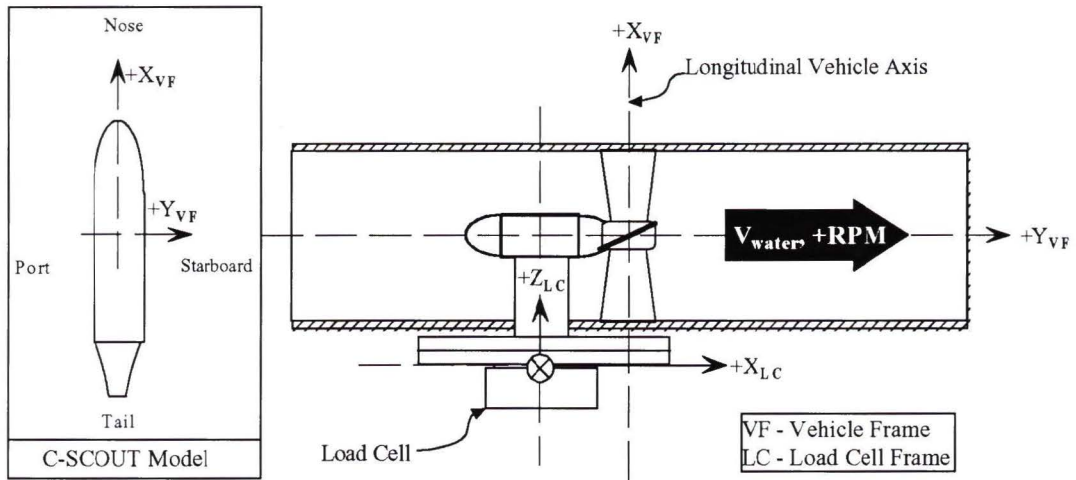


Figure 4.5. Body Axes Definitions

4.1.3 Test Considerations

As mentioned previously, the testing in this thesis involves a single tunnel thruster module mounted in one location on the vehicle. It is expected that hull interaction will play a large role in the experimental results. It should be noted that by only testing one location on the vehicle, there may not be enough information to completely model all the tunnel thrusters in C-SCOUT. In addition, the results may be vehicle dependent and therefore may not be directly applicable to other vehicles. It should also be noted that, due to time constraints with testing time in the tow tank, only one complete set of tests was performed. Because of this, the repeatability of tests was not thoroughly verified. However, spot checks were performed to verify that the data being collected was acceptably repeatable.

4.2 Test Procedure

To ensure the desired information is captured in the test results, a proper test procedure must be developed. The C-SCOUT vehicle was designed to have a top forward speed of 4 m/s. The operational range of the vehicle investigated in this chapter can be split into three general regimes:

- Maneuvering - hovering, including cross current up to 0.5 m/s
- Forward Travel - zero yaw angle forward travel
- High Speed Turning - side-slip experienced while turning at higher speeds

It was therefore important to create a test matrix to cover all three modes of operation. In addition to this, it was also important to obtain both steady state and transient test data for each mode. By testing yaw angles between $\pm 90^\circ$ at speeds up to 0.5 m/s the entire Maneuvering range is satisfied. Testing up to 4 m/s at zero yaw angles covers the Forward Travel condition. The last regime is the high speed turns with side-slip. The yaw frame was not designed to hold the vehicle against large hydrodynamical loads experienced during large yaw angles and high forward speeds. It was therefore necessary to minimize the range of angles tested at higher speeds. In order to obtain an estimated range for sideslip values, a simulation of the ARCS vehicle¹ was run for a maximum-rudder turn at a forward speed of 1.5 m/s. This resulted in a side-slip angle of 20° . The High Speed Turning range was therefore selected to include this point. A pictorial representation of the resulting test matrix can be seen in Figure 4.6, while the detailed test matrix can be found in Appendix A,

¹Simulation code [17] for the International Submarine Engineering Research (ISER) vehicle ARCS

Figure A.3. In total there are 86 test cases for both the steady state and transient tests.

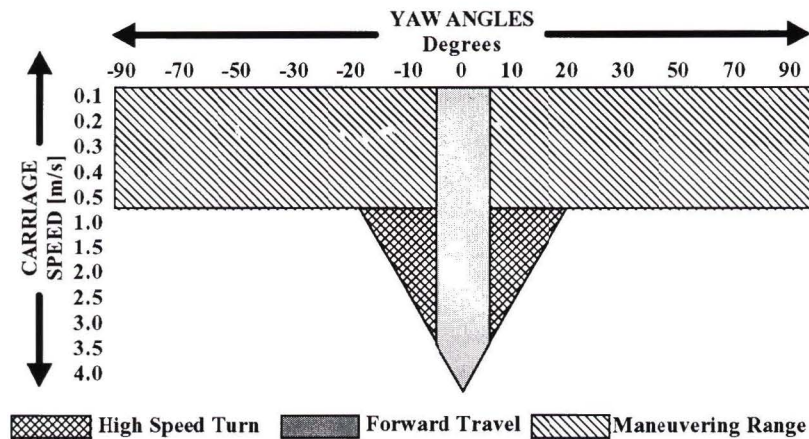


Figure 4.6. Tow Tank Test Matrix

4.3 Tow Tank Results

Before discussing the tow tank results, a few general facts and assumptions must be noted, particularly in regard to the direction of thrust with respect to the orientation of the model. For the steady state tests, the thruster unit was operated in positive rotational direction. This results in water flow from left to right (see Figure 4.4). When oriented at $+90^\circ$ yaw angle, Figure 4.7 c), the oncoming water is going in the same direction as the thruster tries to drive it. As will be seen in the following sections, this causes a decrease in thrust because the propeller RPM is much higher before its advance velocity matches the speed of the incoming water. In Figure 4.7 b) at -90° , the opposite occurs. The water exiting the thruster is being pushed into the oncoming water. It is expected that these complicated flow conditions will have a large effect on the thruster in this configuration.

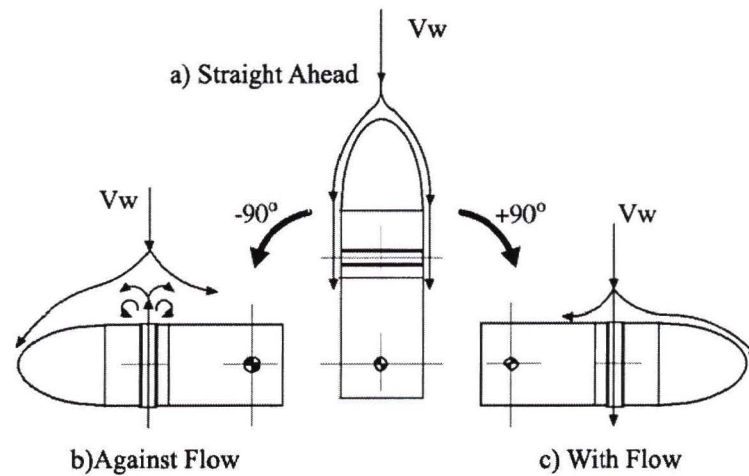


Figure 4.7. Experimental Thruster Outlet Cases

The only important assumption made before beginning these tests is that the amount of asymmetry in the thrust will remain the same as in the tests performed in the stagnant tank. This allows us to use the slope difference for the stationary tests (seen in Figure 3.6) to convert the positive rotation propeller data into negative rotation. The test matrix for the steady state tests was therefore only performed for positive propeller RPM.

4.3.1 Steady State Tests

It would take a very long time to complete an individual test matrix (see Figure 4.6) for several steady-state propeller speeds. In order to reduce test time, the motor speed was slowly ramped from zero to full speed for each constant forward speed and yaw angle from the test matrix. Several values on the ramp were compared to true steady state thrust and the values closely matched. It was therefore assumed that the data from the low speed ramp, was an accurate representation of the steady state

performance.

Again, axial thrust is plotted against propeller RPM squared. Figures 4.8 and 4.9 show two sample plots from the test matrix. The remaining 86 plots are in Appendix A, Figures A.4 through A.25. From this raw form the data can be put into a more compact form. In order to condense all the steady state test data down to a format that can be plotted on a few graphs one can make use of the linear relationship between axial thrust and RPM squared as observed in the previous chapter. It is apparent from Figures A.4 through A.25 that the y-intercept is no longer zero but varies with orientation and carriage speed. The relationship between thrust and RPM squared therefore becomes

$$T = b |n_p| n_p \implies T = a + b |n_p| n_p \quad (4.1)$$

where T is the axial thrust, a is the y-intercept in $[N]$, b is the slope in $[\frac{N}{RPM^2}]$, and n_p is propeller speed in $[RPM]$. For each test case the slope and y-intercept was recorded², the results can be seen in Figures 4.10 to 4.15. In general, an increase in b represents an increase in thrust produced for a given propeller speed. An increase in a corresponds to an increase the drag of the tunnel, thruster leg and propeller, when the propeller is stationary. The fact that all the steady state experimental data shown in Figures A.4 to A.25 follows the relationship given by eq. (4.1) implies that we can study these plots simply by looking at how a and b vary with forward speed and yaw angle.

²Figures A.1 and A.2 in Appendix A contains the tabulated values of slope and intercept.

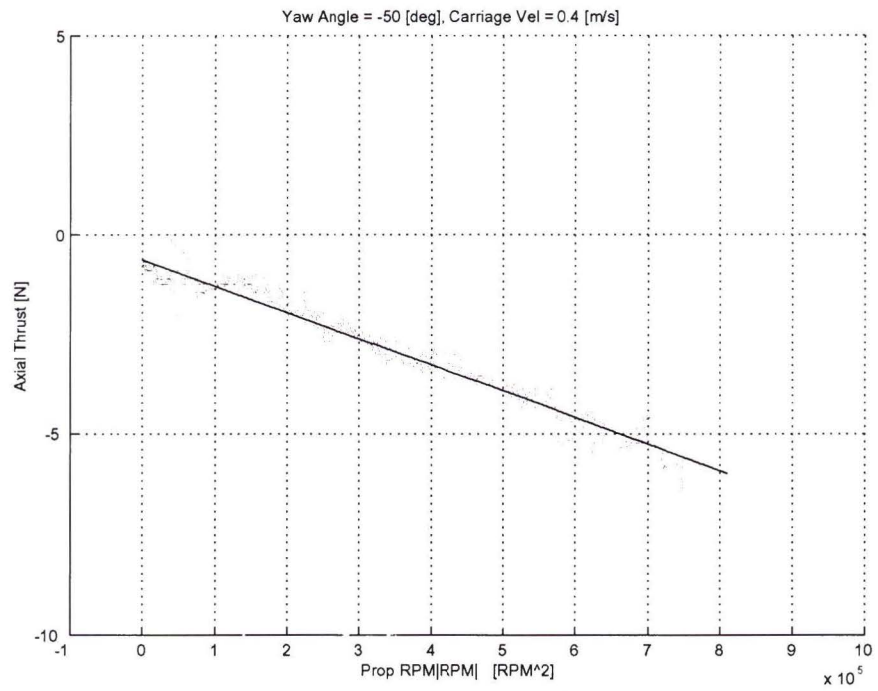


Figure 4.8. Yaw -50 [deg], Carriage Speed 0.4 [m/s]

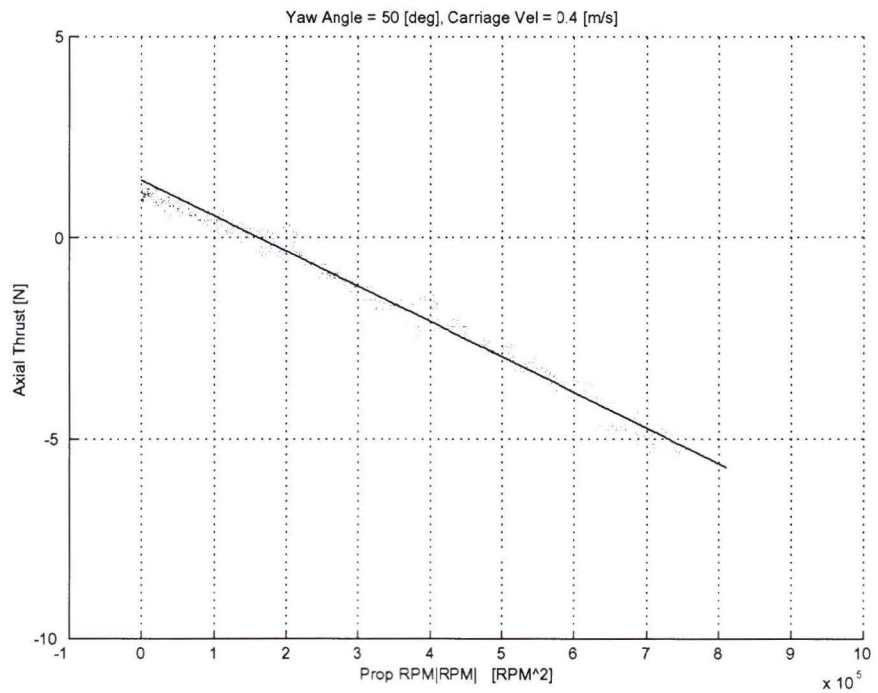


Figure 4.9. Yaw 50 [deg], Carriage Speed 0.4 [m/s]

4.3.1.a Maneuvering Range

The primary motivation behind adding tunnel thrusters to C-SCOUT was to enable low speed maneuvering. As a result the maneuvering range contains the bulk of the experimental testing. In general, axial thrust performance is slightly reduced as carriage speed is increased, as shown in Figure 4.11. At low speeds, the slope values do not change much as a function of yaw angle, mainly due to the insignificant effects of the water at low vehicle velocity. As carriage speed is increased, the magnitude of the slope falls more quickly with speed. For yaw angles between -50° and -70° there is a dramatic drop in axial thrust performance, to about half the low speed value. This is thought to be caused by the fluid interaction at the thruster outlet and the disturbance to the intake caused by the body of the vehicle. This is not of great concern considering what operational mode this quadrant represents. For a negative yaw angle and a positive propeller speed the thruster would be trying to move the vehicle in the same general direction as the oncoming flow. In a station-keeping or hovering operation this would not be a very likely occurrence.

The behaviour of the y-intercept is relatively logical: as the component of the oncoming speed along the thrusters longitudinal axis (X_{LC}) increases (increasing speed, increasing yaw angle), the load cell senses a force in that same direction. When the yaw angle is negative, the y-intercept is also negative and increases in magnitude with increasing speed.

Between $\pm 30^\circ$, the intercept curves do not appear to be affected much by forward velocity. This is thought to be connected to the effects of 'through-flow', or the velocity of water through the tunnel due to the oncoming flow. At lower yaw angles, the component of forward velocity that becomes through-flow will be small. As the

yaw angle increases beyond $\pm 30^\circ$, the forward speed will likely result in a higher amount of through-flow, eventually becoming equal to the forward carriage speed at $\pm 90^\circ$. The same trend is not present in the slope data between $\pm 30^\circ$ suggesting that the amount of axial thrust produced for a given RPM is not tied as strongly to the effects of through-flow.

The complexity of the curves in Figures 4.10 and 4.11 suggest that there is not a simple relationship between forward speed, yaw angle and axial thrust. It is likely that the complex fluid dynamical effects of hull interaction are having a large effect on thruster performance. As a result, the performance characteristics of the tunnel thruster cannot be de-coupled from the C-SCOUT model, making the data vehicle dependent. Because there is no simple fundamental relationship, the method by which the results are incorporated into the numerical model will be parametric rather than analytically based. This will be covered in Chapter 5.

4.3.1.b Forward Travel

The experimental results in this section will help shed some light on how a tunnel thruster performs as the vehicle transitions between maneuvering speeds and forward travel speeds. The intercept and slope data for the high speed tests at zero yaw angle is shown in Figures 4.12 and 4.13 which correspond to the test data in Figures A.4 to A.25 in Appendix A.

Figure 4.12 shows a increasing value for the y-intercept which becomes noticeable at about 1.0 m/s. Because the vehicle is completely symmetrical about its longitudinal plane, the pressure at the tunnel intake and exit should be the same, resulting

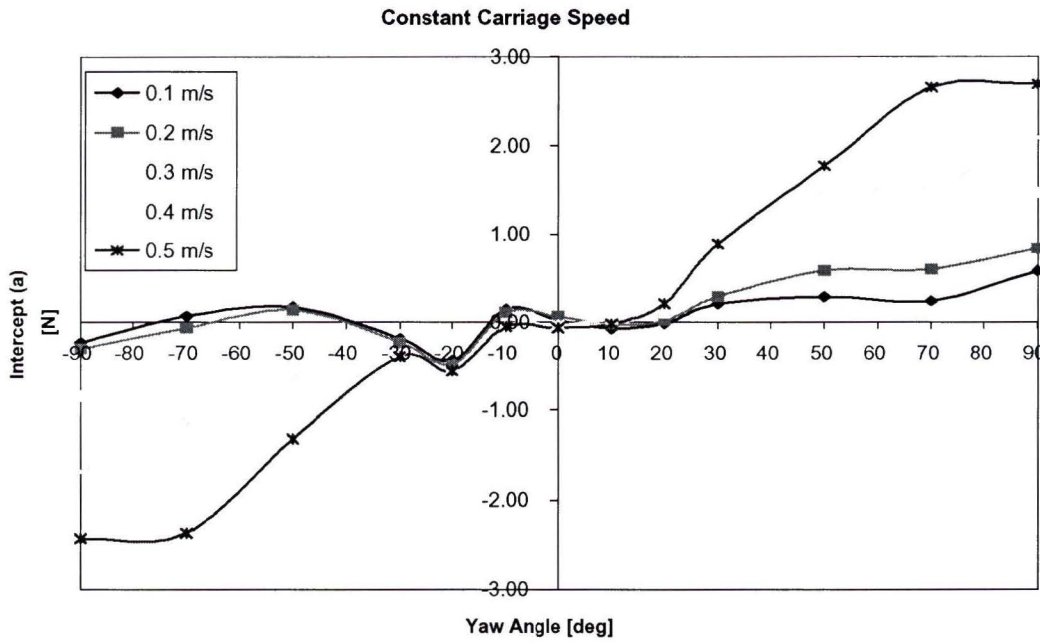


Figure 4.10. Maneuvering Range Axial Thrust Intercept Values

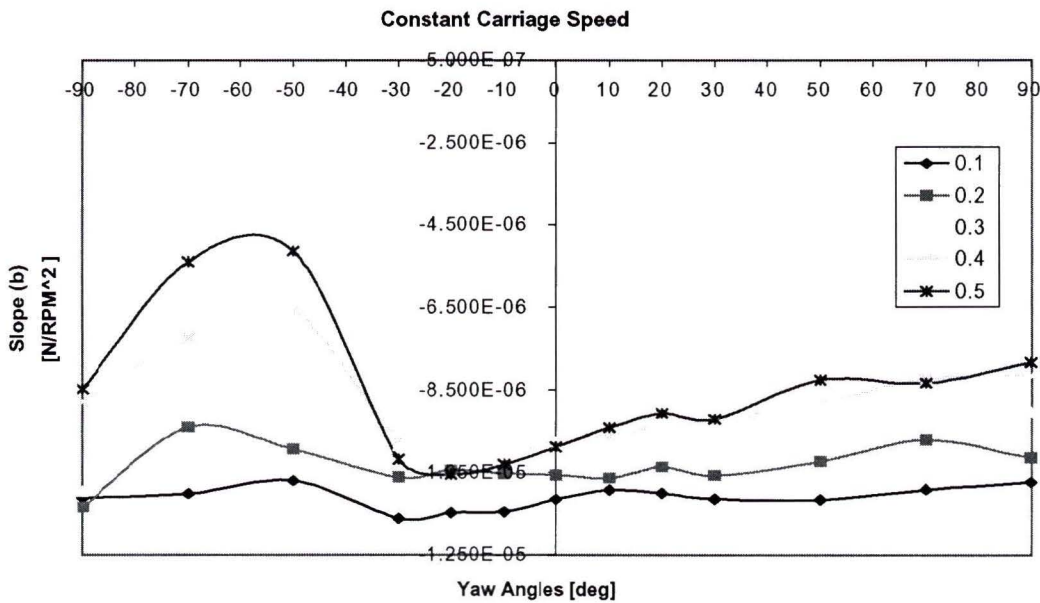


Figure 4.11. Maneuvering Range Axial Thrust Slope Values

in zero net flow through the tunnel at zero RPM. This conflicts with the information in Figure 4.12. The intercept values are very close to zero at low speeds and appear to increase quadratically as a function of forward speed as one would expect for a hydrodynamic load along the axis of the tunnel. Because no logical explanation could be found for this to occur at zero yaw, we suspected that there was a misalignment in the vehicle model with respect to the direction of travel of the tow carriage. This is supported by the information in Figure 4.14. If there was some misalignment and the assumption of zero through-flow at zero yaw is correct, then we would expect to see this zero crossing at some other yaw angle close to the center point. From Figure 4.14 this point appears to be at a yaw angle of about -7° . At the time of the tests, a series of previous measurements and assemblies were relied on to align the vehicle. Because there was no way to accurately verify this alignment with respect to the carriage, the setup was assumed accurate. Based on the mounting used for these tests, a misalignment of 7° between the vehicle (1.75 m below the carriage) and the carriage is plausible. The information in Figure 4.12 is therefore disregarded and it is assumed that the values of intercept will be close to zero for all vehicle speed at zero yaw angle.

There does not seem to be a clear pattern in the slope data of Figure 4.13. This is most likely due to the large amount of scatter in the load data for the higher velocity tests (e.g. Figure A.25 in Appendix A). The large amount of scatter in the data at higher speeds is attributed to the flexibility of the yaw frame. There was a significant amount of flex between the frame and the model, and this lack of rigidity could easily result in variations in measured thrust. From Figure 4.13 it seems reasonable to assume that the slope remains constant within the tolerance of the data.

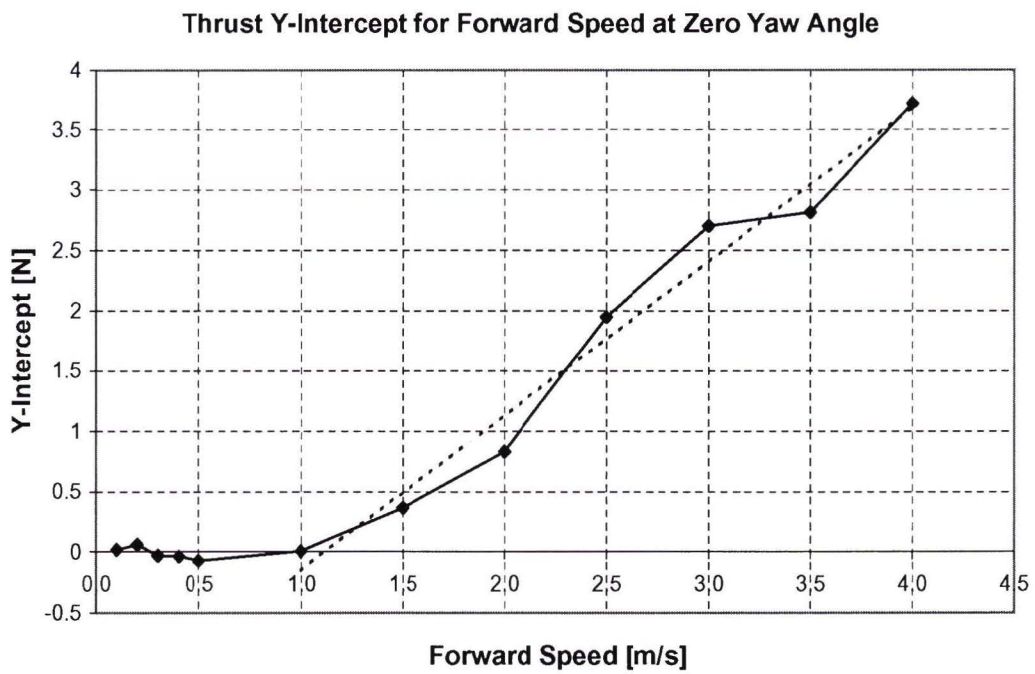


Figure 4.12. Forward Travel Axial Thrust Intercept Values

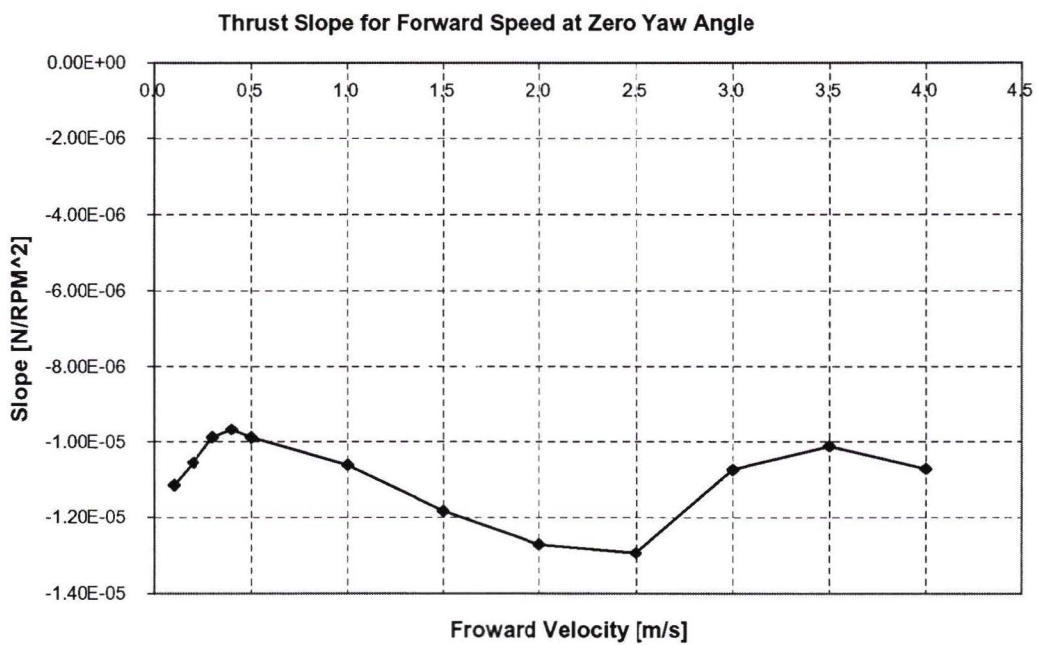


Figure 4.13. Forward Travel Axial Thrust Slope Values

4.3.1.c High Speed Turning

Although it was not the initial intention of the design group to use the tunnel thrusters at higher speeds (in place of, or in combination with the control fins) it may be a useful means of control augmentation. It has been shown by Ridley [21] that bow thrusters are an effective steering aid in surface ships with headway. It is assumed that a similar effect would apply to underwater vehicles using tunnel thrusters. The previous section dealt with a vehicle in forward motion, this section deals with the vehicle in forward motion at high speed, coupled with the side-slip experienced while turning.

Figures 4.14 and 4.15 present the data for the high speed turning range. These two plots are analogous to the two plots discussed for the maneuvering range. For positive yaw angles there appears to be a slight increase in the axial thrust produced for a given RPM when compared to the straight forward case. This is actually the opposite of the effect observed at lower speeds in Figure 4.11. For negative yaw angles the opposite is true, increasing forward speed leads to a reduction in thrust. Additionally, the magnitude of this reduction does not seem to be constant with increasing yaw angles.

One interesting feature in Figure 4.14 is the lack of symmetry about the y-axis (even if shifted by -7°). This is attributed to the asymmetrical configuration of the internal thruster components (e.g. thruster leg). Because this imbalance is significant, it would suggest that having a fully symmetrical tunnel configuration would be beneficial.

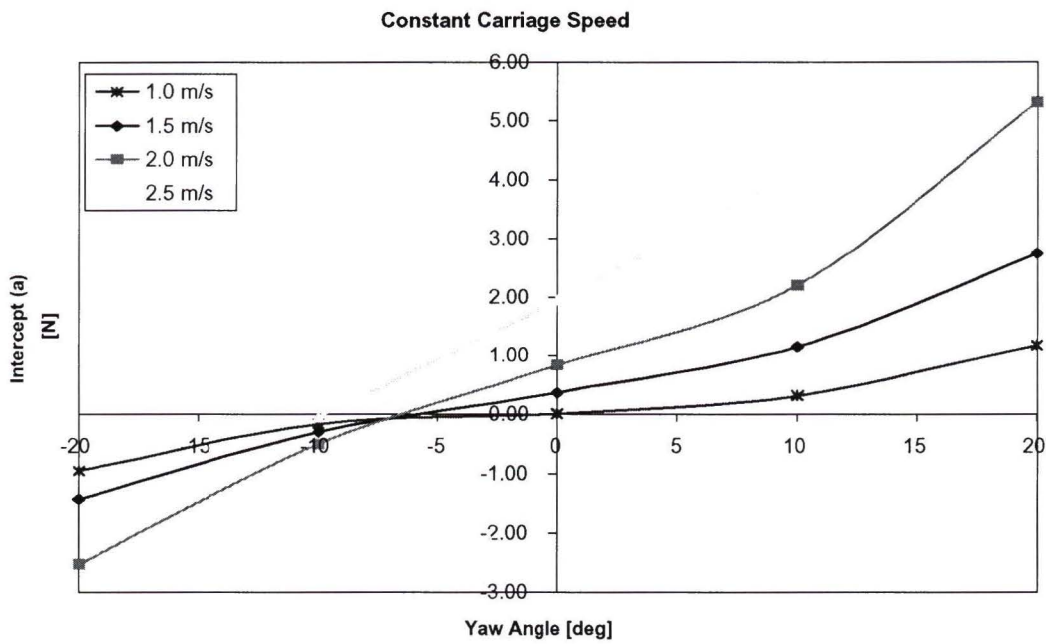


Figure 4.14. Side-Slip Range Axial Thrust Intercept Values

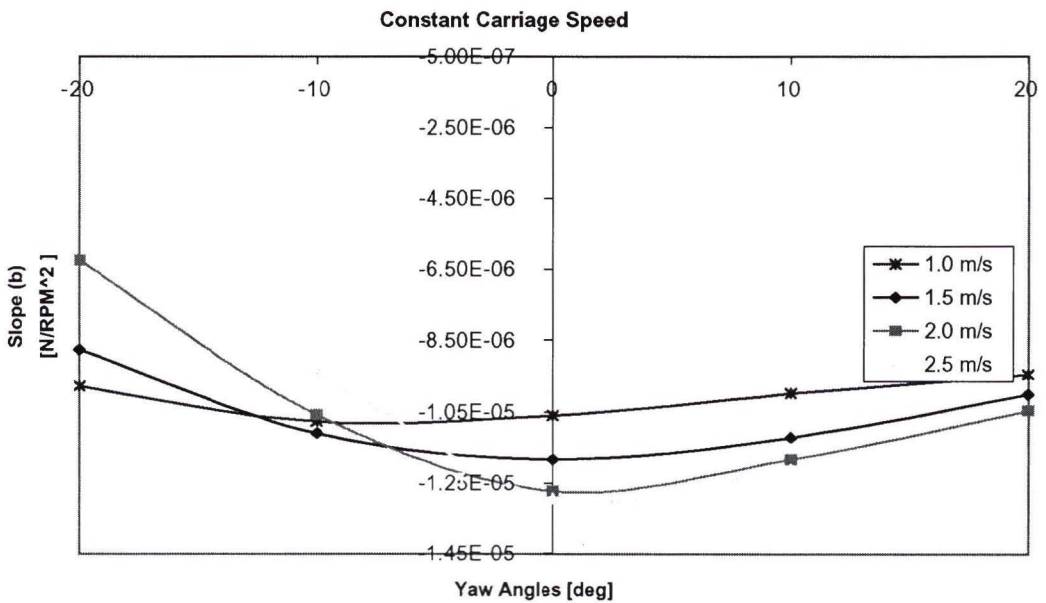


Figure 4.15. Side-Slip Range Axial Thrust Slope Values

4.3.2 Transient Tests

Square wave control wave selected as the test case to capture the transient behavior of the thruster. The same test matrix used in the steady state tests was used for the transient tests. At each of these conditions the thruster was cycled through a series of alternating step inputs from forward speed to reverse speed. The complete set of figures for the transient tests can be found in Appendix A, Figures A.26 through A.46³. In general, within the sampling frequency of the software, the transient behavior did not change significantly with yaw or forward speed.

Figure 4.16 shows the response of the thruster for several values of forward speed at positive 50° yaw. The overall shape and magnitude of the different curves match closely. As seen in Figure 4.16, the only significant difference between the curves is the reduction in steady state thrust as carriage speed is increased. This issue was addressed in some detail in the previous section.

Figure 4.17 shows the raw axial thrust data for +30° yaw. Initially, it appears the transient behavior does not remain constant. Also due to timing issues, there appears to be at least one curve that is partially out of phase. To better illustrate the similarity in transient behavior between the different carriage speeds the force data was aligned at the base of the first step for $\pm 30^\circ$. Once aligned, Figures 4.18 and 4.19 show an almost identical match for the transient portion of the curve. This close match is also observed at higher carriage speeds⁴, thruster response for velocities from 0.1 to 2 [m/s] are plotted for a yaw angle of 20° in Figure 4.20. As shown in Figure 4.21, the same similarity is observed when the comparison is made

³There were a few problems with the quality of the data at higher carriage speeds.

⁴Test data for $V_{\text{carriage}} = 3.0$ to 4.0 [m/s], at Yaw = 0 [deg], was ill-behaved.

for constant carriage speed over the entire $\pm 90^\circ$ range of yaw angles. From this we can conclude that forward speed and orientation do not have a significant effect on transient thruster performance at lower speeds. Additionally, this implies that the thruster transients are not coupled to the body effects of the vehicle at low speeds. As a result, static transient thruster tests can be used with some level of confidence to define the transient performance of the tunnel thruster unit.

4.4 Testing Conclusions

The tow tank tests were successful in revealing a few key issues with thruster operation at various constant yaw angles and forward speeds. For the low speed maneuvering range, axial thrust performance is slightly reduced as carriage speed increases. This effect increases in magnitude for larger yaw angles. The data obtained for the forward travel range suggested little change in thrust performance with increasing forward speed. It was however determined that there was a potential misalignment of the C-SCOUT model. It is therefore suggested that this series of tests be repeated before any concrete conclusions are drawn. The high speed turning range revealed a definite asymmetry in thrust performance for positive and negative side-slip angles. If the tunnel thrusters are to be used for high speed control augmentation, this asymmetry may be important.

In addition to the basic information from the steady state tests, the data also suggests that thruster performance cannot be de-coupled from the hull interaction, thus making the data presented in this thesis vehicle dependent. More tests are required to determine if the data is also strongly dependent on position and orientation

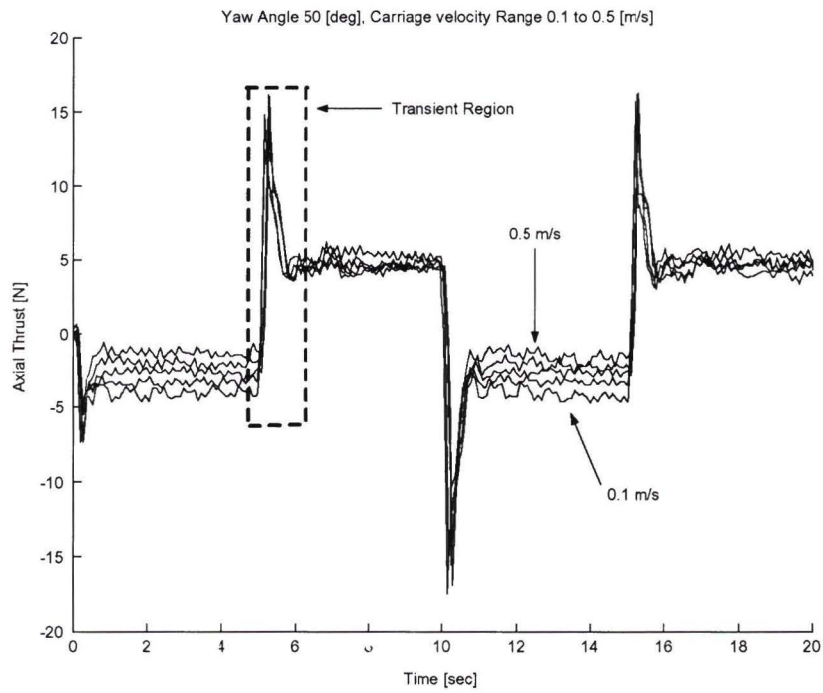


Figure 4.16. Square Wave Response, Yaw Angle 50 [deg]

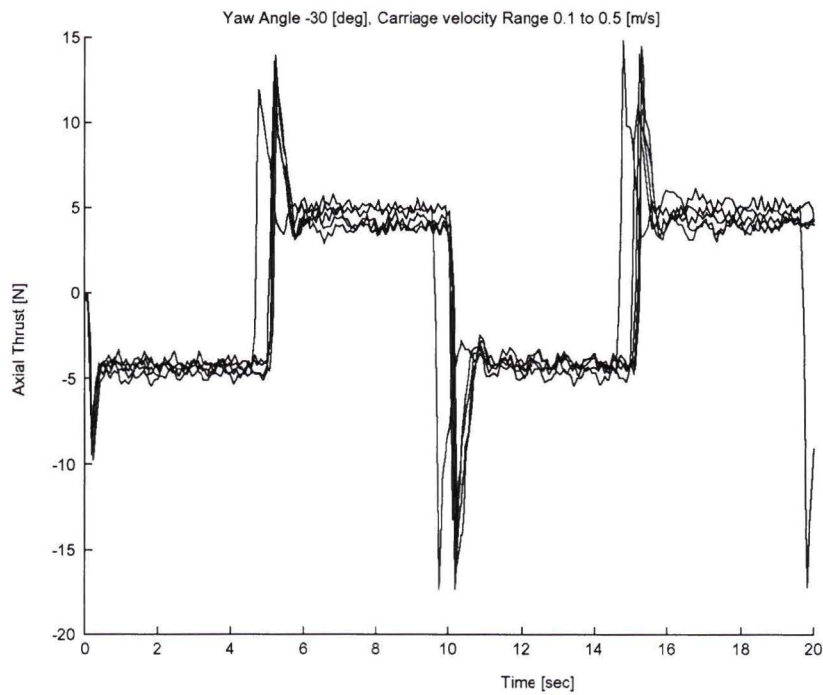


Figure 4.17. Square Wave Response, Yaw Angle 30 [deg], Raw Data

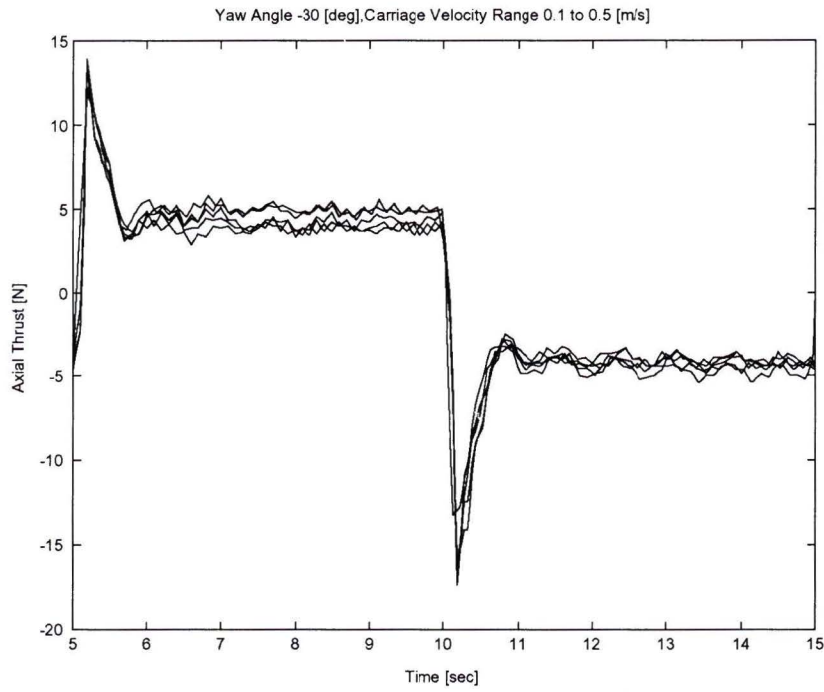


Figure 4.18. Square Wave Response, Yaw Angle -30 [deg], Aligned at First Step

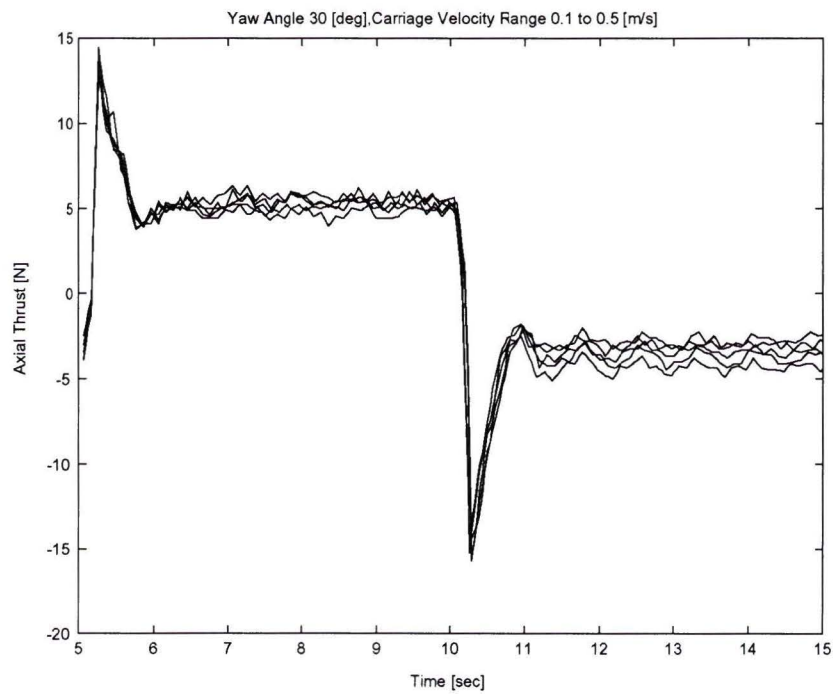


Figure 4.19. Square Wave Response, Yaw Angle 30 [deg], Aligned at First Step

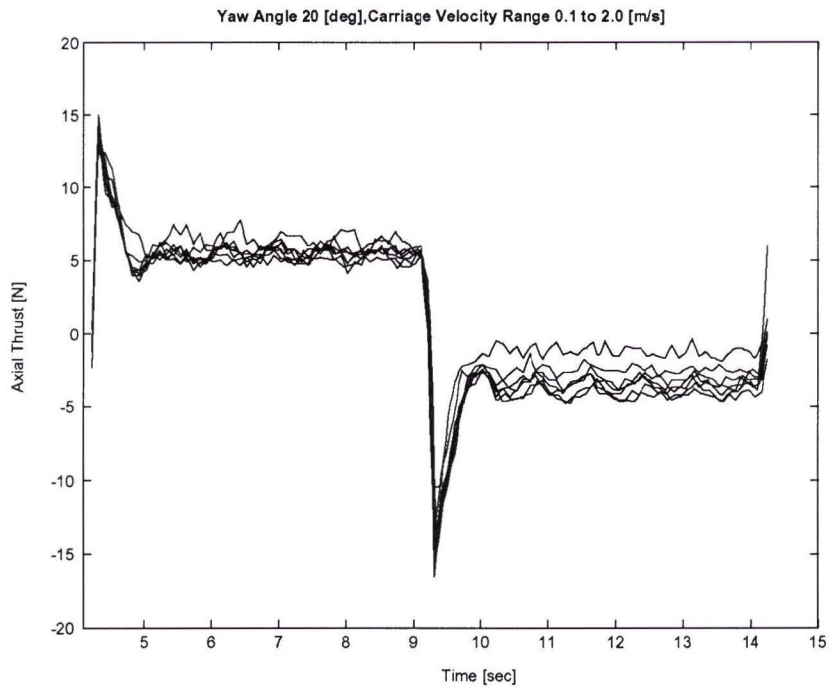


Figure 4.20. Square Wave Response, Yaw Angle 20 [deg], Aligned at First Step

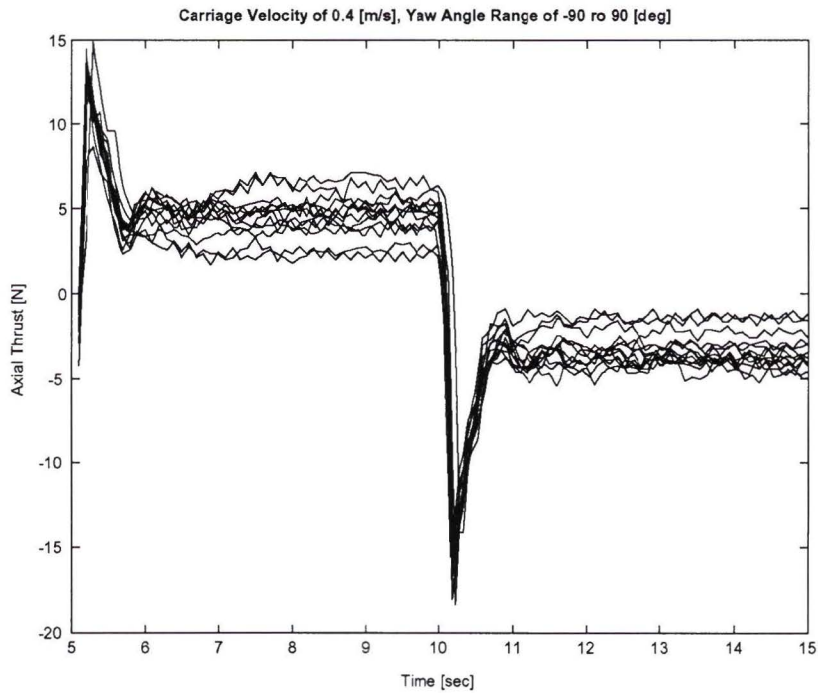


Figure 4.21. Square Wave Response, Carriage Speed 0.4 [m/s], Aligned at First Step

of the tunnel in the vehicle. As a result, it is clear that a simple relationship between forward speed and yaw angle and the resulting through-flow cannot be used to determine thruster performance. This is of importance when attempting to adapt existing (static) tunnel thruster models to free swimming AUV systems.

The other very important performance characteristic was the behavior of the transient data. The transient performance of the thruster did not seem to be affected significantly with changes in yaw angle and forward speed, especially at lower speeds. This is quite important when considering the modeling of tunnel thruster units. Thruster models that include the transient behavior of the thruster are much more complicated than steady state models. Because the transients did not change much over the range of tests, especially for lower speeds, the transient component of existing (static) thruster models should remain valid.

Chapter 5

Modeling

The previous two chapters dealt with experimental results from various tests on a small AUV tunnel thruster. This chapter will introduce theory commonly used to model the performance characteristics of underwater thrusters. The goal of this chapter is to adapt current tunnel thruster models to include the effects of vehicle speed and orientation, based on the experimental results from Chapter 4. Before this is done, it is important to understand the current state of thruster modeling. Section 5.1 introduces a basic steady state model for marine thrusters. Section 5.2 discusses the development of thruster models capable of modeling the thruster's transient behavior. Section 5.3 discusses how the information obtained in Chapter 4 can be incorporated into the basic thruster model to produce an augmented model. Finally, in Section 5.4, both the basic and augmented simulations are compared to experimental data.

5.1 Steady State Modeling

It is well established (see e.g. [25] [27]), that under steady-state bollard-pull conditions, a symmetrical propeller's steady-state axial thrust, $F_{a_{ss}}$, is proportional to the square of its rotational velocity, ω_p . This quadratic relationship can be expressed as

$$F_{a_{ss}} = \rho A \eta^2 P^2 \omega_p |\omega_p| \quad (5.1)$$

where ρ is water density, A is the propeller's swept area, η is the propeller efficiency, and P is the propeller geometric pitch measured in meters of forward travel per radian of rotation. The data presented in Chapter 4 confirms this relationship. It is important to note, however, this relationship only holds true under steady state bollard-pull conditions and is therefore not adequate for representing the thruster's transient performance.

5.2 Transient Modeling

This section discusses the steps involved in creating a nonlinear thruster dynamic model, where the state variable is axial fluid velocity, U_a , with propeller rotational velocity, ω_p , as the single control input. The dynamic model is composed of two parts: the propeller model (discussed in Section 5.2.1) and the hydrodynamic model (discussed in Section 5.2.2). The propeller model is presented in two ways. Section 5.2.1.a covers a method based on open water propeller data, known as $K_T - K_Q - J$ curves. Section 5.2.1.b discusses a method based on the assumption that propeller thrust, torque and axial fluid velocity are related by the lift and drag forces on airfoil shaped blade elements. The latter of the two is the most common approach to

modeling transient tunnel thruster behavior and can be found in [4], [7], [12], [25], and [26]. The basic hydrodynamical flow model in Section 5.2.2 assumes that the propeller operates in stagnant water. Section 5.2.3 then describes how the propeller and hydrodynamic models are assembled to form a complete thruster model.

5.2.1 Propeller Model

5.2.1.a Conventional Open-Water Propeller Data Method

Conventional methods for testing and representing open-water performance of marine propellers have been developed. These methods allow for non-dimensional comparison of various marine propellers. The thrust developed and the torque absorbed are considered primarily dependent on the following parameters: V_a , the velocity of advance; D , propeller diameter; ω_p , propeller rotational speed; ρ , water density; μ , the dynamic viscosity of the fluid; and the pressure of the fluid relative to the vapor pressure [9]. The results are typically plotted in terms of dimensionless thrust and torque coefficients, K_T and K_Q , as functions of the advance coefficient J . These quantities are defined as the follows:

$$K_T = \frac{F_a}{\rho n^2 D^4} \quad (5.2)$$

$$K_Q = \frac{T_p}{\rho n^2 D^5} \quad (5.3)$$

$$J = \frac{V_a}{nD} \quad (5.4)$$

where F_a is propeller thrust, T_p is propeller torque, n is propeller speed in revolutions per second. An example of typical performance curves can be found in Figure 5.1.

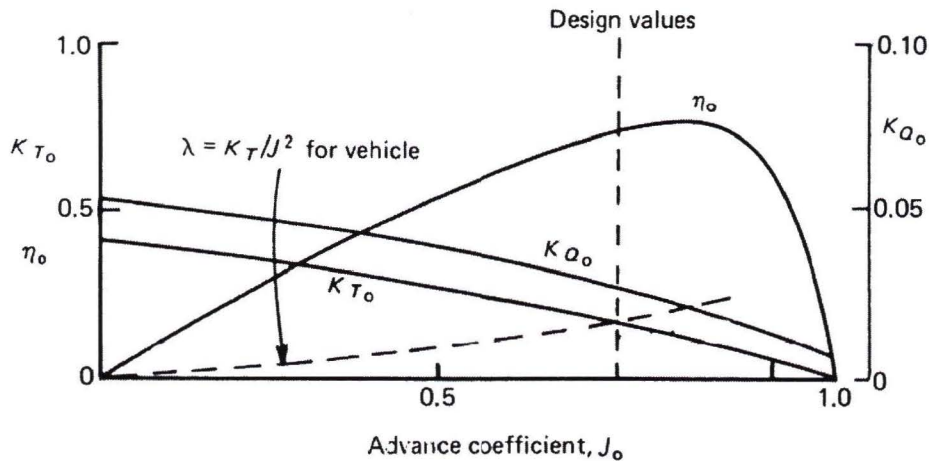


Figure 5.1. Typical Propeller Performance Curves [9]

The information contained in these performance curves applies to open-water tests with the propeller rotation and vehicle speed in the forward direction. Interpolating in the $K_T - K_Q - J$ diagrams of a specific propeller series is all that is needed to solve many classic ship propulsion problems. However, because the $K_T - K_Q - J$ curves are measured for a propeller turning at positive RPM and advancing with a positive V_a , this approach is not intended to model the propeller's thrust and torque characteristics for other combinations of RPM and V_a . As mentioned in Section 1.1, for smaller vessels, including modern day AUVs, the thruster's transient hydrodynamics can dominate the vessel's maneuverability, and therefore cannot be neglected. The full operational range of a propeller/thruster covers four quadrants, as shown in Figure 5.2, while the information in standard performance curves (see Fig 5.1) only covers the first quadrant of propeller operation.

Unfortunately, data covering the entire region of propeller operation is hard to

find and often related to a specific application. The work presented in [6], [11], [22], among others, illustrates $K_T - K_Q - J$ curves for an expanded range of operation and how they can be implemented to represent four-quadrant operation. This is done by making a bilinear approximation that gives good results for steady thrust (quadrants 1 and 3), but may be up to 40% erroneous in the transient case (quadrants 2 and 4) [11]. This, combined with the possibility of cavitation during heavy transients, leads to a high level of uncertainty with this approach. The other problem with this approach is the need for application-specific propeller curves. Separate experiments must be conducted using marine tow tank or cavitation tunnel facilities to construct the extended $K_T - K_Q - J$ curves.

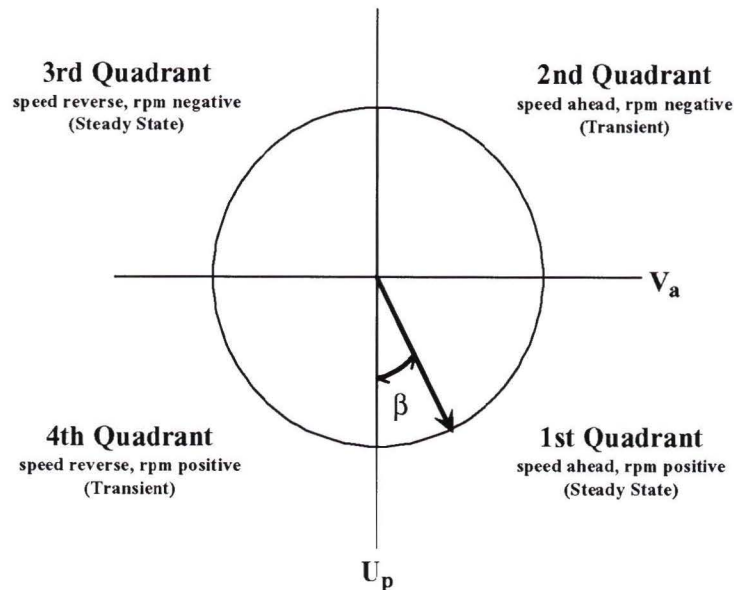


Figure 5.2. Four-Quadrant Propeller Operation, Figure 1.3 reproduced here for convenience.

5.2.1.b Blade Element Method

In an attempt to model four quadrant hydrodynamic performance directly, without the need for additional experimentation, blade element theory can be used to approximate the propeller forces using simple hydrodynamics. This section covers the basic lift and drag blade element approach used in most of the current tunnel thruster models, e.g. [7], [12], [26], [25], and [4]. Assuming the flow pattern around each blade element is the same as for the two-dimensional hydrofoil of infinite span, the hydrodynamic forces on each blade element can be calculated for a given incidence angle of flow [9]. A schematic of the relevant velocities in the tunnel is shown in Figure 5.3.

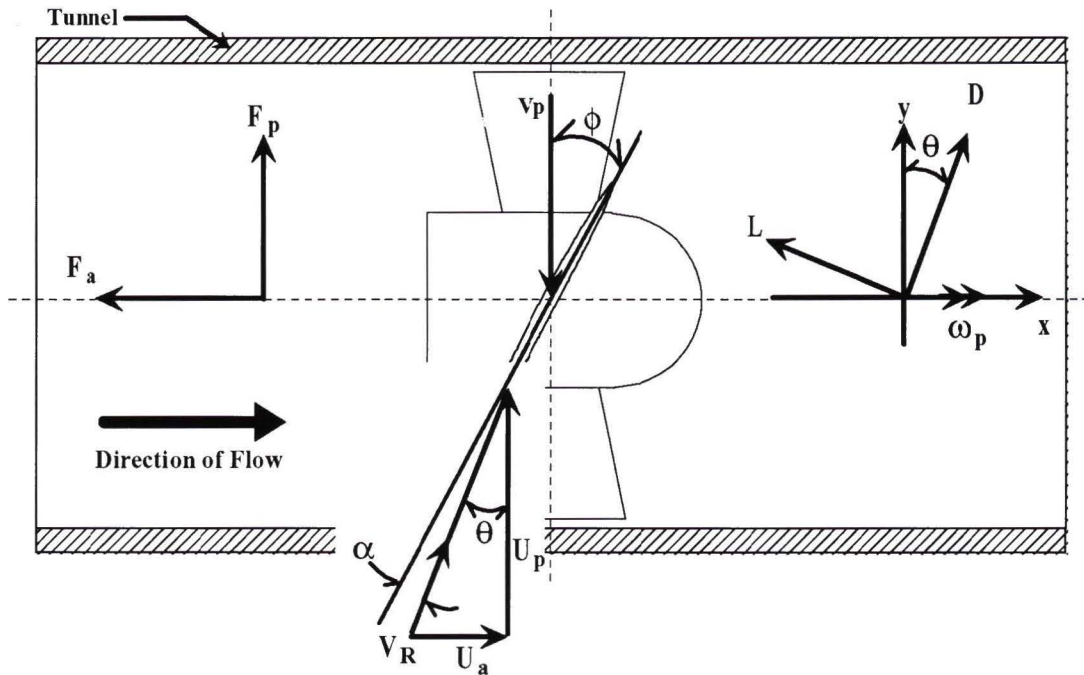


Figure 5.3. Tunnel Configuration

The velocity of the water relative to the propeller is the vector sum of the axial water column velocity U_a , and the tangential water velocity U_p (or the propeller's

velocity due to rotation V_p , reversed). For most modern propellers, the pitch is not constant along the span of the blade. The nominal pitch is therefore taken to be at 70% of the full tip radius¹ [9]. Using this approximation, the tangential velocity of the water relative to the blade can be calculated as,

$$U_p = 0.7 \frac{D}{2} \omega_p \quad (5.5)$$

The magnitude of the resultant velocity vector V_R and corresponding hydrodynamic pitch angle θ can then be found using the following relationships:

$$V_R^2 = (U_a^2 + U_p^2) \quad (5.6)$$

$$\theta = \arctan \left(\frac{U_a}{U_p} \right) \quad (5.7)$$

It can be seen from Figure 5.3 that the angle of incidence can then be computed directly using,

$$\alpha = \phi - \theta \quad (5.8)$$

The resultant hydrodynamic thrust, F_a , and hydrodynamic resistance, F_p , produced by the propeller can be calculated by evaluating the lift and drag forces produced by the blade hydrofoil as it moves through the water. The directions of lift and drag forces are perpendicular and parallel, respectively, to the direction of incident flow. They can then be transformed into the hydrodynamic forces of interest using a rotation matrix:

¹The propeller forces at 0.7R are commonly assumed an acceptable representation of the integrated blade force for Kaplan propellers.

$$\begin{bmatrix} F_a \\ F_p \end{bmatrix} = \begin{pmatrix} \cos \theta & -\sin \theta \\ \sin \theta & \cos \theta \end{pmatrix} \begin{bmatrix} L \\ D \end{bmatrix} \quad (5.9)$$

The torque load on the propeller can then be evaluated according to,

$$T_p = 0.7 \frac{D}{2} F_p \quad (5.10)$$

The complications faced in this method relate to the calculation of lift and drag. Hydrodynamic theory states

$$L = \left(\frac{1}{2} \rho V_R^2 A \right) C_L(\alpha) \quad (5.11)$$

$$D = \left(\frac{1}{2} \rho V_R^2 A \right) C_D(\alpha) \quad (5.12)$$

where A is the tunnel cross-sectional area. Healey *et al.* [12] proposed a simple harmonic form for the lift and drag coefficients with only two disposable parameters, as follows

$$C_L(\alpha) = C_{L\max} \sin(2\alpha) \quad (5.13)$$

$$C_D(\alpha) = C_{D\max}(1 - \cos(2\alpha)) \quad (5.14)$$

This model was proposed as a simplification of the four quadrant Fourier representation presented by Van Lammeran *et al.* [23] which would still retain the most fundamental components of that model. There are, however, several problems with this method of representing lift/drag coefficients. This method assumes that the lift

and drag curves are simple sinusoids. It also assumes a continuous mapping through 360° of angle of attack (and therefore does not consider stall). Rickards [20] illustrates how this sinusoidal approximation works for fully symmetric blade profiles and how it neglects the airfoil stall. Work done by Bachmayer *et al.* [4] suggests that this simple sinusoidal approximation is not adequate and proposes a technique to determine the lift/drag curves experimentally. The experimental derivation of these curves requires sophisticated flow measurement equipment not available for the presented work. The model used in this thesis will therefore more closely follow the work of [7] and [12]. Experimental data will be used to determine the maximum lift/drag coefficients and the simple sinusoidal form of the coefficients, given by (5.13) and (5.14) will be used.

It should also be noted that the blade element theory presented here is in its simplest form. Many improvements have been made, the most significant of which include the effects of induced velocities generated by the propeller's vortex system. The various vortex theories for propellers allow a better representation of flow around the propeller blade and therefore lead to a more accurate estimation of the thrust and hydrodynamical torque of a marine propeller. Blanke *et al.* have discussed this improved propeller modeling in [6].

5.2.2 Static Thruster Hydrodynamic Model

The following section covers the derivation of a hydrodynamic model based on momentum theory for propellers operating in an incompressible fluid. This model can be found in many introductory marine fluid dynamics texts. This section closely follows the well written summary by Whitcomb *et al.* [25].

Using linear momentum theory, the axial thrust force of a ducted propeller operating at steady-state can be equated to the fluid pressure differential across the actuator disk (representing the propeller) and the acceleration of the fluid mass in the duct. The following assumptions are made: gravity effects are negligible, irrotational² incompressible inviscid flow, and replacement of the propeller by an actuator disc. Bernoulli's equation can be applied to the streamlines upstream and downstream of the propeller disk

$$p_\infty + \frac{1}{2}\rho U_\infty^2 = p_u + \frac{1}{2}\rho U_a^2 \quad (\text{upstream}) \quad (5.15)$$

$$p_d + \frac{1}{2}\rho U_a^2 = p_\infty + \frac{1}{2}\rho U_w^2 \quad (\text{downstream}) \quad (5.16)$$

where U_∞ , U_a , and U_w are the fluid velocities far upstream, at the propeller, and far downstream (generally in the wake); while p_∞ , p_u , and p_d are the pressures in the ambient flow and just upstream and just downstream of the propeller. This leads to

$$(p_d - p_u) = \frac{\rho}{2}(U_w^2 - U_\infty^2) \quad (5.17)$$

By applying the linear momentum theorem to the enclosed control volume of the tunnel, the following relationship is obtained.

$$F_a = \rho A l \gamma \frac{d(U_a)}{dt} + A(p_d - p_u) \quad (5.18)$$

²Bachmayer *et al.* [4] included this effect in the model and concluded there was no significant improvement in model accuracy.

where A and l are the tunnel cross-sectional area and length, while γ is an empirically determined added mass coefficient. After substituting in eq. (5.17), F_a becomes

$$F_a = \rho A l \gamma \frac{d(U_a)}{dt} + \frac{1}{2} \rho A (U_w^2 - U_\infty^2) \quad (5.19)$$

where the first term on the right hand side represents the transient effects, while the second term captures the steady state behavior. Again by applying linear momentum theory to the control volume in can be seen that,

$$U_a = \frac{1}{2}(U_w + U_\infty) \quad (5.20)$$

By substituting eq. (5.20) into (5.19) and assuming that the intake axial velocity is zero, $U_\infty = 0$, F_a can then be rewritten as

$$F_a = (\rho A l \gamma) \frac{d(U_a)}{dt} + (2\rho A) U_a |U_a| \quad (5.21)$$

In most publications regarding thruster modeling eq. (5.21) has the form

$$F_a = (\rho A l \gamma) \frac{d(U_a)}{dt} + (\Delta\beta \rho A) U_a |U_a| \quad (5.22)$$

where $\Delta\beta$ is the momentum flux coefficient. This coefficient will typically have a value less than the theoretically predicted value of 2. Whitcomb *et al.* [25] make use of sophisticated flow measurement equipment to experimentally determine this momentum flux coefficient. They report a value of 1.86 for a ducted propeller with a duct length approximately 0.5 of the propeller diameter. Using this same model, Healy *et al.* [12] found two values for $\Delta\beta$, by manually tuning the model to match experimental data. They reported a value of 1.7 for an open propeller, and a value

of 0.2 for a ducted propeller with a duct length approximately 6.5 times the propeller diameter. This would suggest that as duct length increases, the value for the steady momentum flux coefficient decreases significantly from its theoretical value. The tunnel used in this thesis has a length approximately 4 times the propeller diameter, and it is therefore expected that the value of $\Delta\beta$ will be between 0.2 and 1.86.

5.2.3 Basic Simulation

Now that all the individual aspects of the tunnel thruster model have been explained, they can be tied together to create the 'Basic Simulation'. The basic simulation is loosely based on the work by Brown [7] and Healy *et al.* [12]. A block diagram of their simulation is shown in Figure 5.4. The original model included two coupled nonlinear first order differential equations, and thus two state variables. Whitcomb and Yoerger [25] showed that when the motor is equipped with an internal speed sensing loop, the model is reduced to only a single first order differential equation with a single state variable, U_a . Correspondingly, the upper part of the block diagram shown in Figure 5.4 is no longer needed.

The governing equation is formed by letting

$$K_1 = (\rho A l \gamma) \quad (5.23)$$

$$K_2 = (\Delta\beta \rho A) \quad (5.24)$$

Equation (5.22) becomes

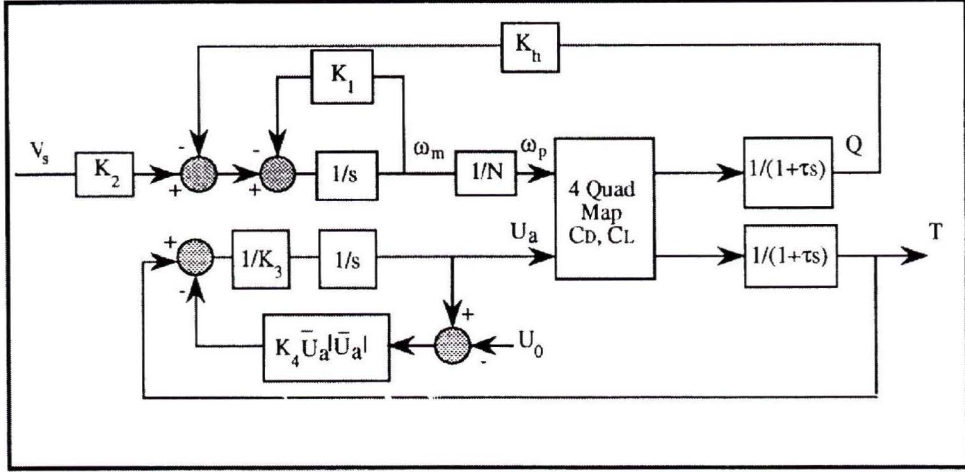


Figure 5.4. System Block Diagram from [12] (Note: Block diagram symbols are different than those used in this thesis)

$$F_a = K_1 \frac{d(U_a)}{dt} + K_2 U_a |U_a| \quad (5.25)$$

Solving for the axial water acceleration, $\frac{d(U_a)}{dt}$ or \dot{U}_a , the nonlinear first order differential equation for the Base Model becomes,

$$\dot{U}_a = \left(\frac{1}{K_1} \right) F_a - \left(\frac{K_2}{K_1} \right) |U_a| U_a \quad (5.26)$$

The reduction in model order from two to one state variables removes the uncertainties involved in modeling the electro-mechanical system by using the speed sensor feedback from the motor. However, it relies on having a robust inner motor speed loop which can be relied on to provide the commanded ω_p accurately and with no lag. This model modification is acceptable, considering most modern day servo motors used in underwater thrusters are fitted with a shaft speed sensor and an inner servo loop. This model configuration corresponds to our experimental setup, and our single differential equation, given by eq. (5.26), in summary can be written as

$$\dot{U}_a = f_1(F_a, \omega_p) \quad (5.27)$$

where ω_p is the control input and

$$F_a = f_2(U_a, \omega_p) \quad (5.28)$$

The resulting model is shown in Figure 5.5. A detailed block-by-block description of the Simulink program for the Basic Simulation can be found in Appendix C.

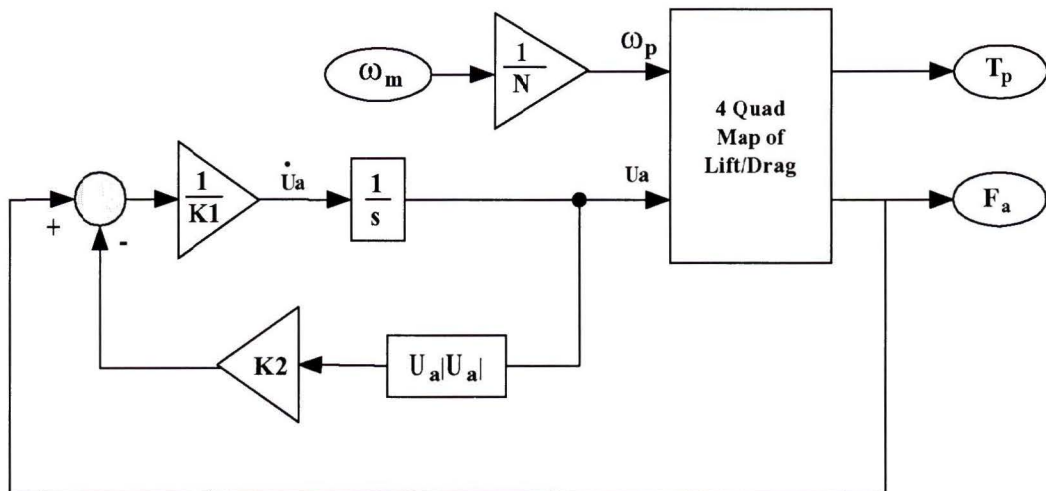


Figure 5.5. System Block Diagram for the Basic Simulation

It is important to understand the limitations of the models discussed above. There are several reasons why the basic simulation cannot be used to simulate a thruster moving with forward speed in a yawed orientation, these include:

- The equations were developed with the assumption that the ambient water velocity, U_∞ , is zero.

- The model presumes symmetry in the thruster's performance in relation to positive/negative RPM. This assumption is not valid, as seen in the results presented in [7] [12], and as was evident in the data shown in Chapter 4.

5.3 Modeling the Effects of Forward Vehicle Speed and Orientation

The most significant limitation of the model presented in the previous section is its assumption of zero ambient axial water velocity. This section discusses a means for including the effects of forward speed and orientation into current tunnel thruster models. In order to model a thruster that is moving through the water with a vehicle, the effect of the inlet water velocity must be taken into consideration. The model presented by Blanke *et al.* [6] included the effects of nonzero vessel speed relative to the water. That model was developed in much the same way as was presented in Section 5.2.2, with the exception that it is not assumed that $U_\infty = 0$. In this case we find that the development leads to

$$F_a = (\rho A l \gamma) \frac{d(U_a)}{dt} + (2\rho A) |U_a| (U_a - U_\infty) \quad (5.29)$$

The usual form of this equation includes the concept of the momentum flux coefficient, which leads to

$$F_a = (\rho A l \gamma) \frac{d(U_a)}{dt} + (\Delta\beta\rho A) |U_a| (U_a - U_\infty) \quad (5.30)$$

where U_∞ is the ambient axial water velocity. In ship modeling U_∞ is usually equivalent to the forward vessel speed. The addition of vessel speed will improve the accuracy of the model for a thruster whose axis is parallel to the direction of travel. However, with a through-body thruster, the thrust axis is very seldom parallel to the direction of travel (with the exception of cross current, $\pm 90^\circ$ yaw). The effect of vehicle orientation must therefore also be taken into account.

In order to capture effects of forward speed and orientation, we return to the experimental results presented in Chapter 4. Initially, it was speculated that the changes in thruster behavior would be dominated by the effects of through-flow. This would have enabled the use of a simple relationship between forward speed and yaw angle to calculate a value for through flow velocity, which in turn would allow the direct use of eq. (5.30), to model the axial thrust. Because the data in Chapter 4 did not show a fundamental relationship that would support this assumption, a method for directly including the experimental tow tank data into the model was required. It was also observed in Chapter 4 that forward speed and orientation had little effect on the transient behavior of the thruster. This allows us to keep the transient portion of Equation (5.22) and concentrate on the modification of the steady state portion. It was shown in Chapter 4 that the experimental steady state results could be condensed into the following relationship,

$$F_{a_{ss}} = a + b |\omega_p| \omega_p \quad (5.31)$$

By replacing the steady state portion of eq. (5.22) with eq. (5.31) the following new single first order differential equation is formed

$$F_a = (\rho A l \gamma) \frac{d(U_a)}{dt} + a + b |\omega_p| \omega_p \quad (5.32)$$

where the model inputs are a and b , the intercept and slope data respectively, and ω_p , the propeller RPM. The single state variable, axial water velocity U_a , remains the same.

5.3.1 Augmented Simulation

Having just presented the equations describing a model capable of capturing the effects of forward speed and yaw angle, it is time to discuss the assembly of an 'Augmented Simulation'. The key differences between the basic and augmented simulations are as follows:

- The effects of forward vehicle speed and orientation are included by using the experimental results from tow tank testing, by using a and b . This is achieved through the use of lookup tables for the entire range of forward speeds and yaw angles tested in this work.
- The effects of asymmetry in transient thruster performance are captured by tuning γ separately for the forward and reverse axial flow case. This is achieved by evaluating the direction of axial water flow, U_a , each pass through the simulation and selecting the appropriate forward or reverse γ .

The simulation equations are formed by letting

$$K_1 = (\rho A l \gamma) \quad (5.33)$$

Equation (5.32) becomes

$$F_a = K_1 \frac{d(U_a)}{dt} + a + b |\omega_p| \omega_p \quad (5.34)$$

Solving for the axial water acceleration, $\frac{d(U_a)}{dt}$ or \dot{U}_a , the nonlinear first order differential equation for the thruster system becomes,

$$\dot{U}_a = \left(\frac{1}{K_1} \right) F_a - \left(\frac{1}{K_1} \right) a - b \left(\frac{1}{K_1} \right) |\omega_p| \omega_p \quad (5.35)$$

Our single differential equation, given by eq. 5.35, in summary can be written as

$$\dot{U}_a = f_1'(a, b, F_a, \omega_p) \quad (5.36)$$

where ω_p is the control input and

$$F_a = f_2(U_a, \omega_p) \quad (5.37)$$

$$a = f_3(\text{Yaw Angle, Forward Vehicle Speed}) \quad (5.38)$$

$$b = f_4(\text{Yaw Angle, Forward Vehicle Speed, Direction of } U_a) \quad (5.39)$$

As was explained in the previous chapter, non zero values for a are due to the forces in the thruster unit for $\omega_p = 0$. As stated in eq. (5.38) a is a function of

yaw angle and forward speed. The value of b represents the slope of the steady state axial thrust. Eq. (5.39) shows that b is a function of yaw angle, forward speed, and the direction U_a . In particular, we must account for the direction of U_a relative to a particular forward speed and yaw angle, as shown in Figure 4.7. The tow tank tests were run for yaw angles of $\pm 90^\circ$, but always for positive ω_p ramps. Therefore, the values of b available are for one direction of U_a corresponding to a particular yaw angle and forward speed. We presume that the values of the slope b for negative ω_p at a particular speed and yaw angle is the same as for positive ω_p at the same speed but the negative yaw angle. In addition to this b , must be modified for to account for the baseline asymmetry in axial thrust performance, as shown in Figure 3.6.

The resulting model is shown in Figure 5.6. A detailed block-by-block description of the Simulink program for the augmented simulation can be found in Appendix C.

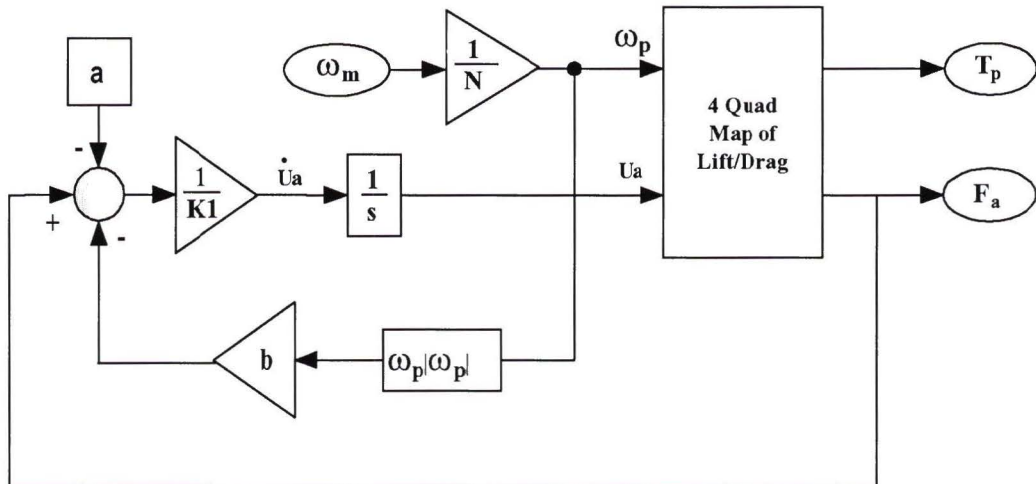


Figure 5.6. System Block Diagram for the Augmented Tunnel Thruster Model

5.4 Simulation Results

5.4.1 Basic Model

The goal of this section is to demonstrate the capabilities of the basic simulation. Later, in Section 5.4.2 the performance of the augmented simulation will be presented. Table 5.1 contains the values used for the model parameters. It is important to note the method of identification for different model parameters. In the basic simulation there are 4 parameters that must be manually selected: γ , the added mass coefficient; $\Delta\beta$, The momentum flux coefficient; $C_{L\max}$, the maximum lift coefficient; and $C_{D\max}$, the maximum drag coefficient. This method is often referred to as "tuning the model", a process by which the model parameters are varied until the simulation output matches an experimental data set. In general the axial force transient peak was matched by adjusting γ and $C_{L\max}$, the steady state thrust by adjusting $\Delta\beta$ and $C_{L\max}$, and finally the propeller hydrodynamical torque load by adjusting $C_{D\max}$. The problem with this type of model is that the parameters are coupled and can not be tuned independently of each other. Because of this, the final values are somewhat arbitrary. However, it is important to ensure sure the values stay within their physically meaningful range, for example: $\Delta\beta$ cannot exceed 2 (explained in Section 5.2.2); for low aspect ratio wing section, $C_{L\max}$ rarely exceeds 1.0; and the flat plate drag $C_{D\max}$ will generally not exceed 2. Once these ranges have been defined, the model can be manually tuned, the resulting parameter values are presented in Table 5.1.

Symbol	Value	Unit	Description	ID Method
D	0.1016	m	Tunnel Diameter	measured
l	0.409575	m	Tunnel Length	measured
A	0.008107	m ²	Tunnel Area	measured
γ	1.2		Added Mass Coefficient	tuned
$\Delta\beta$	1.7		Flux Coefficient	tuned
ρ	998	$\frac{\text{kg}}{\text{m}^3}$	Water Density	hand book
C_{Lmax}	0.6		Max Lift Coefficient	tuned
C_{Dmax}	1.125		Max Drag Coefficient	tuned
ϕ	0.426778	rad	Pitch Angle	measured

Table 5.1. Model Parameters for the Basic Simulation.

5.4.1.a Steady State Simulation Results

Figure 5.7 shows the predicted steady state axial thrust from the basic simulation, compared to experimental data, for a long period positive ω_p ramp. The model was tuned to match the forward steady state thrust as closely as possible. For a long period negative RPM ramp, as shown in Figure 5.8, the simulation output does not match the experimental data set. This supports the previous statement that the basic model is unable to capture the asymmetrical characteristics of the thruster. No single set of parameters was able to capture the thruster asymmetry.

5.4.1.b Transient Simulation Results

Figures 5.9 and 5.10 show the predicted axial thrust from the basic simulation compared to experimental data for two types of transient control inputs. It is apparent from Figure 5.9 that the basic model does an acceptable job of capturing the transient behavior during sharp reversals. It does, however, lack the ability to accurately represent the asymmetry in transient behavior for slower transient, or quasi steady state conditions. This observation, in addition to the transient tow tank results, supports

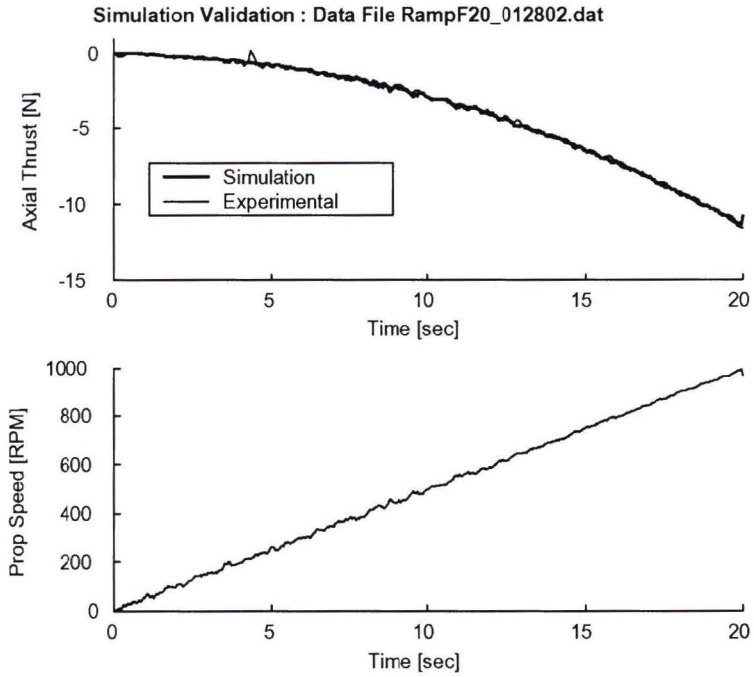


Figure 5.7. Basic Model Thrust Compared with Experimental Data, Forward Ramp Control

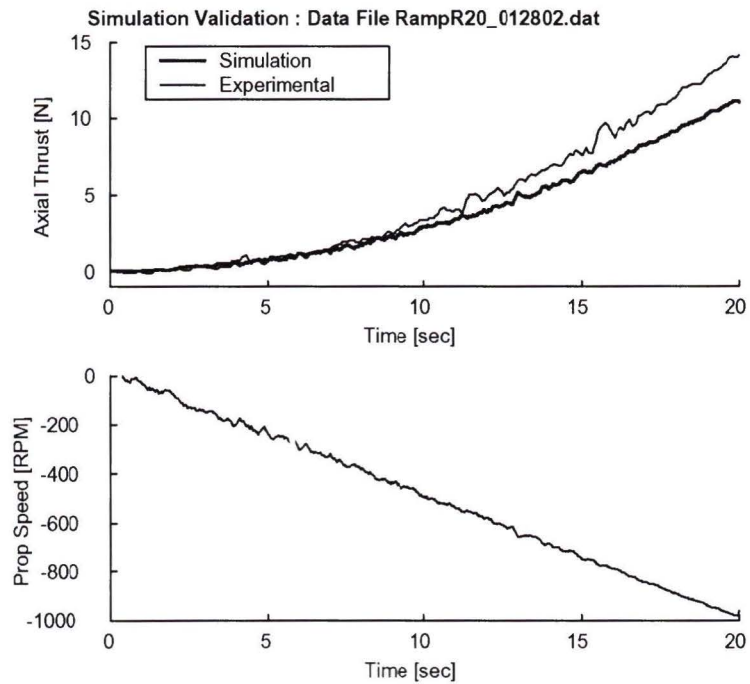


Figure 5.8. Basic Model Thrust Compared with Experimental Data, Reverse Ramp Control

the idea that only the steady state portion of the model needs to be replaced.

The next step is to compare the simulation to the experimental data from the forward speed and yawed orientation tests. Figures 5.11 through 5.14 show four test cases from the tow tank tests. For a low forward of $V_{\text{carriage}} = 0.1$ [m/s] and Yaw = 0 [deg], as shown in Figures 5.11 and 5.12, the simulated axial thrust matches the experimental data quite well. This does not hold true as the forward speed and yaw angle are increased. To illustrate this, the test case of $V_{\text{carriage}} = 0.5$ [m/s] and Yaw = 90 [deg] is plotted in Figures 5.13 and 5.14. It is very clear that the basic model is unable to model the axial thrust. Both Figures 5.13 and 5.14 show a significant mismatch in steady state and transient thrust between the model and experimental data.

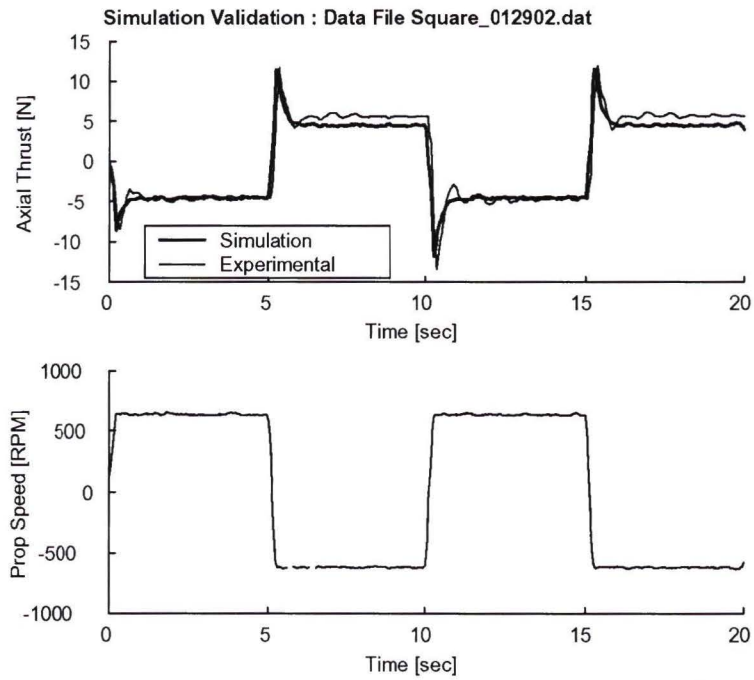


Figure 5.9. Basic Model Thrust Compared with Experimental Data, Square Wave Control

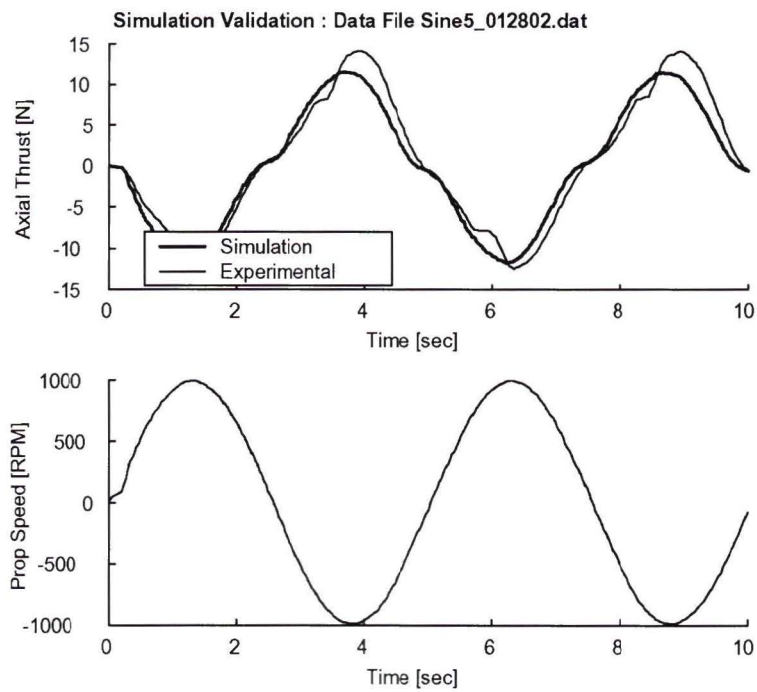


Figure 5.10. Basic Model Thrust Compared with Experimental Data, Sine Wave Control

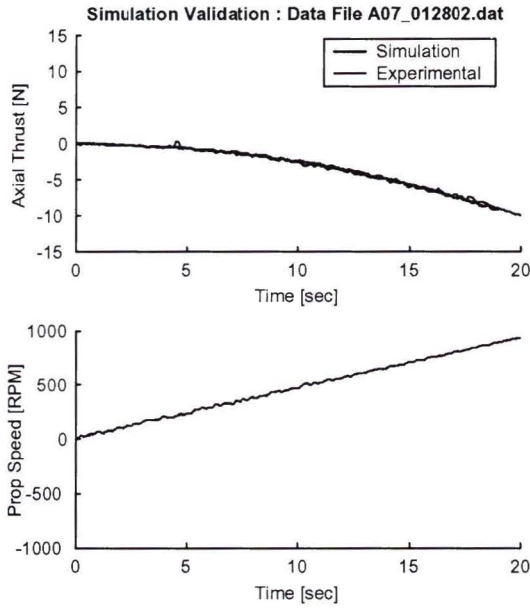


Figure 5.11. Basic Model Thrust Compared with Experimental Data, Ramp, $V_{\text{carriage}} = 0.1$ [m/s] and Yaw = 0 [deg]

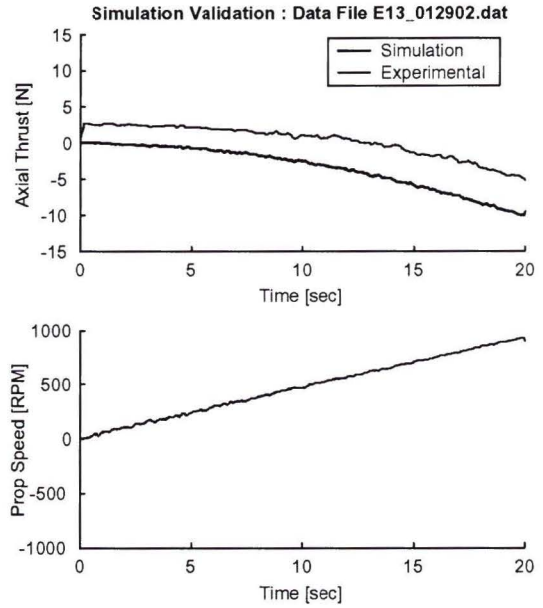


Figure 5.13. Basic Model Thrust Compared with Experimental Data, Ramp, $V_{\text{carriage}} = 0.5$ [m/s] and Yaw = 90 [deg]

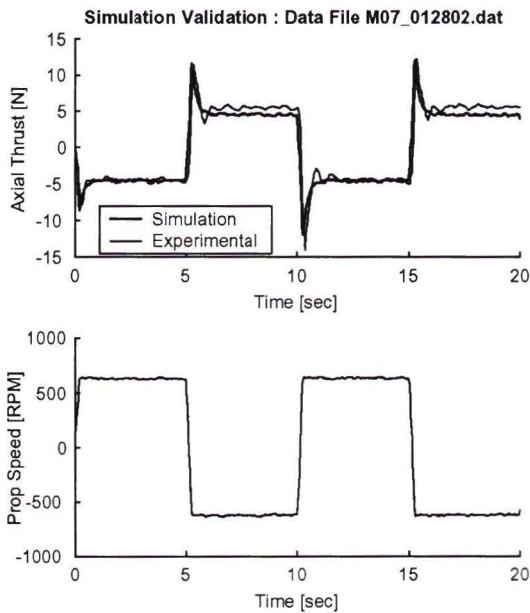


Figure 5.12. Basic Model Thrust Compared with Experimental Data, Square, $V_{\text{carriage}} = 0.1$ [m/s] and Yaw = 0 [deg]

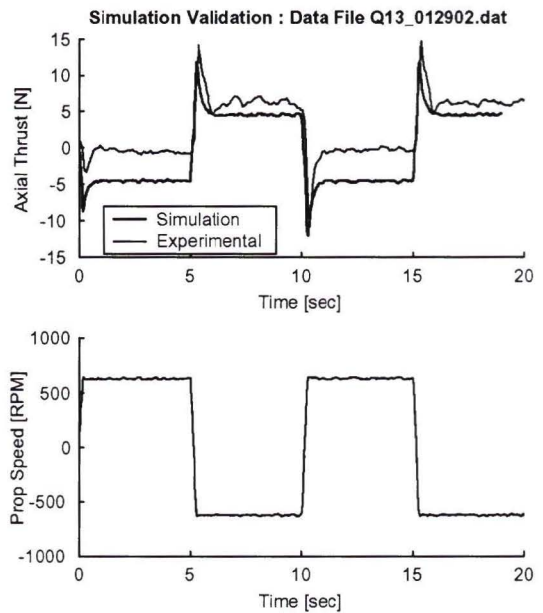


Figure 5.14. Basic Model Thrust Compared with Experimental Data, Square, $V_{\text{carriage}} = 0.5$ [m/s] and Yaw = 90 [deg]

5.4.2 Augmented Model

This section will compare the results of the augmented simulation with experimental data. Table 5.2 contains the values used for the model parameters. For this simulation there are only three tuned parameters: γ , $C_{L\max}$ and $C_{D\max}$, with the added mass coefficient having a distinct value for forward and reverse axial water velocity. Because the propeller geometry does not change, there is no justification for changing the value of $C_{L\max}$ or $C_{D\max}$ from the previous section. This leaves only one variable to tune, γ , which has a different value for forward and reverse axial flow directions. In general an increase in γ results in an increase in thrust overshoot and settling time. Values for γ_F and γ_R were obtained by tuning the model for the stationary thruster case. The new additions to the model are the experimentally fit values of intercept and slope, a and b , from Chapter 4. These values were integrated into the simulation using lookup tables. As stated in eq. (5.38) the intercept is a function of yaw angle, and therefore it only has to be looked up once for each simulation. Eq. (5.39) shows that the slope value is a function of forward speed and yaw angle. As mentioned in Section 5.3.1 the value of b must be obtained for both positive and negative yaw for each test case. In addition to this, the value of b must be modified if ω_p is in the negative direction³ to account for the asymmetry in steady state thrust. This is done by multiplying b by a modifier, $bMod$, calculated from steady state tests. Overall the augmented model requires less tuning due to the addition of experimental data. The resulting parameter values for the augmented simulation are presented in Table 5.2.

³Because the test matrix was only completed for positive ω_p the asymmetry in steady state thrust is accounted for using the percentage thrust difference, see Figure 3.6.

Symbol	Value	Unit	Description	ID Method
D	0.1016	m	Tunnel Diameter	measured
l	0.409575	m	Tunnel Length	measured
A	0.008107	m ²	Tunnel Area	measured
γ_F	0.6		Added Mass Coefficient, $+U_a$	tuned
γ_R	0.9		Added Mass Coefficient, $-U_a$	tuned
ρ	998	$\frac{\text{kg}}{\text{m}^3}$	Water Density	hand book
$C_{L\text{max}}$	0.6		Max Lift Coefficient	tuned
$C_{D\text{max}}$	1.125		Max Drag Coefficient	tuned
ϕ	0.426778	rad	Pitch Angle	measured
a	lookup table	N	Axial Thrust Intercept	measured
b	lookup table	$\frac{\text{N}}{(\text{rad/sec})^2}$	Axial Thrust Slope	measured
bMod	1.26729		Axial Thrust Slope Modifier, 26.7% increase	measured

Table 5.2. Model Parameters for the Augmented Simulation.

5.4.2.a Steady State Simulation Results

In order to demonstrate the capabilities of the augmented model, 12 test cases were selected from the tow tank test matrix. This sampling of test cases includes some of the more extreme operation in order to demonstrate the capabilities of the simulation. Figure 5.15 shows the simulation compared to the experiment at a very slow carriage speed and zero yaw. From this figure, it is apparent that the augmented simulation closely matches the experimental data. Figure 5.17 shows model performance for a more extreme case, $V_{\text{carriage}} = 2.5$ [m/s] and yaw = 0 [deg]. With the exception of the noise in the data, the simulation is still a very good match of the experiment. One thing worth noting is the separation between the simulation and experimental data near the start of the simulation. This can be seen clearly in Figures 5.25 and 5.26. This lag in model response for the first few seconds is to be expected because the simulation is being started from rest (i.e. the initial condition does not match the steady state operating condition). Overall it is clear that the simulation is able

to closely model the thruster's steady state performance.

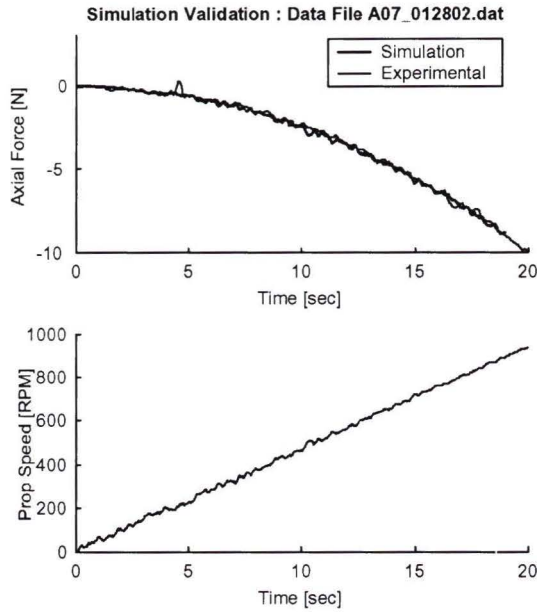


Figure 5.15. Model Thrust Compared with Experimental Data, Ramp Control, $V_{\text{carriage}} = 0.1$ [m/s] and Yaw = 0 [deg]

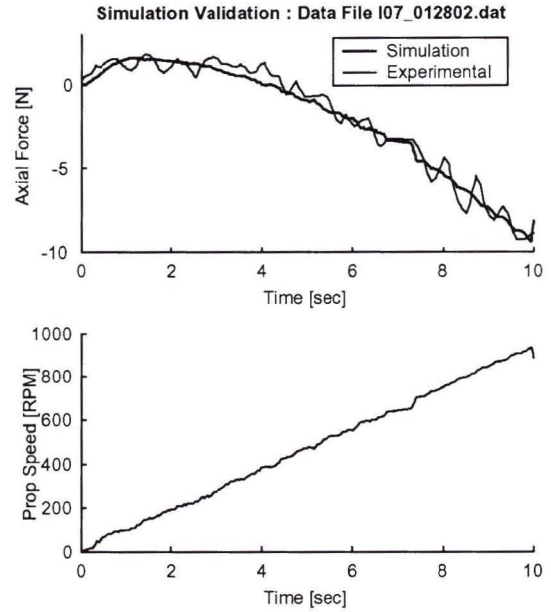


Figure 5.17. Model Thrust Compared with Experimental Data, Ramp Control, $V_{\text{carriage}} = 2.5$ [m/s] and Yaw = 0 [deg]

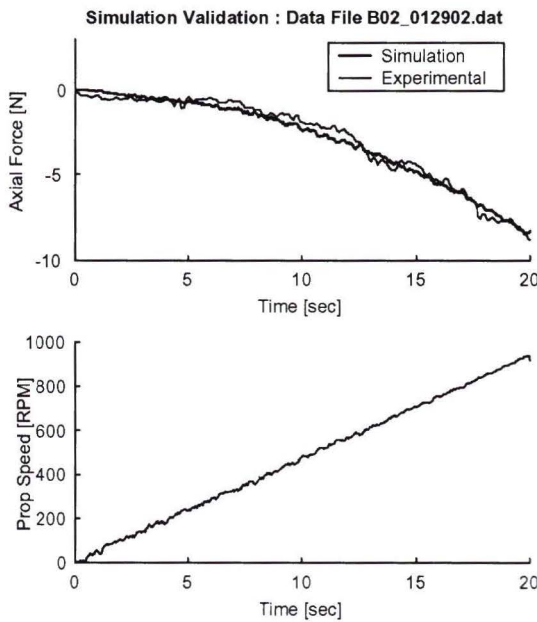


Figure 5.16. Model Thrust Compared with Experimental Data, Ramp Control, $V_{\text{carriage}} = 0.2$ [m/s] and Yaw = -70 [deg]

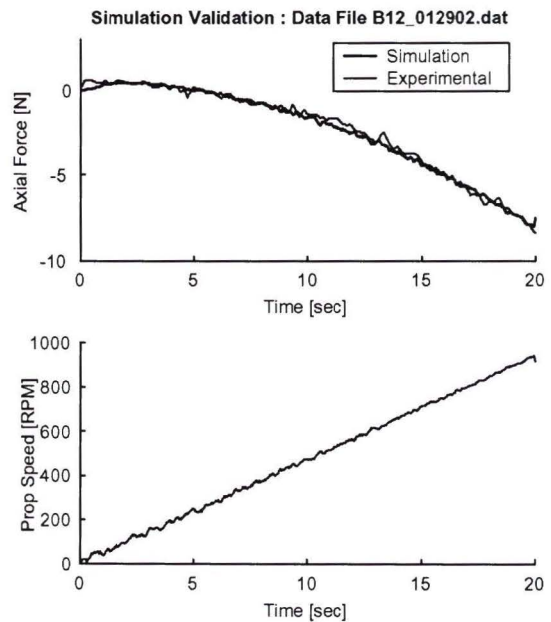


Figure 5.18. Model Thrust Compared with Experimental Data, Ramp Control, $V_{\text{carriage}} = 0.2$ [m/s] and Yaw = 70 [deg]

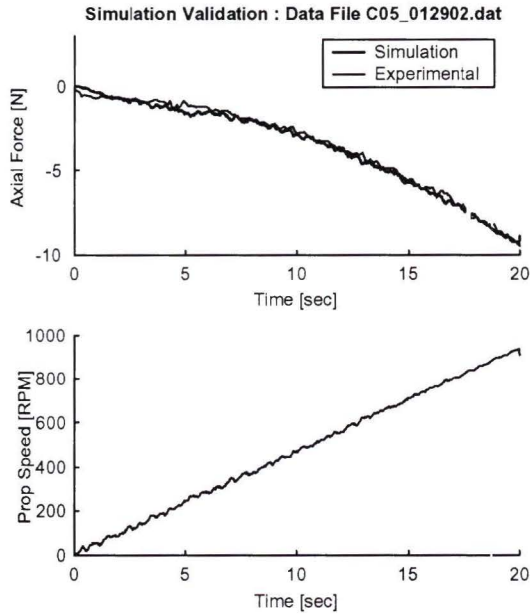


Figure 5.19. Model Thrust Compared with Experimental Data, Ramp Control, $V_{\text{carriage}} = 0.3$ [m/s] and Yaw = -20 [deg]

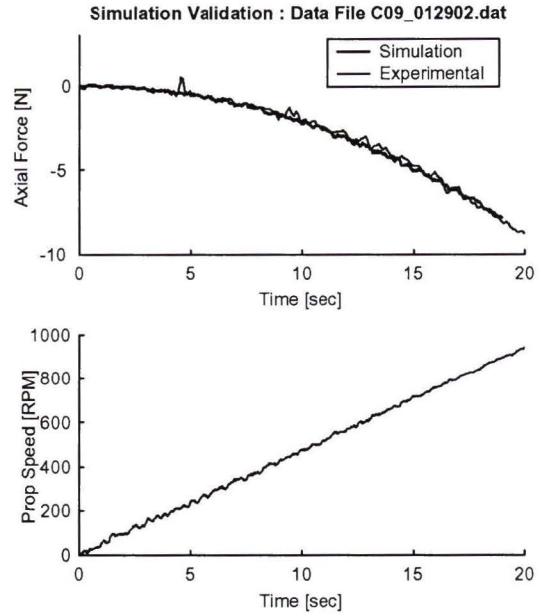


Figure 5.21. Model Thrust Compared with Experimental Data, Ramp Control, $V_{\text{carriage}} = 0.3$ [m/s] and Yaw = 20 [deg]

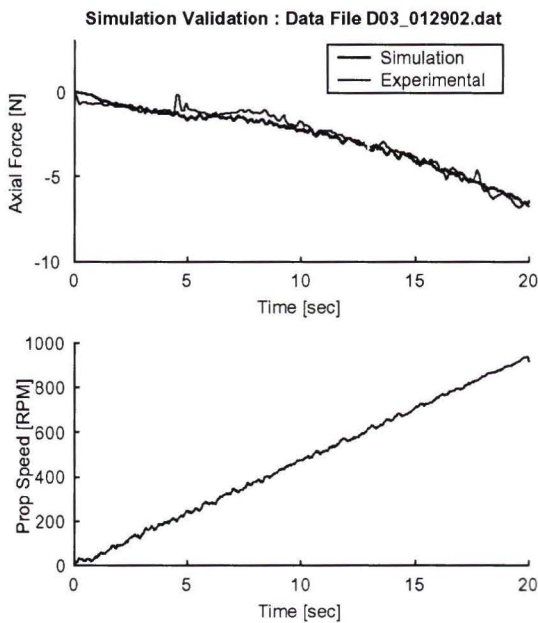


Figure 5.20. Model Thrust Compared with Experimental Data, Ramp Control, $V_{\text{carriage}} = 0.4$ [m/s] and Yaw = -50 [deg]

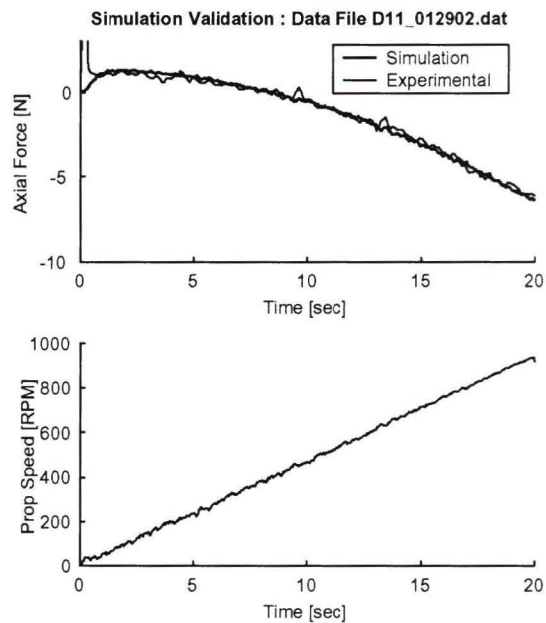


Figure 5.22. Model Thrust Compared with Experimental Data, Ramp Control, $V_{\text{carriage}} = 0.4$ [m/s] and Yaw = 50 [deg]

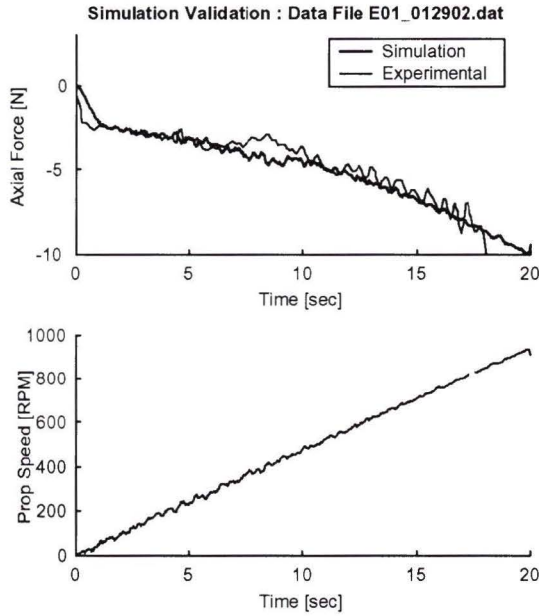


Figure 5.23. Model Thrust Compared with Experimental Data, Ramp Control, $V_{\text{carriage}} = 0.5$ [m/s] and Yaw = -90 [deg]

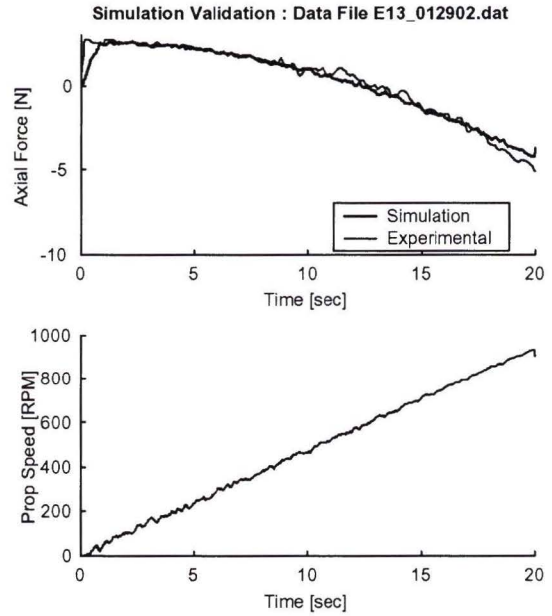


Figure 5.25. Model Thrust Compared with Experimental Data, Ramp Control, $V_{\text{carriage}} = 0.5$ [m/s] and Yaw = 90 [deg]

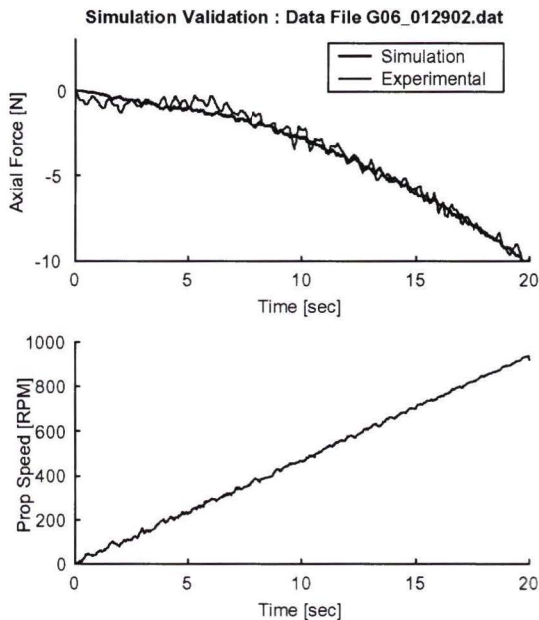


Figure 5.24. Model Thrust Compared with Experimental Data, Ramp Control, $V_{\text{carriage}} = 1.5$ [m/s] and Yaw = -10 [deg]

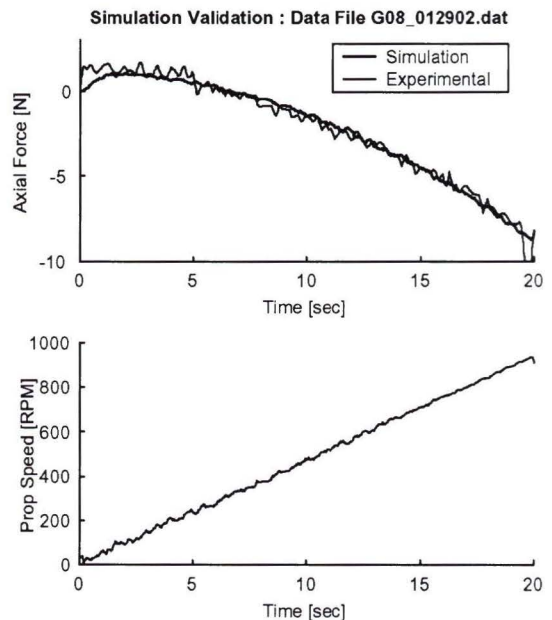


Figure 5.26. Model Thrust Compared with Experimental Data, Ramp Control, $V_{\text{carriage}} = 1.5$ [m/s] and Yaw = 10 [deg]

5.4.2.b Transient Simulation Results

The same 12 test cases presented in the steady state section are used here to demonstrate performance under transient conditions, Figures 5.27 through 5.38. Overall, the general trends of the model output closely matched the measured thruster performance. The exceptions to this were at large yaw angles and speeds above 0.4 m/s. Figures 5.35 and 5.37 show that the settling time of the predicted thrust overshoot does not match the experimental data at these conditions. This mismatch at large yaw angles is most likely due to the error induced in fitting the a 's and b 's to the experimental thruster data due to the large amount of scatter for these more extreme test cases, as discussed in Chapter 4. The other aspect that the model was unable to represent was the small, low frequency oscillations seen shortly after the thrust overshoot, e.g. Figures 5.27 and 5.38. This low frequency 'ringing' is not reported in related work, [4], [7], [12], [25], [26] and similar, and is therefore attributed to structural flexibility in the test setup. As previously stated in Chapter 4, the stiffness of the frame holding the C-SCOUT model in the water was poor. During flow reversal, this flex would most likely result in a small amount of sway in the model, resulting in a slight amount of surge from the thruster. The model was, however, able to capture the asymmetry in transient behavior very well. In summary, the results from the augmented simulation are well within acceptable limits for representing the performance of the tunnel thruster during forward speed and yawed orientation. The small mismatches in modeled performance would most likely have little or no effect on the vehicle's overall operation.

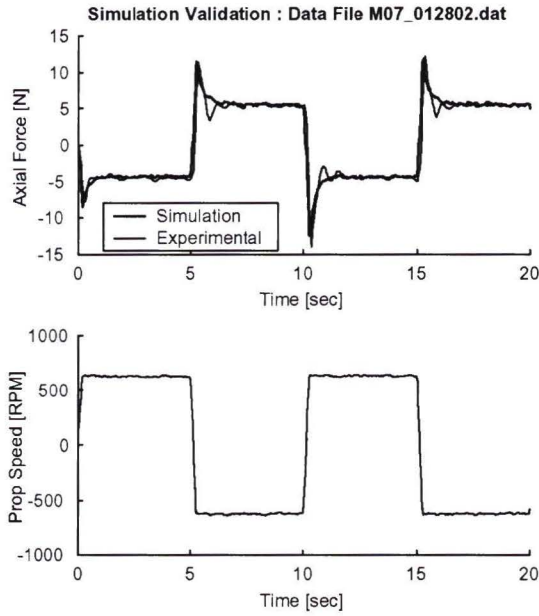


Figure 5.27. Model Thrust Compared with Experimental Data, Square Wave Control, $V_{\text{carriage}} = 0.1$ [m/s] and Yaw = 0 [deg]

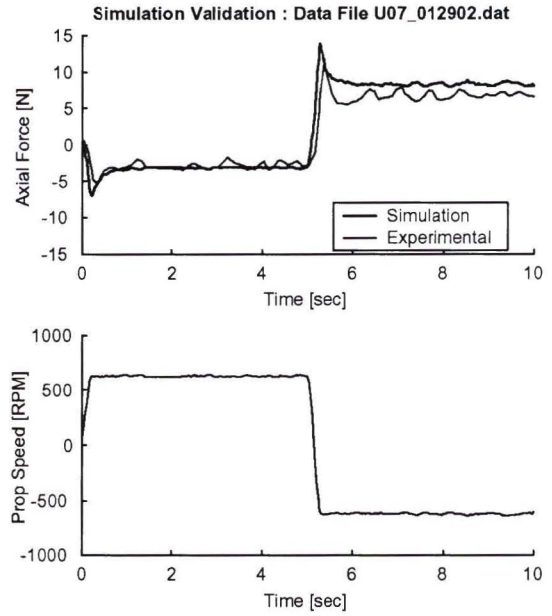


Figure 5.29. Model Thrust Compared with Experimental Data, Square Wave Control, $V_{\text{carriage}} = 2.5$ [m/s] and Yaw = 0 [deg]

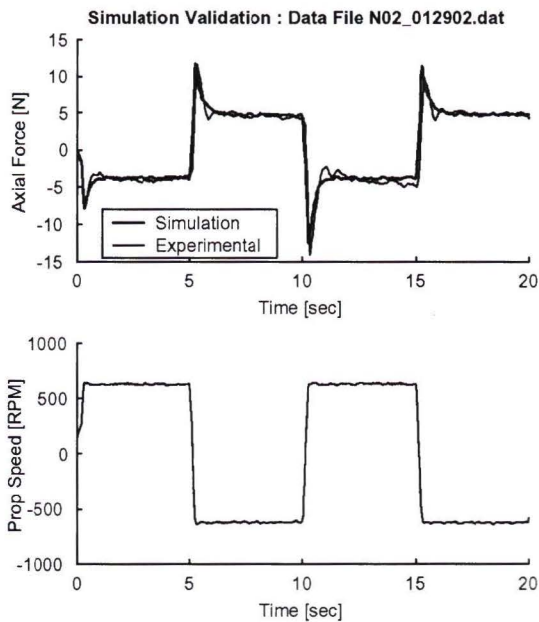


Figure 5.28. Model Thrust Compared with Experimental Data, Square Wave Control, $V_{\text{carriage}} = 0.2$ [m/s] and Yaw = -70 [deg]

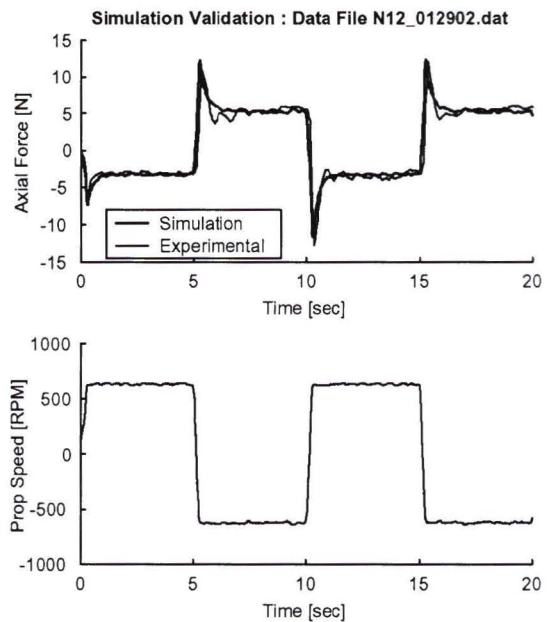


Figure 5.30. Model Thrust Compared with Experimental Data, Square Wave Control, $V_{\text{carriage}} = 0.2$ [m/s] and Yaw = 70 [deg]

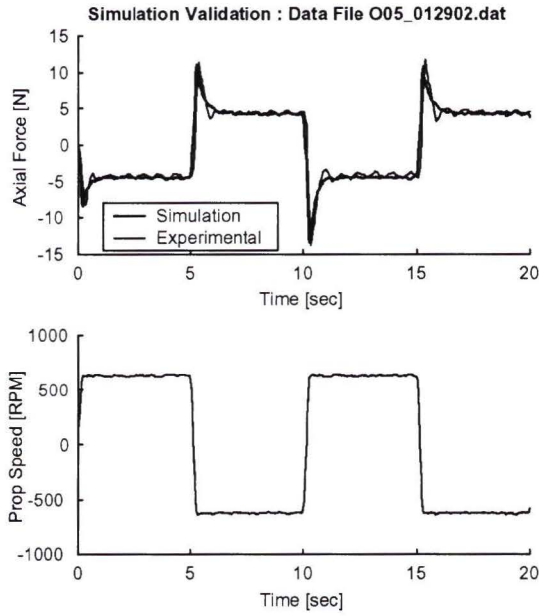


Figure 5.31. Model Thrust Compared with Experimental Data, Square Wave Control, $V_{\text{carriage}} = 0.3$ [m/s] and Yaw = -20 [deg]

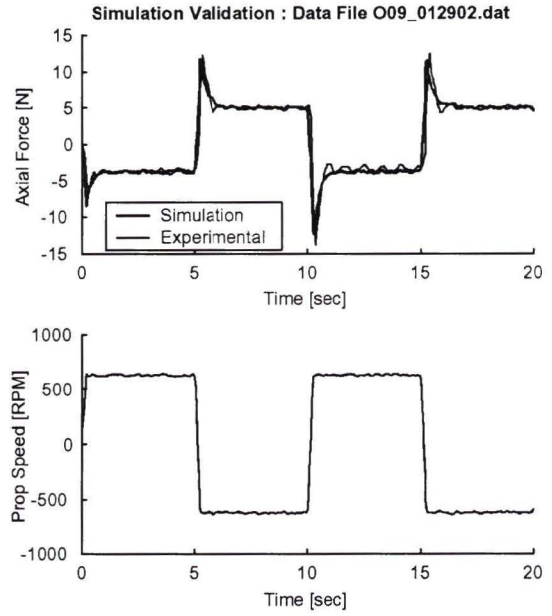


Figure 5.33. Model Thrust Compared with Experimental Data, Square Wave Control, $V_{\text{carriage}} = 0.3$ [m/s] and Yaw = 20 [deg]

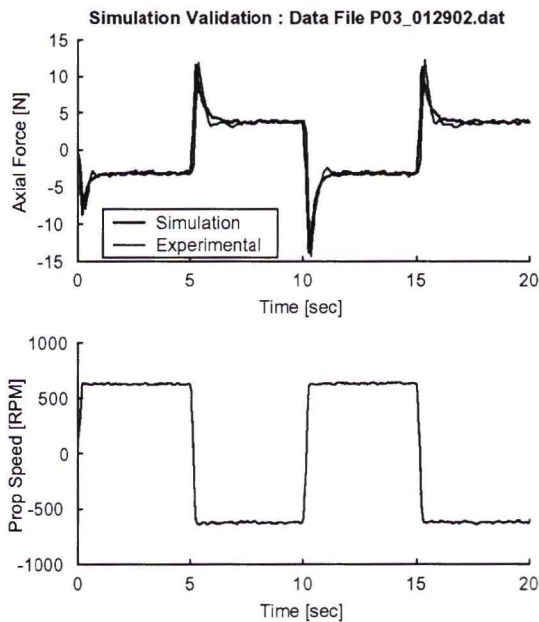


Figure 5.32. Model Thrust Compared with Experimental Data, Square Wave Control, $V_{\text{carriage}} = 0.4$ [m/s] and Yaw = -50 [deg]

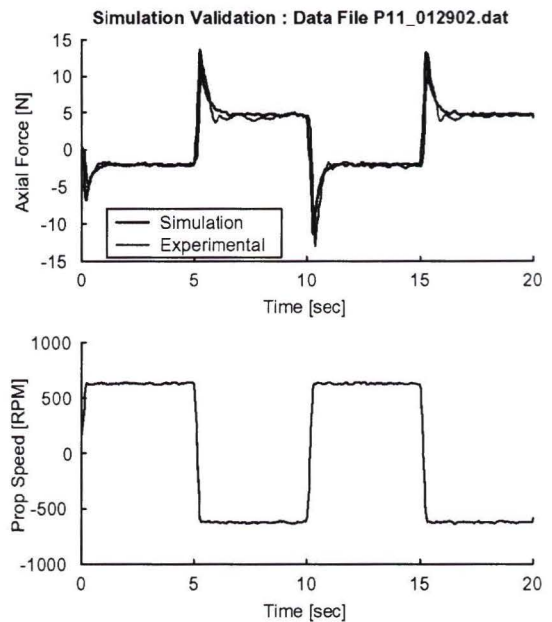


Figure 5.34. Model Thrust Compared with Experimental Data, Square Wave Control, $V_{\text{carriage}} = 0.4$ [m/s] and Yaw = 50 [deg]

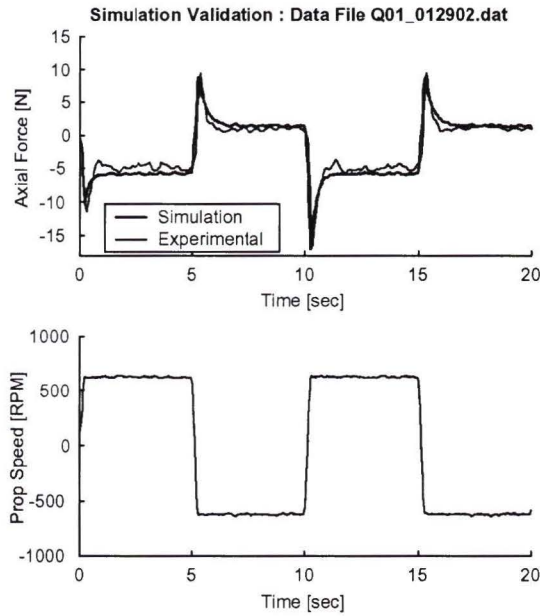


Figure 5.35. Model Thrust Compared with Experimental Data, Square Wave Control, $V_{\text{carriage}} = 0.5$ [m/s] and Yaw = -90 [deg]

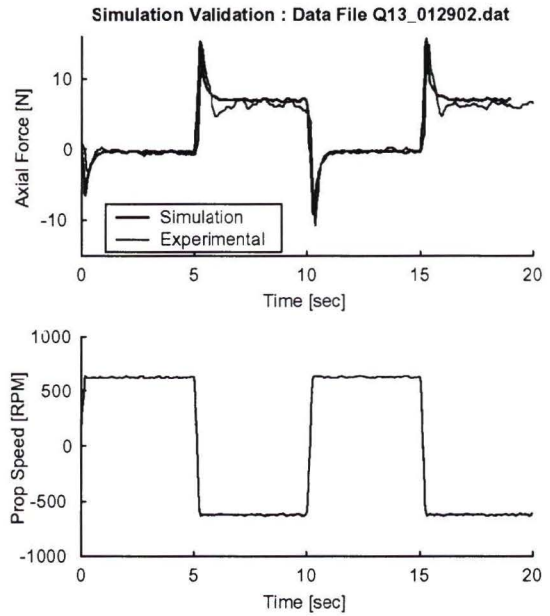


Figure 5.37. Model Thrust Compared with Experimental Data, Square Wave Control, $V_{\text{carriage}} = 0.5$ [m/s] and Yaw = 90 [deg]

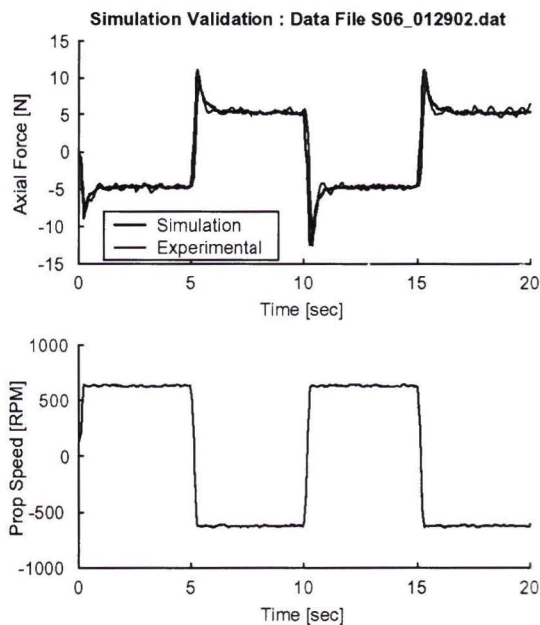


Figure 5.36. Model Thrust Compared with Experimental Data, Square Wave Control, $V_{\text{carriage}} = 1.5$ [m/s] and Yaw = -10 [deg]

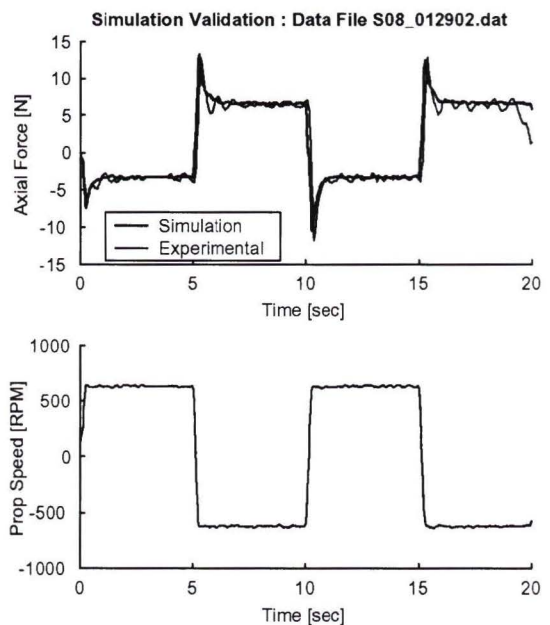


Figure 5.38. Model Thrust Compared with Experimental Data, Square Wave Control, $V_{\text{carriage}} = 1.5$ [m/s] and Yaw = 10 [deg]

Chapter 6

Conclusions and Recommendations

6.1 Experimental System Design and Testing

The goal of building a highly portable test system was met. The experimental system was designed and tested locally at the University of Victoria and transported across Canada, to St. John's Newfoundland, where the second phase of testing was completed successfully in Memorial University's tow tank facilities. The modular design of the C-SCOUT vehicle proved to be a vital feature for enabling collaborative research on an AUV testbed.

The small tank testing was successful in obtaining initial test data to ensure our results were similar to others. This verified the software and test procedure developed for the tunnel thruster system was working correctly. The limitations of testing in a small tank were presented, the most significant being the effect of slosh, or the standing wave, that forms during a thruster test. The small test tank had a slosh frequency of 0.6Hz, a value very close to that published by another group using a

similar experimental setup [16].

The initial small tank testing verified the well known linear relationship between axial thrust and propeller rotational speed squared. This fundamental relationship became the method used to present and model the effects of forward speed and yaw angle on steady state thruster performance. This phase of testing also revealed a distinct asymmetry in thruster performance for both steady state and transient test cases. As stated previously, small underwater vehicles react quickly to changes in the amount and direction of thrust from manoeuvring thrusters. As a result, asymmetrical thruster performance may have significant effect on station-keeping capabilities of URVs and should be accounted for.

Another finding of interest was the difference between current and speed control of the servo motor on thruster response. When commanding the current of the motor, the spikes in axial thrust commonly observed immediately after propeller reversal when using speed control, disappear. When comparing work published by different research groups it is therefore important to understand the difference between the two methods of control.

Overall, the tow tank testing revealed that the effects of yaw and forward speed are fairly complex, suggesting that complicated fluid dynamics effects dominate steady state thruster performance. Using the fundamental linear relationship between axial thrust and propeller rotational speed squared, we were able to study steady state thruster performance by simply looking at how the coefficients a and b vary with forward speed and yaw angle. Using this relationship, the results from all the steady state tests were collapsed onto a few plots. The key observations included:

- Thruster performance during low speed maneuvering is only slightly reduced by forward speed. Additionally, this decrease in steady state thrust becomes more pronounced as the yaw angle is increased.
- The complicated hull-fluid interaction dominates thruster performance.
- There exists a definite asymmetry in thruster performance between positive and negative yaw angles.

The transient test results also revealed transients are not affected by forward speed and yaw angles, for low speeds. This suggests the transient portion of conventional static thruster models will remain unchanged. It was, however, noted that there was an asymmetry in transient performance throughout the entire range of transient tests.

The last important issue that came from the tow tank tests revolved around the mounting of the C-SCOUT model to the tow carriage. Experimental data from the zero yaw case suggested there was a small misalignment between the model and the direction of travel of the carriage. This small misalignment had significant effects on the data at higher speeds. It was also observed that the yaw frame and mounting struts did not provide a very rigid mount between the vehicle and tow carriage. The test data at higher forward speeds had a significant amount of scatter which was attributed to this lack of stiffness. In addition to this, small low frequency oscillations appeared after many of the transient spikes during thrust reversal.

6.2 Modeling and Simulation

It was shown that existing tunnel thruster models do not capture asymmetry in axial thrust performance, and definitely cannot model the effects of forward speed and yaw angle. A new tunnel thruster model was assembled, loosely based on a conventional thruster model similar to those presented in [4], [7], [12], [25], and [26]. Because the results in Chapter 4 did not show a fundamental relationship between axial thrust and through-flow, a method for directly including the tow tank data into the model was required. The end result was a model that made use of experimental test data to incorporate the effects of forward speed and yaw angle into the model.

Because the transient behavior did not appear to vary significantly with yaw angle and forward speed, only the steady state portion of the tunnel thruster model needed to be modified. Asymmetry in transient behavior was handled by tuning an individual added mass coefficient, γ , for the forward and reverse axial flow conditions. The results from Chapter 4, in the form of coefficients a and b , were used directly to replace the steady state part of the tunnel thruster model.

For both the steady state and transient tests, the model output closely matched the experimental data, even at higher carriage speeds where noisy data sets resulted in poor fits of a and b . The model was successful in capturing the effects of forward speed and yawed orientation as well as asymmetry in thruster performance.

6.3 Recommendations

Recommendations for improving the experimental work contained in this thesis are as follows.

- Add baffles to the small tank to damp out water disturbances. This would reduce the wait time between tests and potentially decrease the effects of recirculation.
- Improve the LabVIEW DAC interface, increase sampling frequency if possible to ensure that the transient load data is not under sampled.
- Optimize the weight and size of the mechanical system in order to fit 3 tunnel thruster units within one C-SCOUT module.
- Design a new Yaw frame and mounting configuration to provide a rigid mount between the model and tow carriage.
- Ensure the vehicle model is correctly aligned with the direction of carriage travel.

6.4 Future Work

It would be useful to better understand how variations in tunnel thruster performance due to forward speed and yawed orientation affect the operation of a free swimming C-SCOUT. Future experimental work could include testing different tunnel locations in the vehicle (e.g. vertical tunnel arrangement, or the aft tunnel module location).

Once these tests are completed, there would be enough information to create a full vehicle simulation. Adding the tunnel thruster model presented in this thesis into a full vehicle simulation would allow the investigation of C-SCOUT control augmentation using tunnel thrusters.

Further testing may shed some light on the hydrodynamical effect of the fluid body interaction. One possibility would be the addition of a flow sensor to measure components of cross-flow and through-flow at the thruster inlet and exit. If the patterns in flow velocity can be better understood, it may be possible to predict a and b from fundamental principles rather than having to find them experimentally.

Once the basic effects of forward speed and yawed orientation have been quantified, a further step might be to improve the thruster's performance. One way to do this would be through a study of the intake/exit geometry. Publications dealing with bow thrusters in surface ships, such as [2], [5], and [19] emphasize that the shape of the intake/exit is very important to thruster performance. It would be reasonable to assume that these effects would also apply to underwater vehicles.

Appendix A

Experimental Results

Steady State Linear Fit - Intercept Data

deg speed	-90	-70	-50	-30	-20	-10	0
0.1 m/s	-0.23392	0.06552	0.17169	-0.18801	-0.44341	0.14669	0.02064
0.2 m/s	-0.30686	-0.06884	0.13915	-0.23312	-0.48406	0.10558	0.06011
0.3 m/s	-0.84887	-0.68678	-0.25061	-0.37022	-0.59200	-0.03797	-0.02996
0.4 m/s	-1.67823	-1.14046	-0.63445	-0.41355	-0.60917	-0.05040	-0.03739
0.5 m/s	-2.42948	-2.36387	-1.31926	-0.39856	-0.56213	-0.05359	-0.06887
1.0 m/s					-0.95584	-0.16575	0.00675
1.5 m/s					-1.42696	-0.30160	0.36665
2.0 m/s					-2.53035	-0.50222	0.83194
2.5 m/s						-0.05600	1.94944
3.0 m/s							2.70102
3.5 m/s							2.81664
4.0 m/s							3.72176



0	10	20	30	50	70	90	deg speed
0.02064	-0.07450	-0.01925	0.20544	0.29096	0.24342	0.58512	0.1 m/s
0.06011	-0.02969	0.01706	0.28897	0.58984	0.60552	0.84241	0.2 m/s
-0.02996	0.03258	0.10593	0.41691	0.80641	1.00661	1.46828	0.3 m/s
-0.03739	-0.00755	0.11774	0.55147	1.42178	1.56197	2.09036	0.4 m/s
-0.06887	-0.01592	0.21189	0.89205	1.77149	2.65010	2.69039	0.5 m/s
0.00675	0.30882	1.17032					1.0 m/s
0.36665	1.14895	2.75071					1.5 m/s
0.83194	2.20497	5.31757					2.0 m/s
1.94944	4.15893						2.5 m/s
2.70102							3.0 m/s
2.81664							3.5 m/s
3.72176							4.0 m/s



Figure A.1. Values for Intercept, Data Fit for Steady State Tests

Steady State Linear Fit - Slope Data

deg speed	-90	-70	-50	-30	-20	-10	0
0.1 m/s	-1.111E-05	-1.1E-05	-1.069E-05	-1.160E-05	-1.146E-05	-1.145E-05	-1.114E-05
0.2 m/s	-1.134E-05	-9.401E-06	-9.926E-06	-1.061E-05	-1.043E-05	-1.052E-05	-1.055E-05
0.3 m/s	-1.095E-05	-8.487E-06	-7.666E-06	-9.854E-06	-9.875E-06	-9.752E-06	-9.875E-06
0.4 m/s	-8.775E-06	-7.227E-06	-6.601E-06	-9.717E-06	-9.855E-06	-1.010E-05	-9.665E-06
0.5 m/s	-8.472E-06	-5.408E-06	-5.141E-06	-1.017E-05	-1.054E-05	-1.030E-05	-9.873E-06
1.0 m/s					-9.771E-06	-1.077E-05	-1.060E-05
1.5 m/s					-8.760E-06	-1.109E-05	-1.182E-05
2.0 m/s					-6.251E-06	-1.058E-05	-1.272E-05
2.5 m/s						-9.356E-06	-1.294E-05
3.0 m/s							-1.074E-05
3.5 m/s							-1.011E-05
4.0 m/s							-1.070E-05



0	10	20	30	50	70	90	deg speed
-1.114E-05	-1.092E-05	-1.100E-05	-1.114E-05	-1.115E-05	-1.090E-05	-1.073E-05	0.1 m/s
-1.055E-05	-1.062E-05	-1.035E-05	-1.056E-05	-1.022E-05	-9.702E-06	-1.014E-05	0.2 m/s
-9.875E-06	-1.026E-05	-9.806E-06	-9.848E-06	-8.660E-06	-9.076E-06	-9.039E-06	0.3 m/s
-9.665E-06	-9.607E-06	-9.351E-06	-9.230E-06	-8.801E-06	-8.219E-06	-8.145E-06	0.4 m/s
-9.873E-06	-9.407E-06	-9.064E-06	-9.202E-06	-8.253E-06	-8.332E-06	-7.832E-06	0.5 m/s
-1.060E-05	-9.973E-06	-9.445E-06					1.0 m/s
-1.182E-05	-1.121E-05	-1.001E-05					1.5 m/s
-1.272E-05	-1.183E-05	-1.045E-05					2.0 m/s
-1.294E-05	-1.209E-05						2.5 m/s
-1.074E-05							3.0 m/s
-1.011E-05							3.5 m/s
-1.070E-05							4.0 m/s



Figure A.2. Values for Intercept, Data Fit for Steady State Tests

MUN Tow Tank Test Matrix File Naming Convention														
deg m/s	-90	-70	-50	-30	-20	-10	0	10	20	30	50	70	90	
0.1	A01	A02	A03	A04	A05	A06	A07	A08	A09	A10	A11	A12	A13	0.1
0.2	B01	B02	B03	B04	B05	B06	B07	B08	B09	B10	B11	B12	B13	0.2
0.3	C01	C02	C03	C04	C05	C06	C07	C08	C09	C10	C11	C12	C13	0.3
0.4	D01	D02	D03	D04	D05	D06	D07	D08	D09	D10	D11	D12	D13	0.4
0.5	E01	E02	E03	E04	E05	E06	E07	E08	E09	E10	E11	E12	E13	0.5
1.0					F05	F06	F07	F08	F09					1.0
1.5					G05	G06	G07	G08	G09					1.5
2.0					H05	H06	H07	H08	H09					2.0
2.5	Ramp					I06	I07	I08						2.5
3.0						J1	J07	J3						3.0
3.5							K07							3.5
4.0							L07							4.0

deg m/s	-90	-70	-50	-30	-20	-10	0	10	20	30	50	70	90	
0.1	M01	M02	M03	M04	M05	M06	M07	M08	M09	M10	M11	M12	M13	0.1
0.2	N01	N02	N03	N04	N05	N06	N07	N08	N09	N10	N11	N12	N13	0.2
0.3	O01	O02	O03	O04	O05	O06	O07	O08	O09	O10	O11	O12	O13	0.3
0.4	P01	P02	P03	P04	P05	P06	P07	P08	P09	P10	P11	P12	P13	0.4
0.5	Q01	Q02	Q03	Q04	Q05	Q06	Q07	Q08	Q09	Q10	Q11	Q12	Q13	0.5
1.0					R05	R06	R07	R08	R09					1.0
1.5					S05	S06	S07	S08	S09					1.5
2.0					T05	T06	T07	T08	T09					2.0
2.5	Square					U06	U07	U08						2.5
3.0							V07							3.0
3.5							W07		Bad test data					3.5
4.0							X07							4.0

Figure A.3. Detailed Test Matrix and File Name Convention

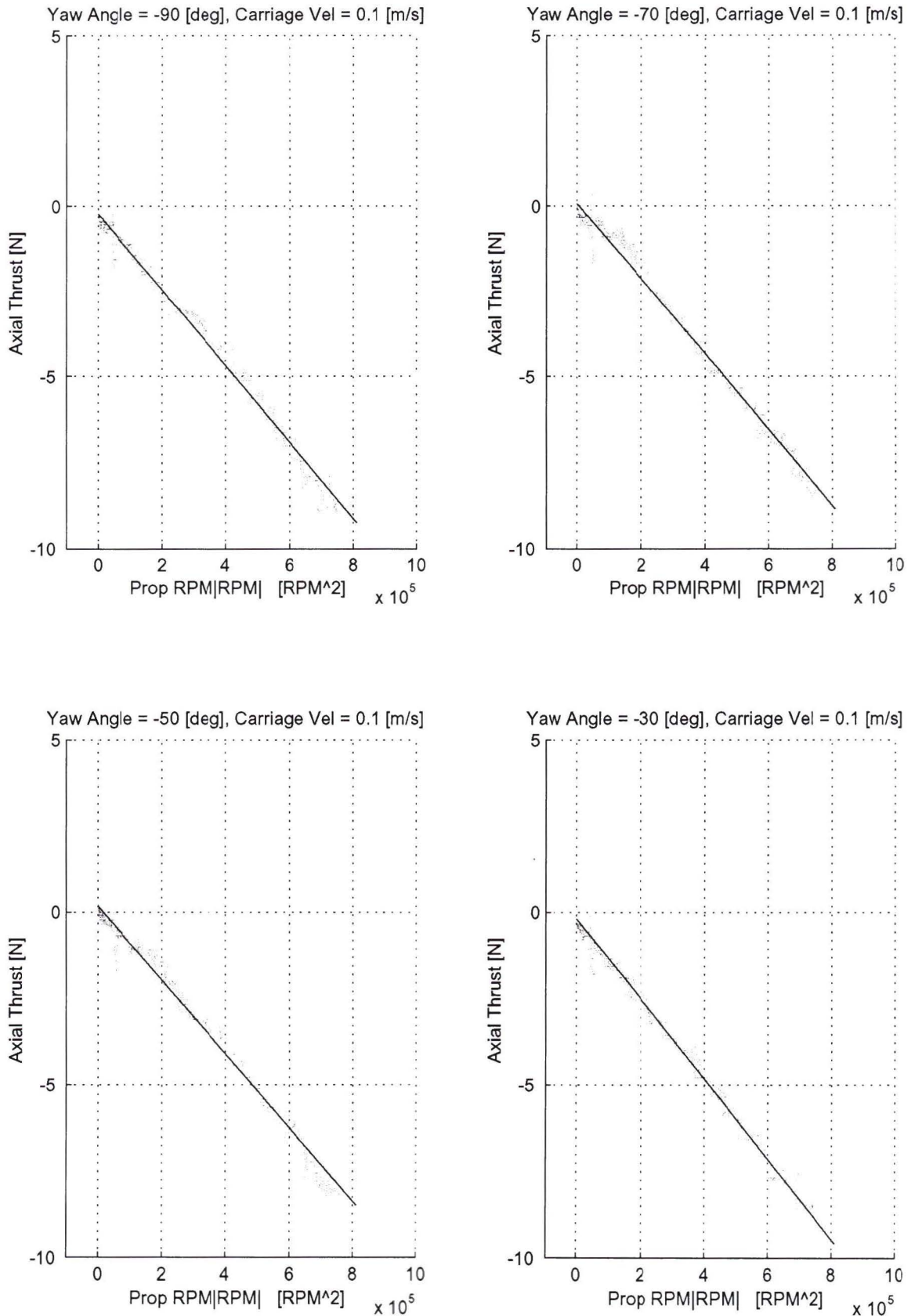


Figure A.4. Tow Tank Data, Test Matrix Elements A01 to A04

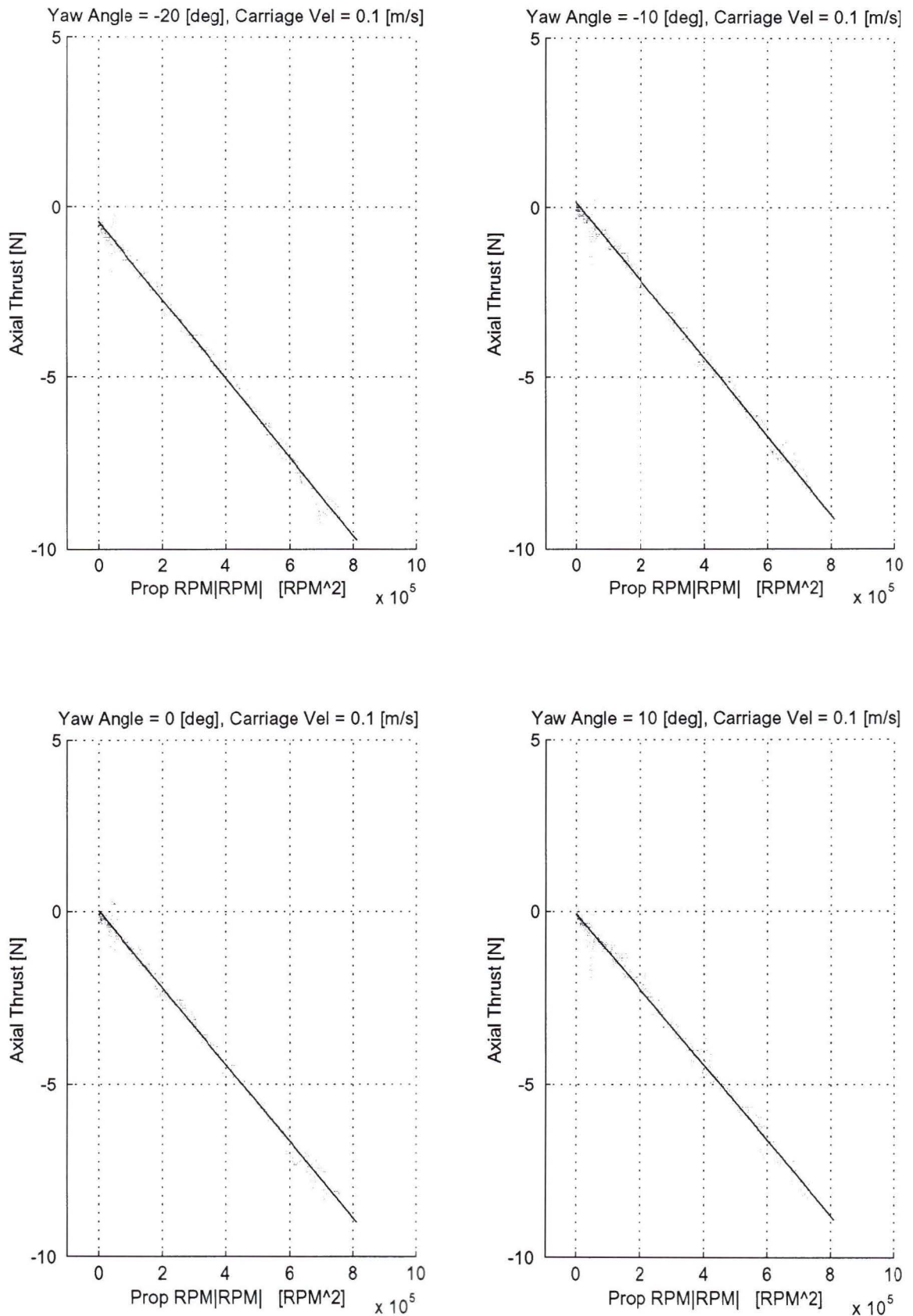


Figure A.5. Tow Tank Data, Test Matrix Elements A05 to A08

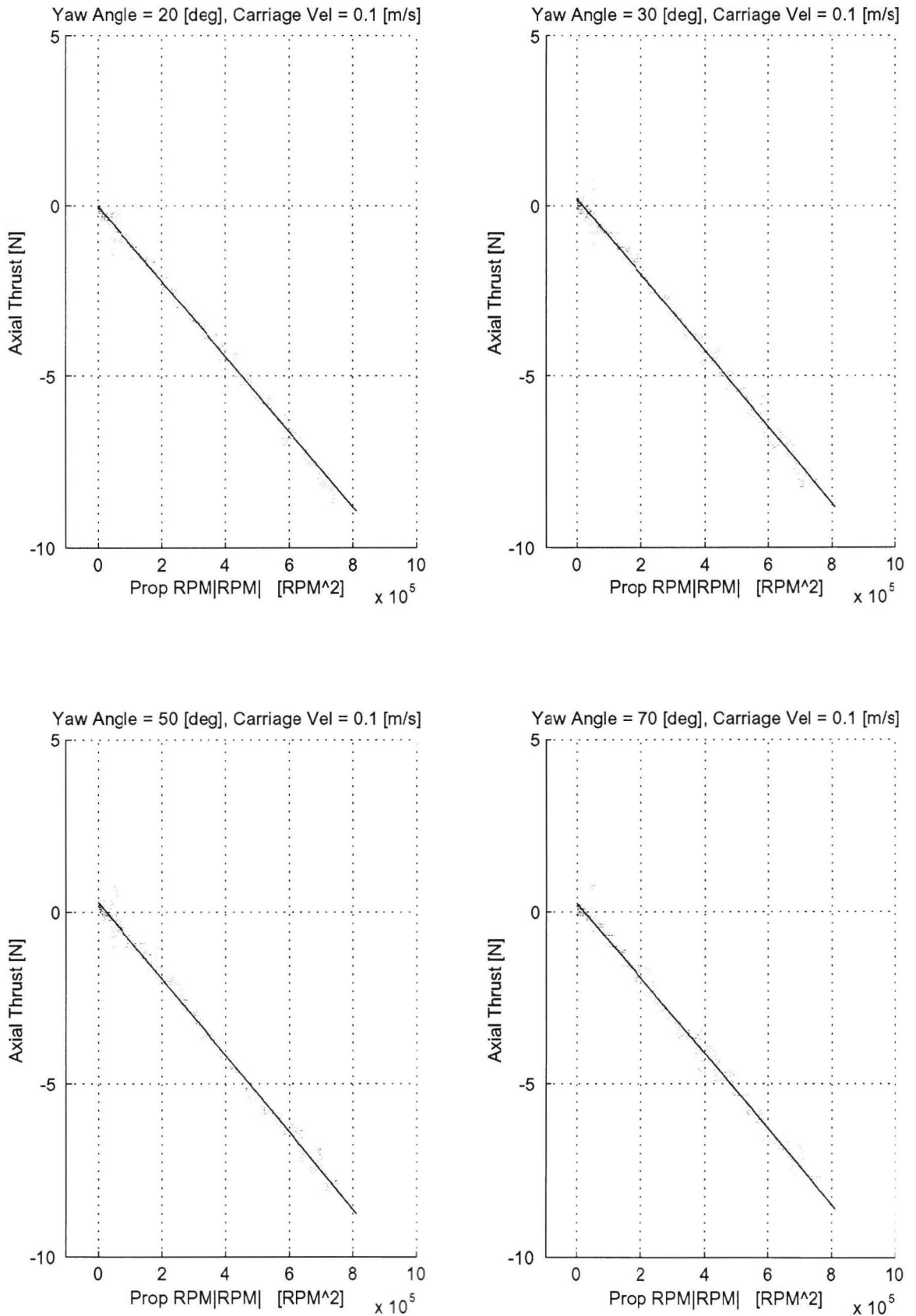


Figure A.6. Tow tank Data, Test Matrix Elements A09 to A12

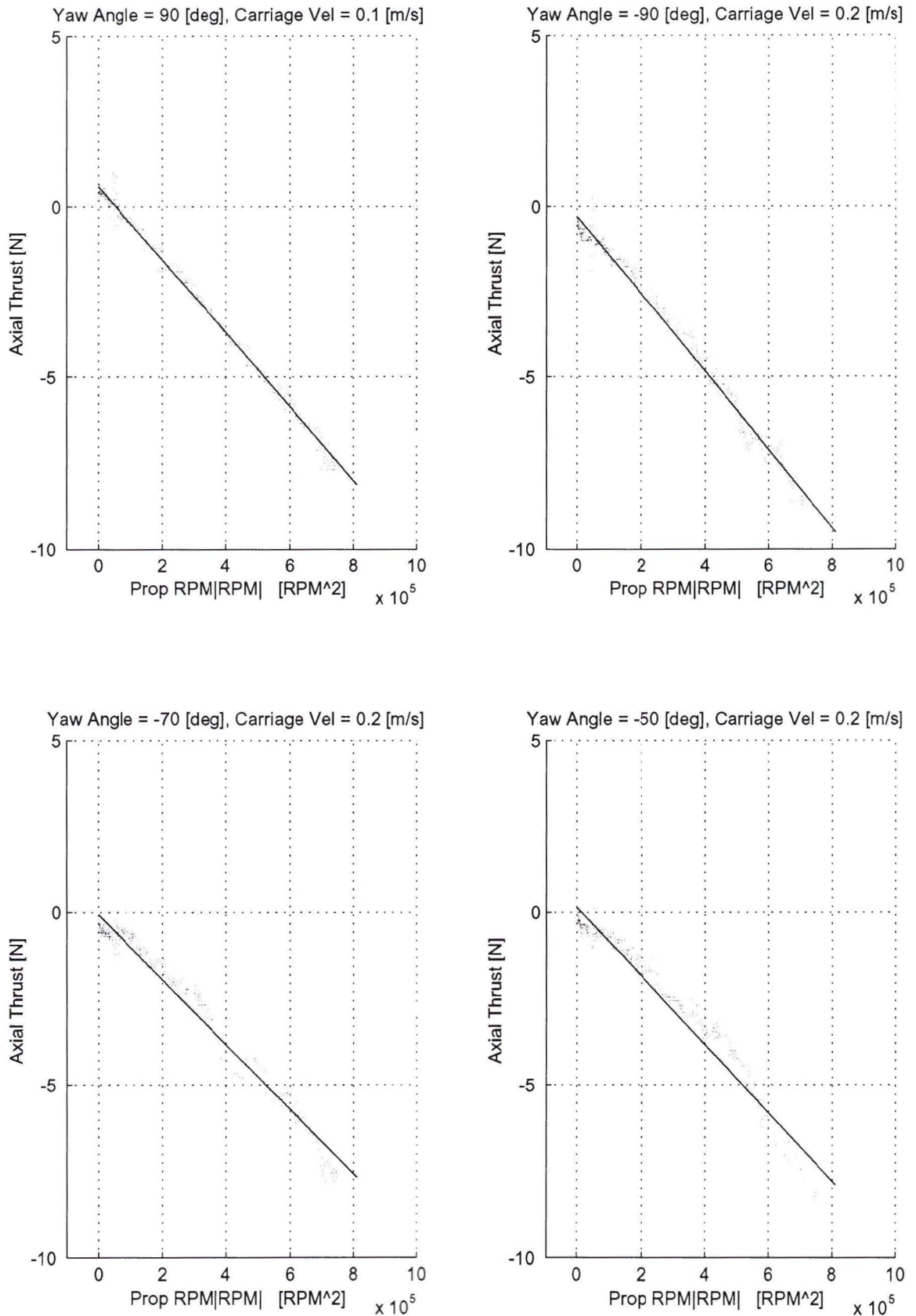


Figure A.7. Tow tank Data, Test Matrix Elements A13 to B03

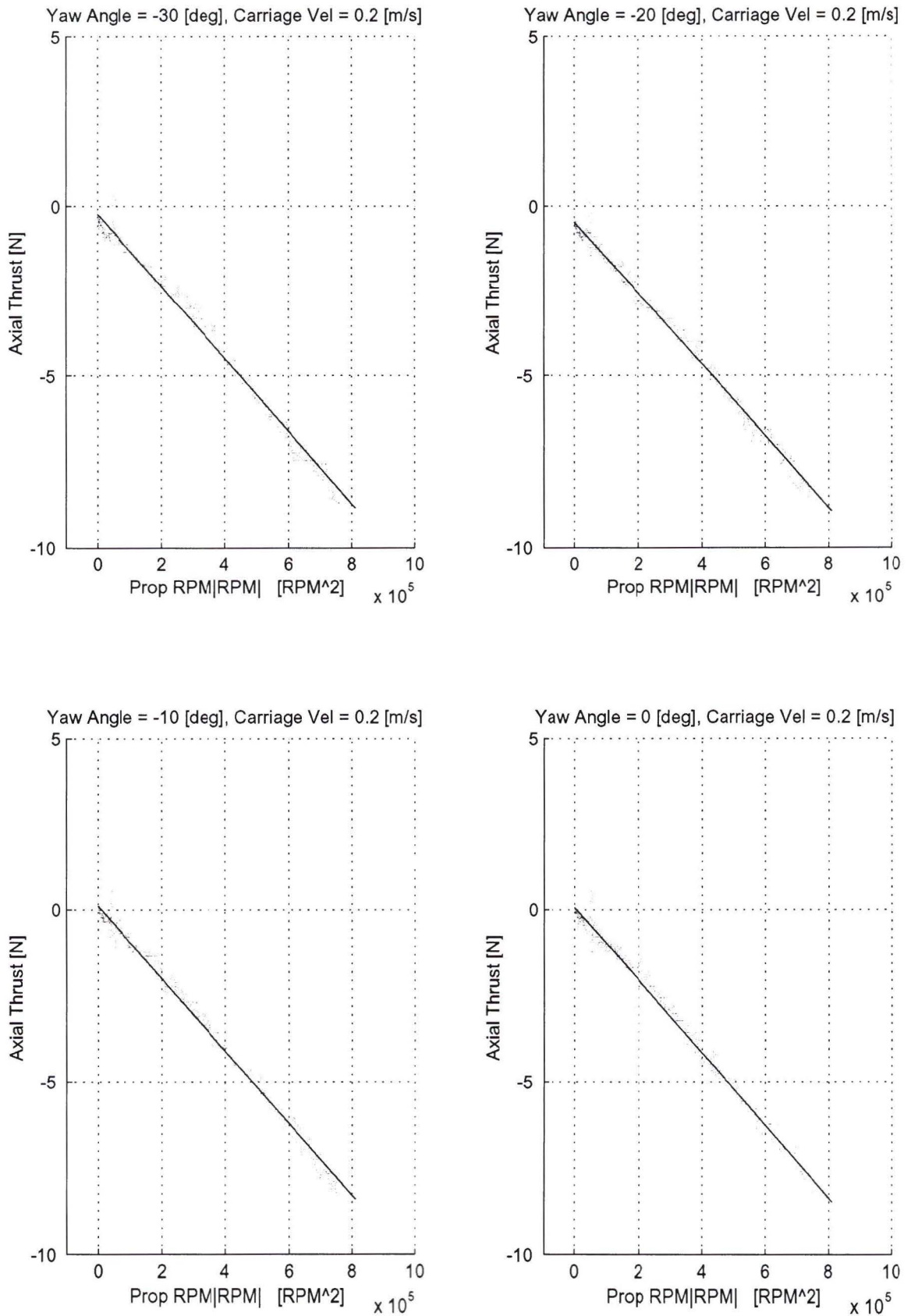


Figure A.8. Tow tank Data, Test Matrix Elements B04 to B07

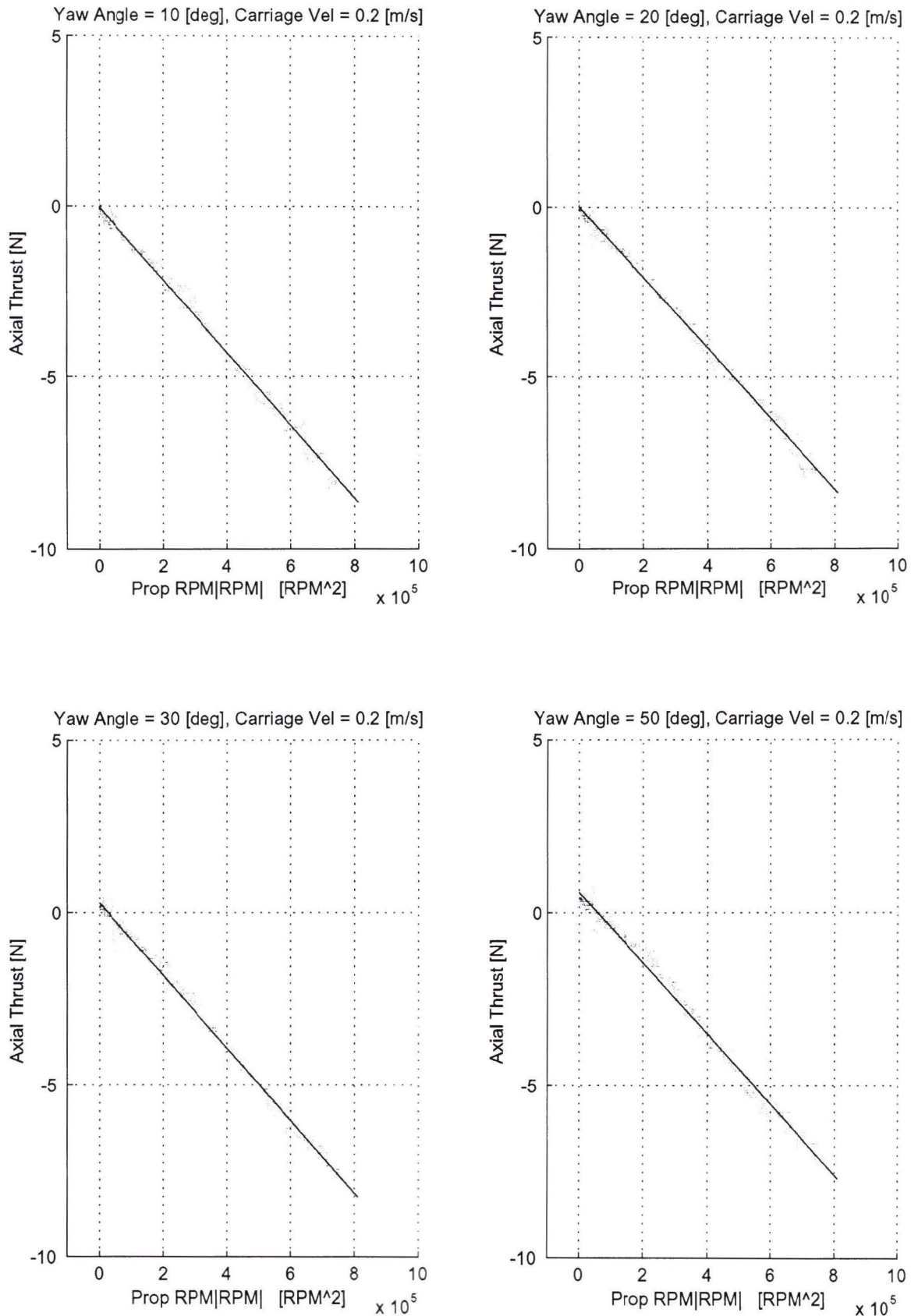


Figure A.9. Tow tank Data, Test Matrix Elements B08 to B11

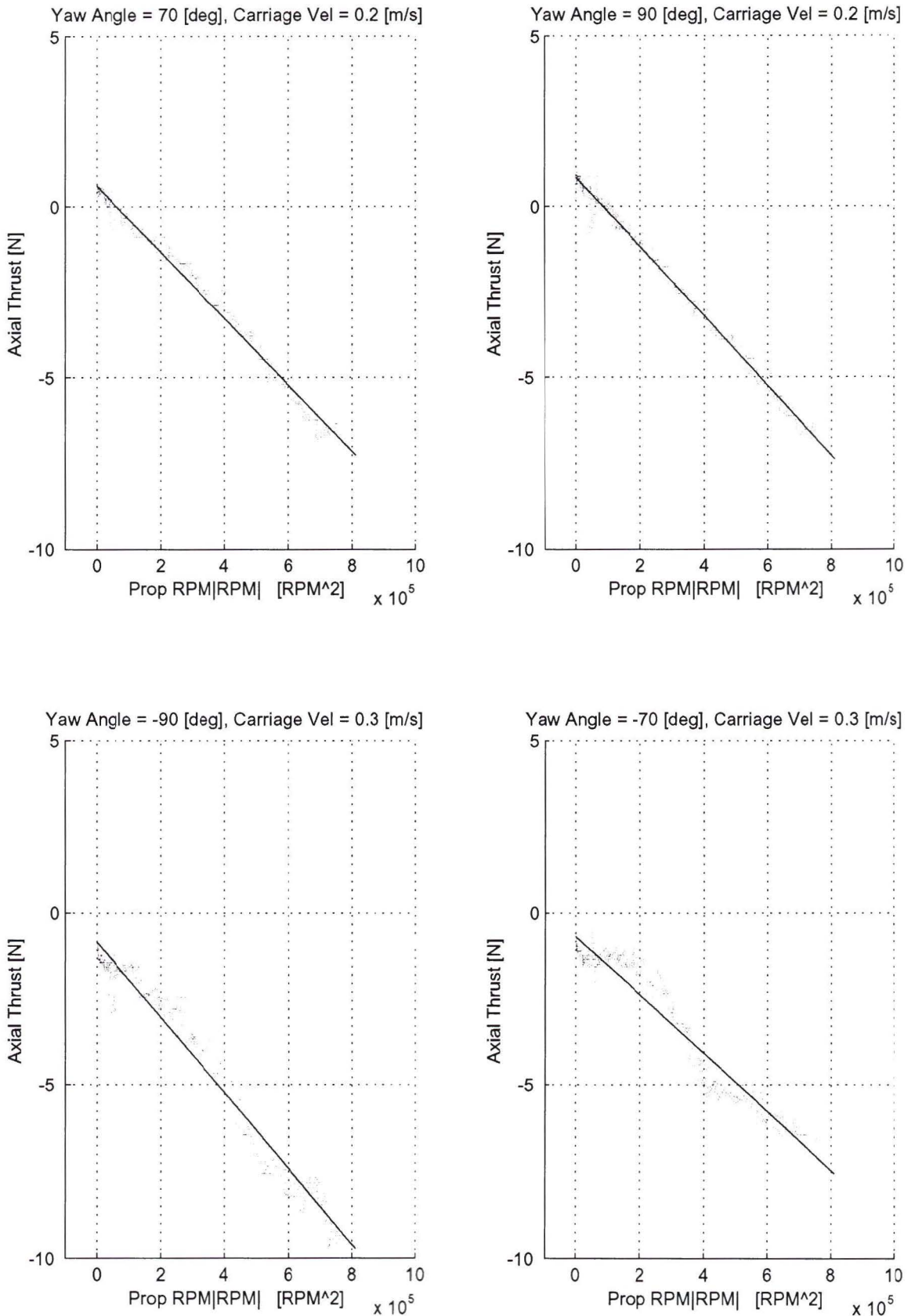


Figure A.10. Tow tank Data, Test Matrix Elements B12 to C02

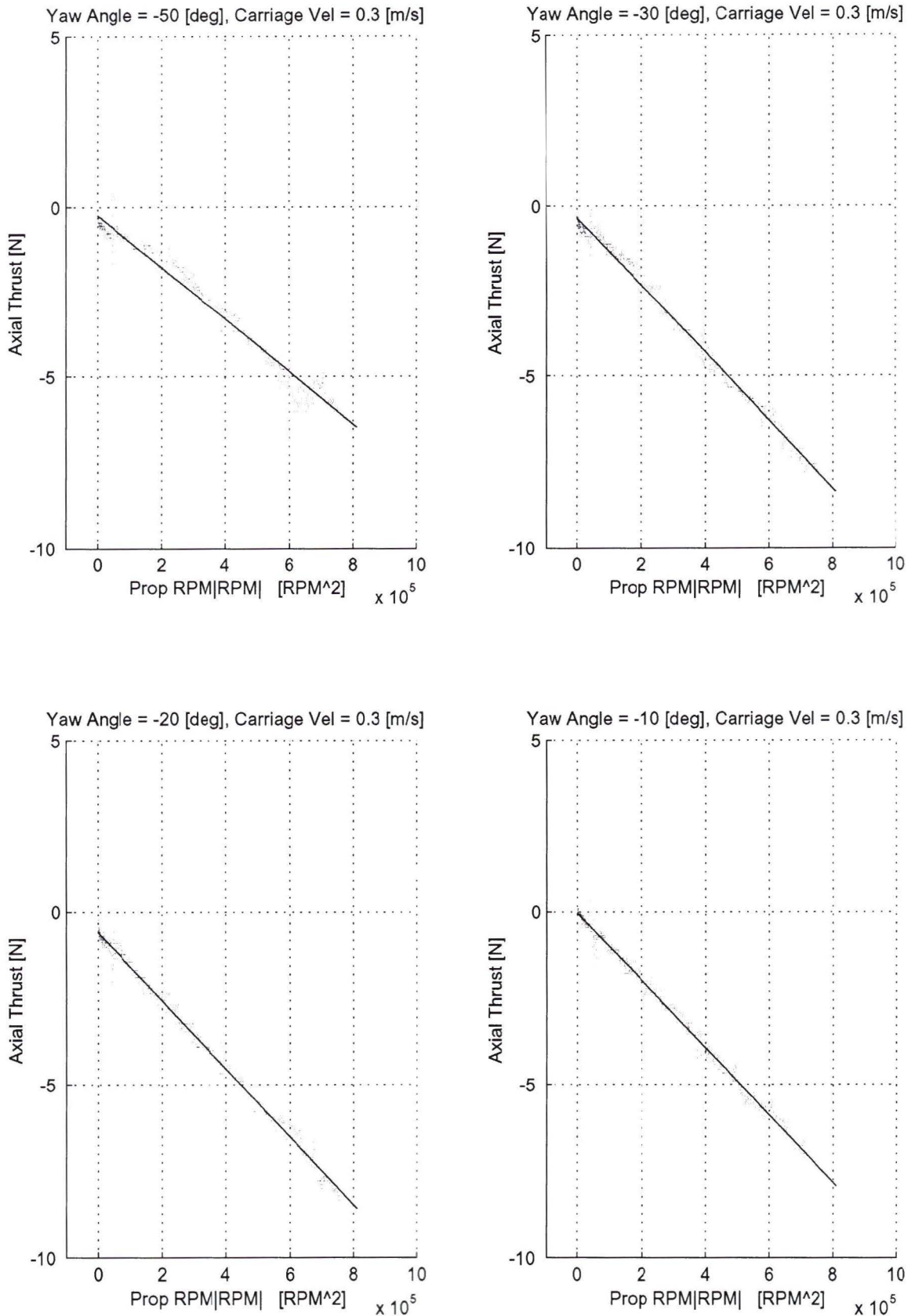


Figure A.11. Tow tank Data, Test Matrix Elements C03 to C06

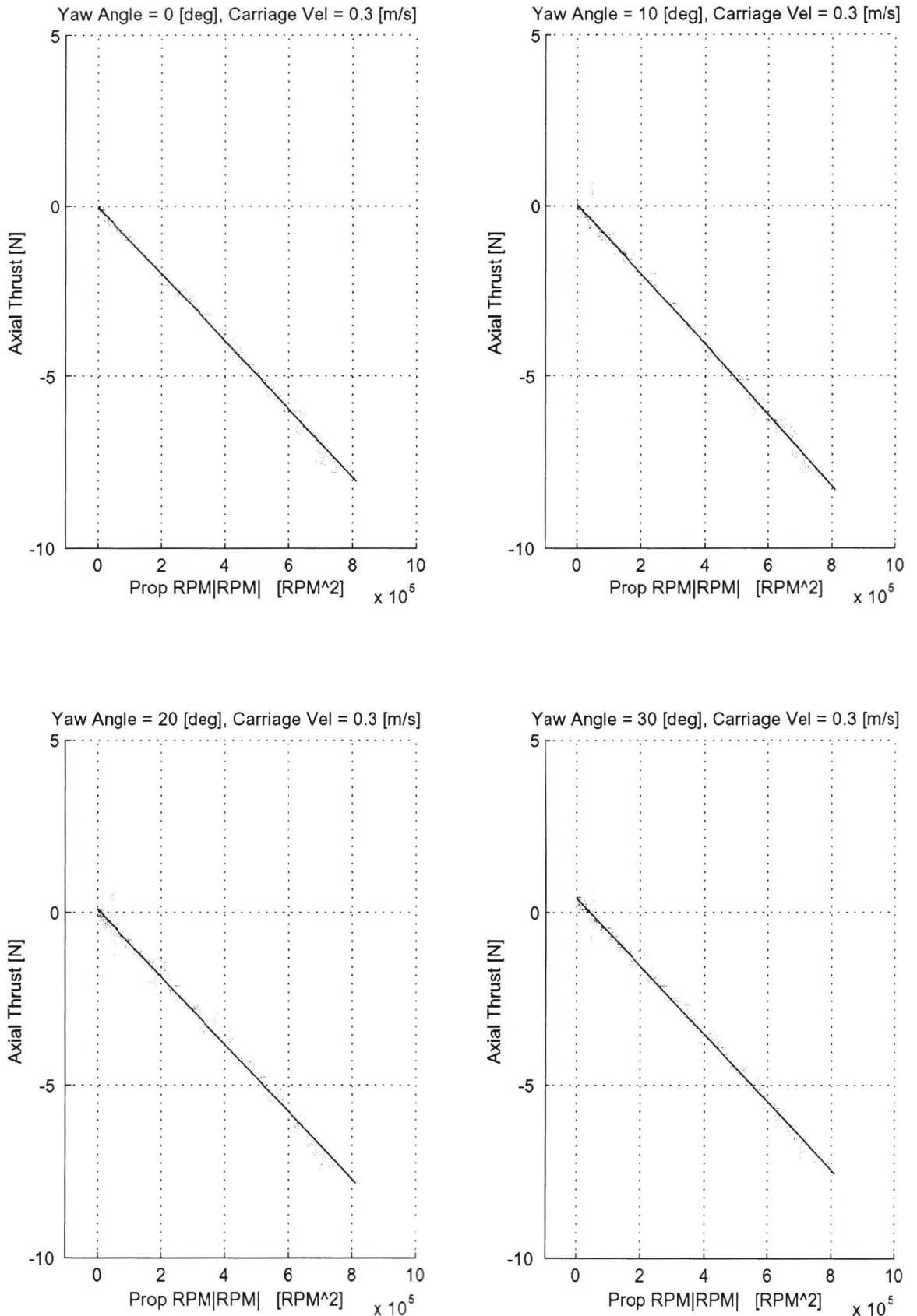


Figure A.12. Tow tank Data, Test Matrix Elements C07 to C10

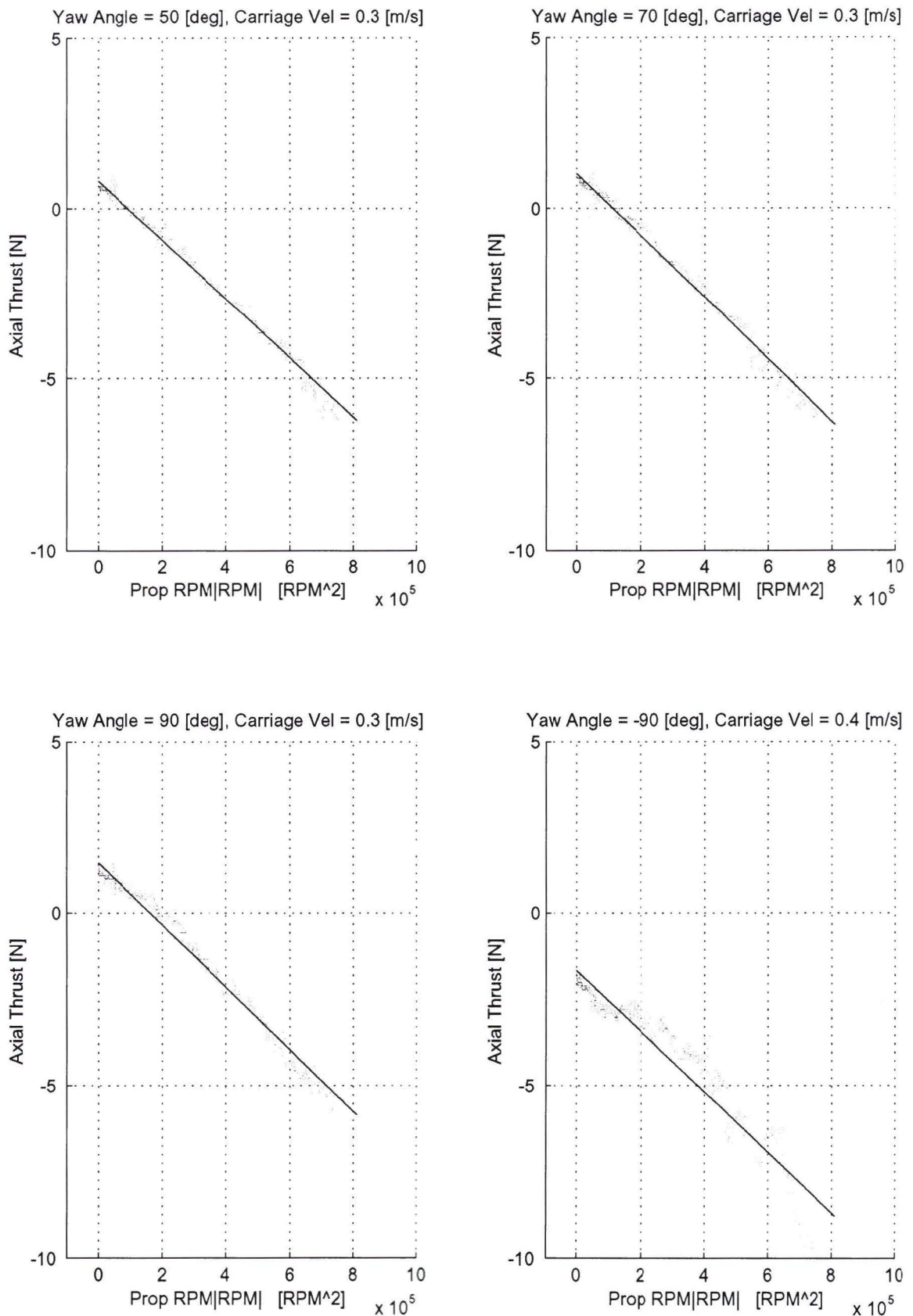


Figure A.13. Tow tank Data, Test Matrix Elements C11 to D01

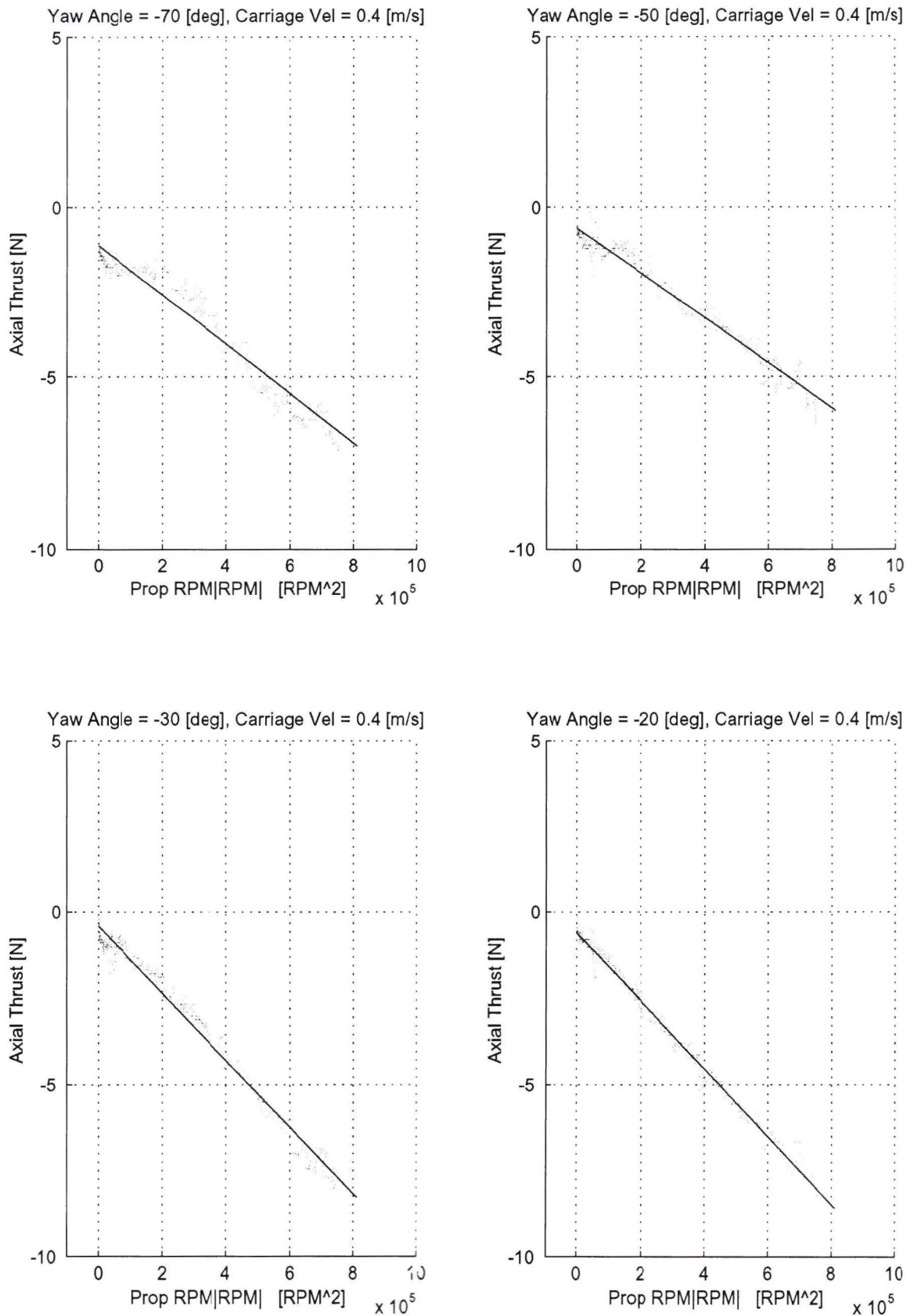


Figure A.14. Tow tank Data, Test Matrix Elements D02 to D05

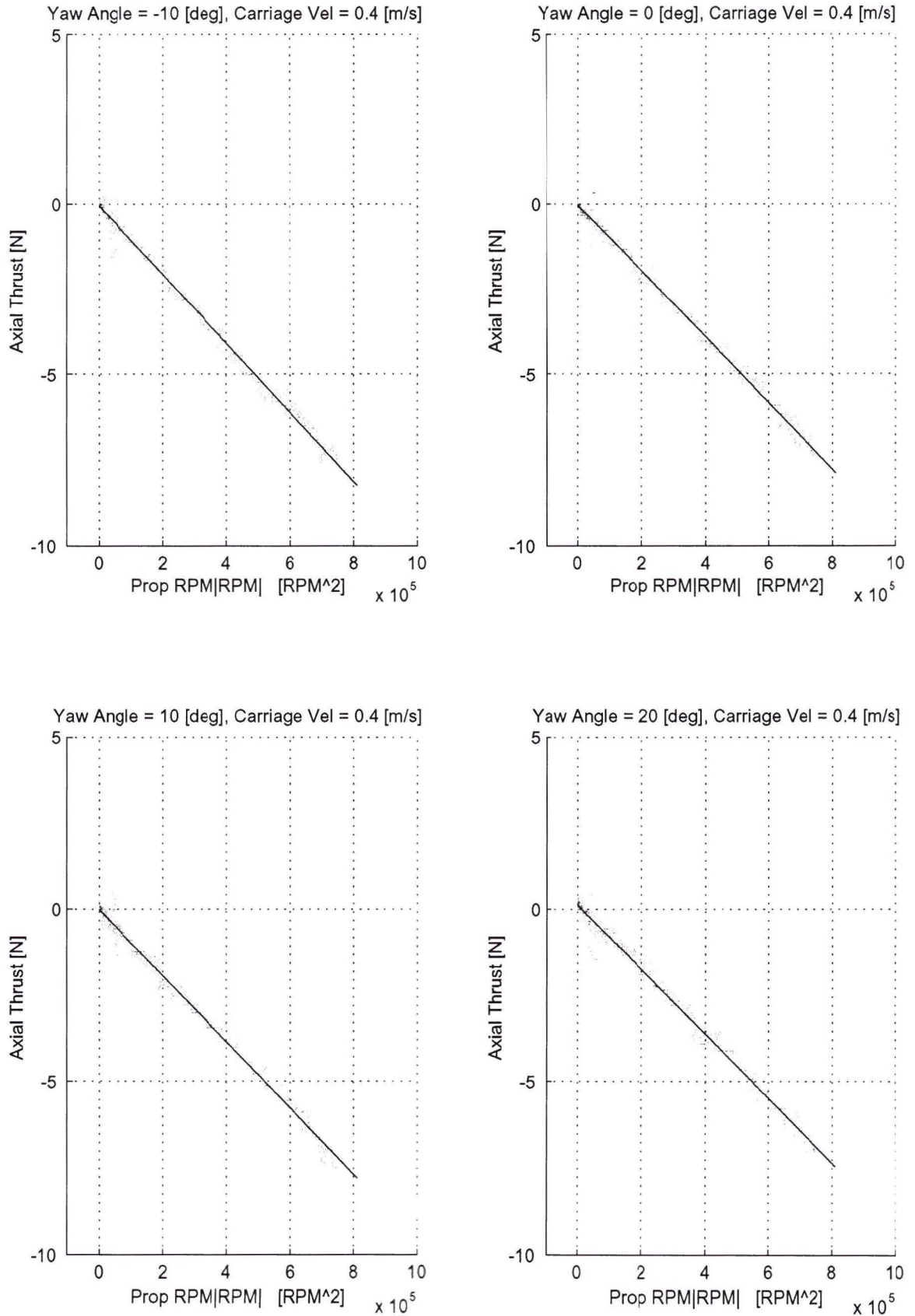


Figure A.15. Tow tank Data, Test Matrix Elements D06 to D09

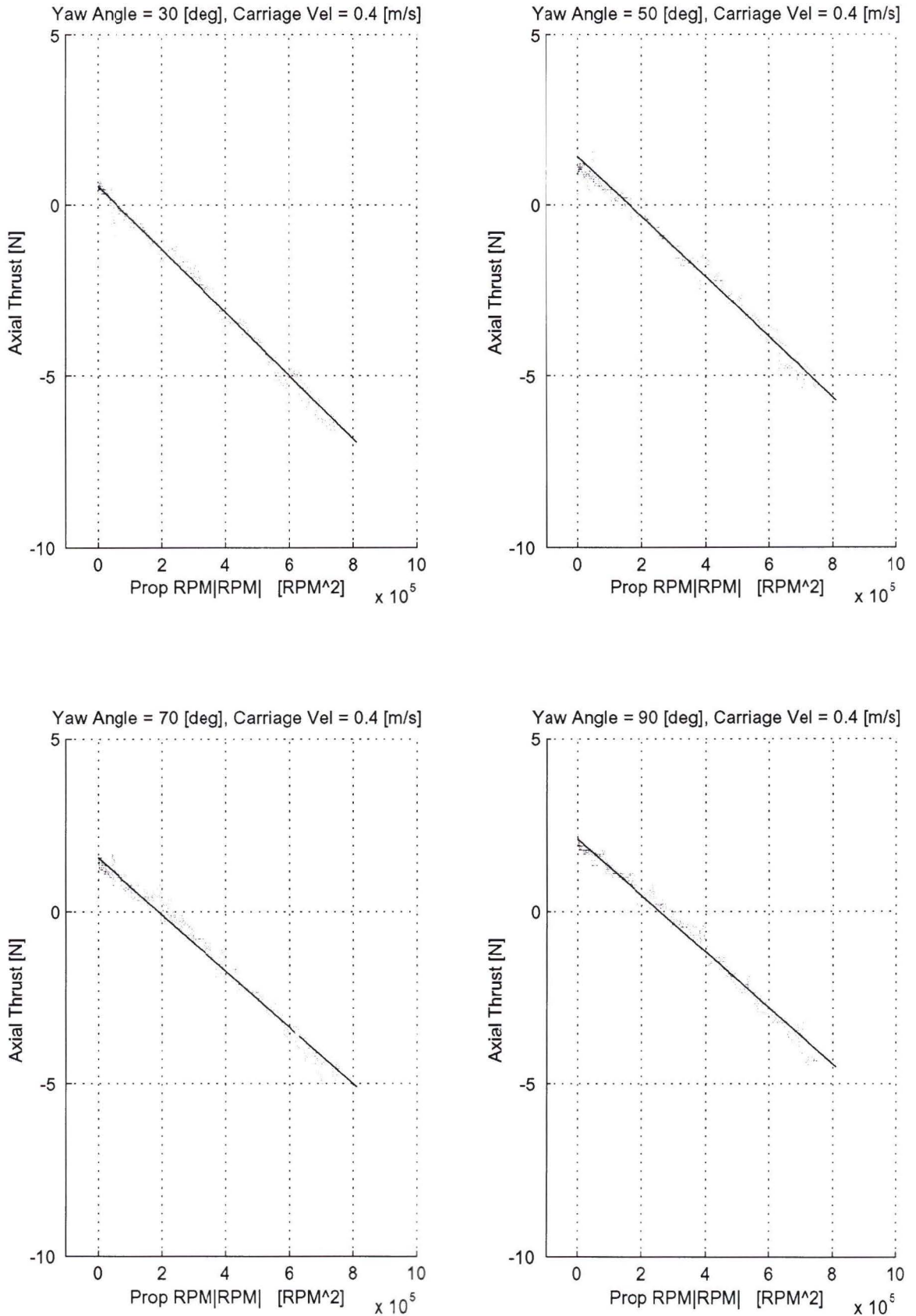


Figure A.16. Tow tank Data, Test Matrix Elements D10 to D13

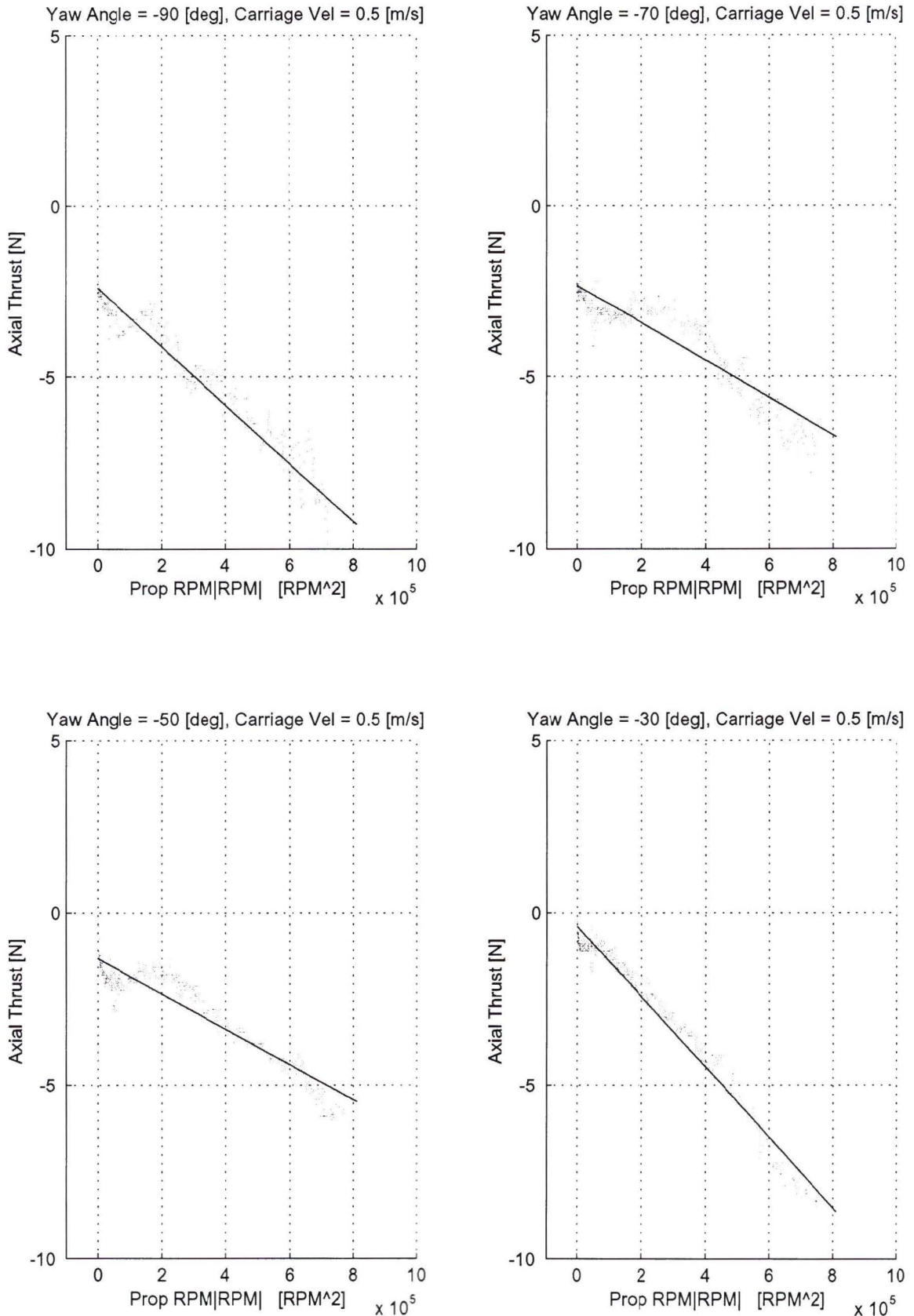


Figure A.17. Tow tank Data, Test Matrix Elements E01 to E04

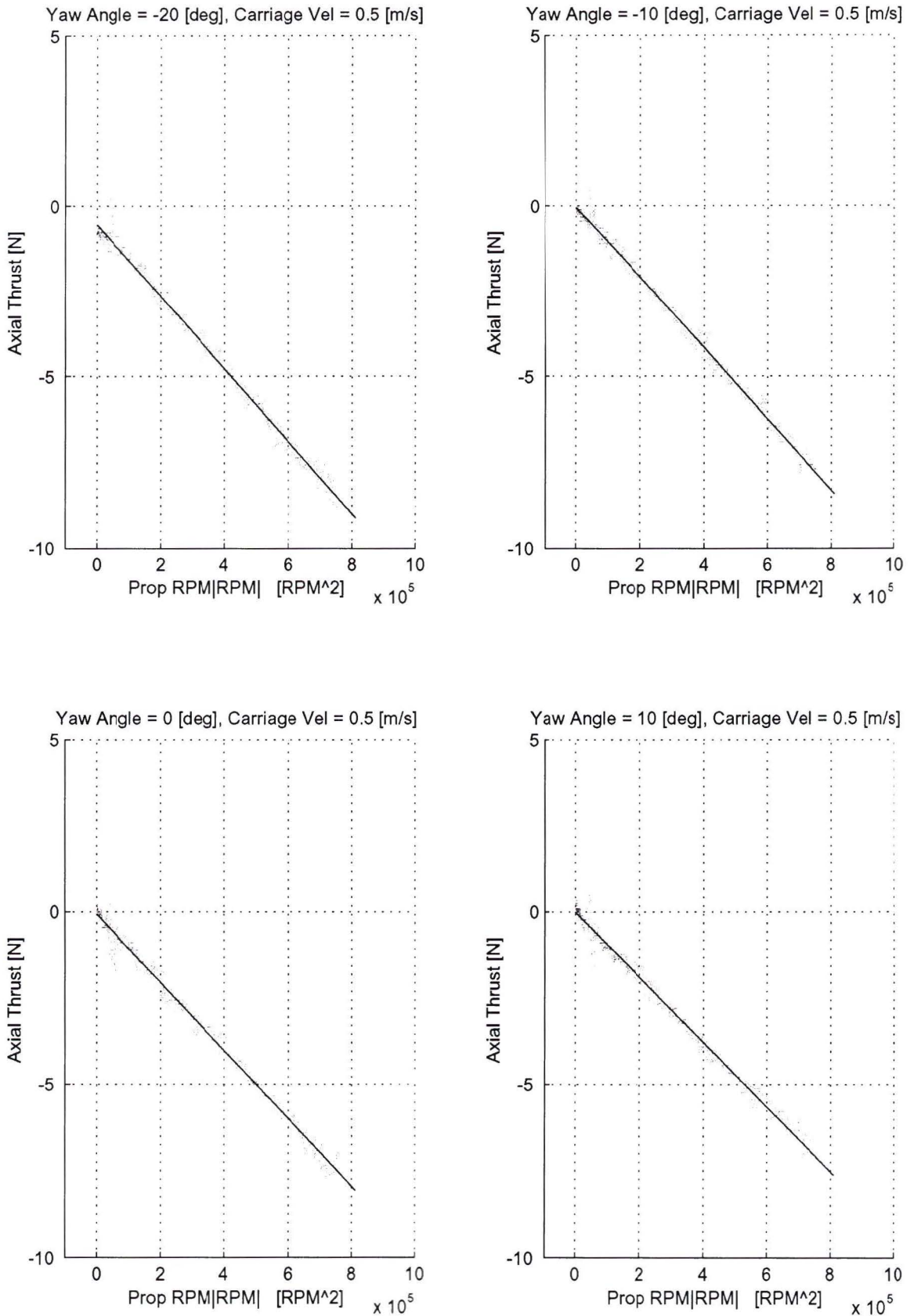


Figure A.18. Tow tank Data, Test Matrix Elements E05 to E08

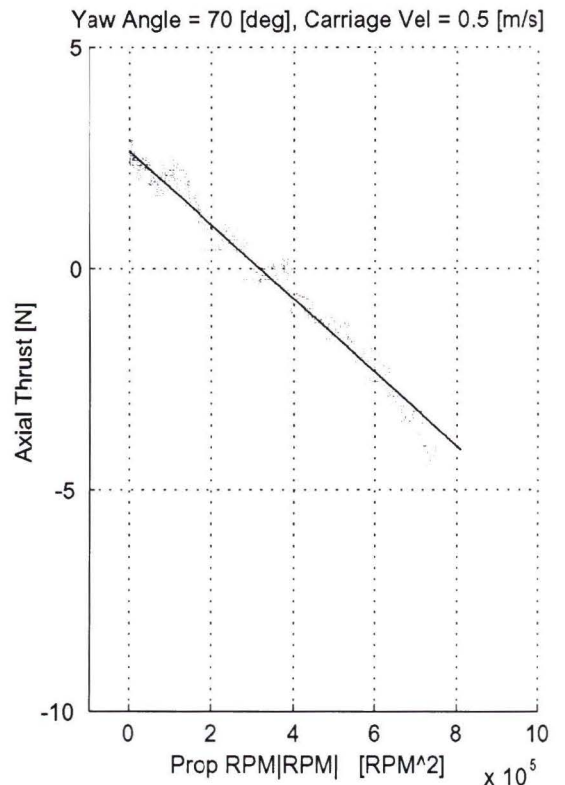
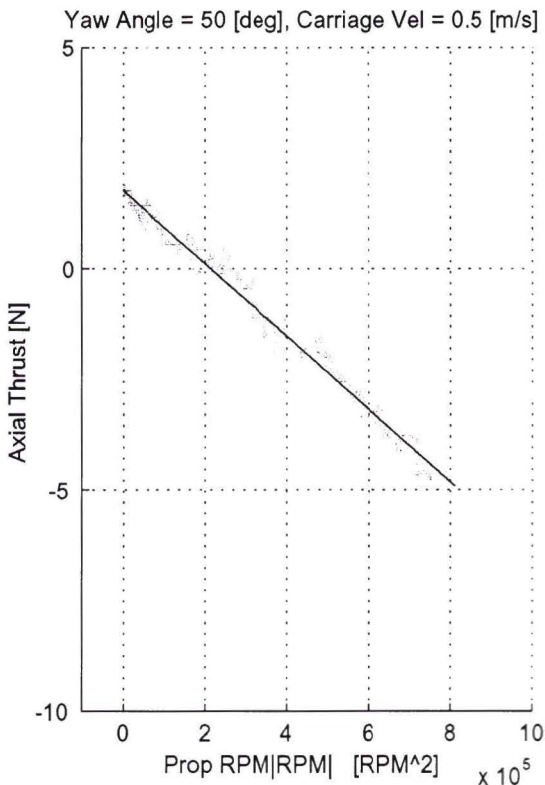
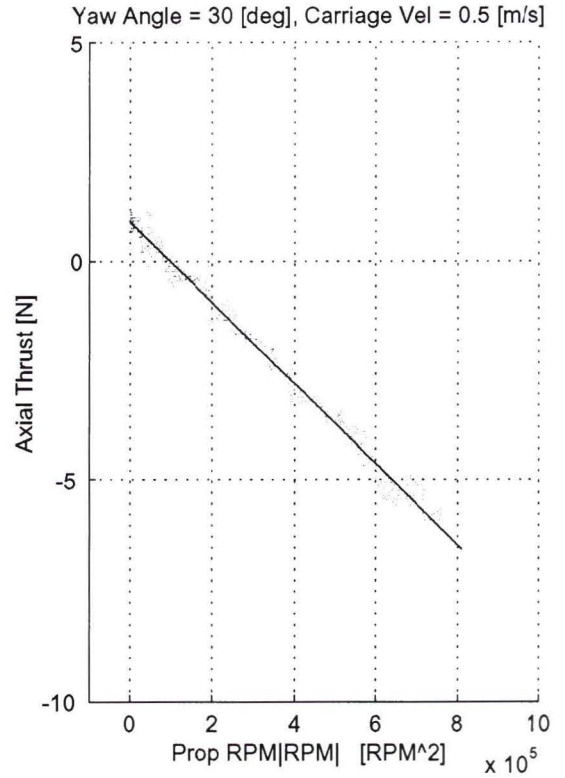
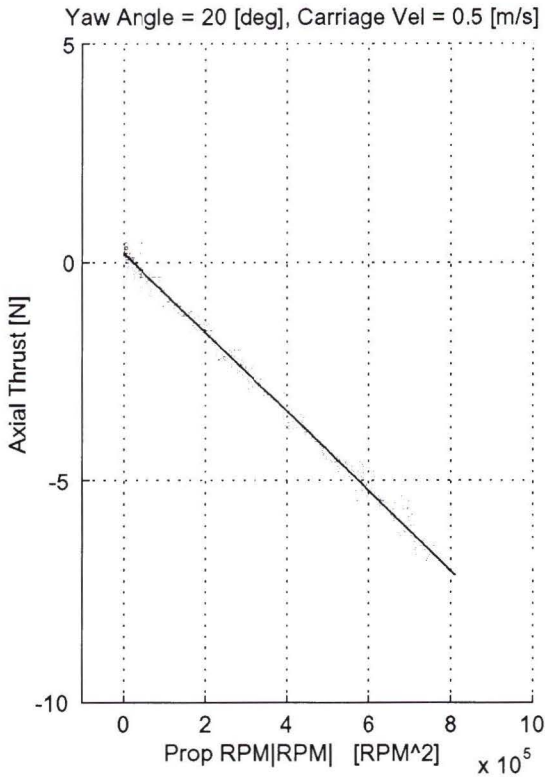


Figure A.19. Tow tank Data, Test Matrix Elements E09 to E12

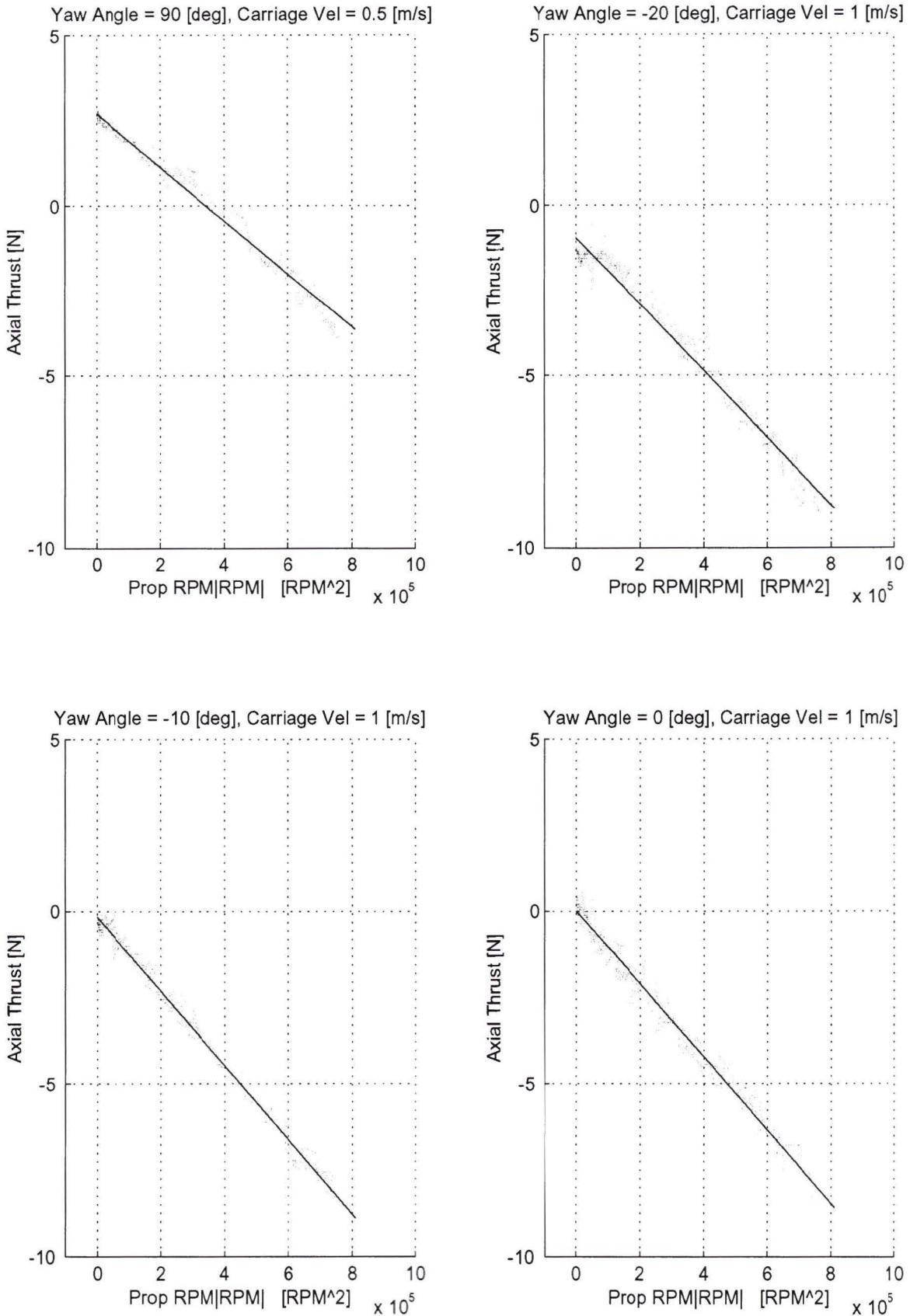


Figure A.20. Tow tank Data, Test Matrix Elements E13 to F07

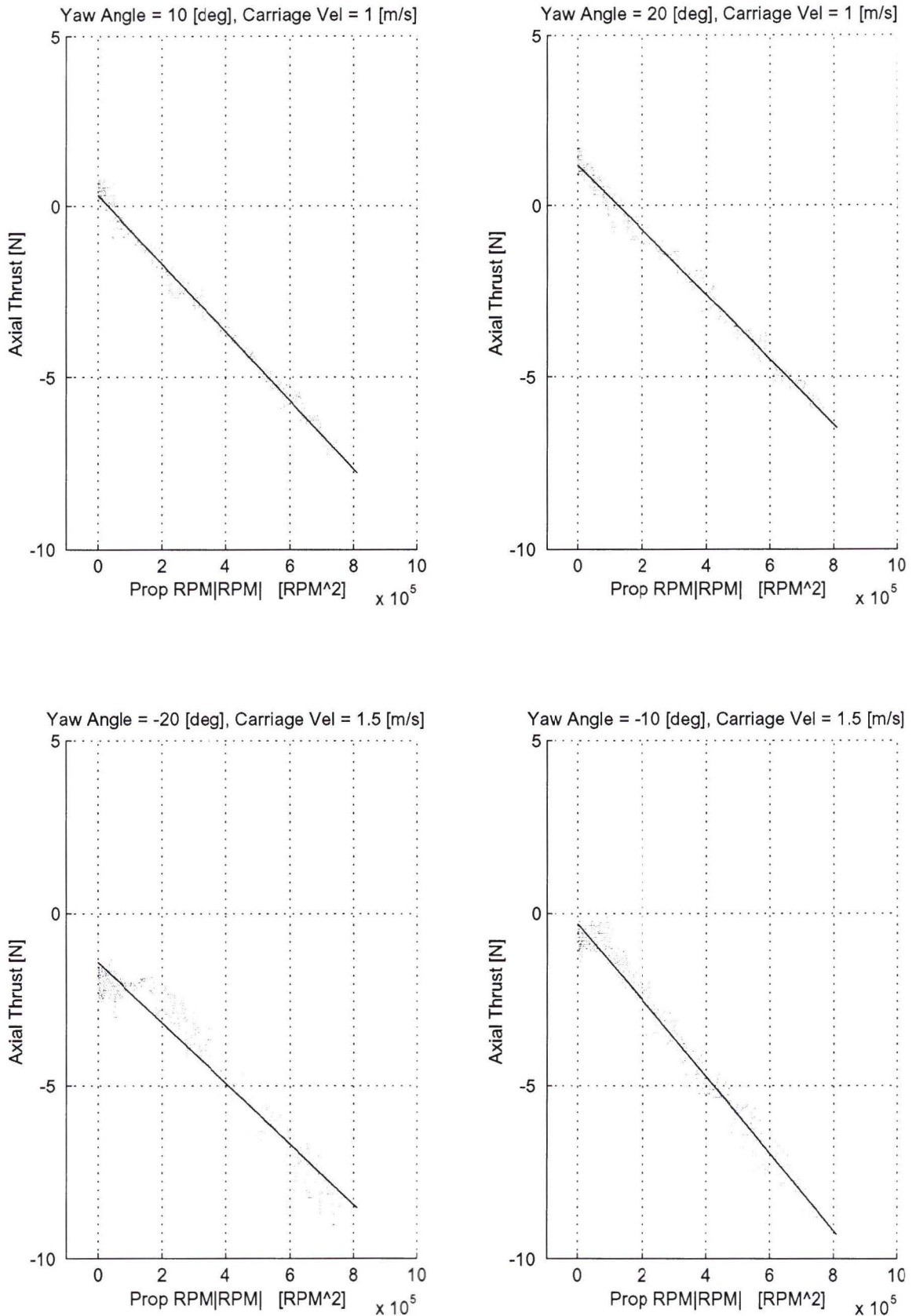


Figure A.21. Tow tank Data, Test Matrix Elements F08 to G06

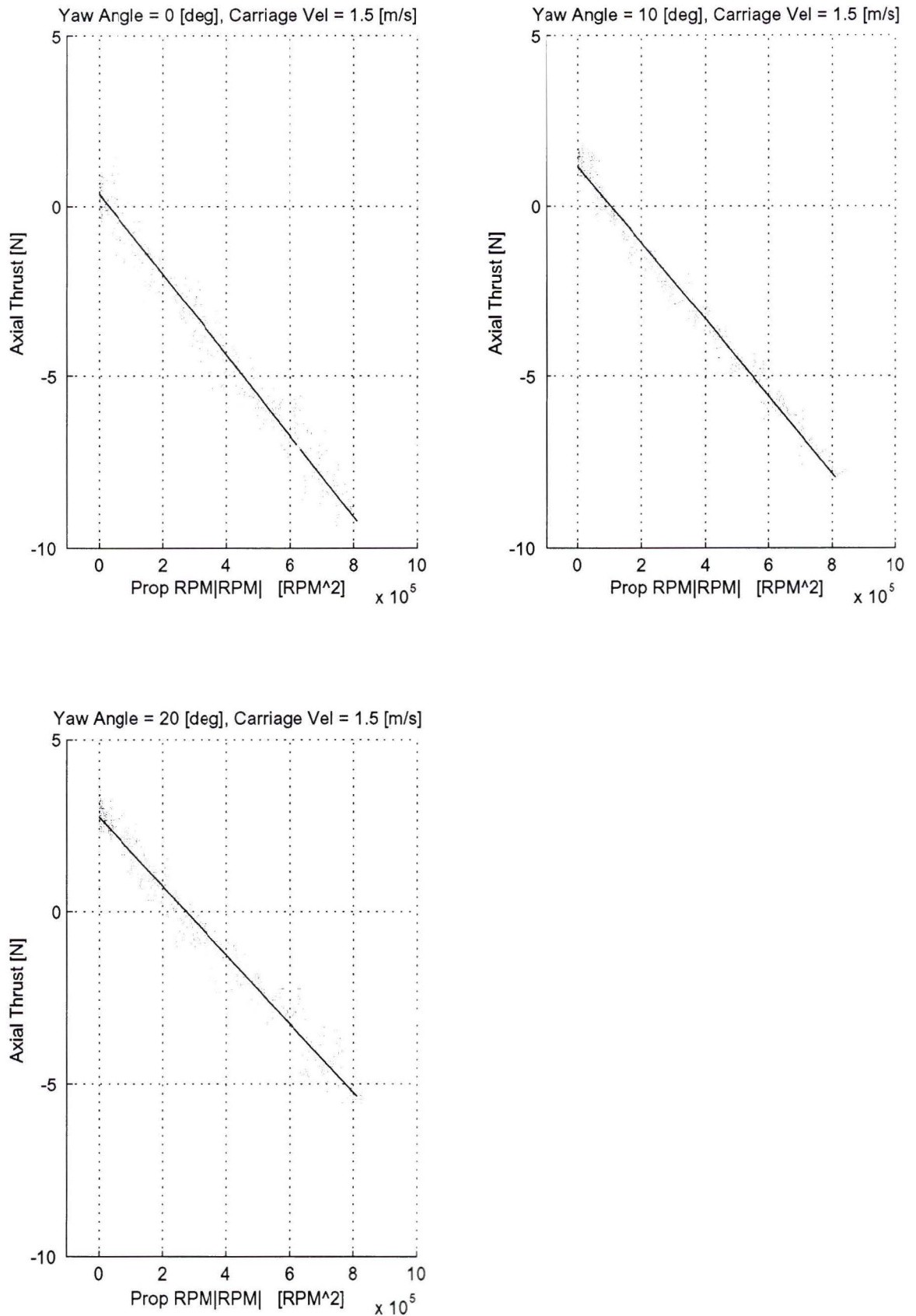


Figure A.22. Tow tank Data, Test Matrix Elements G07 to G09

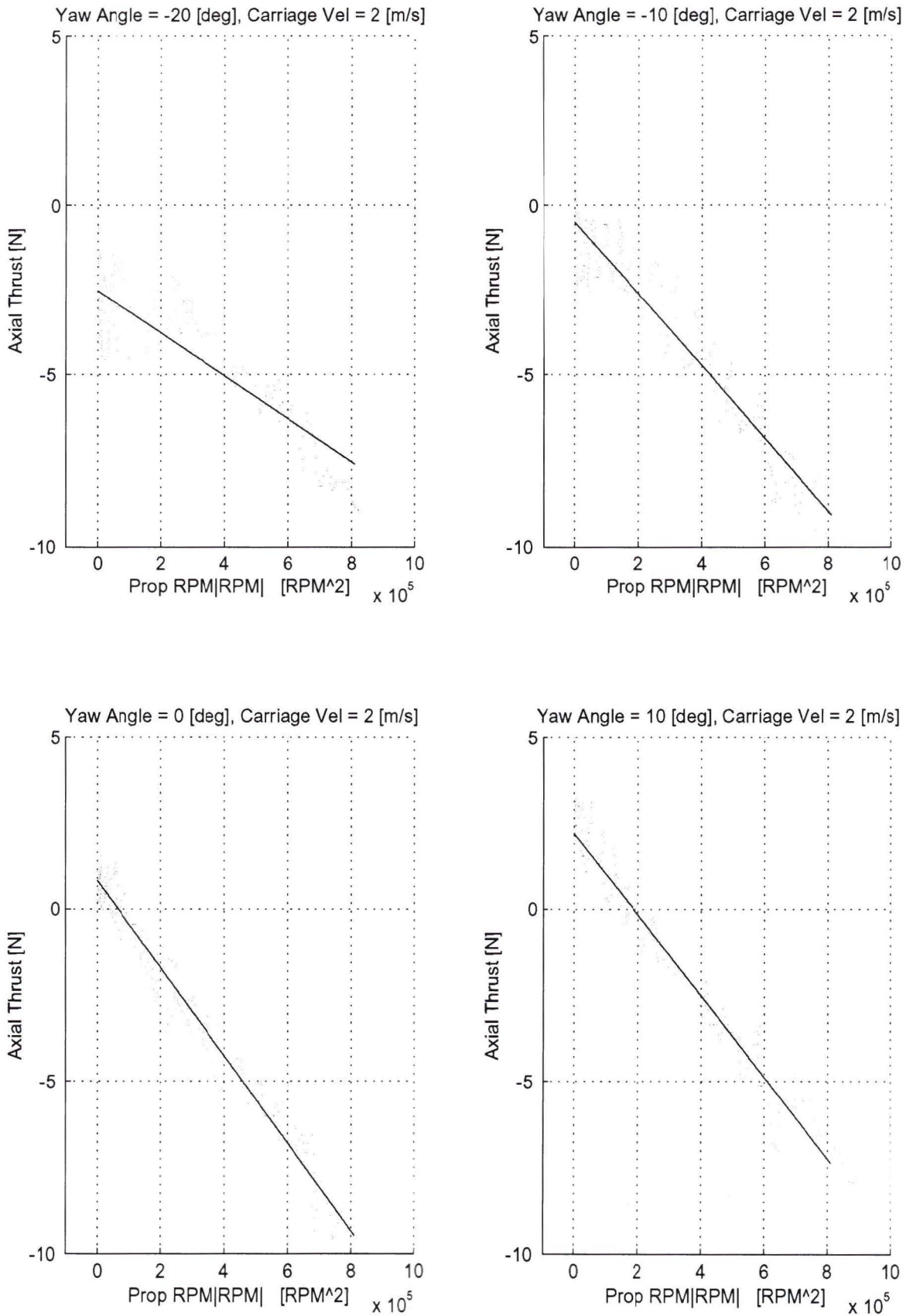


Figure A.23. Tow tank Data, Test Matrix Elements H05 to H08

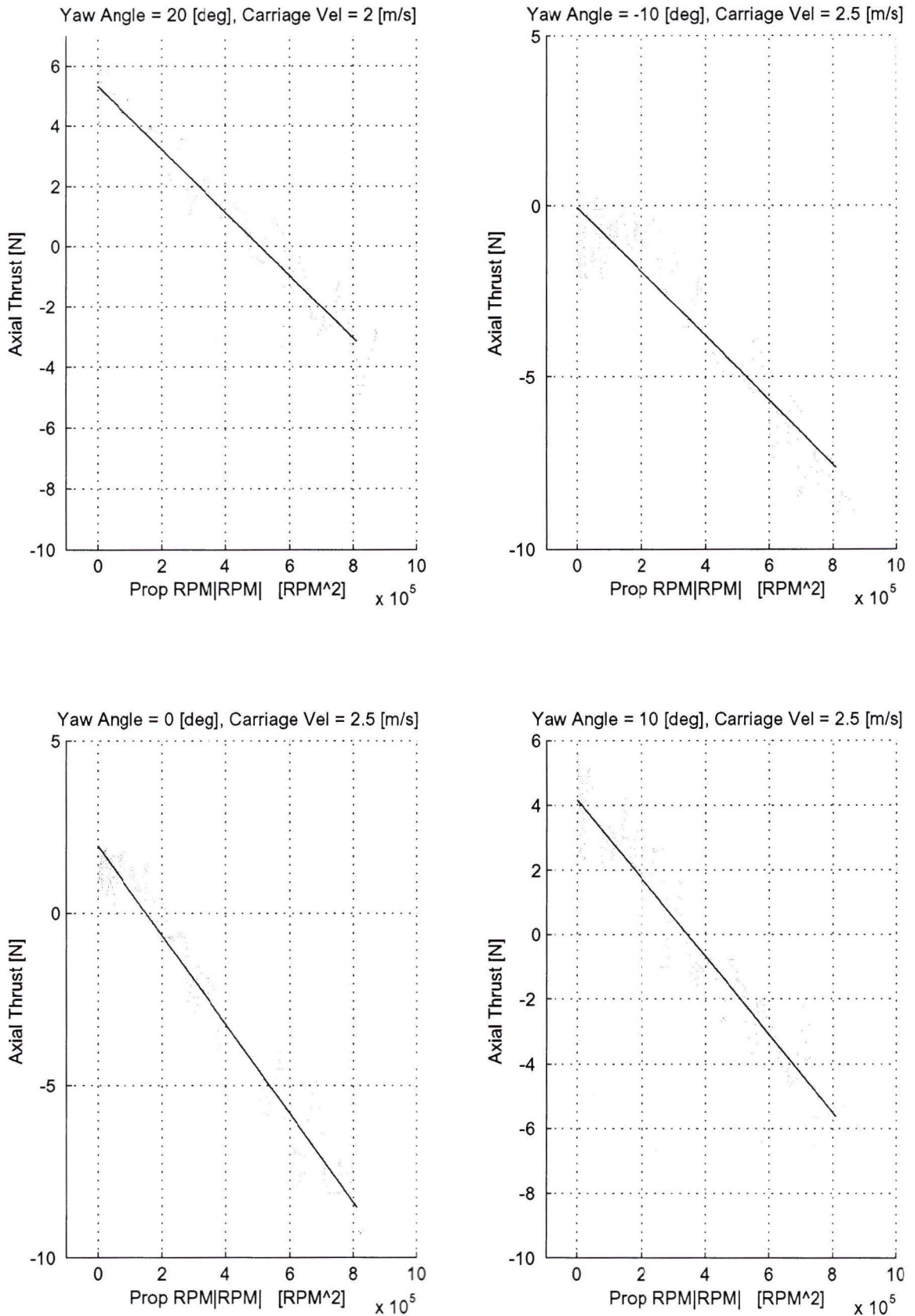


Figure A.24. Tow tank Data, Test Matrix Elements H09 to I08

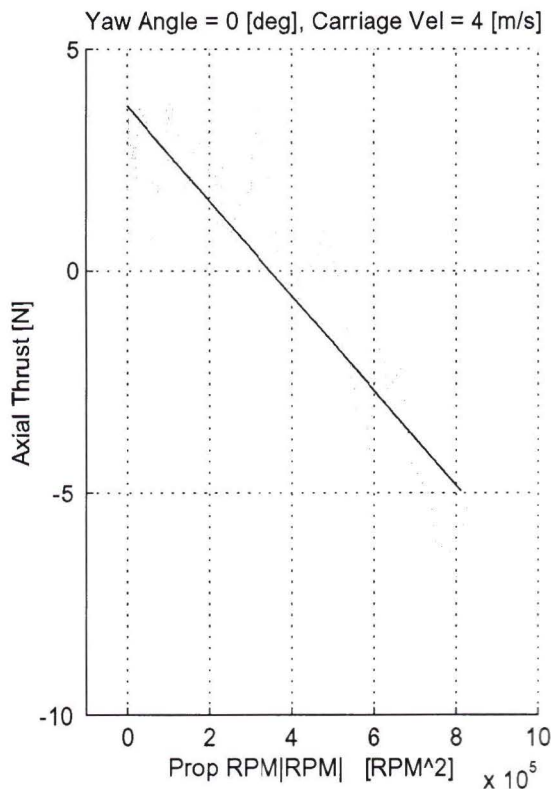
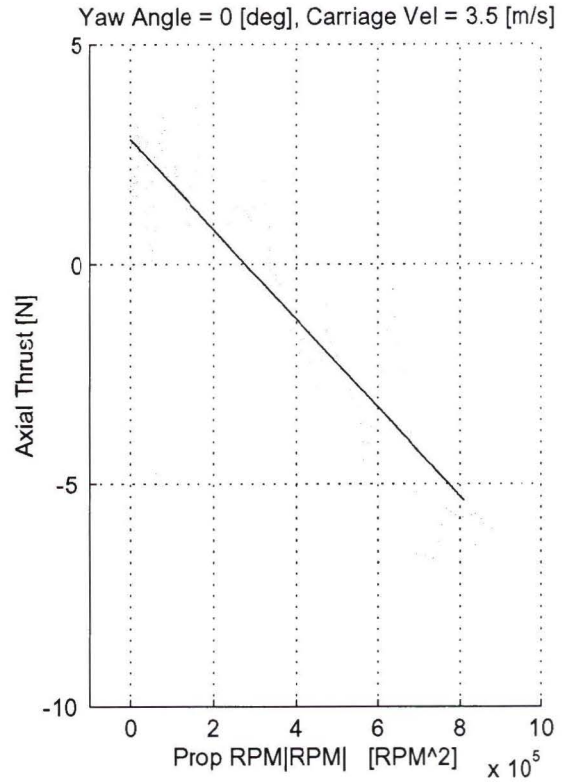
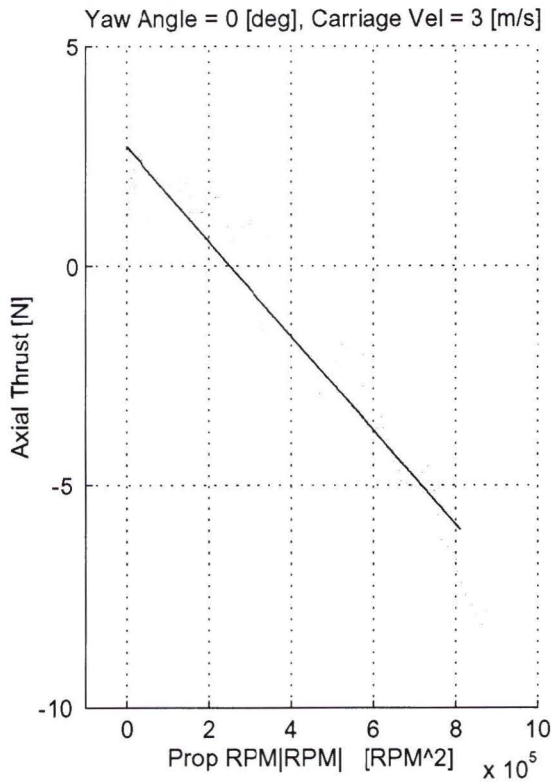


Figure A.25. Tow tank Data, Test Matrix Elements J07 to K07

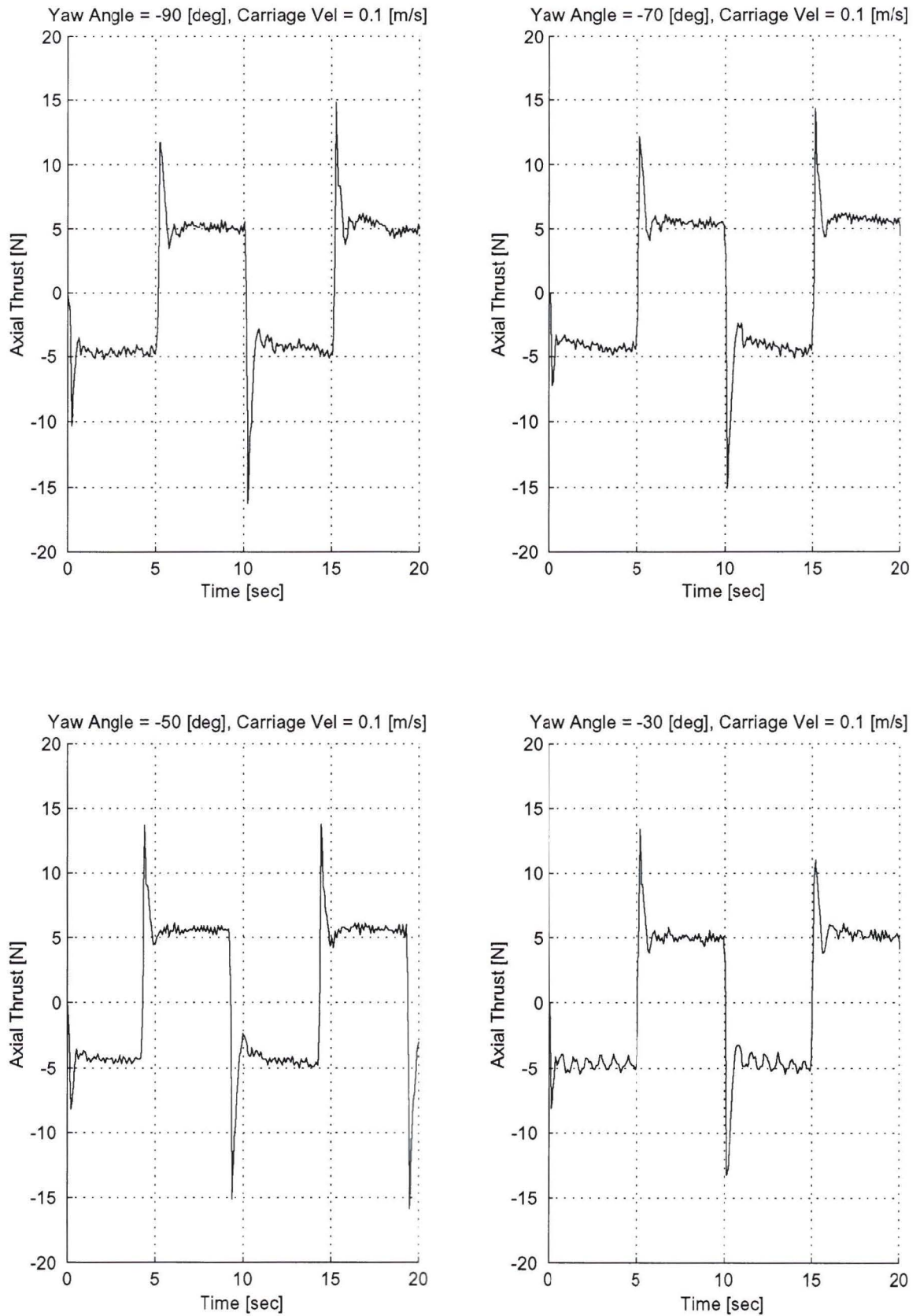


Figure A.26. Tow tank Data, Test Matrix Elements M01 to M04

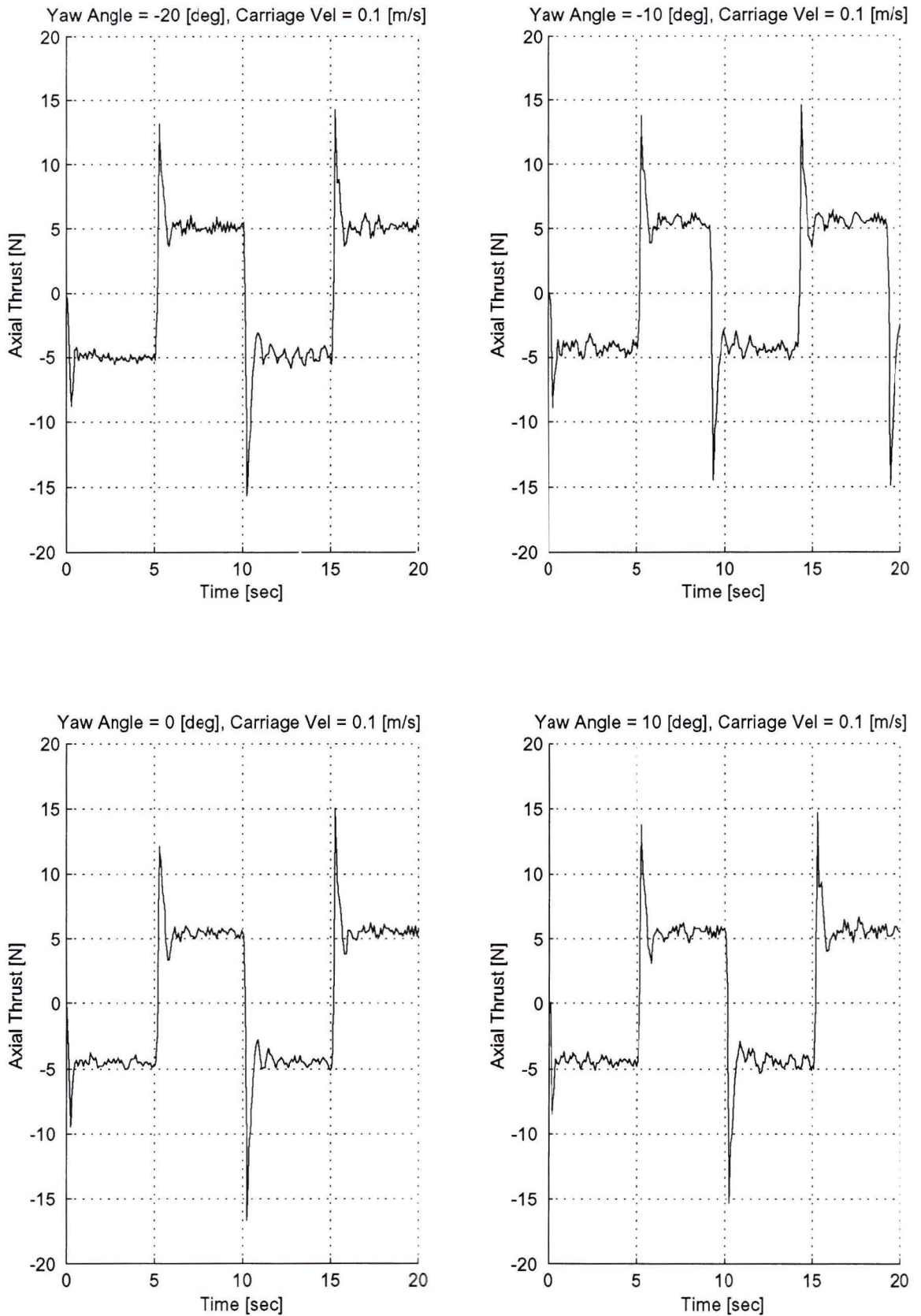


Figure A.27. Tow Tank Data, Test Matrix Elements M05 to M08

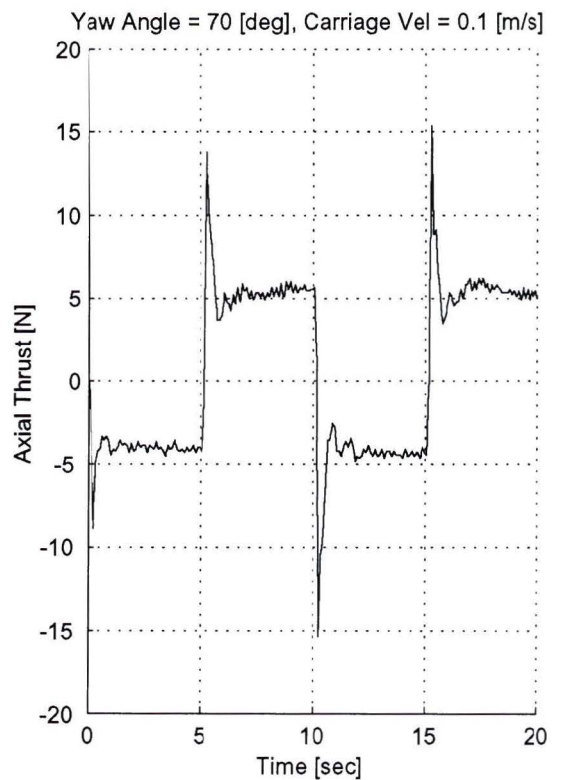
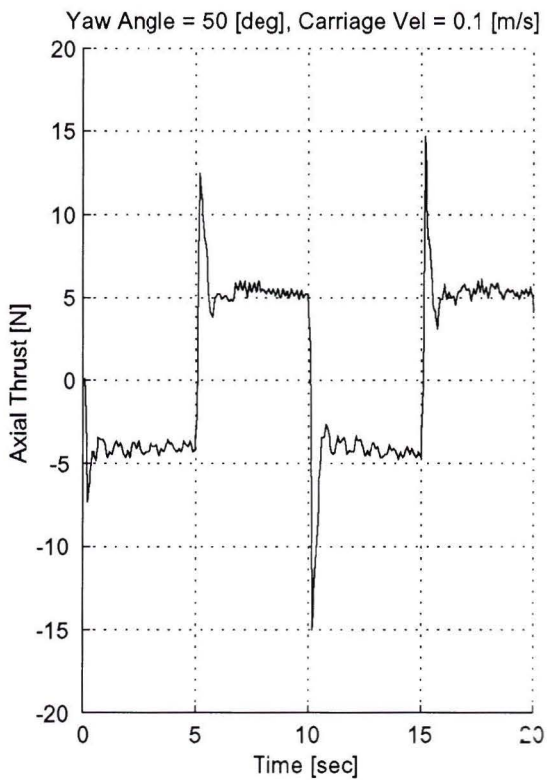
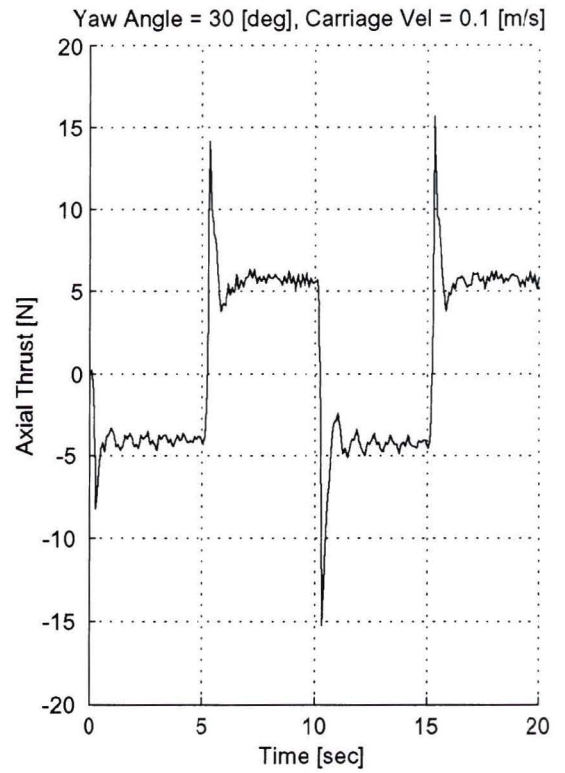
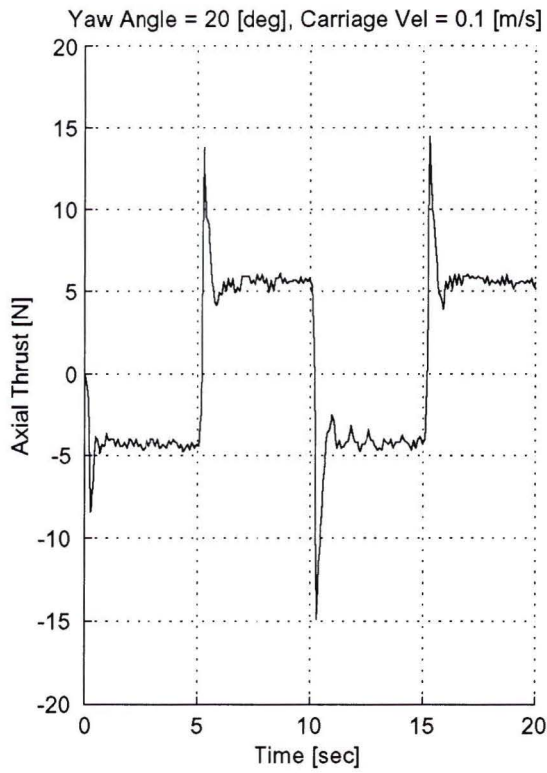


Figure A.28. Tow tank Data, Test Matrix Elements M09 to M12

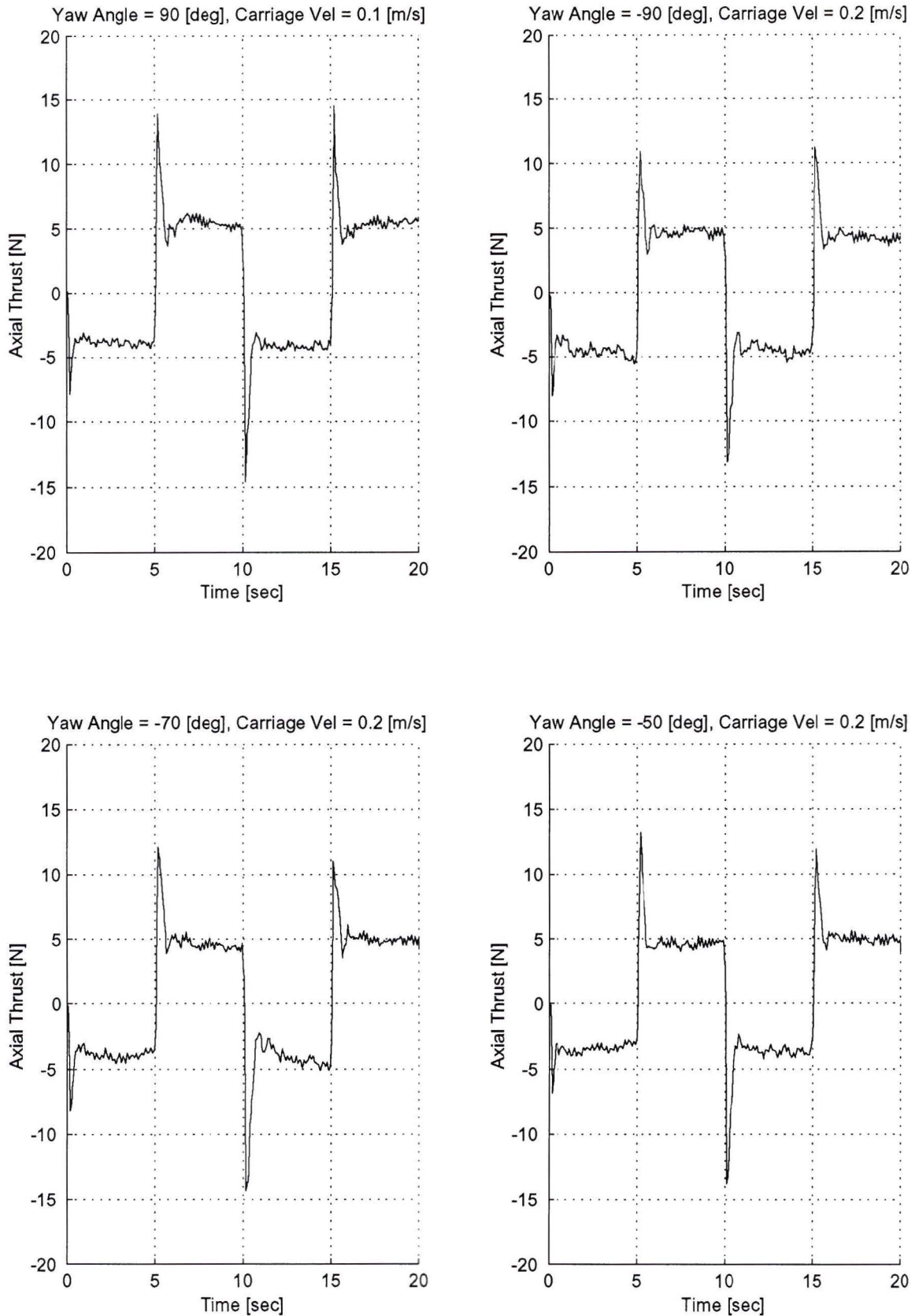


Figure A.29. Tow tank Data, Test Matrix Elements M13 to N03

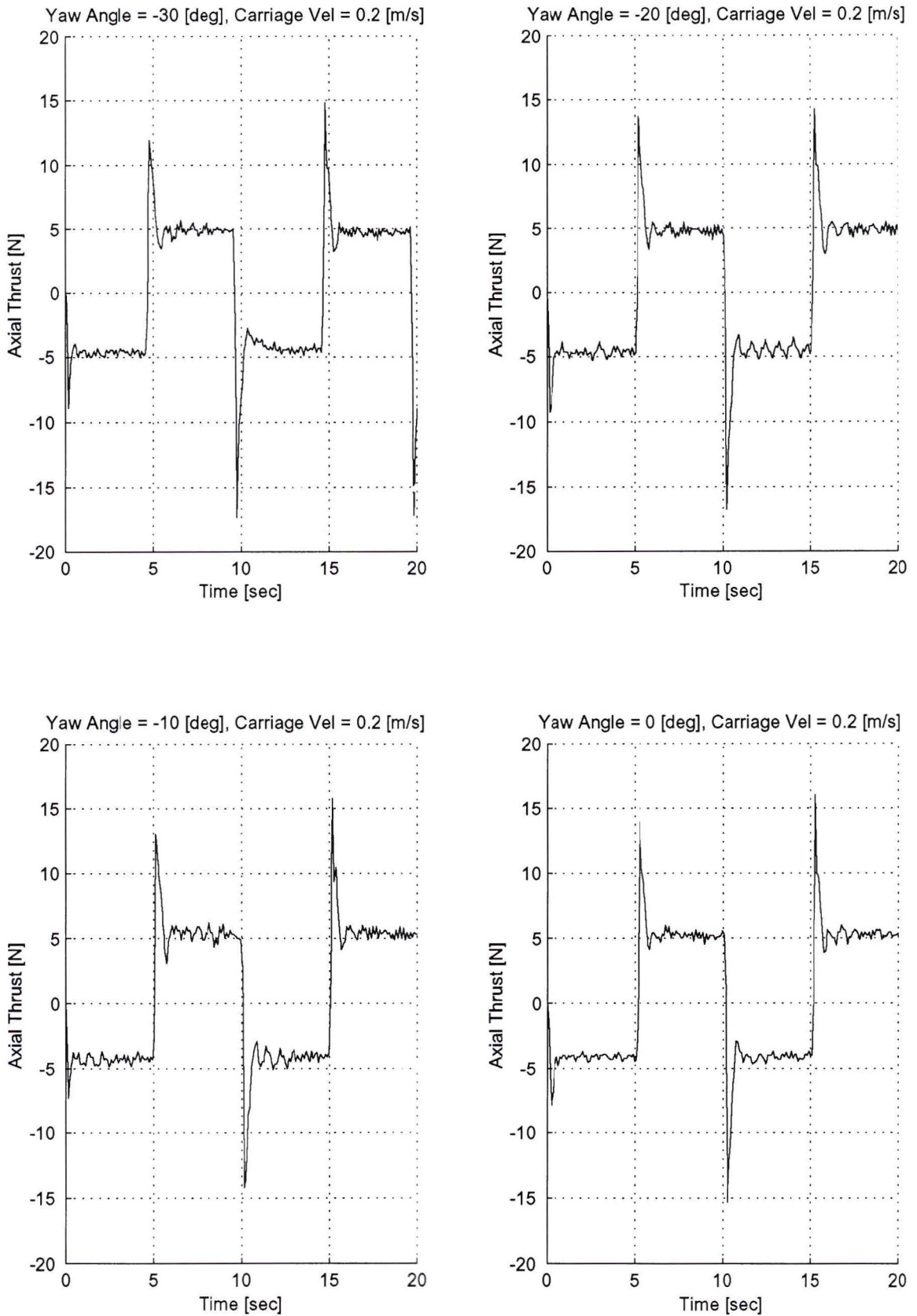


Figure A.30. Tow tank Data, Test Matrix Elements N04 to N07

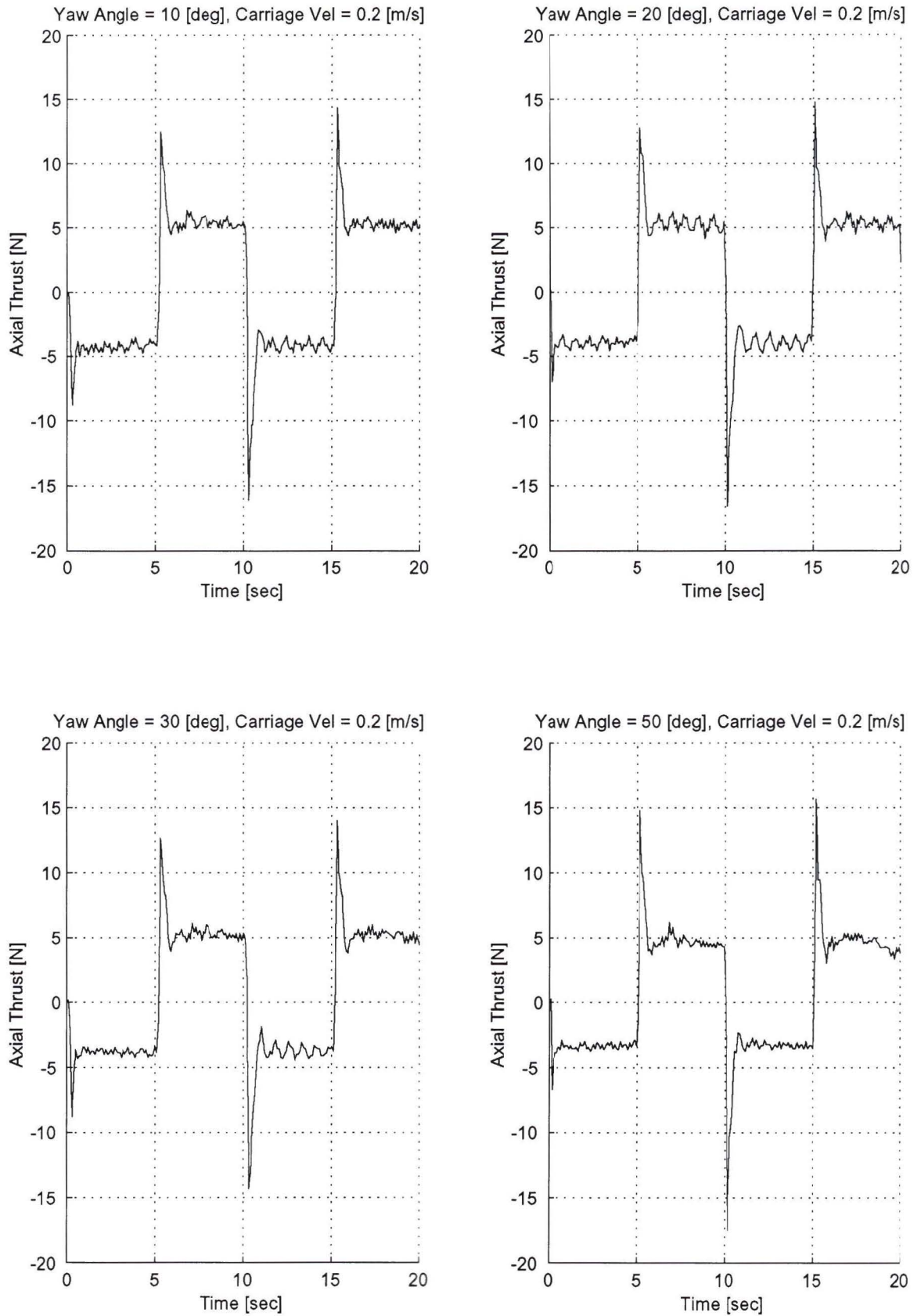


Figure A.31. Tow tank Data, Test Matrix Elements N08 to N11

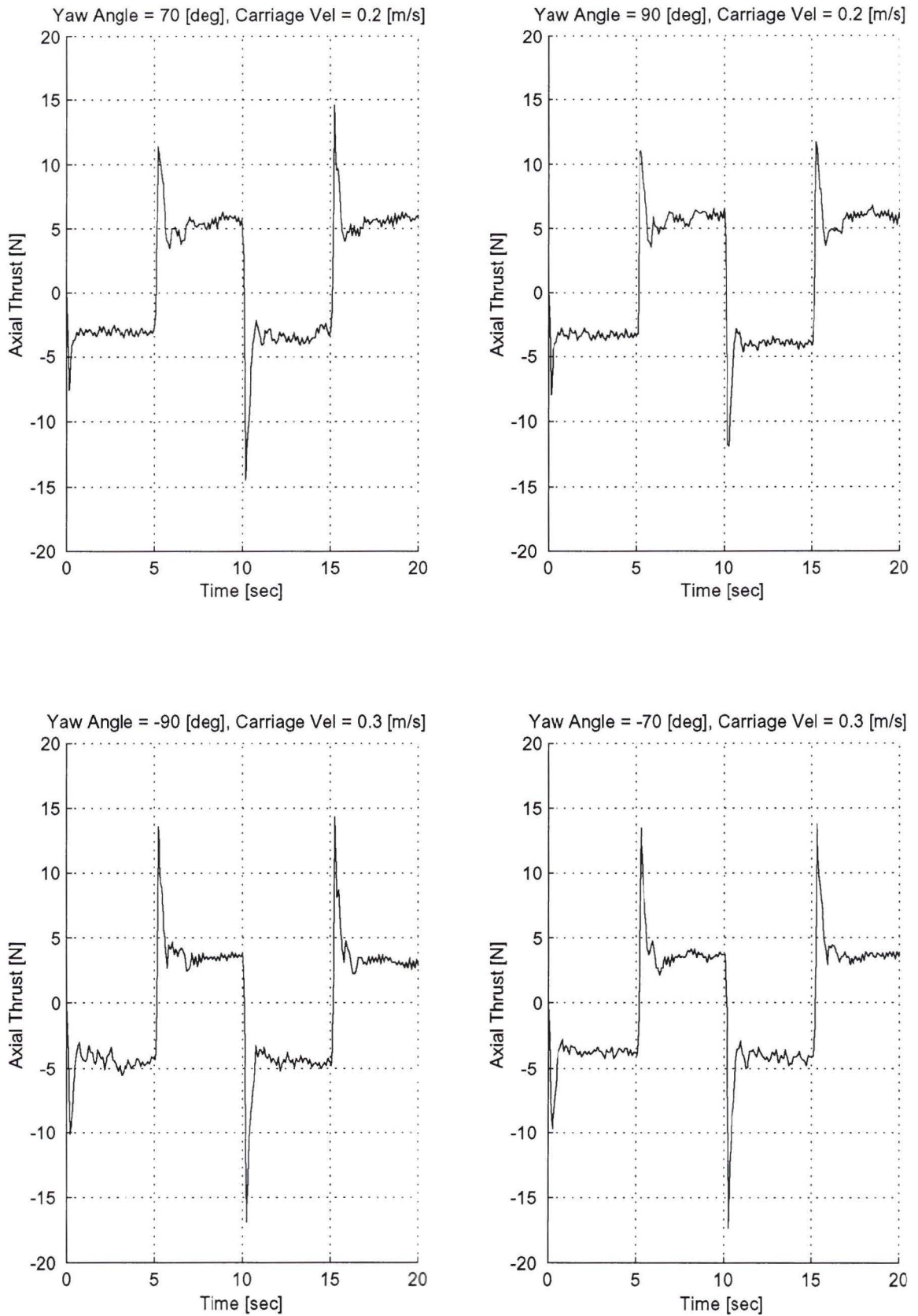


Figure A.32. Tow tank Data, Test Matrix Elements N12 to O02

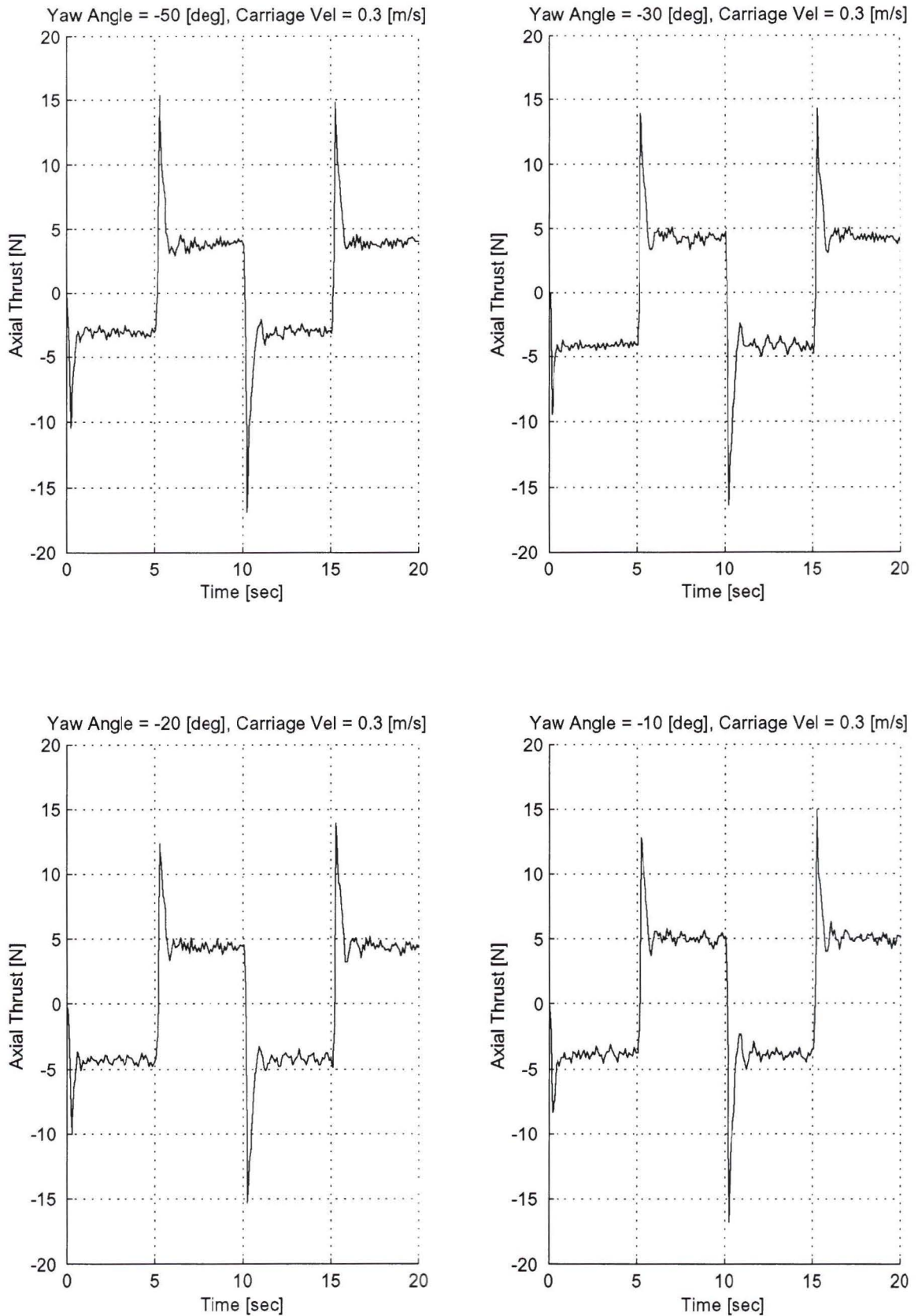


Figure A.33. Tow tank Data, Test Matrix Elements O03 to O06

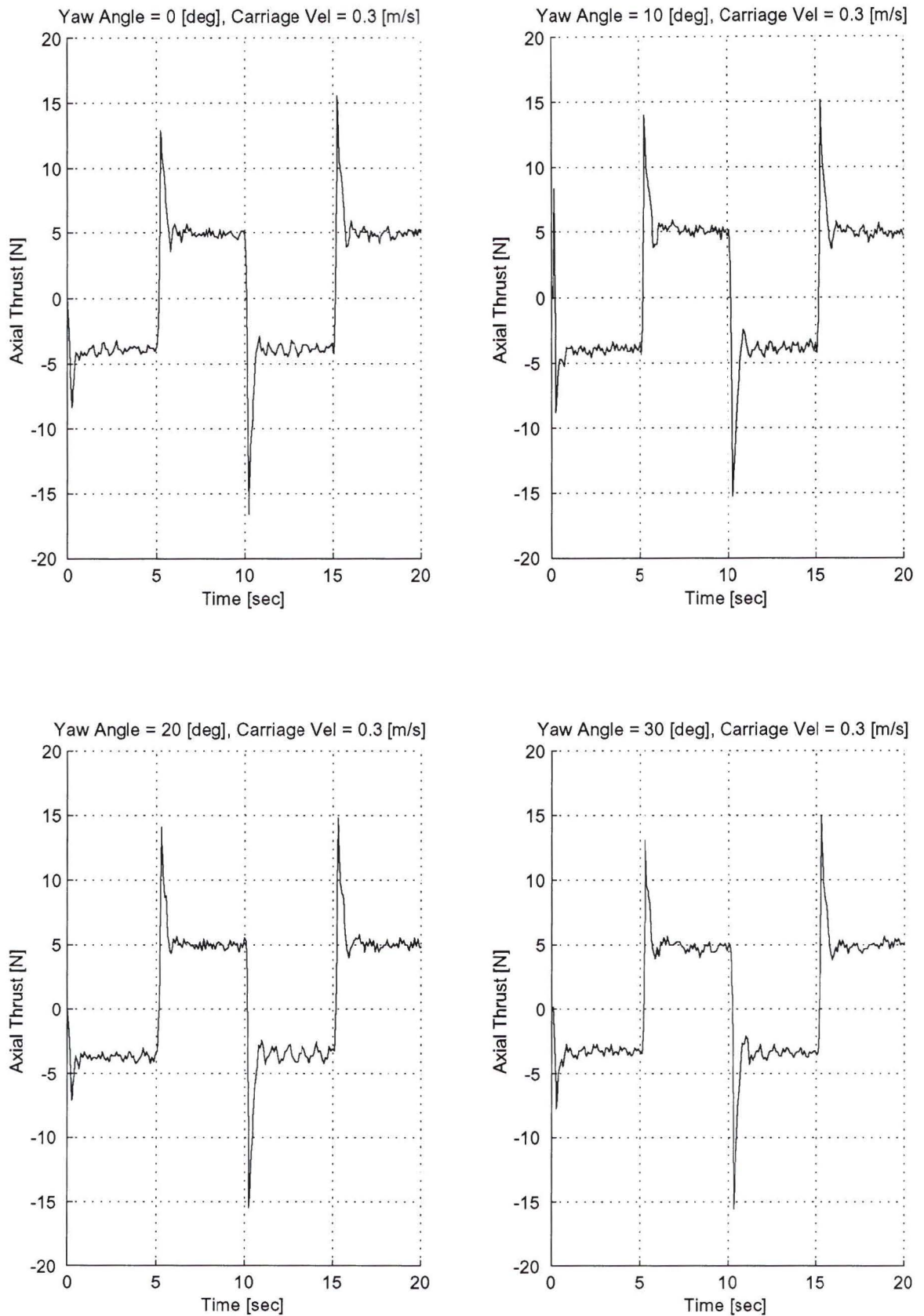


Figure A.34. Tow tank Data, Test Matrix Elements O07 to O10

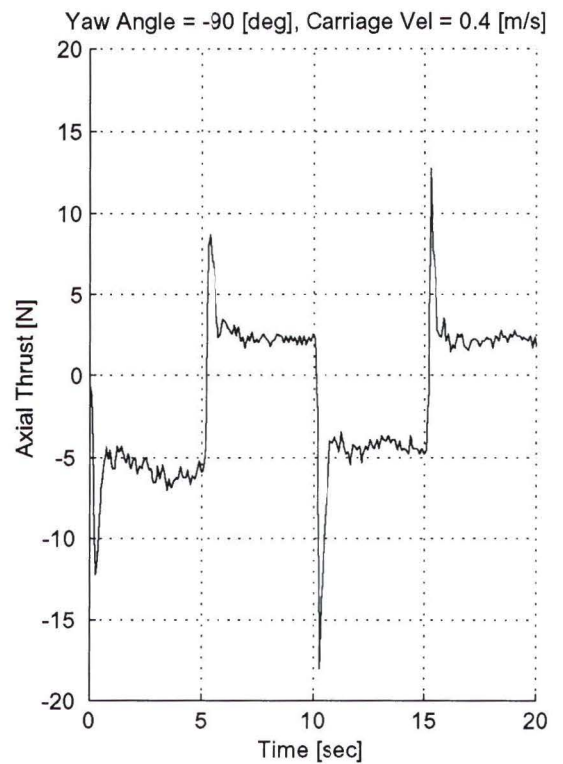
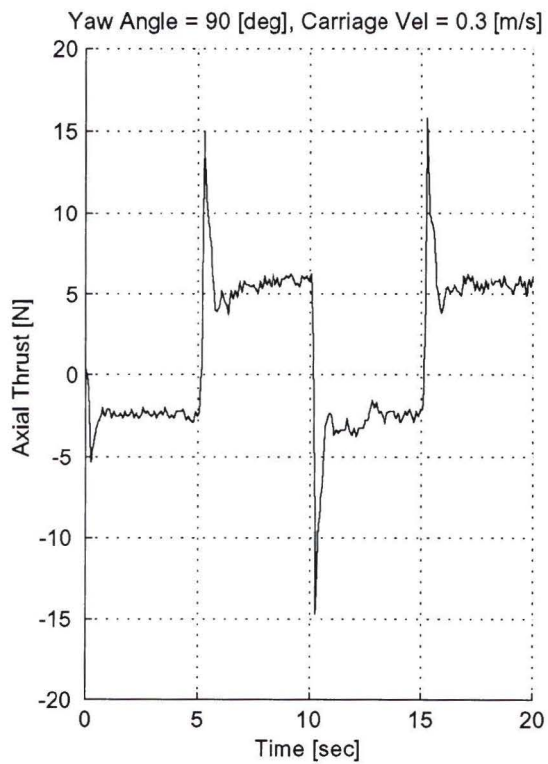
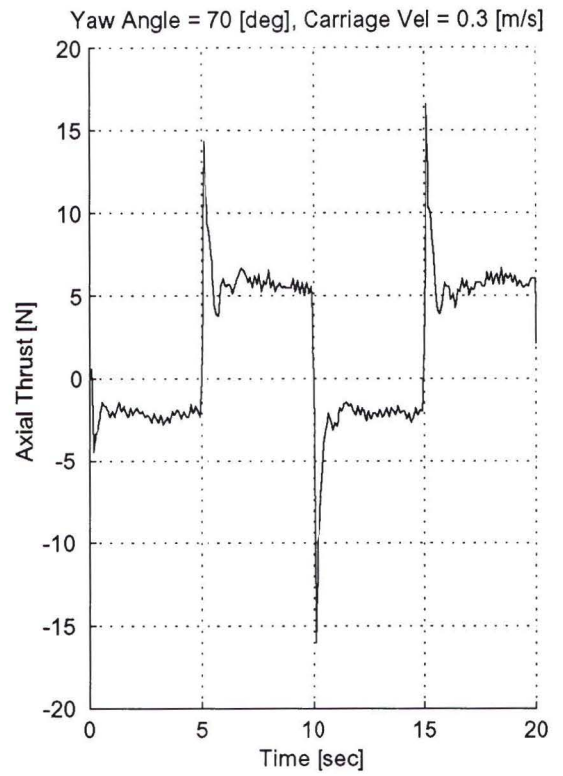
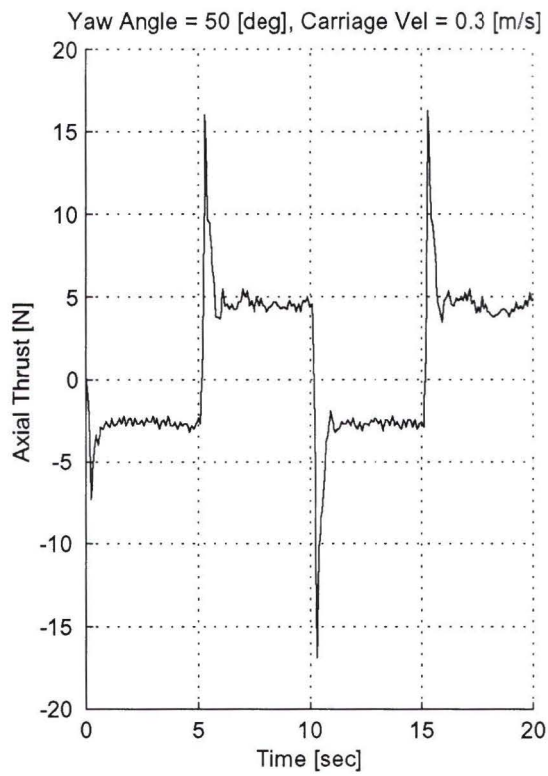


Figure A.35. Tow tank Data, Test Matrix Elements O11 to P01

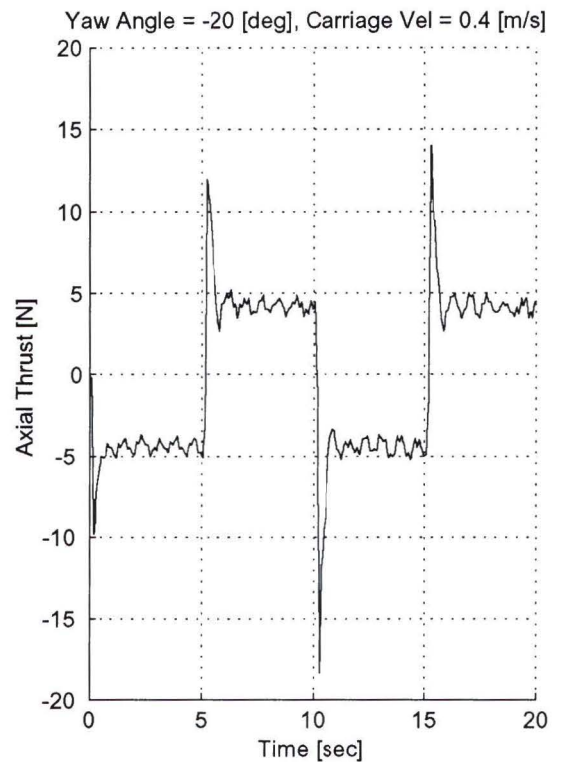
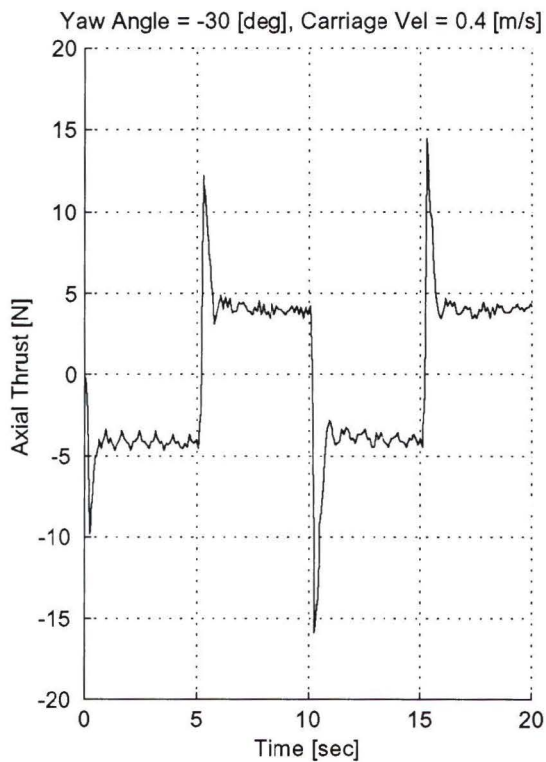
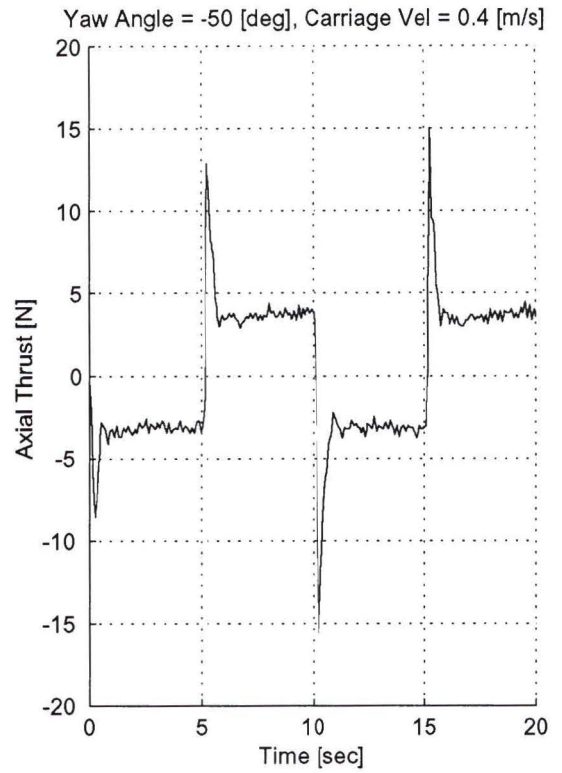
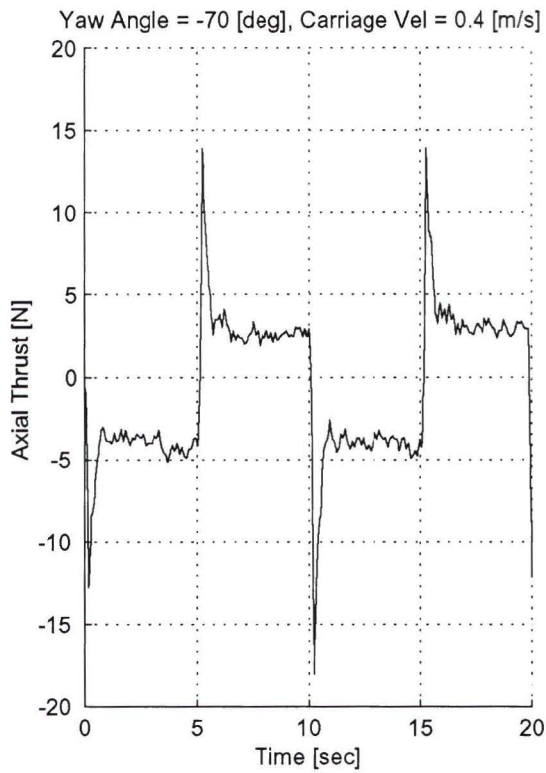


Figure A.36. Tow tank Data, Test Matrix Elements P02 to P05

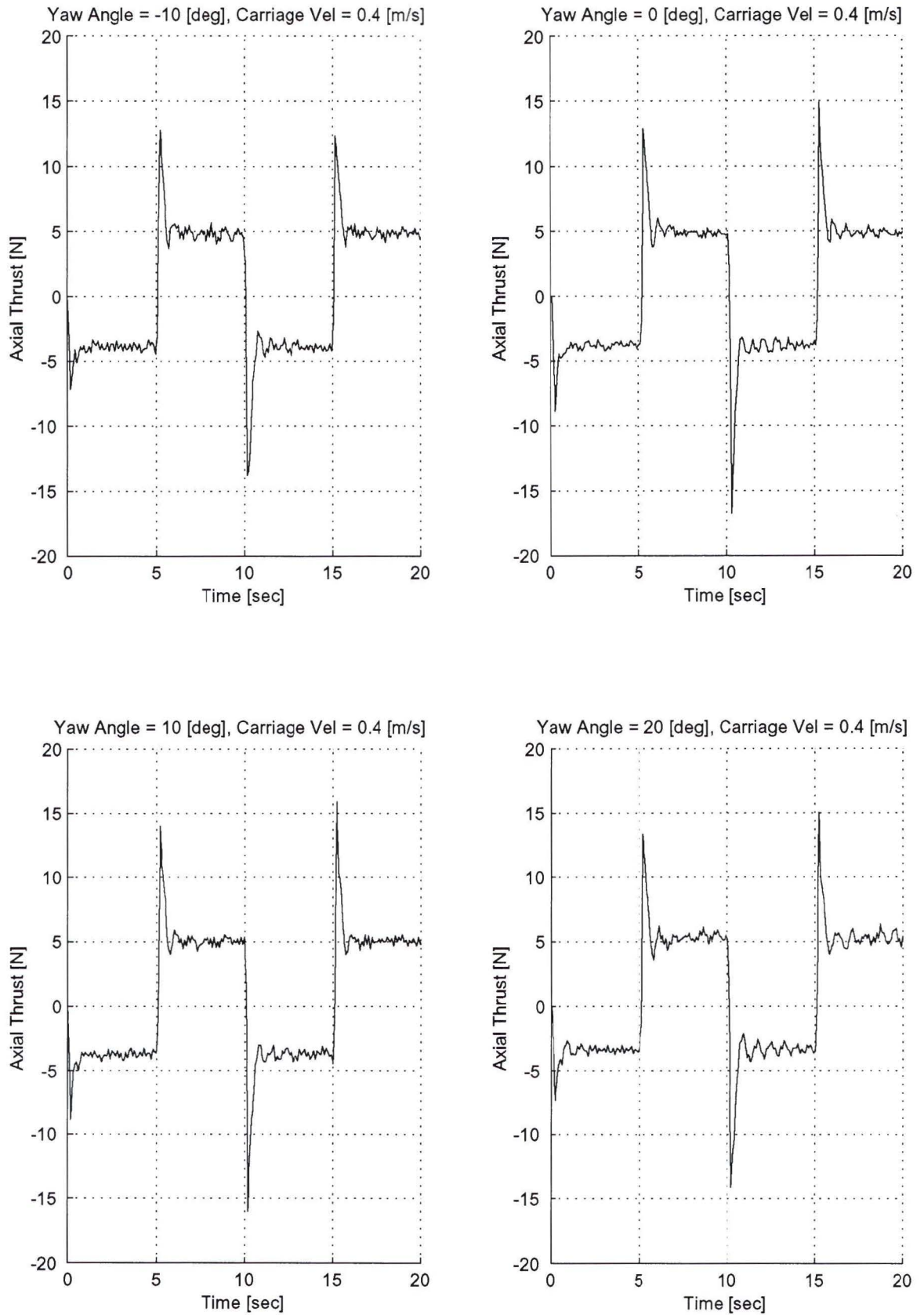


Figure A.37. Tow tank Data, Test Matrix Elements P06 to P09

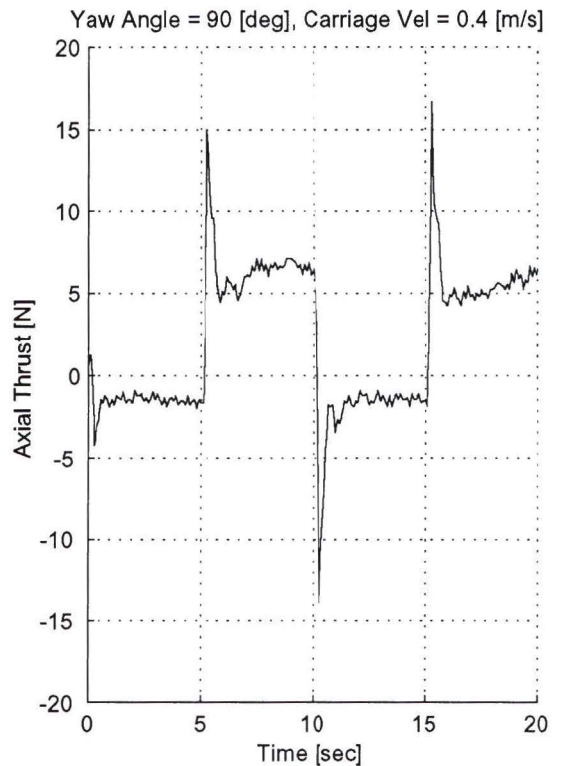
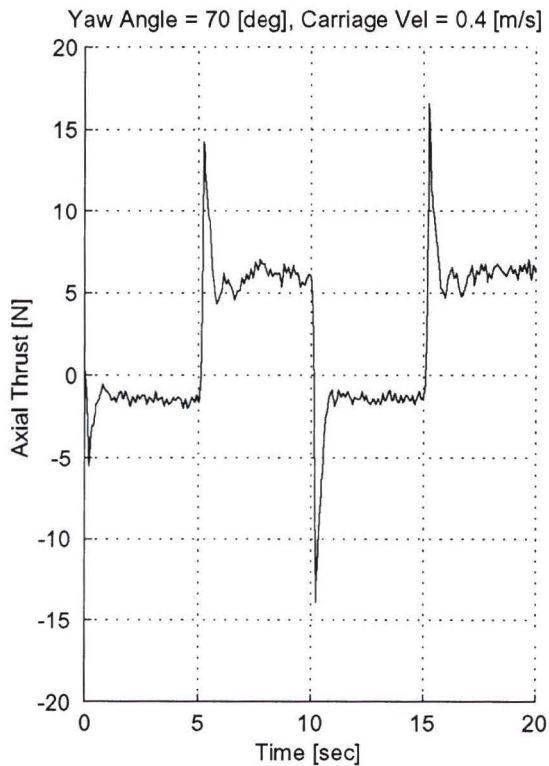
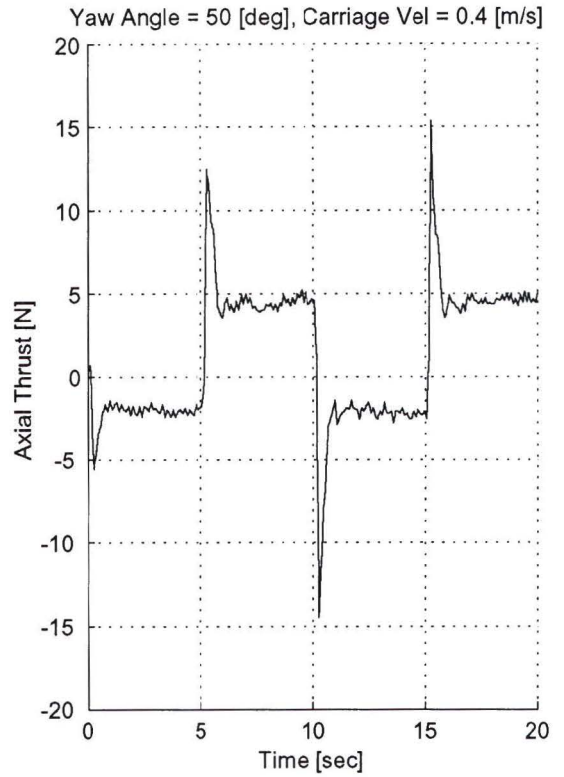
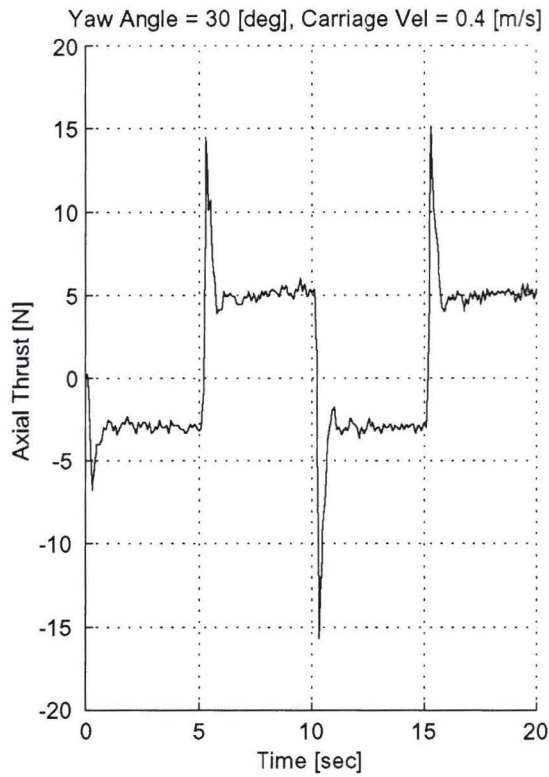


Figure A.38. Tow tank Data, Test Matrix Elements P10 to P13

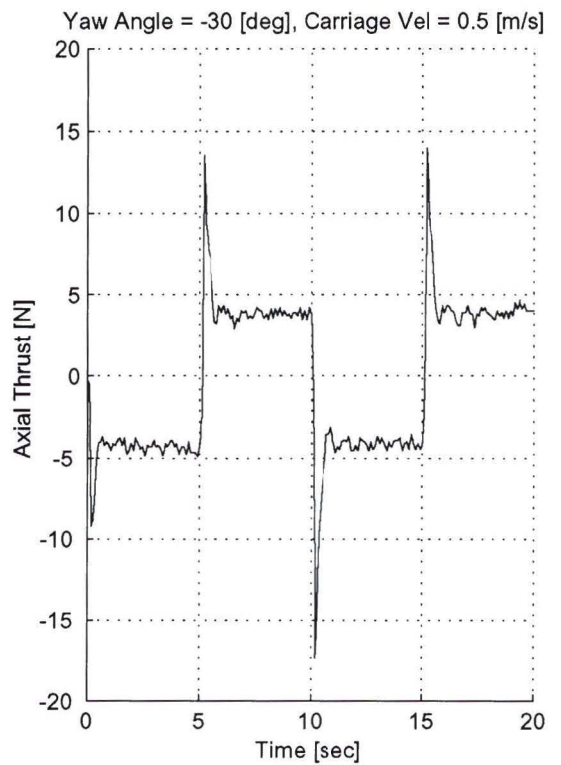
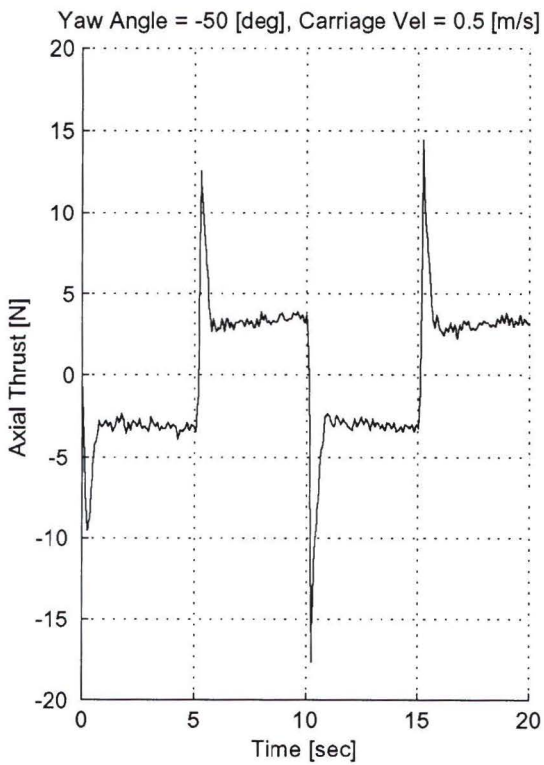
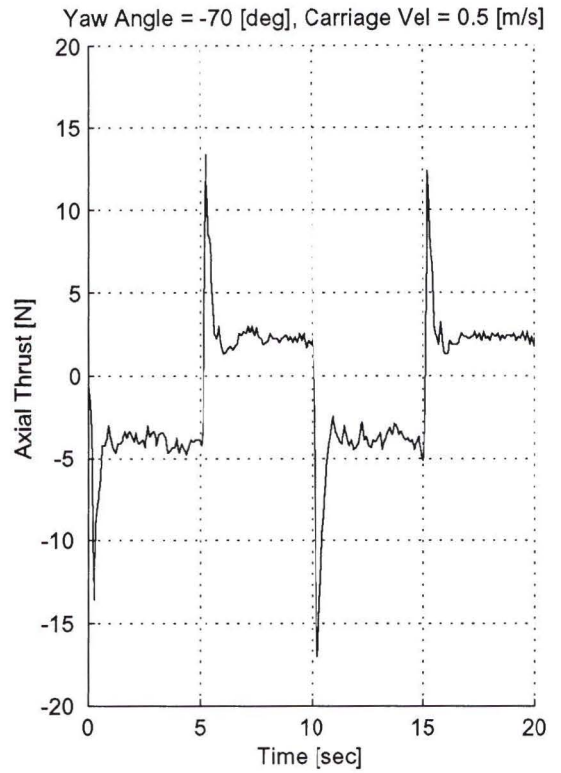
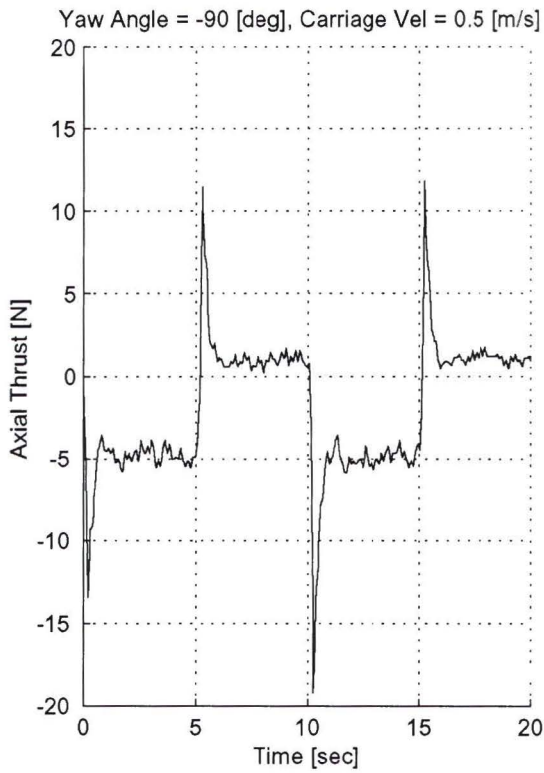


Figure A.39. Tow tank Data, Test Matrix Elements Q01 to Q04

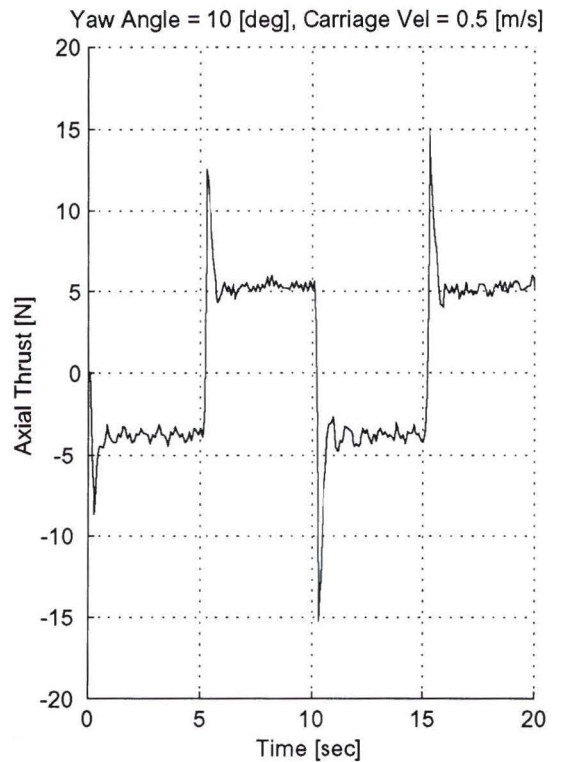
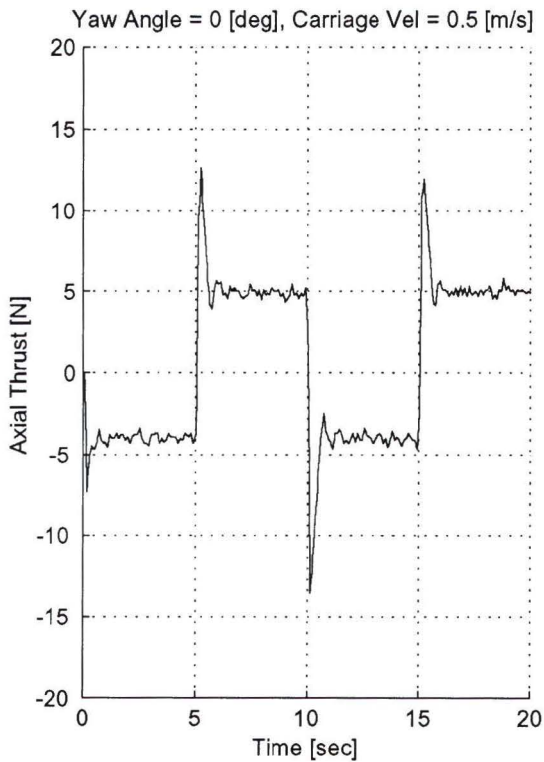
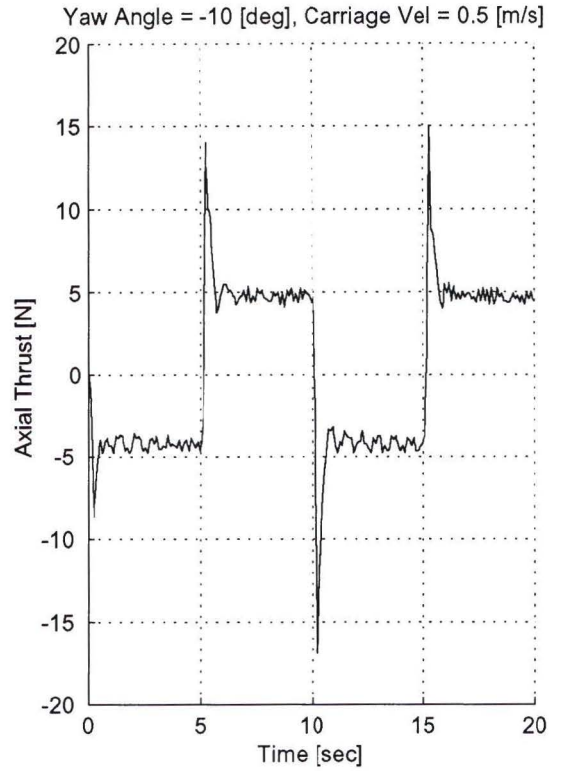
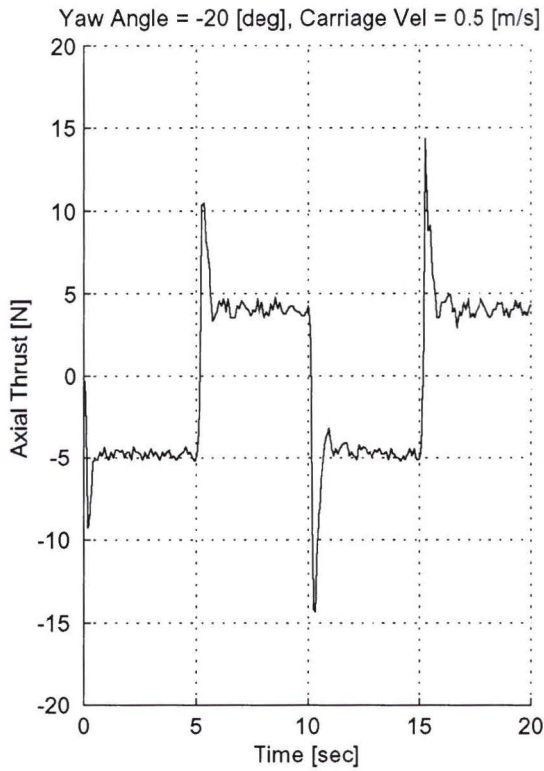


Figure A.40. Tow tank Data, Test Matrix Elements Q05 to Q08

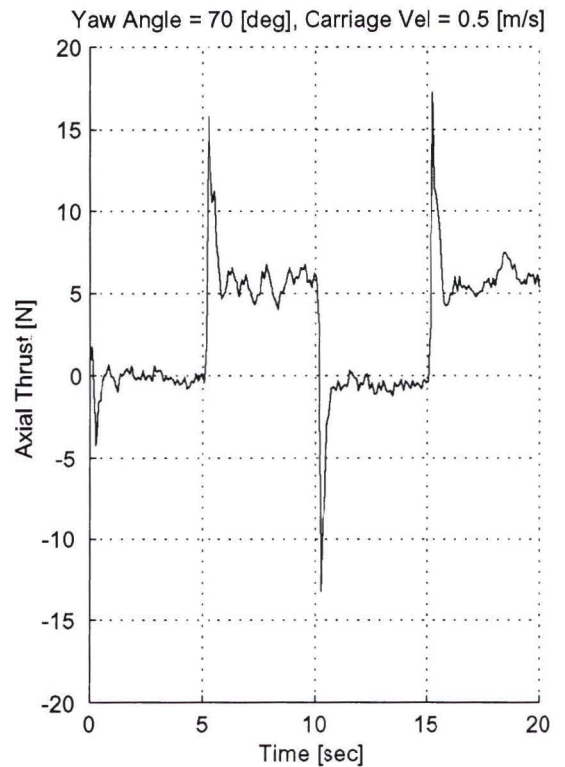
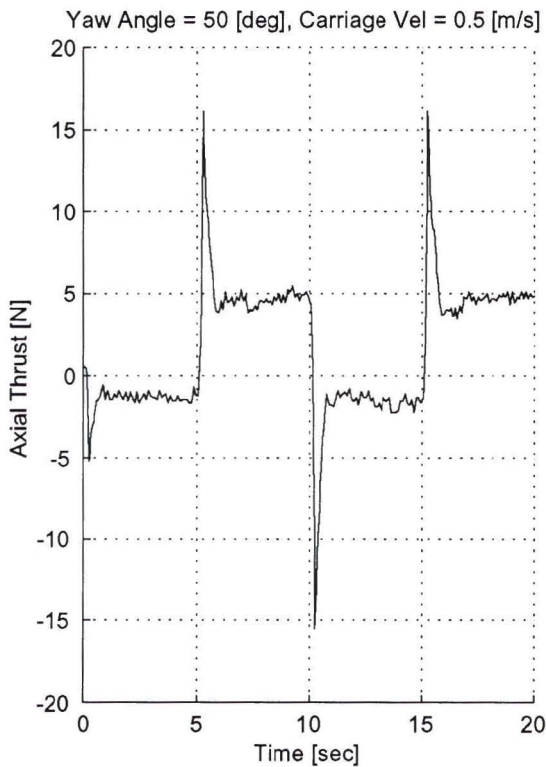
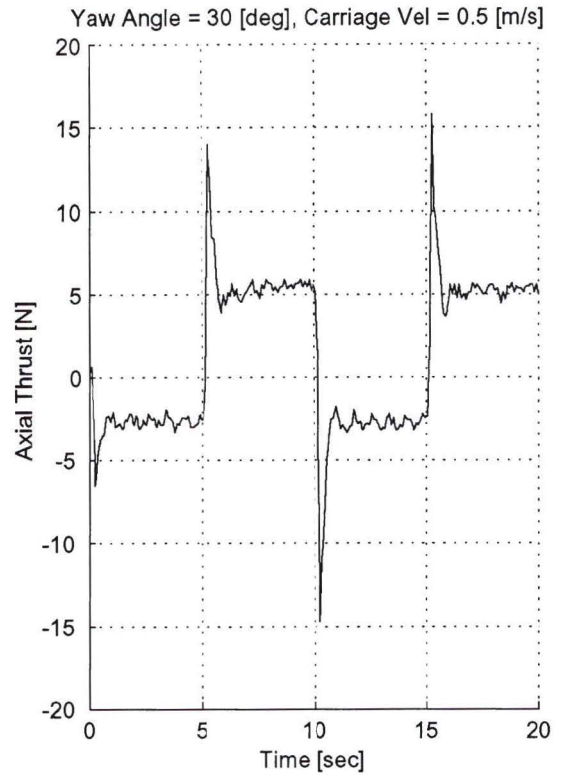
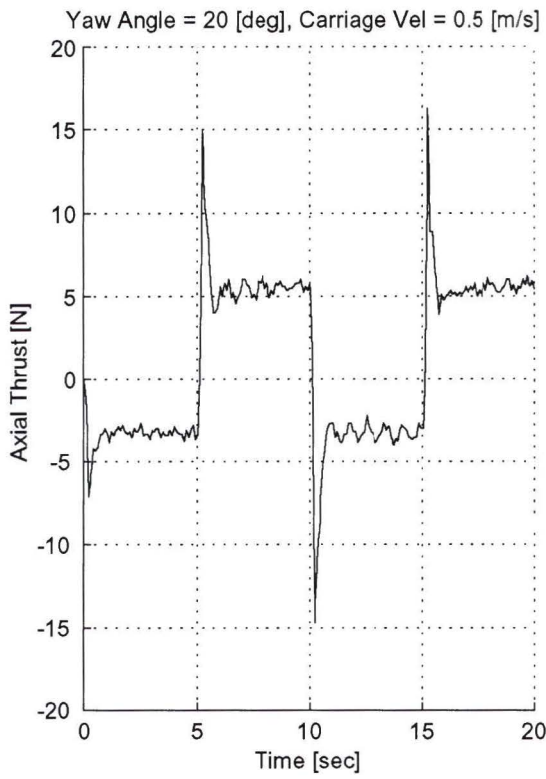


Figure A.41. Tow tank Data, Test Matrix Elements Q09 to Q12

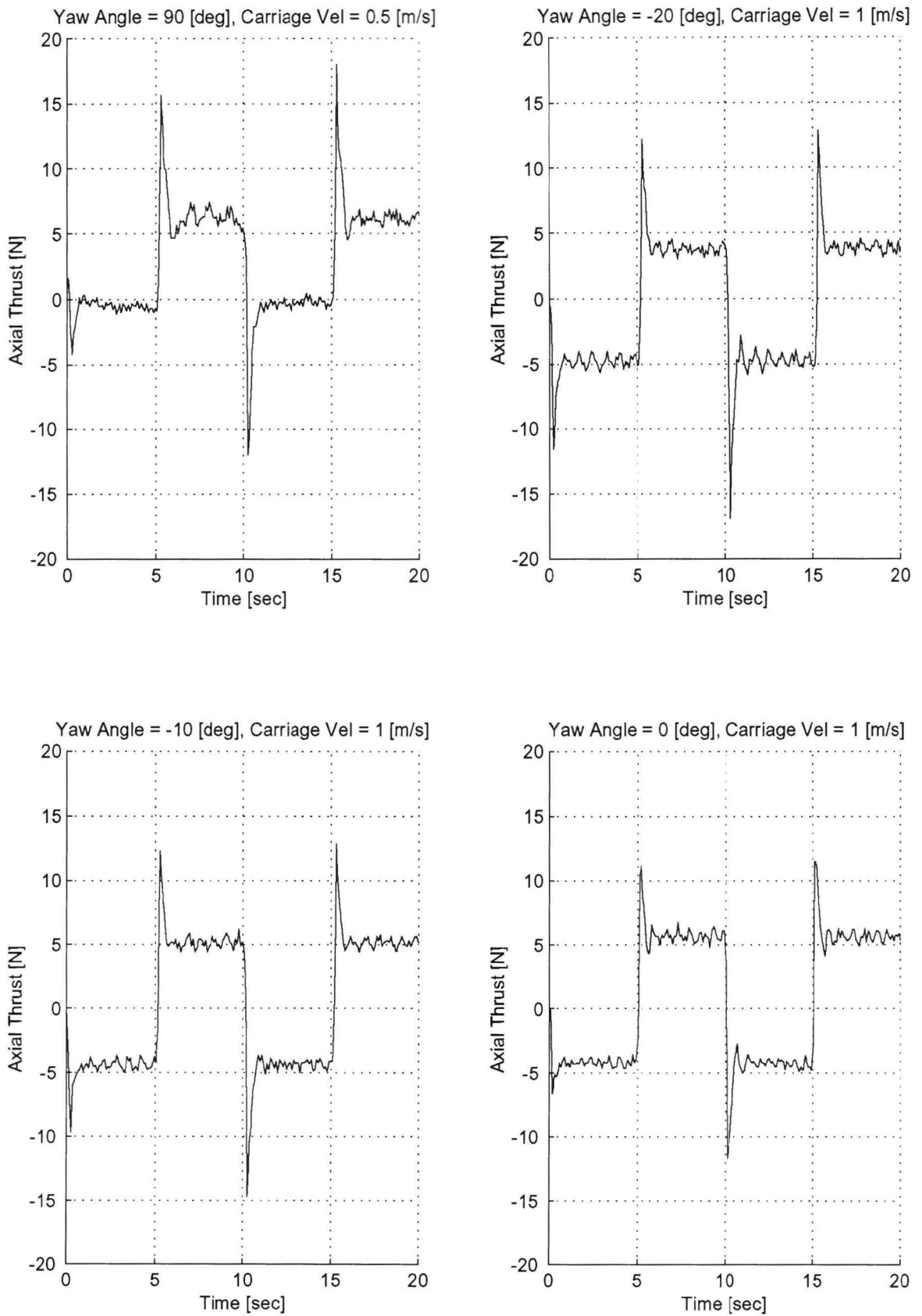


Figure A.42. Tow tank Data, Test Matrix Elements Q13 to R07

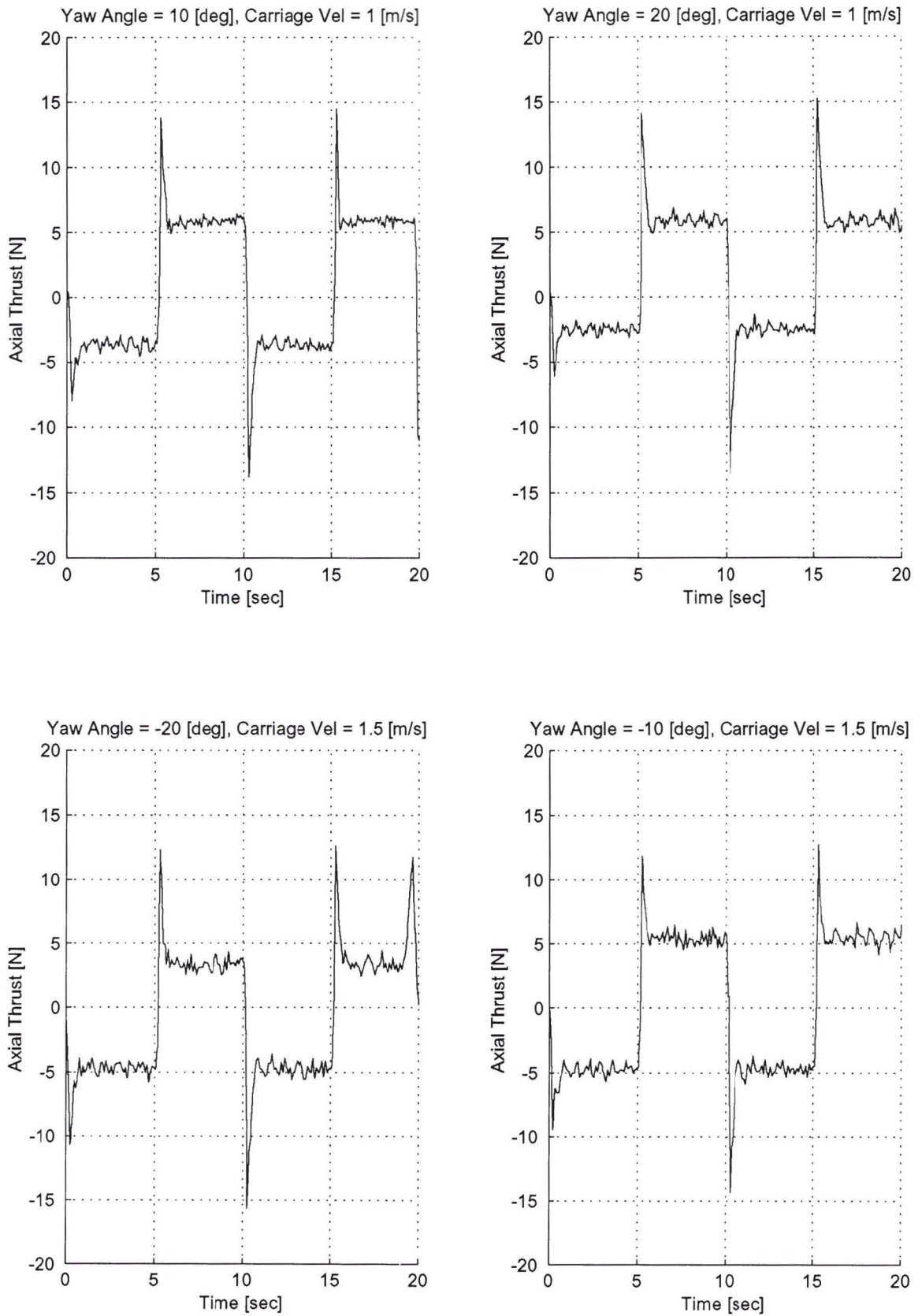


Figure A.43. Tow tank Data, Test Matrix Elements R08 to S06

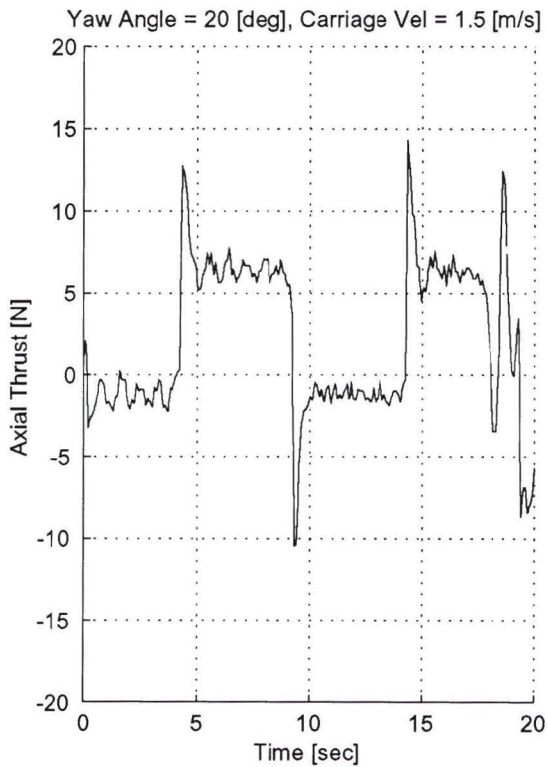
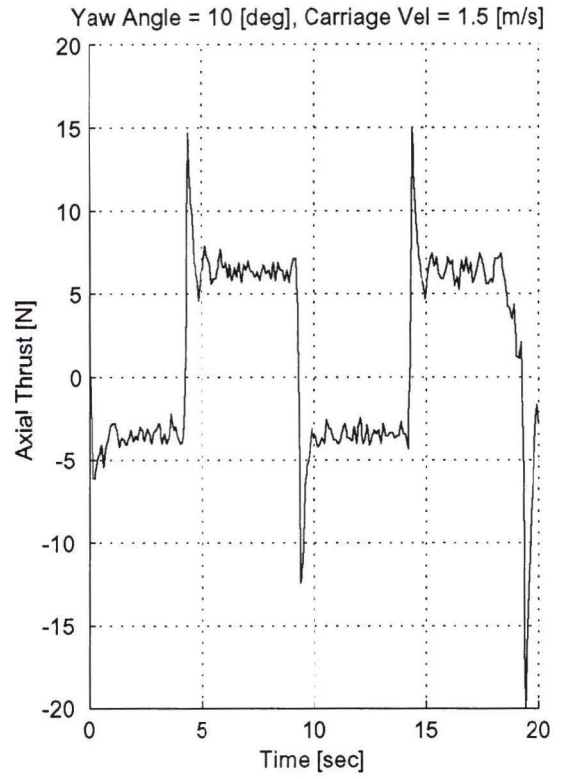
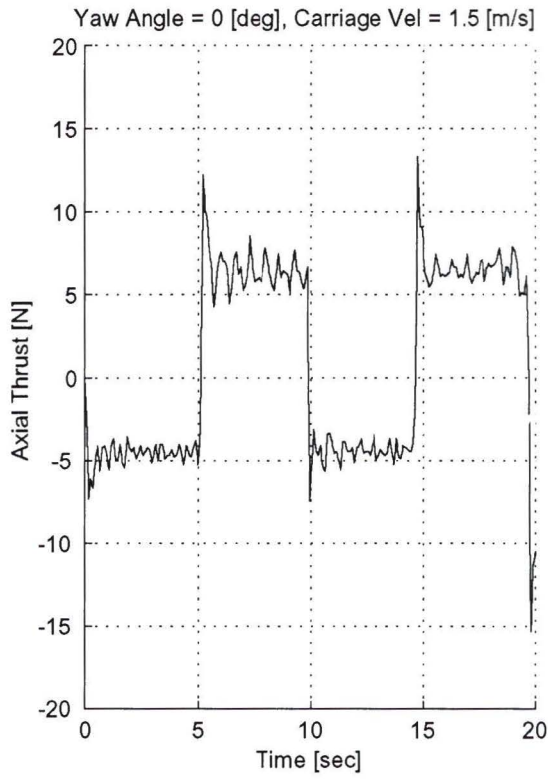


Figure A.44. Tow tank Data, Test Matrix Elements S07 to S09

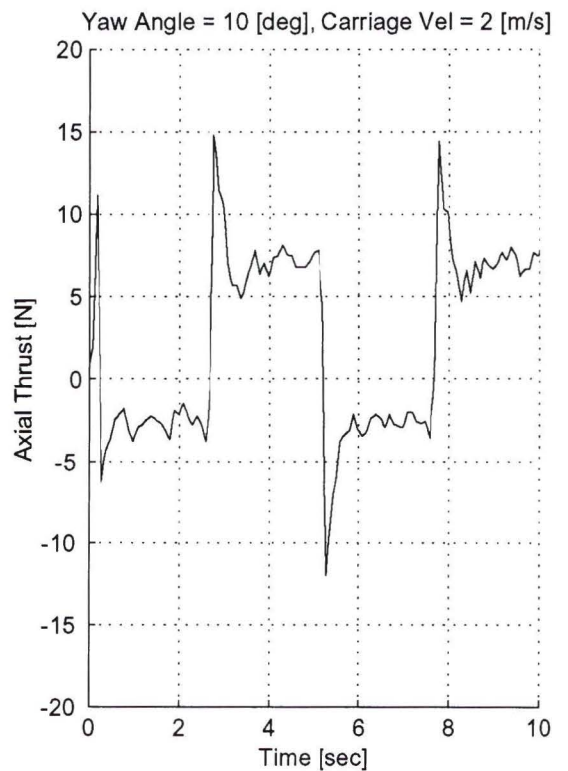
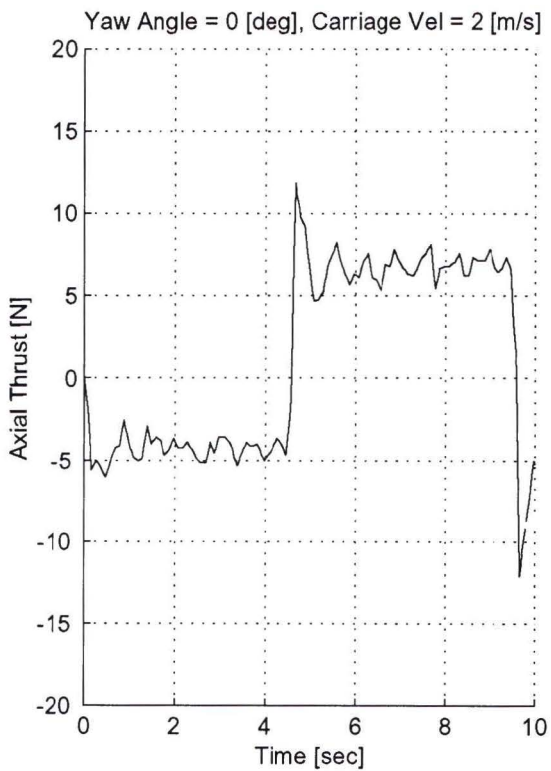
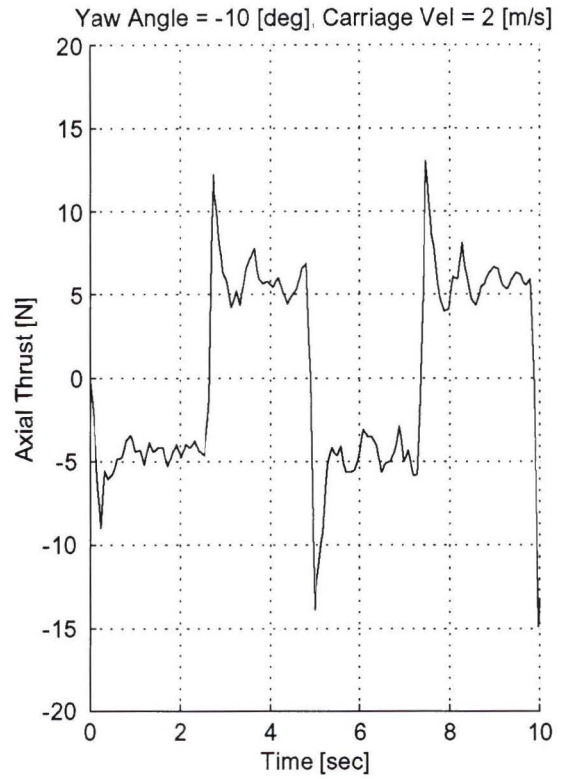
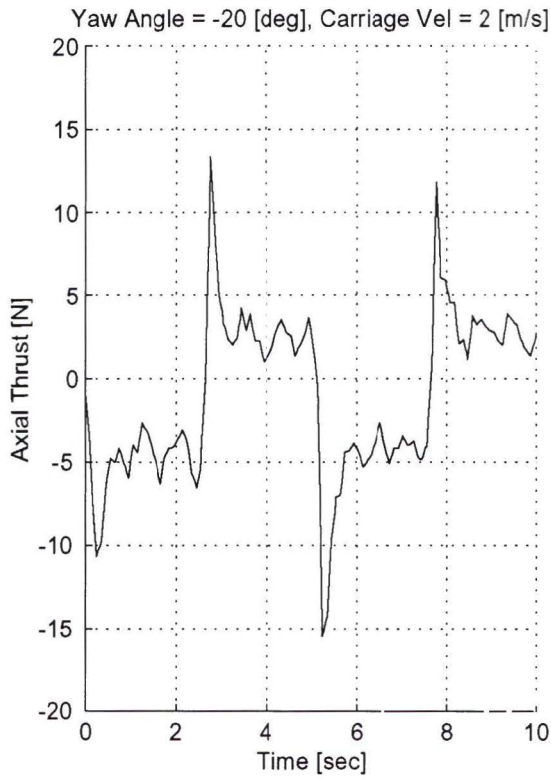


Figure A.45. Tow tank Data, Test Matrix Elements T05 to T08

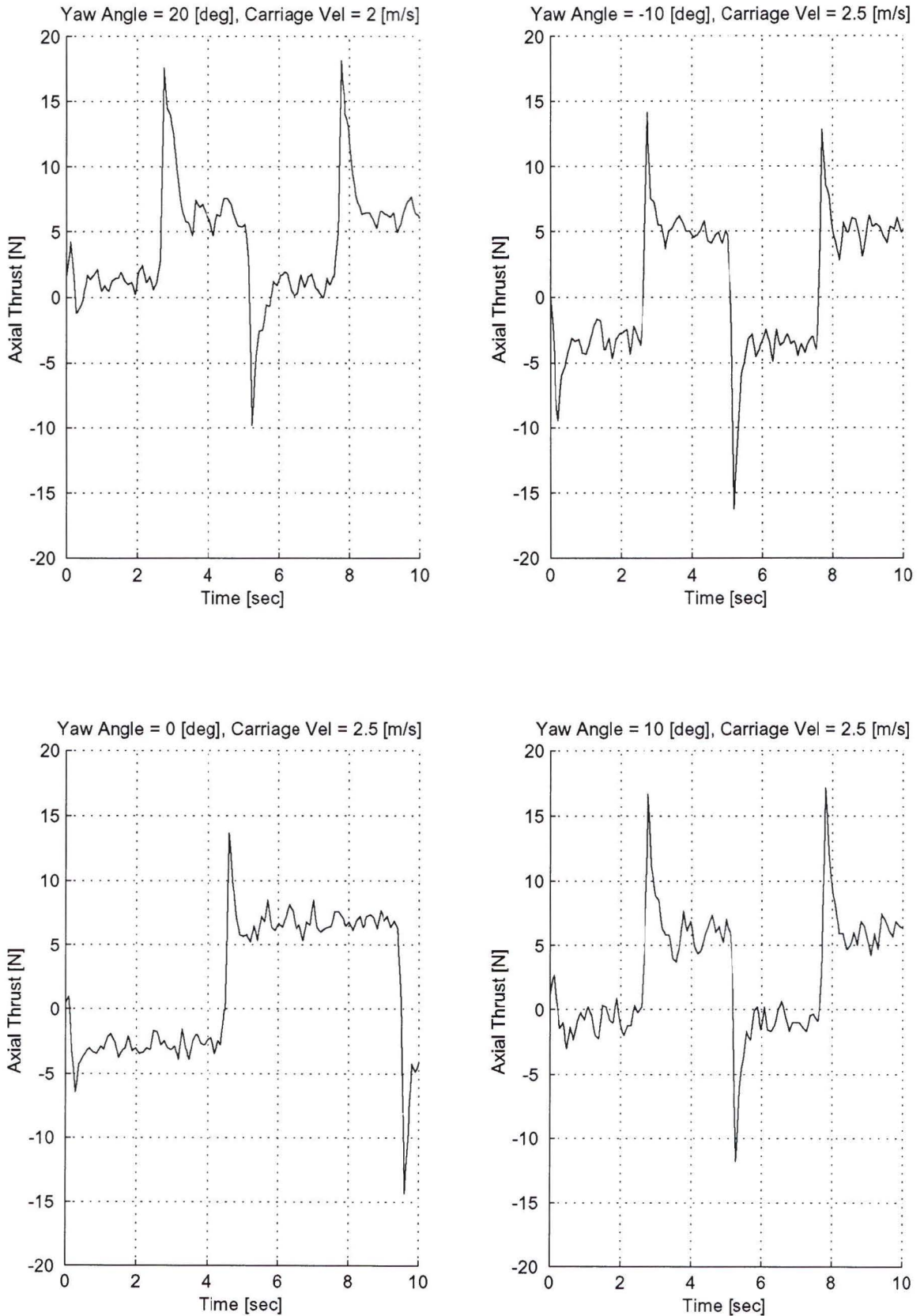


Figure A.46. Tow tank Data, Test Matrix Elements T09 to U08

Appendix B

LabVIEW

B.1 LabVIEW Program

Because the majority of the LabVIEW experimental test program is specific to the test setup used for the work in this thesis, only a brief description is given here. Figures B.1 and B.2 contain the main program 'VI'. Figure B.1 shows the left hand side of the main program. In that figure, Sequence 1, which consists of 4 frames, completes the initial setup of the hardware and data file. Sequence 1 frame 0, shown in Figure B.1, creates a data file, prepares it for writing, and writes the file header. Details on the data file structure are given in Section B.2. Sequence 1 frame 1, shown in Figure B.3, initializes and configures the F/T sensor. Sequence 1 frame 2, shown in Figure B.4, configures the Maxon servo amplifier/controller. Sequence 1 frame 3, shown in Figure B.5, initializes and configures the Keithley DAC and specifies the waveform output. Figures B.6 through B.12 show the sub 'VIs' that calculate the waveform. The right hand side of the main program, shown in Figure B.2, contains the main program loop. The while loop runs at a preset frequency and for a specified

length of time while reading the F/T sensor and motor speed/current information, writing it to file once per loop. At the end of the test the frame on the far right of Figure B.2 writes test notes and any errors then closes the data file. The true/false cases in Figure B.2 are shown in Figures B.13 through B.15.

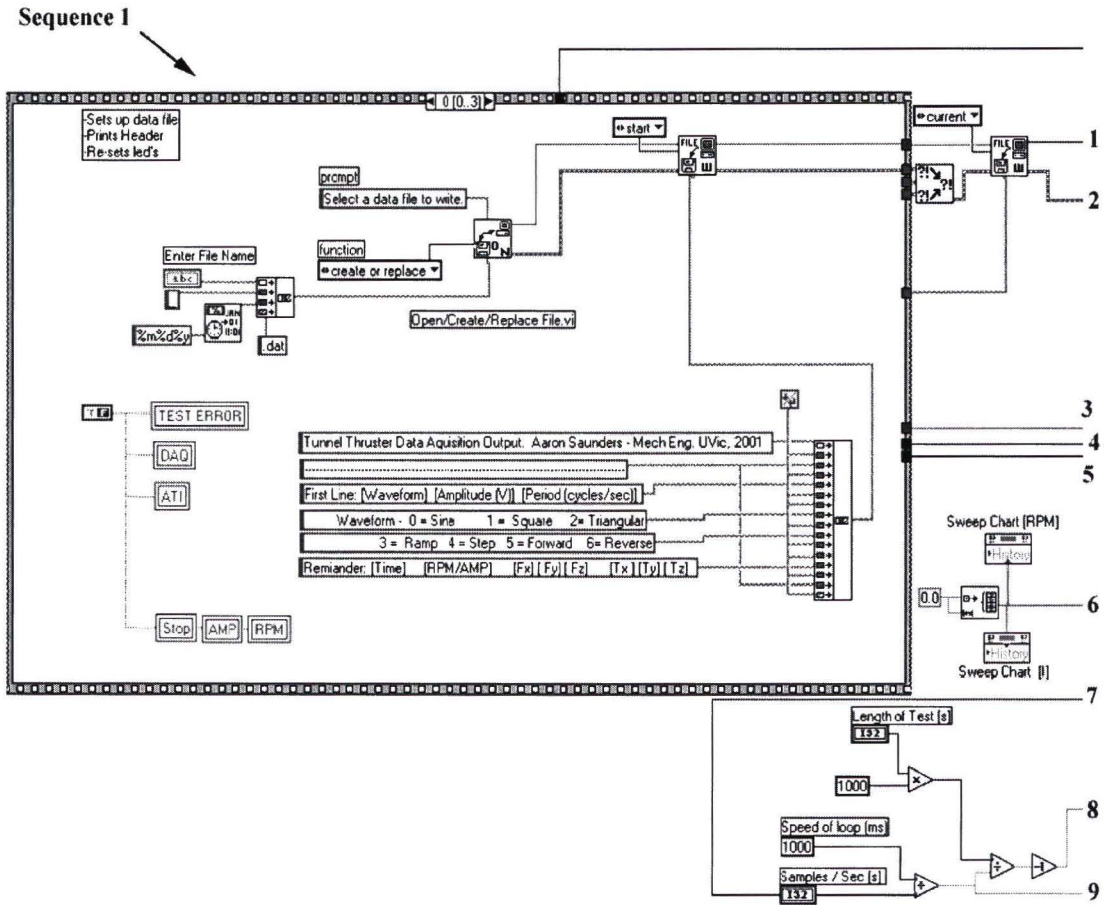


Figure B.1. LabVIEW Program: Main Diagram Part 1 of 2

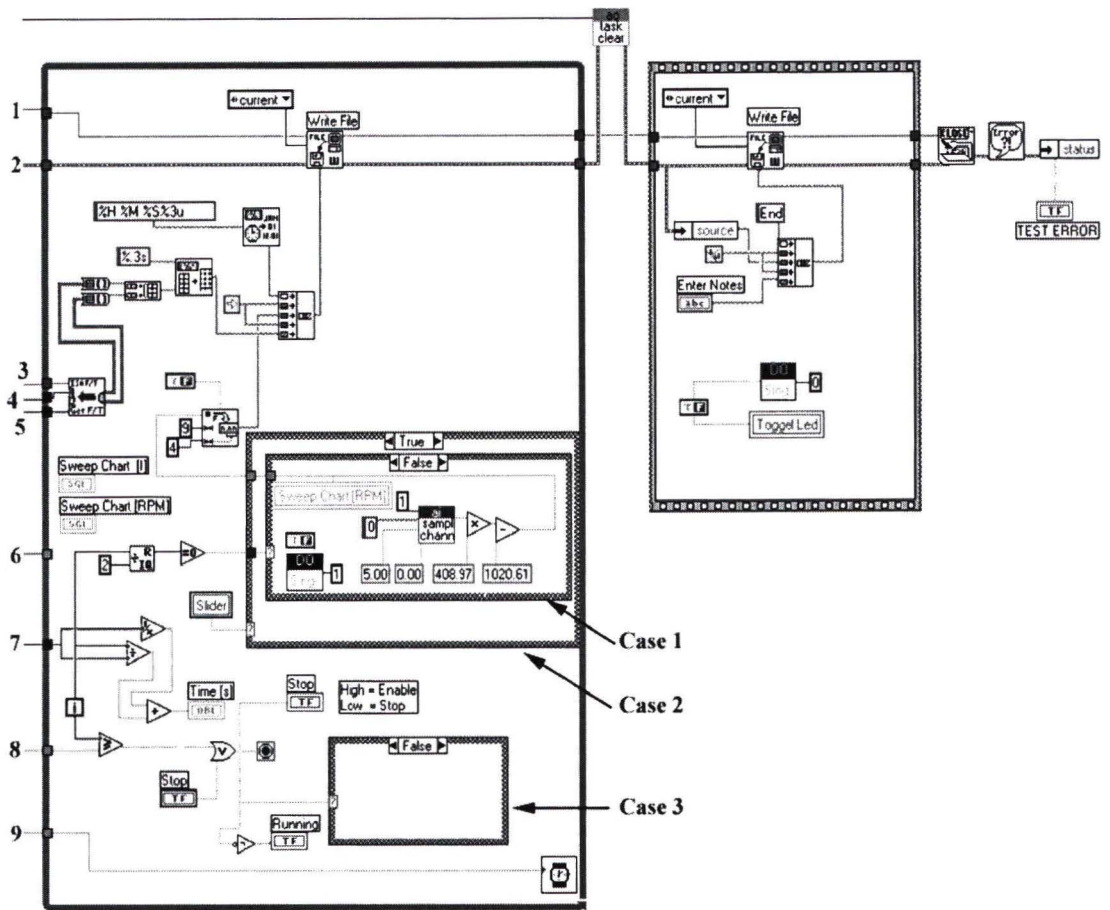


Figure B.2. LabVIEW Program: Main Diagram Part 2 of 2

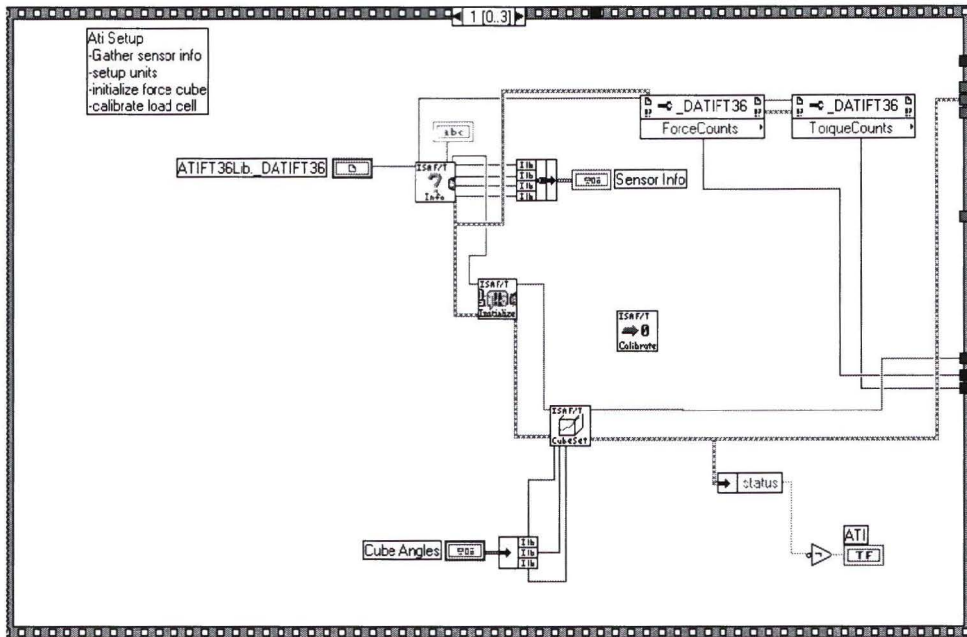


Figure B.3. LabVIEW Program: Sequence 1, Frame 1

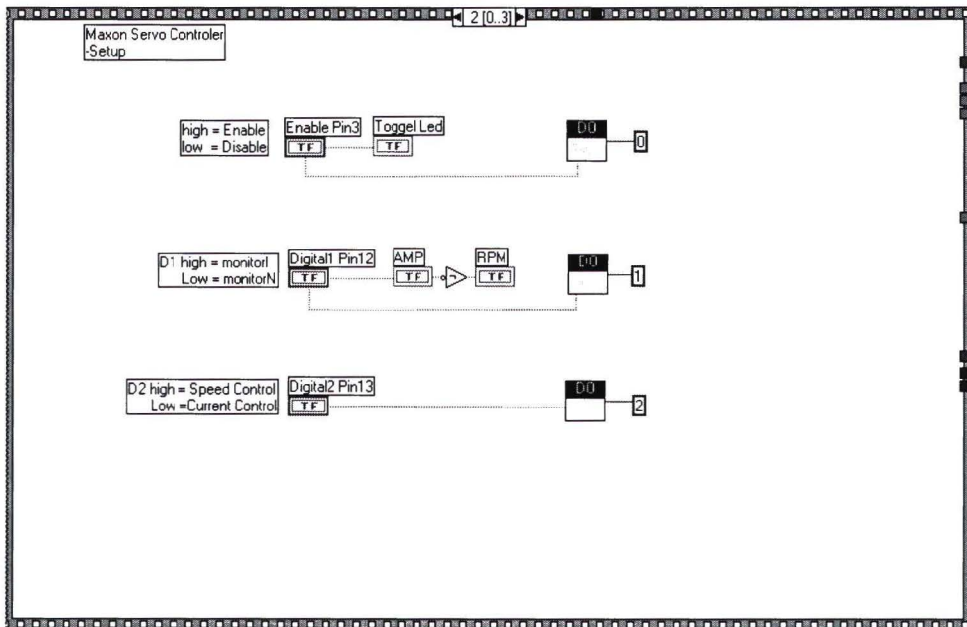


Figure B.4. LabVIEW Program: Sequence 1, Frame 2

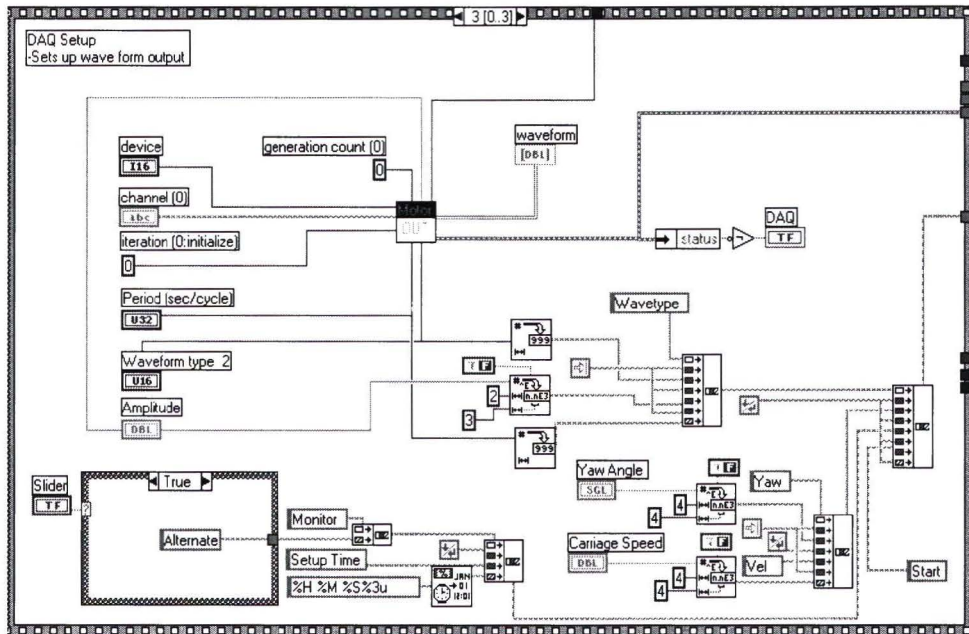


Figure B.5. LabVIEW Program: Sequence 1, Frame 3

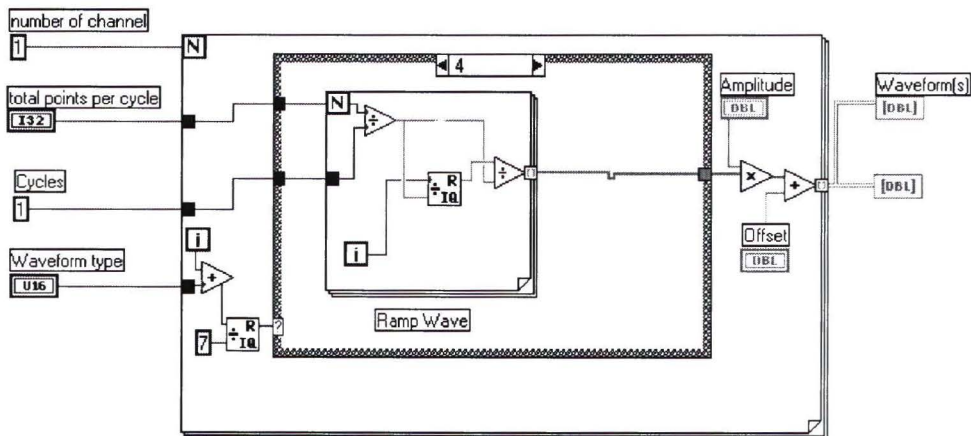


Figure B.6. LabVIEW Control Wave Program: Main Frame, with Sub Frame 4

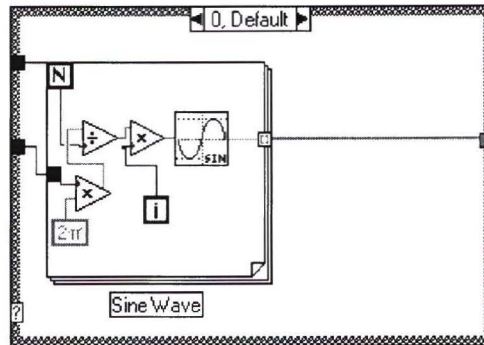


Figure B.7. LabVIEW Control Wave Program: Sub Frame 0, Sine Wave

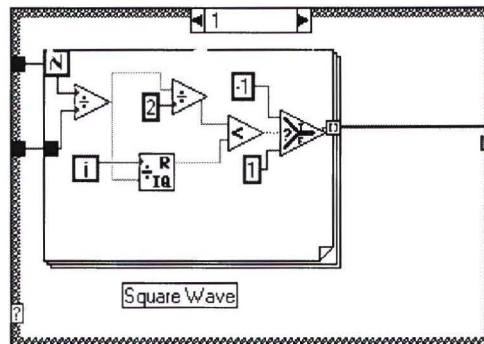


Figure B.8. LabVIEW Control Wave Program: Sub Frame 1, Square Wave

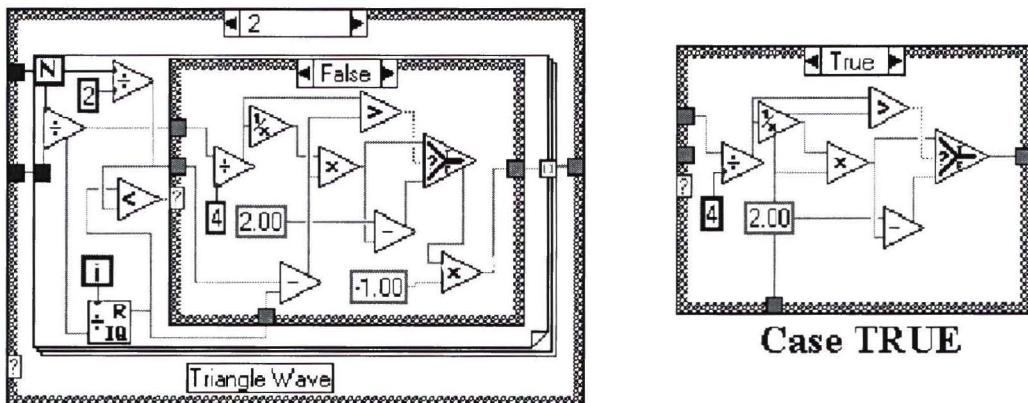


Figure B.9. LabVIEW Control Wave Program: Sub Frame 2, Triangular Wave

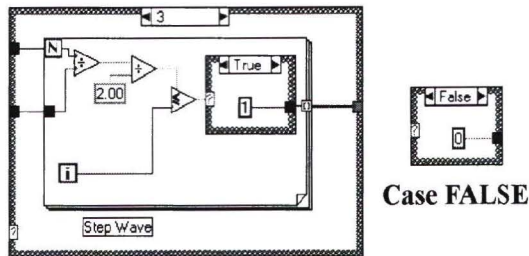


Figure B.10. LabVIEW Control Wave Program: Sub Frame 3, Step Wave

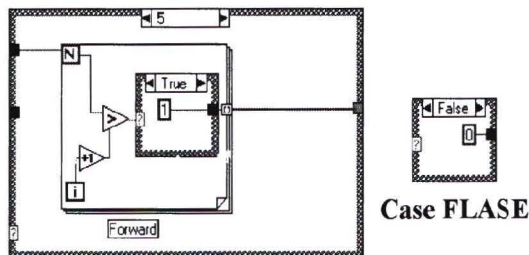


Figure B.11. LabVIEW Control Wave Program: Sub Frame 5, Constant Forward Speed

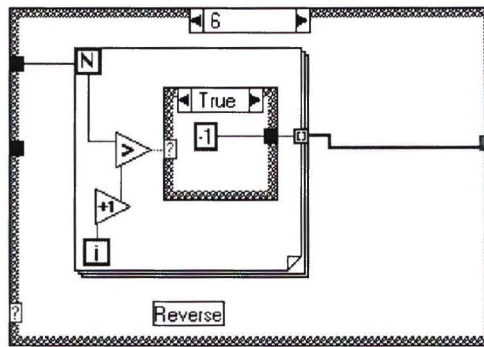


Figure B.12. LabVIEW Control Wave Program: Sub Frame 6, Constant Reverse Speed

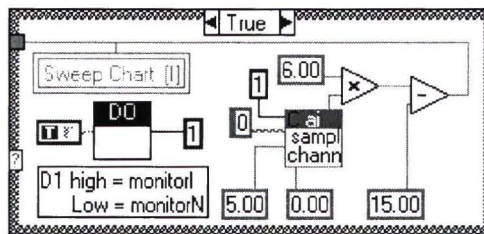


Figure B.13. LabVIEW Program: Case 1, State TRUE

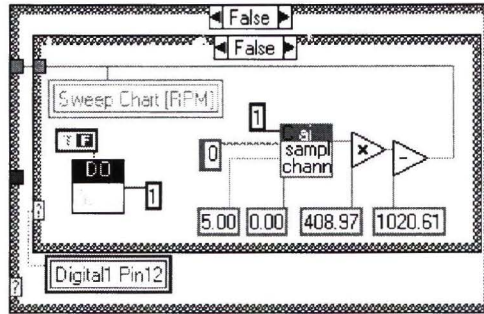


Figure B.14. LabVIEW Program: Case 2, State FALSE

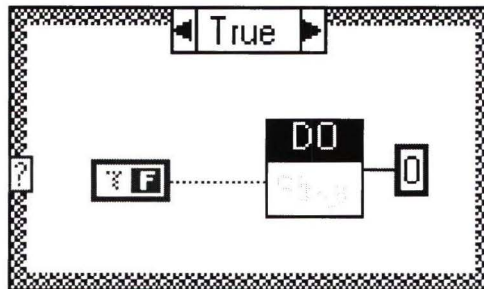


Figure B.15. LabVIEW Program: Case 3, State TRUE

B.2 Data File Structure

Figure B.16 shows a sample data file. The file header contains the structure of the data file. This is followed by waveform information, servo motor monitor type. Finally the motor speed/current data and F/T sensor data are recorded, each data point is time stamped. The last thing written to the data file are the test notes entered into the GUI by the user and any test errors.

```

A01_012902.dat - Notepad
File Edit Search Help
-----
Tunnel Thruster Data Acquisition Output.  Aaron Saunders - Mech Eng. UVic, 2001
-----
First Line: [Waveform] [Amplitude (V)] [Period (cycles/sec)]
           Waveform - 0 = Sine      1 = Square    2= Triangular
                   3 = Ramp    4 = Step    5 = Forward    6= Reverse
Remiander: [Time]      [RPM/AMP]    [Fx] [ Fy] [ Fz]    [Tx ] [Ty ] [ Tz]
-----
Wavetype      4      9.000E+0      20
Yaw      -90.0000E+0
Vel      100.0000E-3
Monitor Speed
Setup Time 13 10 51.165
Start
13 10 51.185      -0.9932      -0.075  0.025  0.025  -0.100  -0.050  0.000
:
:
:
13 11 11.214      548.0984      -2.475  0.025  -0.075  -1.075  -11.850  0.300
End

30 samp/sec
ATI 100Hz IIR 6M

```

Figure B.16. Data File Structure

Appendix C

Simulink Diagrams

C.1 Basic Simulation Simulink Program

Figure C.1 shows the Simulink program used to simulate the thrust and torque of the C-SCOUT through-body thruster. Below, a description is given of each block of this program is given.

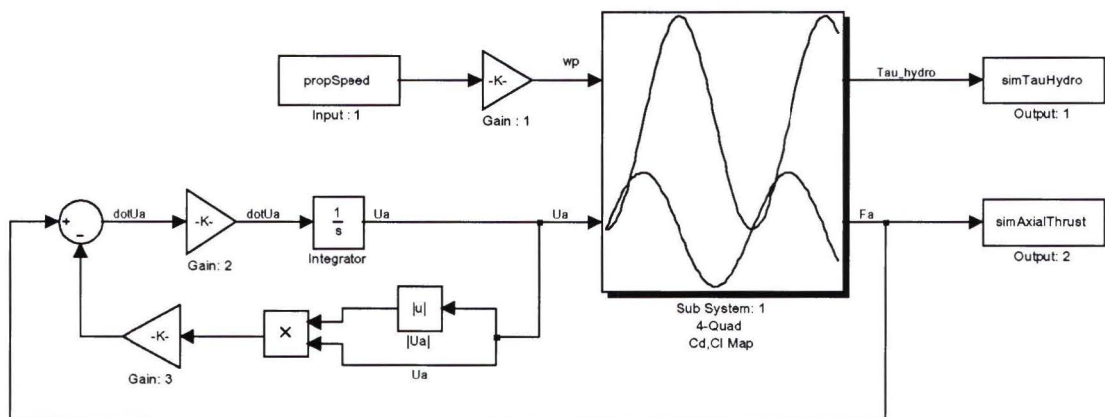


Figure C.1. Basic Simulation Simulink Diagram

- **Input: 1**, Propeller rotational speed in [RPM]. The motor speed has already been converted to prop speed using the gear reduction ratio by the LabVIEW GUI before being written to the data file.
- **Output: 1**, Simulated hydrodynamical torque of the propeller, T_p
- **Output: 2**, Simulated axial thrust, F_a
- **Gain 1:**, Converts propeller speed in [RPM] to $\left[\frac{\text{rad}}{\text{sec}}\right]$
- **Gain 2:**, Corresponds to $\frac{1}{K1}$, where $K1$ can be found in eq. (5.23)
- **Gain 2:**, Corresponds to $K2$, found in eq. (5.24)
- **Sub System: 1**, This sub system, shown in Figure C.2, is the four quadrant map of lift and drag. This sub system receives as inputs the propeller speed, ω_p , and the axial water velocity, U_a , and returns axial thrust, F_a , and propeller torque, T_p . This system corresponds to the theory covered in Section 5.2.1.b.
 - **Gain: S1-1**, Converts prop speed to tangential water velocity, corresponding to eq. (5.5).
 - **Gain: S1-2**, Converts tangential force, F_p , to torque prop load, T_p , corresponding to eq. (5.10).
 - **Function: S1-1**, Calculates the magnitude of the incoming water velocity vector, corresponds to eq. (5.6).
 - **Function: S1-2**, Calculates blade lift, L , Corresponding to eq. (5.11).
 - **Function: S1-3**, Calculates blade drag, D , Corresponding to eq. (5.12).

- **Functions: S1-4 & S1-5**, The blade lift and drag are transformed into forces of interest using the transformation matrix in eq. (5.9).
- **Sub System: S1**, This sub system, shown in Figure C.3, calculates the angle of incidence, α , and hydrodynamic pitch angle, θ , from the axial and tangential water velocity components, U_a and U_p . It handles the division by zero when $U_p = 0$ by setting $\theta = \frac{\pi}{2}$.
 - * **Function: S2-1**, Calculates hydrodynamic pitch angle, corresponding to eq. (5.7).
 - * **Function: S2-2**, Calculates the angle of attack, corresponding to eq. (5.8).

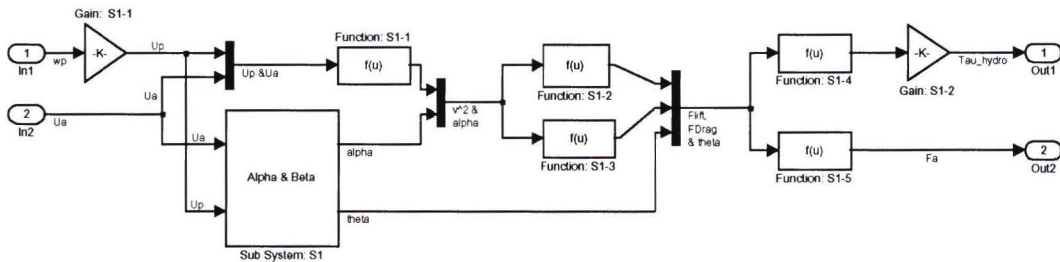


Figure C.2. Sub System: 1

C.2 Augmented Simulation Simulink Program

For the augmented simulation, shown in Figure C.4, only the blocks that differ from the basic simulation will be described. For the description of all the other blocks see the previous section.

- **Sub System: 2**, This sub system, shown in Figure C.5, calls the sub system that looks up the slope value, b , based on the direction of axial water velocity, U_a .

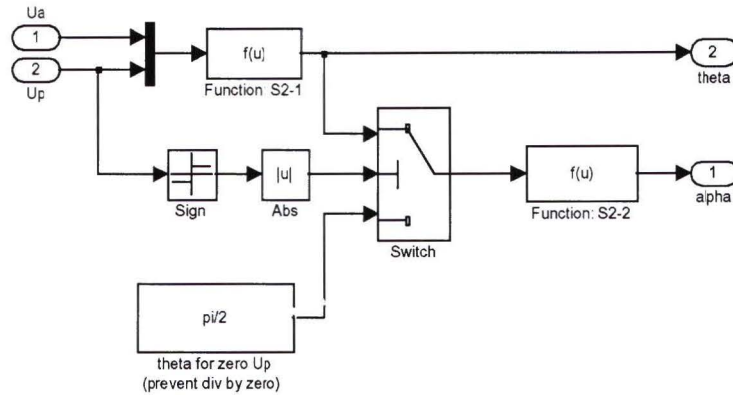


Figure C.3. Sub System: S1

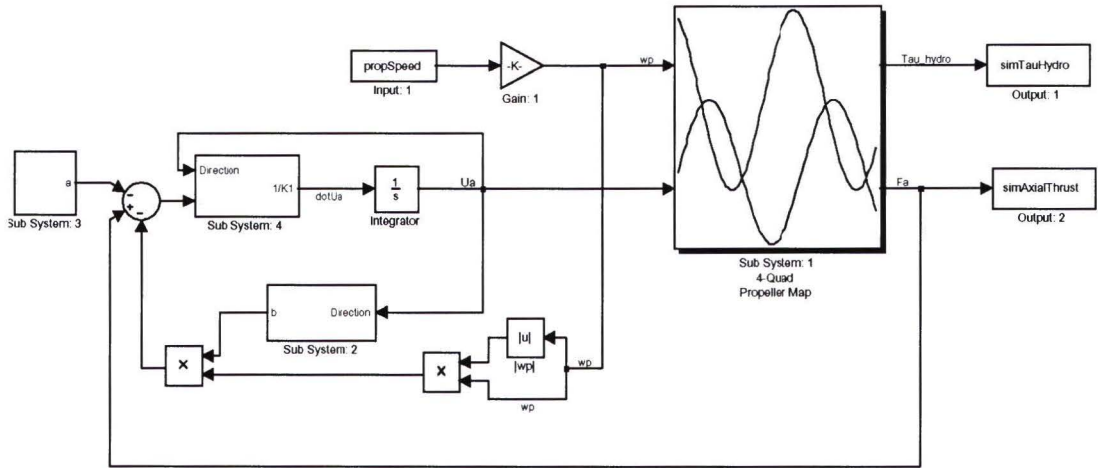


Figure C.4. Augmented Simulation Simulink Diagram

- **Sub System: S2-1**, This sub system, shown in Figure C.6, looks up the slope value for the corresponding test case and $+U_a$. The inputs to the lookup table are element locations in the slope (or test) matrix. This sub system corresponds to the relationship in eq. (5.39).

* **Gain: S2-1-1**, Slope values have to be converted from $\frac{N}{(\text{RPM})^2}$ to $\frac{N}{(\text{rad/sec})^2}$.

- **Sub System: S2-2**, This sub system, shown in Figure C.7, looks up the slope value for the corresponding test case and $-U_a$. The inputs to the

lookup table are element locations in the slope (or test) matrix. This sub system corresponds to the relationship in eq. (5.39).

- * **Gain: S2-2-1**, Adjusts for asymmetry in thruster performance using $bMod$, accounts for the percent increase in thrust between positive and negative prop RPM, calculated from steady state tests.
- * **Gain: S2-2-2**, Slope values have to be converted from $\frac{N}{(RPM)^2}$ to $\frac{N}{(rad/sec)^2}$.
- **Sub System: 3**, This sub system, shown in Figure C.8, looks up the value for the axial thrust intercept, a , for the corresponding test case. The inputs to the lookup table are element locations in the test matrix
- **Sub System: 4**, This sub system, shown in Figure C.9, selects the correct value for $K1$, in eq. (5.34).
 - **Gain: S2-1a**, Calculates $K1$ for γ_F .
 - **Gain: S2-1b**, Calculates $K1$ for γ_R .

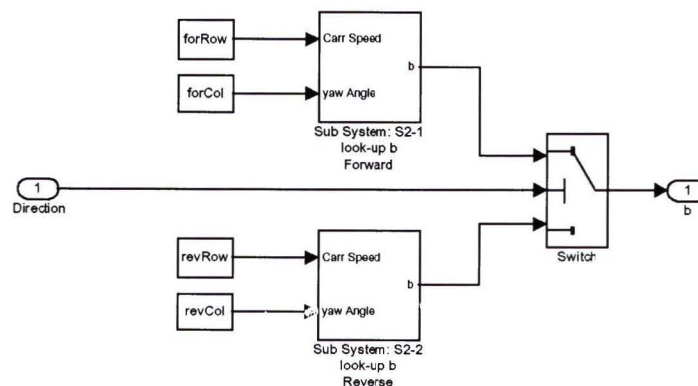


Figure C.5. Sub System: 2

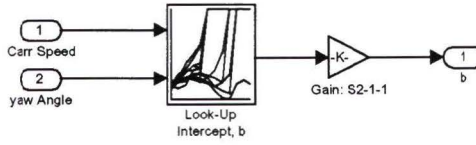


Figure C.6. Sub System: S2-1

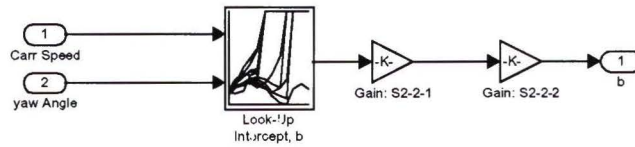


Figure C.7. Sub System: S2-2

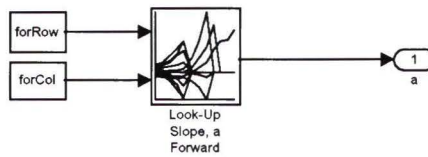


Figure C.8. Sub System: 3

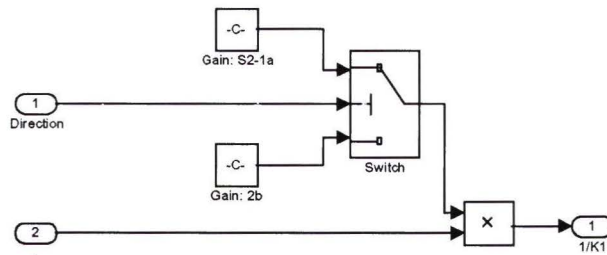


Figure C.9. Sub System: 4

References

- [1] Abbott, I. and A. von Doenhoff: 1949, *Theory of Wing Sections*. McGraw-Hill.
- [2] Anon: 1979, 'Advancing Technology for Lateral Thrusters'. *The Motor Ship* **59**(703), 55–56.
- [3] Bachmayer, R., M. Whitcomb, and M. Grosenbaugh: 1998, 'A Four Quadrant Finite Dimensional Thruster Model'. In: *IEEE/OES Conference Proceedings OCEANS'98*, Vol. 2. Nice, France.
- [4] Bachmayer, R., D. Yoerger, and M. Grosenbaugh: 2000, 'An Accurate Four-Quadrant Nonlinear Dynamical Model for Marine Thrusters: Theory and Experimental Validation'. *IEEE Journal of Oceanic Engineering* **25**(1), 146–159.
- [5] Beveridge, J.: 1972, 'Design and Performance of Bow Thrusters'. *Marine Technology* **9**(4), 439–453.
- [6] Blanke, M., K. Lingaard, and T. Fossen: 2000, 'Dynamic Model for Thrust Generation of Marine Propellers'. In: *Conference on Marine Craft Maneuvering and Control*.
- [7] Brown, J.: 1993, 'Four Quadrant Dynamical Model of the AUV II Thruster'. Master's thesis, Naval Postgraduate School, Monterey, California.
- [8] Carlton, J.: 1994, *Marine Propellers and Propulsion*. Boston: Oxford, Butterworth-Heinemann.
- [9] Clayton, B. and R. Bishop: 1982, *Mechanics of Marine Vehicles*, Chapt. 7. Gulf Publishing Company. ISBN 0-87201-897-0.
- [10] Curtis, T., D. Perrault, C. Williams, and N. Bose: 2000, 'C-SCOUT: A General-Purpose AUV for Systems Research'. *Presented at Underwater Technology 2000*.
- [11] Fossen, T.: 1994, *Guidance and Control of Ocean Vehicles*. NY: John Wiley and Sons Ltd.

- [12] Healey, A., S. Rock, S. Cody, and J. Brown: 1995, 'Toward an Improved Understanding of Thruster Dynamics for Underwater Vehicles'. *IEEE Journal of Oceanic Engineering* **20**(4), 354–361.
- [13] Mailfert, G. and J. LeMaire: 1998, 'REDERMOR: an Experimental platform for ROV/AUV field sea trial'. In: *Oceans Conference Record (IEEE) Oceans 1998*, Vol. 1. Nice, France.
- [14] Marco, D. and A. Healey: 2000, 'Current Developments in Underwater Vehicle Control and Navigation: The NPS ARIES AUV'. In: *Oceans Conference Record (IEEE) Oceans 2000*. Providence, RI.
- [15] Maxon, Precision, Motors, and Inc.: 2000, 'Maxon 2000 Main Catalog'. pp. 22–23, 131.
- [16] McLean, M.: 1991, 'Dynamical Performance of Small Diameter Tunnel Thrusters'. Master's thesis, Naval Postgraduate School, Monterey, California.
- [17] Nahon, M.: 1996, 'A Simplified Dynamics Model for Autonomous Underwater Vehicles'. In: *IEEE Proceedings of Autonomous Underwater Vehicle Technology*. pp. 373–379.
- [18] National and Instruments: 2000, *National Instruments Labview User Manual*. Austin, Texas:.
- [19] Norrby, R. and D. Ridley: 1980, 'Notes on Thrusters for Ship Maneuvering and Dynamic Positioning'. *SNAME Transactions* **88**, 377–402.
- [20] Rickards, M.: 1970, 'Cycloidal Propulsion of Submersibles'. *Journal Hydronautics* **4**(2), 66–72.
- [21] Ridley, D.: 1971, 'Observations on the Effect of Vessel Speed on Bow Thruster Performance'. *Marine Technology* pp. 93–96.
- [22] Sorensen, A., A. Adnanes, T. Fossen, and J. Strand: 1997, 'Dynamic Model for Thrust Generation of Marine Propellers'. In: *Conference on Marine Craft Maneuvering and Control*.
- [23] van Lammeren, W., J. van Manen, and M. Ooseterveld: 1969, 'The Wageningen B-Screw Series'. *Trans. SNAME* pp. 269–317.
- [24] Wang, H., R. Marks, T. McLain, S. Fleischer, D. Miles, G. Sapilewski, and S. Rock: 1995, 'Otter: A Testbed Submersible for Robotics Research'. In: *Proceedings of ANS 95*. Monterey, California.

- [25] Whitcomb, L. and D. Yoerger: 1999, 'Development, Comparison, and Preliminary Experimental Validation of Non-Linear Dynamic thruster Models'. *IEEE Journal of Oceanic Engineering* **24**, 495–506.
- [26] Whitney, J. and S. Smith: 1998, 'Observations on the Dynamic Performance of Tunnel Thrusters'. In: *Oceans Conference Record (IEEE) Oceans 1998*. Nice, France.
- [27] Yoerger, D., J. Cooke, and J. Soltine: 1990, 'The Influence of Thruster Dynamics on Underwater Vehicle Behaviour and their Incorporation Into Control System Design'. *IEEE Journal of Oceanic Engineering* **15**(3), 167–178.

Vita

Surname: Saunders

Given Names: Aaron

Place of Birth: Edmonton, Alberta, Canada

Date of Birth: July 07, 1978

Educational Institutions Attended:

University of Alberta

1996 to 2000

University of Victoria

2000 to 2002

Degrees Awarded:

B. Eng. (Mechanical) University of Alberta

2000

Publications:

C.D.Williams, D.Perrault, T.Curtis, H.Bijleveld, A.Saunders, N.Bose, S.O'Young,
"Autonomous Vehicle Systems Research at NRC-IMD", NATO SCI symposium,
Berlin, GE 13 -15 May 2002

J.A.Smith, A.Saunders, R.Chaldney, R.Toogood, "Polar Bear - Rugged Outdoor Mo-
bile Robotic Platform", Proceedings of the International Symposium on Robotics
2000, May 14-17 2000, Montreal, Canada

Partial Copyright License

I hereby grant the right to lend my thesis to users of the University of Victoria Library, and to make single copies only for such users or in response to a request from the Library of any other university, or similar institution, on its behalf or for one of its users. I further agree that permission for extensive copying of this thesis for scholarly purposes may be granted by me or a member of the University designated by me. It is understood that copying or publication of this thesis for financial gain shall not be allowed without my written permission.

Title of Thesis:

The Effect of Velocity and Orientation on the Simulation and Experimental Characterization of an AUV Tunnel Thruster

Author



Aaron Saunders
June 15, 2003